

**CONTROLLED HYDROTHERMAL SYNTHESIS AND  
STRUCTURE-PROPERTY RELATIONSHIPS OF  
TRANSITION METAL VANADATES**

---

A Dissertation Presented to  
the Faculty of the Department of Chemistry  
University of Houston

---

In Partial Fulfillment  
of the Requirements for the Degree  
Doctor of Philosophy

---

By  
Kewen Sun

December 2014

**CONTROLLED HYDROTHERMAL SYNTHESIS AND  
STRUCTURE-PROPERTY RELATIONSHIPS OF  
TRANSITION METAL VANADATES**

---

Kewen Sun

APPROVED:

---

Dr. Angela Möller, Chair

---

Dr. Arnold M. Guloy

---

Dr. Shoujun Xu

---

Dr. James K. Meen

---

Dr. Jakoah Brgoch

---

Dean, College of Natural Sciences and  
Mathematics

*Dedicated to*

*My parents: Yunlong Sun, Yi Wang*

*and*

*Yangkai Peng*

*for their never ending love, encouragement, support, and prayers*

## Acknowledgments

Foremost, I would also like to thank my advisor, Dr. Angela Möller, for the support of my PhD study and research, for her patience, enthusiasm, and immense knowledge. Her guidance helped me in all the time of research and writing of this thesis. I could not have imagined having a better advisor and mentor.

I would also like to thank the members of my committee, Dr. Arnold M. Guloy, Dr. Shoujun Xu, Dr. James K. Meen, and Dr. Jakoah Brgoch, for their helpful suggestions concerning my research. I am thankful to Dr. Alexander P. Litvinchuk, Dr. James K. Meen, and Dr. Bernd Lorenz for their guidance and assistance in my research.

I would like to thank my parents, Yunlong Sun and Yi Wang, for their constant love, understanding, and encouragement. To my girl friend, Yangkai Peng, I can feel your love and care even across the Pacific Ocean. I would not have today's achievements without your support.

I would like to thank Dr. Dana E. Gheorghe, not only for helping me when I began my research, but also for the continuous suggestions for my life.

I would also like to thank my group members and friends whom I will miss so much: Dr. Yan Chen, Dr. Ngozi E. Amuneke, Michaela Bratsch, Joshua Tapp, Anna Duke, Mat Bosch, Phillip Daniel, Sven Waniek, and all the other friends I made while in graduate school.



**CONTROLLED HYDROTHERMAL SYNTHESIS AND  
STRUCTURE-PROPERTY RELATIONSHIPS OF  
TRANSITION METAL VANADATES**

---

An Abstract of a Dissertation Presented to  
the Faculty of the Department of Chemistry  
University of Houston

---

In Partial Fulfillment  
of the Requirements for the Degree  
Doctor of Philosophy

---

By  
Kewen Sun  
December 2014

## Abstract

This dissertation focuses on the synthesis and structure-property relationships of multi-anionic transition metal vanadates. Hydrothermal synthesis methods have been optimized and used to obtain compounds with intriguing structural features.  $\text{Ba}_2\text{XCu}(\text{OH})[\text{V}_2\text{O}_7]$  with  $X = \text{Cl}, \text{Br}$  crystallizes in a new structure type ( $Pnma$ ,  $a \approx 15.1 \text{ \AA}$ ,  $b \approx 6.1 \text{ \AA}$ ,  $c \approx 9.6 \text{ \AA}$ ) which features pseudo-honeycomb  ${}^2_\infty[\text{Ba}_2\text{X}]^{3+}$  layers and isolated  ${}^1_\infty[\text{CuO}_{2/2}(\text{OH})_{2/2}\text{O}_{2/1}]^{5-}$  chains. Two polymorphs of the  $M_2(\text{OH})[\text{VO}_4]$  compound were obtained with  $M = \text{Mn}$  ( $Pnma$ ,  $a = 14.911(1) \text{ \AA}$ ,  $b = 6.1225(3) \text{ \AA}$ ,  $c = 9.1635(5) \text{ \AA}$ ) and  $M = \text{Cu}$  ( $P2_12_12_1$ ,  $a = 6.0564(1) \text{ \AA}$ ,  $b = 8.5581(2) \text{ \AA}$ ,  $c = 14.954(1) \text{ \AA}$ ). These two structures are similar with respect to the  $M\text{--O--}M$  connectivity, which results in corrugated layers. The  $M_{6+x}(\text{OH})_3[\text{VO}_4]_{4-2z}[\text{V}_2\text{O}_7]_z$  series of compounds with  $M = \text{Mn}, \text{Co}, \text{Mg}, \text{and Fe}$  crystallize in the acentric  $P6_3mc$  space group with lattice parameters  $a \approx 12.9 - 13.2 \text{ \AA}$ ,  $c \approx 5.1 - 5.3 \text{ \AA}$  featuring a metal-based framework with isolated chains of face-sharing  $[\text{MO}_6]$ -units.  $\text{BaMn}_9[\text{VO}_4]_6(\text{OH})_2$  crystallizes in the space group  $P2_13$  with  $a = 12.8417(2) \text{ \AA}$  and has the unique structural feature of a chiral paddle-wheel. Further investigations of thermodynamic properties reveal for: i)  $\text{Ba}_2\text{XCu}(\text{OH})[\text{V}_2\text{O}_7]$  an antiferromagnetic quasi 1D  $S = 1/2$  Heisenberg system; ii)  $\text{Cu}_2(\text{OH})[\text{VO}_4]$  an antiferromagnetically coupled 2D lattice with ferrimagnetic long-range order; iii)  $M_{6+x}(\text{OH})_3[\text{VO}_4]_{4-2z}[\text{V}_2\text{O}_7]_z$  an antiferromagnetic framework ferrimagnetically coupled to the incorporated chains; iv)  $\text{BaMn}_9[\text{VO}_4]_6(\text{OH})_2$  a canted antiferromagnet due to geometrical frustration.

## Table of Contents

List of Figures .....	xii
List of Tables .....	xxiii
Abbreviations and Acronyms .....	xxvii
Chapter 1 General Introduction .....	1
References. ....	3
Chapter 2 Experimental Methods .....	5
2.1 Hydrothermal Synthesis. ....	6
2.1.1 Introduction to Hydrothermal Synthesis.....	6
2.1.2 Synthesis Conditions. ....	7
2.2 Structure Determination Methods. ....	9
2.2.1 Introduction to X-ray Diffraction. ....	9
2.2.2 Selection of Single Crystal for X-ray Diffraction Studies.....	11
2.2.3 Single Crystal X-ray Diffraction. ....	11
2.2.4 Powder X-ray Diffraction. ....	12
2.3 Scanning Electron Microscopy and Energy Dispersive X-ray Spectrometry. ....	12
2.4 Differential Scanning Calorimetry. ....	13
2.5 Vibrational Spectroscopy. ....	15

2.5.1 Introduction to Vibrational Spectroscopy.....	15
2.5.2 Vibrational Spectroscopy of Vanadates. ....	17
2.5.3 Infrared Spectroscopy.....	19
2.5.4 Raman Spectroscopy. ....	21
2.5.5 Instrumentation of Infrared and Raman Spectroscopy. ....	23
2.6 Physical Properties. ....	24
2.6.1 Introduction to Magnetism. ....	24
2.6.2 Introduction to Specific Heat ( $C_p$ ). ....	27
2.6.3 Magnetic Measurement. ....	28
2.6.4 Specific Heat Measurement.....	29
2.7 References .....	30

Chapter 3 Synthesis, Crystal Structures, Lattice Dynamics, and Magnetic Properties of $\text{Ba}_2\text{XCu}(\text{OH})[\text{V}_2\text{O}_7]$ with $X = \text{Cl}, \text{Br}$ .....	34
3.1 Introduction. ....	34
3.2 Synthesis of Single Crystals of $\text{Ba}_2\text{XCu}(\text{OH})[\text{V}_2\text{O}_7]$ , $X = \text{Cl}, \text{Br}$ .....	35
3.3 Scanning Electron Microscopy-Energy Dispersive X-ray Spectroscopy (SEM-EDX) of $\text{Ba}_2\text{XCu}(\text{OH})[\text{V}_2\text{O}_7]$ , $X = \text{Cl}, \text{Br}$ . ....	37
3.4 Single Crystal X-ray Diffraction of $\text{Ba}_2\text{XCu}(\text{OH})[\text{V}_2\text{O}_7]$ , $X = \text{Cl}, \text{Br}$ .....	39
3.5 Powder X-ray Diffraction and Refinement of $\text{Ba}_2\text{XCu}(\text{OH})[\text{V}_2\text{O}_7]$ , $X = \text{Cl}, \text{Br}$ .....	45
3.6 Crystal Structure Description and Discussion for $\text{Ba}_2\text{XCu}(\text{OH})[\text{V}_2\text{O}_7]$ , $X = \text{Cl}, \text{Br}$ . ....	48
3.7 Spectroscopy for $\text{Ba}_2\text{XCu}(\text{OH})[\text{V}_2\text{O}_7]$ , $X = \text{Cl}, \text{Br}$ .....	53

3.8 Physical Properties of $\text{Ba}_2\text{XCu}(\text{OH})[\text{V}_2\text{O}_7]$ , $X = \text{Cl}, \text{Br}$ .	59
3.9 Conclusions.	63
3.10 References.	65
3.11 Supplemental Material.	67
Chapter 4 Synthesis, Crystal Structures, and Physical Properties of $\text{M}_2(\text{OH})[\text{VO}_4]$ with $\text{M} = \text{Mn}, \text{Cu}$ .	85
4.1 Introduction.	85
4.2 Synthesis of Single Crystals of $\text{M}_2(\text{OH})[\text{VO}_4]$ with $\text{M} = \text{Mn}, \text{Cu}$ .	86
4.3 Single Crystal X-ray Diffraction of $\text{M}_2(\text{OH})[\text{VO}_4]$ with $\text{M} = \text{Mn}, \text{Cu}$ .	89
4.4 Powder X-ray Diffraction and Refinement of $\text{Cu}_2(\text{OH})[\text{VO}_4]$ .	91
4.5 Crystal Structure Description and Discussion for $\text{M}_2(\text{OH})[\text{VO}_4]$ with $\text{M} = \text{Mn}, \text{Cu}$ .	93
4.6 Physical Properties of $\text{Cu}_2(\text{OH})[\text{VO}_4]$ .	101
4.7 Conclusions.	108
4.8 References.	110
4.9 Supplemental Material.	111
Chapter 5 Synthesis, Crystal Structures, and Physical Properties of a Unique Canted Antiferromagnet: $\text{BaMn}_9[\text{VO}_4]_6(\text{OH})_2$ .	120
5.1 Introduction.	120
5.2 Synthesis of Single Crystals of $\text{BaMn}_9[\text{VO}_4]_6(\text{OH})_2$ .	121

5.3 Scanning Electron Microscopy-Energy Dispersive X-ray Spectroscopy (SEM-EDX) of $\text{BaMn}_9[\text{VO}_4]_6(\text{OH})_2$ .....	123
5.4 Single Crystal X-ray Diffraction of $\text{BaMn}_9[\text{VO}_4]_6(\text{OH})_2$ .....	124
5.5 Powder X-ray Diffraction and Refinement of $\text{BaMn}_9[\text{VO}_4]_6(\text{OH})_2$ .....	126
5.6 Crystal Structure Description and Discussion for $\text{BaMn}_9[\text{VO}_4]_6(\text{OH})_2$ .....	128
5.7 Spectroscopy for $\text{BaMn}_9[\text{VO}_4]_6(\text{OH})_2$ .....	133
5.8 Physical Properties of $\text{BaMn}_9[\text{VO}_4]_6(\text{OH})_2$ .....	136
5.9 Discussion of the Structure-Property Relationship. ....	146
5.10 Conclusions. ....	149
5.11 References. ....	150
5.12 Supplemental Material. ....	153

## Chapter 6 Synthesis, Crystal Structures, Lattice Dynamics and Physical Properties of Dumortierite-Like Compounds: $M_{6+x}(\text{OH})_3[\text{VO}_4]_{4-2z}[\text{V}_2\text{O}_7]_z$ with $M = \text{Mn, Co, Mg, Fe}$

.....	161
6.1 Introduction. ....	161
6.2 Synthesis of Single Crystals of $M_{6+x}(\text{OH})_3[\text{VO}_4]_{4-2z}[\text{V}_2\text{O}_7]_z$ .....	163
6.3 Scanning Electron Microscopy-Energy Dispersive X-ray Spectroscopy (SEM-EDX) of $M_{6+x}(\text{OH})_3[\text{VO}_4]_{4-2z}[\text{V}_2\text{O}_7]_z$ .....	167
6.4 Single Crystal X-ray Diffraction of $M_{6+x}(\text{OH})_3[\text{VO}_4]_{4-2z}[\text{V}_2\text{O}_7]_z$ .....	168
6.5 Powder X-ray Diffraction and Refinement of $M_{6+x}(\text{OH})_3[\text{VO}_4]_{4-2z}[\text{V}_2\text{O}_7]_z$ .....	172
6.6 Crystal Structure Description and Discussion for $M_{6+x}(\text{OH})_3[\text{VO}_4]_{4-2z}[\text{V}_2\text{O}_7]_z$ ....	174
6.7 Spectroscopy for $M_{6+x}(\text{OH})_3[\text{VO}_4]_{4-2z}[\text{V}_2\text{O}_7]_z$ .....	184

6.8 Physical Properties of $M_{6+x}(\text{OH})_3[\text{VO}_4]_{4-2z}[\text{V}_2\text{O}_7]_z$ .....	193
6.9 Discussion of the Structure-Property Relationship. ....	201
6.10 Conclusions. ....	203
6.11 References. ....	204
6.12 Supplemental Material. ....	206
 Chapter 7 Summary .....	 228

## List of Figures

Figure 2.1	<i>Left:</i> Stainless steel autoclave. <i>Right:</i> Teflon liner. ....	7
Figure 2.2	Geometrical illustration of the Braggs' law. ....	10
Figure 2.3	The electromagnetic spectrum. ....	20
Figure 2.4	Energy level diagram for Raman scattering; (1) Stokes scattering, (2) Rayleigh scattering, (3) anti-Stokes scattering. ....	22
Figure 2.5	Temperature dependent magnetic susceptibility in an antiferromagnetic compound, and a ferromagnetic compound .....	26
Figure 2.6	Possible ordering of electron spins. ....	27
Figure 3.1	Photos of magnified crystals. <i>Left:</i> $\text{Ba}_2\text{ClCu}(\text{OH})[\text{V}_2\text{O}_7]$ . <i>Right:</i> $\text{Ba}_2\text{BrCu}(\text{OH})[\text{V}_2\text{O}_7]$ . ....	35
Figure 3.2	Morphologies of $\text{Ba}_2\text{BrCu}(\text{OH})[\text{V}_2\text{O}_7]$ crystals grown at different pH values. Crystals were synthesized at initial pH = 7.8 ( <i>top left</i> ), 8.5 ( <i>top right</i> ), 9.1 ( <i>bottom left</i> ), 9.8 ( <i>bottom right</i> ). ....	36
Figure 3.3	SEM pictures of carbon-coated samples indicating the morphology of the crystals: $\text{Ba}_2\text{ClCu}(\text{OH})[\text{V}_2\text{O}_7]$ ( <i>left</i> ), $\text{Ba}_2\text{BrCu}(\text{OH})[\text{V}_2\text{O}_7]$ ( <i>right</i> ). ....	37
Figure 3.4	<i>Left:</i> Image of reflections for $\text{Ba}_2\text{ClCu}(\text{OH})[\text{V}_2\text{O}_7]$ showing three domains circled by different colors. The main domain is Domain 1 (blue). <i>Right:</i> Matrices representing the orientations of the other two domains as related to Domain 1. Domain 2 (green) is clockwise rotated by $64.46^\circ$ , with respect to	



	<i>a</i> axis, and Domain 3 (red) is counterclockwise rotated by 64.64° with respect to <i>a</i> axis. ....	41
Figure 3.5	Photo of magnified Ba <sub>2</sub> BrCu(OH)[V <sub>2</sub> O <sub>7</sub> ] crystals under polarized light....	42
Figure 3.6	<i>Left</i> : Image of reflections for Ba <sub>2</sub> BrCu(OH)[V <sub>2</sub> O <sub>7</sub> ] showing streaks between unique reflections. <i>Right</i> : Indexed reflections showing the orientation of the streaks. ....	42
Figure 3.7	2 <i>F<sub>o</sub></i> - <i>F<sub>c</sub></i> electron density maps of Ba <sub>2</sub> BrCu(OH)[V <sub>2</sub> O <sub>7</sub> ] generated from crystal data ( <i>bc</i> plane). <i>Top</i> : Ba-Br pseudo-honeycomb type of arrangement. <i>Bottom</i> : Cu-O chains connected to [V <sub>2</sub> O <sub>7</sub> ]. Peaks (green), holes (red).....	44
Figure 3.8	Powder refinement data for Ba <sub>2</sub> ClCu(OH)[V <sub>2</sub> O <sub>7</sub> ] ( <i>left</i> ); Ba <sub>2</sub> BrCu(OH)[V <sub>2</sub> O <sub>7</sub> ] ( <i>right</i> ). Observed (red), calculated (black), Bragg positions (green) and difference (blue). ....	46
Figure 3.9	Projection of the crystal structure of Ba <sub>2</sub> XCu(OH)[V <sub>2</sub> O <sub>7</sub> ], X = Cl, Br.....	48
Figure 3.10	Projection of the intergrown $\frac{2}{\infty}$ [Ba <sub>2</sub> X] <sup>3+</sup> layer with the [V <sub>2</sub> O <sub>7</sub> ] <sup>4-</sup> in the center of a pseudo-honeycomb type of arrangement in Ba <sub>2</sub> XCu(OH)[V <sub>2</sub> O <sub>7</sub> ], X = Cl, Br. ....	49
Figure 3.11	Perspective view of [V <sub>2</sub> O <sub>7</sub> ] <sup>4-</sup> in the center of distorted hexagonal ring of $\frac{2}{\infty}$ [Ba <sub>2</sub> X] <sup>3+</sup> layer indicating a freedom of rotation between the [V <sub>2</sub> O <sub>7</sub> ] <sup>4-</sup> dimer and the $\frac{2}{\infty}$ [Ba <sub>2</sub> X] <sup>3+</sup> layer. ....	50
Figure 3.12	Perspective view of the $\frac{1}{\infty}$ [CuO <sub>2/2</sub> (OH) <sub>2/2</sub> O <sub>2/1</sub> ] <sup>5-</sup> chain in Ba <sub>2</sub> XCu(OH)[V <sub>2</sub> O <sub>7</sub> ], X = Cl, Br. ....	51

Figure 3.13	Experimental MIR-spectra and calculated displacements for $\text{Ba}_2\text{XCu}(\text{OH})[\text{V}_2\text{O}_7]$ , $X = \text{Cl}, \text{Br}$ .....	53
Figure 3.14	Vibrational patterns of $\text{Ba}_2\text{BrCu}(\text{OH})[\text{V}_2\text{O}_7]$ IR modes from DFT calculations related to Cu-O6 displacements. <i>Left</i> : $\text{B}_{2u}$ at $632 \text{ cm}^{-1}$ , <i>Right</i> : $\text{B}_{3u}$ at $586 \text{ cm}^{-1}$ . Cu (cyan), O (purple). .....	56
Figure 3.15	Polarized single crystal Raman data for $\text{Ba}_2\text{BrCu}(\text{OH})[\text{V}_2\text{O}_7]$ . .....	57
Figure 3.16	Vibrational patterns of two $\text{Ba}_2\text{BrCu}(\text{OH})[\text{V}_2\text{O}_7]$ Raman modes from DFT calculations. <i>Left</i> : $\text{A}_g$ at $976 \text{ cm}^{-1}$ , <i>Right</i> : $\text{B}_{2g}$ at $946 \text{ cm}^{-1}$ . .....	58
Figure 3.17	<i>Insets</i> : The field dependent magnetization data measured at 2 K for $\text{Ba}_2\text{XCu}(\text{OH})[\text{V}_2\text{O}_7]$ , $X = \text{Cl}$ (bullets) or Br (circles) with an overall fit (red) to Brillouin function [27] for $S = 1/2$ for the determination of the defect concentration (green) and to the assumed linear behavior in $H$ for an AFM chain compound (blue), see text. ( <i>Main panels</i> ) The measured susceptibility in applied fields of 1 T (ZFC) for $\text{Ba}_2\text{XCu}(\text{OH})[\text{V}_2\text{O}_7]$ , $X = \text{Cl}$ or Br. The fit (red) of the experimental data is given by the combination of AFM chain (blue) and a defect (green) contribution. ....	60
Figure 3.18	<i>Top panel</i> : The total specific heat data measured in zero-field is given. <i>Bottom panels</i> : $C_p/T$ versus $T^2$ for $\text{Ba}_2\text{XCu}(\text{OH})[\text{V}_2\text{O}_7]$ , $X = \text{Cl}$ (black bullets) and Br (black circles) at low temperatures. The fits (red) to the experimental data are composed of the phonon (green) and magnetic (blue) contributions at low temperatures. ....	62
Figure 3.19	Depiction of selected IR active modes in $\text{BaBrCu}(\text{OH})[\text{V}_2\text{O}_7]$ . ....	81

Figure 3.20	Depiction of selected Raman active modes in BaBrCu(OH)[V <sub>2</sub> O <sub>7</sub> ].	82
Figure 4.1	Photo of magnified Mn <sub>2</sub> (OH)[VO <sub>4</sub> ] crystals.	86
Figure 4.2	Photos of magnified Cu <sub>2</sub> (OH)[VO <sub>4</sub> ] crystals from two different reactions. <i>Left</i> : dark orange hexagonal plate-shaped crystals of Cu <sub>2</sub> (OH)[VO <sub>4</sub> ] from reaction i). <i>Right</i> : orange plate-shaped crystals of Cu <sub>2</sub> (OH)[VO <sub>4</sub> ] from reaction ii).	86
Figure 4.3	Polarized photos of magnified Cu <sub>2</sub> (OH)[VO <sub>4</sub> ] crystals.	88
Figure 4.4	Powder refinement data for Cu <sub>2</sub> (OH)[VO <sub>4</sub> ]. Observed (black), calculated (red), Bragg positions (green) and difference (blue).	91
Figure 4.5	A projection of the crystal of Mn <sub>2</sub> (OH)[VO <sub>4</sub> ] along [011].	93
Figure 4.6	Polyhedral representations of Mn <sub>2</sub> (OH)[VO <sub>4</sub> ], Mn1 (red), Mn2 (yellow) and Mn3 (orange).	94
Figure 4.7	The second coordination spheres around V atoms linked via O atoms. <i>Left</i> : V1. <i>Right</i> : V2.	95
Figure 4.8	The <i>M-M</i> connectivity per layer with each connecting line representing a link exclusively via edge-sharing. <i>Left</i> : Mn <sub>2</sub> (OH)[VO <sub>4</sub> ]. <i>Right</i> : Cu <sub>2</sub> (OH)[VO <sub>4</sub> ].	96
Figure 4.9	Cu-O and Cu-O-Cu connectivity of Cu <sub>2</sub> (OH)[VO <sub>4</sub> ]. <i>Left</i> : Cu1. <i>Right</i> : Cu2.	97
Figure 4.10	Cu-O and Cu-O-Cu connectivity of Cu <sub>2</sub> (OH)[VO <sub>4</sub> ]. <i>Left</i> : Cu3. <i>Right</i> : Cu4.	97
Figure 4.11	Colored plaquettes representing the magnetic structure of Cu <sub>2</sub> (OH)[VO <sub>4</sub> ].	98

Figure 4.12	Ladder type magnetic arrangement along [100] for $\text{Cu}_2(\text{OH})[\text{VO}_4]$ , corner-sharing (green), dimers (red), and end member (grey). .....	99
Figure 4.13	Hydrogen bonding for $M_2(\text{OH})[\text{VO}_4]$ with $M = \text{Mn}, \text{Cu}$ . <i>Left:</i> $\text{Mn}_2(\text{OH})[\text{VO}_4]$ . <i>Right:</i> $\text{Cu}_2(\text{OH})[\text{VO}_4]$ . Ellipsoids are of 75% probability. 99	
Figure 4.14	Inverse susceptibility data for $\text{Cu}_2(\text{OH})[\text{VO}_4]$ with a fit to the Curie-Weiss law. ....	101
Figure 4.15	Susceptibility data for $\text{Cu}_2(\text{OH})[\text{VO}_4]$ below 50 K. ....	102
Figure 4.16	Susceptibility ( $\chi T(T)$ ) data for $\text{Cu}_2(\text{OH})[\text{VO}_4]$ . ....	103
Figure 4.17	Magnetization data for $\text{Cu}_2(\text{OH})[\text{VO}_4]$ : $M(H)$ per Cu data at 2 K. ....	104
Figure 4.18	Total specific heat data for $\text{Cu}_2(\text{OH})[\text{VO}_4]$ at zero field. ....	105
Figure 4.19	The total and magnetic specific heat, $C_p(T)/T$ (black), $C_m(T)/T$ (blue) below 30 K. The red line represents the fit to the data between 17 K and 30 K. ....	106
Figure 4.20	The magnetic part of the specific heat, $C_p(T)/T$ (black), $C_m(T)/T$ (blue) $C_L(T)/T$ (red) for $\text{Cu}_2(\text{OH})[\text{VO}_4]$ and the associated entropy, $S_m(T)$ (green), below 17 K. ....	107
Figure 4.21	Powder XRD data for $\text{H}_2\text{V}_3\text{O}_8$ . Observed (red), calculated (black). ....	111
Figure 5.1	<i>Left:</i> Photo of magnified $\text{BaMn}_9[\text{VO}_4]_6(\text{OH})_2$ crystals. <i>Right:</i> SEM picture of the carbon-coated sample showing one Octahedral block-shaped crystal of $\text{BaMn}_9[\text{VO}_4]_6(\text{OH})_2$ . ....	122
Figure 5.2	Photos with polarized light under different angles of magnified $\text{BaMn}_9[\text{VO}_4]_6(\text{OH})_2$ crystals. From left to right, angles are $0^\circ$ , $45^\circ$ , and $90^\circ$ . ....	123

Figure 5.3	<i>Top:</i> Powder refinement data for $\text{BaMn}_9[\text{VO}_4]_6(\text{OH})_2$ . Observed (black), calculated (red), Bragg positions (green) and difference (blue). <i>Bottom:</i> Difference in calculated intensities for the (120) reflection. Experimental data (black circles). ....	126
Figure 5.4	Unit cell of $\text{BaMn}_9[\text{VO}_4]_6(\text{OH})_2$ with dashed lines showing the close-packing layers. Color theme: Ba (orange), Mn (green), V (grey), O (blue), H atoms not shown here. ....	128
Figure 5.5	Close-packing arrangement (Ba/O): polyhedral for layer A central atoms are depicted. Color theme: Ba (orange), O (blue). ....	130
Figure 5.6	Occupancy of $\text{O}_h$ (Mn) and $\text{T}_d$ (V) sites in $\text{BaMn}_9[\text{VO}_4]_6(\text{OH})_2$ adjacent to A-type layers. ....	131
Figure 5.7	Occupancy of $\text{O}_h$ (Mn) and $\text{T}_d$ (V) sites in $\text{BaMn}_9[\text{VO}_4]_6(\text{OH})_2$ adjacent to pure O-packing B and C layers. ....	131
Figure 5.8	The two features of Mn–O–Mn connectivity with the center of Mn1 and Mn2. <i>Left:</i> centered triangle. <i>Right:</i> double-cube. ....	133
Figure 5.9	IR-spectrum for $\text{BaMn}_9[\text{VO}_4]_6(\text{OH})_2$ in the spectral region of Mn–O and V–O stretching vibrations, $\nu$ . <i>Inset:</i> In- and out-of phase O–H modes. ....	134
Figure 5.10	Single crystal Raman-spectrum for $\text{BaMn}_9[\text{VO}_4]_6(\text{OH})_2$ for parallel (HH) and crossed (HV) polarizations of incident and scattered light. <i>Inset:</i> In-phase O–H mode. ....	135
Figure 5.11	Inverse susceptibility data for $\text{BaMn}_9[\text{VO}_4]_6(\text{OH})_2$ with fits to the Curie–Weiss law. ....	136

Figure 5.12	Susceptibility data for $\text{BaMn}_9[\text{VO}_4]_6(\text{OH})_2$ at various fields. ....	137
Figure 5.13	Susceptibility ( $\chi T(T)$ ) data for $\text{BaMn}_9[\text{VO}_4]_6(\text{OH})_2$ at 0.1 T. ....	138
Figure 5.14	Susceptibility ( $\chi T(T)$ ) data for $\text{BaMn}_9[\text{VO}_4]_6(\text{OH})_2$ at various fields. ....	139
Figure 5.15	Magnetization data for $\text{BaMn}_9[\text{VO}_4]_6(\text{OH})_2$ at various temperatures. ....	141
Figure 5.16	Total specific heat data for $\text{BaMn}_9[\text{VO}_4]_6(\text{OH})_2$ at zero field. ....	141
Figure 5.17	Specific heat data for $\text{BaMn}_9[\text{VO}_4]_6(\text{OH})_2$ : low temperature $C_p(T)/T$ data for various applied fields (data offset: $0.5 \text{ J mol}^{-1} \text{ K}^{-2}$ per increasing applied field). The dashed line represents the fitted lattice contribution, $C_L(T)/T$ . ....	142
Figure 5.18	The magnetic part of the specific heat, $C_m(T)/T$ for $\text{BaMn}_9[\text{VO}_4]_6(\text{OH})_2$ at zero fields (black) and the associated entropy, $S_m(T)$ , (blue). ....	143
Figure 5.19	Temperature dependence of the dielectric constant for $\text{BaMn}_9[\text{VO}_4]_6(\text{OH})_2$ . <i>Inset</i> : Derivative of the dielectric constant indicating an anomaly at $T_C$ . .	144
Figure 5.20	Sketch of the proposed chiral spin arrangement. <i>Top</i> : the centrosymmetric. <i>Bottom</i> : the acentric case. Note the inverted spin-alignment (orange arrows) for the latter. ....	147
Figure 6.1	Powder XRD data for synthesis of the MnII compound with different concentrations of starting mixture based on $[\text{VO}_4]^{3-}$ . The $\text{Mn}_2\text{V}_2\text{O}_7$ (blue) and MnII (red) simulated powder XRD pattern are also plotted for comparison. ....	165
Figure 6.2	Photos of magnified crystals of all synthesized transition metal compounds ( $M_{6+x}(\text{OH})_3[\text{VO}_4]_{4-2z}[\text{V}_2\text{O}_7]_z$ ). ....	166

Figure 6.3	Polarized photos of magnified randomly orientated transparent crystals of $(\text{Mg})_{6+x}(\text{OH})_{3-y}(\text{H}_2\text{O})_y[\text{VO}_4]_{4-2z}[\text{V}_2\text{O}_7]_z$ . From left to right, polarization angles are $0^\circ$ , $60^\circ$ , and $90^\circ$ . ....	166
Figure 6.4	X-ray powder data for $(\text{M1})_6(\text{OH})_3[\text{VO}_4]_3(\text{M2})_x\{[\text{VO}_4]_{1-2z}[\text{V}_2\text{O}_7]_z\}$ . Observed (black), calculated (red), Bragg positions (green) and difference (blue). ....	172
Figure 6.5	Unit cell of the idealized crystal structure of $(\text{M1})_6(\text{OH})_3[(\text{V1})\text{O}_4]_3(\text{M2})[(\text{V2})\text{O}_4]$ in a polyhedra representation. Color theme: <i>M1</i> (gold), <i>M2</i> (orange), <i>V1</i> (grey), <i>V2</i> (lavender), O and H atoms are not shown here. ....	174
Figure 6.6	Connectivity of <i>M1</i> –O– <i>M1</i> ( <i>left</i> ) and <i>M2</i> –O– <i>M2</i> ( <i>right</i> ). Note the partial occupancy for the <i>M2</i> site (denoted <i>x</i> ). Ellipsoids are of 75% probability (here <i>M</i> = Co). ....	175
Figure 6.7	Kagome-like arrangement of <i>M1</i> dimmers in a polyhedral representation. Color theme: <i>M1</i> (gold), <i>M2</i> (orange). ....	176
Figure 6.8	Statistical occupancy (denoted <i>z</i> ) for <i>V21/V22</i> along [001]. <i>Left</i> : Occupancy only with $[(\text{V21})\text{O}_4]^{3-}$ , <i>z</i> = 0. <i>Right</i> : Replacement of two $[(\text{V21})\text{O}_4]^{3-}$ units with one $[\text{V}_2\text{O}_7]^{4-}$ entity. Ellipsoids are of 75% probability ( <i>M</i> = Co). ....	177
Figure 6.9	<i>Left</i> : Hydrogen bonding for hydroxide (O3–H). <i>Right</i> : Hydrogen bonding for water (O3–(H2) <sub>2</sub> ) in the case of MgII. Ellipsoids are of 75% probability. ....	178

Figure 6.10	Site occupancies $x$ ( $M2$ ) and $z$ ( $V22$ ). The dashed line represents the theoretical charge balanced relation: If the $M2$ site is only occupied by $M^{3+}$ , then $x = 1 - 2/3z$ would be required.....	180
Figure 6.11	$M$ -O distances in relation to the lattice constants. Dashed lines serve as a guide to the eye. <i>Top: <math>M1</math>-O. Bottom: <math>M2</math>-O</i> .....	182
Figure 6.12	IR spectra for the Co-series compared with the MgII compound. ....	184
Figure 6.13	IR spectra for the Co-series in comparison with the MgII compound (*) denotes $H_2O$ stretching vibrations.....	185
Figure 6.14	Selected displacements of $\nu(M-O)$ and $\delta(V-O)$ ( $375 - 450\text{ cm}^{-1}$ ) based on DFT calculations for $Mn_7(OH)_3[VO_4]_4$ . Wavenumbers of assigned modes from experimental data for MnII. For better visualization all atoms not involved are omitted.....	186
Figure 6.15	Displacements of the coupled $V1/V2$ -type with noticeable H-displacement contributions ( $655\text{ cm}^{-1}$ ) based on DFT calculations for $Mn_7(OH)_3[VO_4]_4$ . Wavenumbers of assigned modes from experimental data for MnII. For better visualization all atoms not involved are omitted.....	187
Figure 6.16	Displacements of coupled O-H liberation modes ( $830 - 950\text{ cm}^{-1}$ ) based on DFT calculations for $Mn_7(OH)_3[VO_4]_4$ . Wavenumbers of assigned modes from experimental data for MnII. For better visualization all atoms not involved are omitted.....	188



Figure 6.17	Single crystal Raman spectra of the MnII compound. The inset presents a 19 times magnification. Markers: Assigned modes based on phonon calculations for the idealized $\text{Mn}_7(\text{OH})_3[\text{VO}_4]_4$ structure. ....	189
Figure 6.18	IR spectra for the Mn series in comparison with $\text{Mn}_2\text{V}_2\text{O}_7$ . Markers: Assigned modes based on phonon calculations for the idealized $\text{Mn}_7(\text{OH})_3[\text{VO}_4]_4$ structure. ....	192
Figure 6.19	Reciprocal susceptibility per formula unit for the compounds of Co-series at 0.1 T (symbols: open (ZFC) and full (FC)). Curie-Weiss fit to the temperature range 100 - 300 K (line). The grey line serves as a guide to the eye and indicates $T_C$ . ....	193
Figure 6.20	Reciprocal susceptibility per formula unit for MnII at 0.1 T (symbols: open (ZFC) and full (FC)). Curie-Weiss fit to the temperature range 100 - 300 K (line). ....	194
Figure 6.21	Magnetization, $M(H)$ , per formula unit the compounds of Co series at 2 K. ....	195
Figure 6.22	Extraction of the magnetic part of specific heat for CoII, $C_m(T)$ , from the $C_p(T)$ data by subtracting the lattice contribution, $C_L(T)$ , represented by a baseline derived from the non-magnetic MgII data. ....	197
Figure 6.23	Specific heat data for the compounds of Co series at 0 T. <i>Main panels:</i> Magnetic part of the specific heat. $C_m/T$ . <i>Insets:</i> Magnetic entropy, $S_m$ ....	198

Figure 6.24	Extraction of the magnetic part of specific heat for MnII, $C_m(T)$ , from the $C_p(T)$ data by subtracting the lattice contribution, $C_L(T)$ , represented by a baseline derived from the non-magnetic MgII data. ....	199
Figure 6.25	Specific heat data for MnII at 0 T. <i>Main panels</i> : Magnetic part of the specific heat, $C_m/T$ . <i>Insets</i> : Magnetic entropy, $S_m$ . ....	200
Figure 6.26	Sketch of the proposed spin arrangement of M1 framework. <i>Left</i> : M1–O–M1 connectivity for the M1 ladder along [001]. <i>Right</i> : Kagome-like arrangement in the $ab$ plane. (Blue bond: AFM correlation. Yellow bond: FM correlation. Red arrow: spin).....	201
Figure 6.27	Selected Depiction of displacements in the idealized $\text{Mn}_7(\text{OH})_3[\text{VO}_4]_4$ structure. ....	223

## List of Tables

Table 2.1	List of all chemical used for the synthesis of compounds. ....	8
Table 2.2	Factor group analysis of the $[\text{VO}_4]$ unit.....	19
Table 3.1	Atomic composition for $\text{Ba}_2\text{XCu}(\text{OH})[\text{V}_2\text{O}_7]$ , $X = \text{Cl}, \text{Br}$ . ....	38
Table 3.2	Crystal data and details of the structure determination for $\text{Ba}_2\text{XCu}(\text{OH})[\text{V}_2\text{O}_7]$ , $X = \text{Cl}, \text{Br}$ . (refined with twin law) .....	40
Table 3.3	Integral reflection conditions for $Pnma$ (No. 62). ....	43
Table 3.4	Powder refinement results of $\text{Ba}_2\text{XCu}(\text{OH})[\text{V}_2\text{O}_7]$ , $X = \text{Cl}, \text{Br}$ , orthorhombic space group $Pnma$ ( $Z = 4$ ). ....	47
Table 3.5	Distances and angles for Ba–X bonds. ....	49
Table 3.6	Cu–O distances and Cu–O–Cu angles of $\text{Ba}_2\text{XCu}(\text{OH})[\text{V}_2\text{O}_7]$ , $X = \text{Cl}$ or $\text{Br}$ , referring to Figure 3.9. ....	51
Table 3.7	Assignments of MIR-spectra for $\text{Ba}_2\text{BrCu}(\text{OH})[\text{V}_2\text{O}_7]$ compared with DFT data. ....	54
Table 3.8	Atomic composition for $\text{Ba}_2\text{ClCu}(\text{OH})[\text{V}_2\text{O}_7]$ . ....	67
Table 3.9	Atomic composition for $\text{Ba}_2\text{BrCu}(\text{OH})[\text{V}_2\text{O}_7]$ . ....	68
Table 3.10	Fractional atomic coordinates and isotropic or equivalent isotropic displacement parameters ( $\text{\AA}^2$ ) for $\text{Ba}_2\text{ClCu}(\text{OH})[\text{V}_2\text{O}_7]$ . ....	70
Table 3.11	Fractional atomic coordinates and isotropic or equivalent isotropic displacement parameters ( $\text{\AA}^2$ ) for $\text{Ba}_2\text{BrCu}(\text{OH})[\text{V}_2\text{O}_7]$ . ....	71
Table 3.12	Selected interatomic distances ( $\text{\AA}$ ) for $\text{Ba}_2\text{ClCu}(\text{OH})[\text{V}_2\text{O}_7]$ . ....	72

Table 3.13	Selected interatomic distances (Å) for Ba <sub>2</sub> BrCu(OH)[V <sub>2</sub> O <sub>7</sub> ].	73
Table 3.14	Selected angles (°) for Ba <sub>2</sub> ClCu(OH)[V <sub>2</sub> O <sub>7</sub> ].	75
Table 3.15	Selected angles (°) for Ba <sub>2</sub> BrCu(OH)[V <sub>2</sub> O <sub>7</sub> ].	77
Table 4.1	Crystal data and details of the structure determination for M <sub>2</sub> (OH)[VO <sub>4</sub> ], M = Mn, Cu.	90
Table 4.2	Powder refinement results for Cu <sub>2</sub> (OH)[VO <sub>4</sub> ], orthorhombic space group P2 <sub>1</sub> 2 <sub>1</sub> 2 <sub>1</sub> .	92
Table 4.3	Interatomic distances and angles for O-donor (O <sup>D</sup> ) and O-acceptor (O <sup>A</sup> ) contacts for Mn <sub>2</sub> (OH)[VO <sub>4</sub> ] (Pnma).	100
Table 4.4	Interatomic distances and angles for O-donor (O <sup>D</sup> ) and O-acceptor (O <sup>A</sup> ) contacts for Cu <sub>2</sub> (OH)[VO <sub>4</sub> ] (P2 <sub>1</sub> 2 <sub>1</sub> 2 <sub>1</sub> ).	100
Table 4.5	Fractional atomic coordinates and isotropic or equivalent isotropic displacement parameters (Å <sup>2</sup> ) for Mn <sub>2</sub> (OH)[VO <sub>4</sub> ] (Pnma).	112
Table 4.6	Fractional atomic coordinates and isotropic or equivalent isotropic displacement parameters (Å <sup>2</sup> ) for Cu <sub>2</sub> (OH)[VO <sub>4</sub> ] (P2 <sub>1</sub> 2 <sub>1</sub> 2 <sub>1</sub> ).	113
Table 4.7	Selected Interatomic Distances (Å) for Mn <sub>2</sub> (OH)[VO <sub>4</sub> ] (Pnma).	114
Table 4.8	Selected Interatomic Distances (Å) for Cu <sub>2</sub> (OH)[VO <sub>4</sub> ] (P2 <sub>1</sub> 2 <sub>1</sub> 2 <sub>1</sub> ).	115
Table 4.9	Selected angles (°) for Mn <sub>2</sub> (OH)[VO <sub>4</sub> ] (Pnma).	116
Table 4.10	Selected angles (°) for Cu <sub>2</sub> (OH)[VO <sub>4</sub> ] (P2 <sub>1</sub> 2 <sub>1</sub> 2 <sub>1</sub> ).	118
Table 5.1	Atomic composition for BaMn <sub>9</sub> [VO <sub>4</sub> ] <sub>6</sub> (OH) <sub>2</sub> .	123
Table 5.2	Crystal Data and Details of the Structure Determination for BaMn <sub>9</sub> [VO <sub>4</sub> ] <sub>6</sub> (OH) <sub>2</sub> .	125

Table 5.3	Powder refinement results for $\text{BaMn}_9[\text{VO}_4]_6(\text{OH})_2$ , Both space groups of $Pa\bar{3}$ and $P2_13$ are listed respectively. ....	127
Table 5.4	Selected Interatomic Distances and $\text{O}^{\text{donor}}-\text{H}\cdots\text{O}^{\text{acceptor}}$ angle for $\text{BaMn}_9[\text{VO}_4]_6(\text{OH})_2$ ( $Pa\bar{3}$ ). ....	129
Table 5.5	Atomic composition for $\text{BaMn}_9[\text{VO}_4]_6(\text{OH})_2$ . ....	153
Table 5.6	Fractional atomic coordinates and isotropic or equivalent isotropic displacement parameters ( $\text{\AA}^2$ ) for $\text{BaMn}_9[\text{VO}_4]_6(\text{OH})_2$ ( $Pa\bar{3}$ ). ....	156
Table 5.7	Fractional atomic coordinates and isotropic or equivalent isotropic displacement parameters ( $\text{\AA}^2$ ) for $\text{BaMn}_9[\text{VO}_4]_6(\text{OH})_2$ ( $P2_13$ ) ....	157
Table 5.8	Selected Interatomic Distances ( $\text{\AA}$ ) for $\text{BaMn}_9[\text{VO}_4]_6(\text{OH})_2$ . ( $Pa\bar{3}$ and $P2_13$ ) .....	158
Table 5.9	Selected angles ( $^\circ$ ) for $\text{BaMn}_9[\text{VO}_4]_6(\text{OH})_2$ . ( $Pa\bar{3}$ and $P2_13$ ) ....	159
Table 6.1	Atomic composition for $M_{6+x}(\text{OH})_3[\text{VO}_4]_{4-2z}[\text{V}_2\text{O}_7]_z$ . ....	167
Table 6.2	Crystallographic data and details of the structure determination for $\text{CoII}$ and $\text{CoIIFeIII}$ at 293 K with 61 refined parameters. ( $Z = 2$ ) ....	169
Table 6.3	Crystallographic data and details of the structure determination for $\text{CoIIMnII}$ and $\text{CoIIMnIII}$ at 293 K with 61 refined parameters. ( $Z = 2$ ) ...	170
Table 6.4	Crystallographic Data and Details of the Structure Determination for $\text{MnII}$ , $\text{MnIIMnIII}$ , and $\text{MgII}$ at 293 K with 61 refined parameters. ( $Z = 2$ ) .....	171
Table 6.5	Powder refinement results for $M_{6+x}(\text{OH})_3[\text{VO}_4]_{4-2z}[\text{V}_2\text{O}_7]_z$ with the space group of $P6_3mc$ . ....	173
Table 6.6	Selected Interatomic Distances ( $\text{\AA}$ ) for $M_{6+x}(\text{OH})_3[\text{VO}_4]_{4-2z}[\text{V}_2\text{O}_7]_z$ . ....	175

Table 6.7	Atomic composition for $M_{6+x}(\text{OH})_3[\text{VO}_4]_{4-2z}[\text{V}_2\text{O}_7]_z$ .....	206
Table 6.8	Fractional atomic coordinates and isotropic or equivalent isotropic displacement parameters ( $\text{\AA}^2$ ) for $M_{6+x}(\text{OH})_3[\text{VO}_4]_{4-2z}[\text{V}_2\text{O}_7]_z$ .....	212
Table 6.9	Selected Interatomic Distances ( $\text{\AA}$ ) for $M_{6+x}(\text{OH})_3[\text{VO}_4]_{4-2z}[\text{V}_2\text{O}_7]_z$ .....	219
Table 6.10	Selected angles ( $^\circ$ ) for $M_{6+x}(\text{OH})_3[\text{VO}_4]_{4-2z}[\text{V}_2\text{O}_7]_z$ .....	221

## Abbreviations and Acronyms

$\theta$	angle
$\Theta$	Weiss constant
$\lambda$	wavelength
$\mu_B$	Bohr magneton(s)
$\mu\text{L}$	microliter(s)
$\mu\text{m}$	micrometer(s)
$\chi^2$	weighted difference factor
$\text{\AA}$	angstrom
AFM	antiferromagnetic
aq	aqueous solution
atm	standard atmosphere
BASF	batch scale factor
C	Curie constant
$^{\circ}\text{C}$	degrees Celsius
CCD	Charge-coupled device
ccp	cubic close packing
cif	crystallographic information file
cm	centimeter
$\text{cm}^{-1}$	wavenumber
$C_m$	magnetic part of specific heat

$C_p$	specific heat
C.W.	Curie-Weiss
$d$	distance
D	dimensional
DFT	density functional theory
DSC	differential scanning calorimetry
EDX	energy dispersive X-ray
eV	electron volt(s)
FC	field-cooling
FIR	far infrared
FM	ferromagnetic
g	gram(s)
GooF	Goodness-of-fit
$h$	Planck constant
$H$	magnetic field
$hkl$	Miller indices
IP	image plate
IR	infrared
J	Joule(s)
$J$	magnetic exchange coupling constant
$k, k_B$	Boltzmann constant
K	Kelvin



LRO	long-range order
MIR	mid infrared
mg	milligram
mJ	milli Joule(s)
mm	millimeter
min	minute(s)
MPa	megapascal
mW	milli Watt(s)
$n$	integer
$N$	number of atoms
$N_A$	Avogadro's number
NIR	near infrared
nm	nanometer(s)
Pa	pascal
$r$	radius
$R$	gas constant
$R_I$	Rietveld factor
$R_{\text{int}}$	Rietveld factor
s	second(s)
$S$	spin
$S_{\text{eff}}$	spin effective
SEM	scanning electron microscopy

$S_m$	entropy
SRO	short-range order
T	tesla
$T$	temperature
$T_C$	Curie temperature
$T_N$	Néel temperature
TWIN	twinning command
UV	ultraviolet
vis	visible
$wR2$	Rietveld factor
XRD	x-ray diffraction
$Z$	number of formula units per unit cell
ZFC	zero-field cooling

## **Chapter One**

### **General Introduction**

Magnetic solids with low-dimensional structural features often exhibit interesting physical properties with relevance to new applications. Hence, experimental and theoretical studies have been devoted to the characterization of low-dimensional spin-systems in one and two dimensions which are represented by chains, [1-3] triangular, [4, 5] honeycomb, [6, 7] or Kagomé [8, 9] lattices. Among these classes of magnetic materials, those with geometrical frustration [10] are of particular interest because they might lead to the rare occurrence of canted antiferromagnetism, [11, 12] competing anti- and ferromagnetic correlations, [13, 14] or helimagnetism. [15] These properties are of relevance to the field of multiferroics. [16, 17] Thus, the chemical synthesis of new materials and the investigation of structure-property relationships is an important research area for the discovery of next generation applications and devices.

This research project focuses on the hydrothermal synthesis of novel compounds with unique magnetic structural features. We selected multi-anionic systems to gain access to unprecedented connectivities. To comply with the goal of selectively addressing entities which exhibit geometrical frustration, we choose transition metal vanadates. The vanadate plays an important role as a building block or linker to facilitate the formation of equilateral triangles of the respective magnetic transition metal cations. Dimensional

control of the transition metal cation connectivity can be tuned by hydroxide or halide incorporation into the respective structure.

Examples of vanadate-halides are  $\text{KBa}_2\text{Cl}[\text{V}_2\text{O}_7]$ ,  $\text{KBaClCu}[\text{V}_2\text{O}_7]$ , or  $\text{Ba}_5\text{Cl}_2[\text{V}_2\text{O}_7]_2$  and these have been synthesized by classical solid-state methods via flux-melt methods. [18-20] In this research, an alternative route was used. Hydrothermal synthesis [21] provides access to hydroxide-containing species from the aqueous solutions and mimics the formation of minerals, such as  $\text{Cu}_3\text{V}_2\text{O}_7(\text{OH})_2 \cdot 2\text{H}_2\text{O}$  (volborthite),  $\text{Al}_2(\text{OH})_3(\text{VO}_4)$  (augelite), and  $\text{BaFe}[\text{PO}_4](\text{OH})$  (nepheline-type). [22-24] Our synthetic approach has been devoted to study controlled conditions for phase-pure single crystal growth. In this respect, it relates also to the vanadate vs. divanadate formation as a function of the pH-value and the respective vanadate concentration. These dependencies have only previously been systematically investigated for aqueous solutions. [25, 26]

In this work selected transition metal vanadate compounds have been synthesized and investigated by X-ray diffraction (crystal structure), infrared, and Raman spectroscopy in combination with DFT-methods (lattice dynamics), and thermodynamic measurements (magnetic properties). Twelve compounds belonging to four series will be discussed in this respect:  $\text{Ba}_2\text{XCu}(\text{OH})[\text{V}_2\text{O}_7]$  with  $X = \text{Cl}, \text{Br}$ ;  $M_2(\text{OH})[\text{VO}_4]$  with  $M = \text{Mn}, \text{Cu}$ ;  $\text{BaMn}_9[\text{VO}_4]_6(\text{OH})_2$ ; and  $M_{6+x}(\text{OH})_3[\text{VO}_4]_{4-2z}[\text{V}_2\text{O}_7]_z$  with  $M = \text{Mn}, \text{Co}, \text{Mg}, \text{Fe}$ . These compounds exhibit unique structural features which relate to their intriguing magnetic properties.

## References.

- [1] Breunig, O.; Garst, M.; Sela, E.; Buldmann, B.; Becker, P.; Bohatý, L.; Müller, R.; Lorenz, T. *Phys. Rev. Lett.*, **2013**, *111*, 187202.
- [2] Janson, O.; Tsirlin, A. A.; Osipova, E. S.; Berdonosov, P. S.; Olenov, A. V.; Dolgikh, V. A.; Rosner, H. *Phys. Rev. B*, **2011**, *83*, 144423.
- [3] Pan, B.; Wang, Y.; Zhang, L.; Li, S. *Inorg. Chem.*, **2014**, *53*, 3606.
- [4] Amuneke, N. E.; Tapp, J.; de la Cruz, C. R.; Möller, A. *Chem. Mater.*, **2014**, *26*, 5930.
- [5] Greedan, J. E. *J. Mater. Chem.*, **2001**, *11*, 37.
- [6] Bratsch, M.; Tapp, J.; Litvinchuk, A. P.; Möller, A. *Inorg. Chem.*, **2014**, *53*, 4994.
- [7] Yan, Y. J.; Li, Z. Y.; Zhang, T.; Luo, X. G.; Ye, G. J.; Xiang, Z. J.; Cheng, P.; Zou, L. J.; Chen, X. H. *Phys. Rev. B*, **2012**, *85*, 085102.
- [8] Yan, S.; Huse, D. A.; White, S. R. *Science*, **2011**, *332*, 1173.
- [9] Shores, M. P.; Nytko, E. A.; Bartlett, B. M.; Nocera, D. G. *J. Am. Chem. Soc.*, **2005**, *127*, 13462.
- [10] Moessner, R.; Ramirez, A. R. *Phys. Today*, **2006**, *59*, 24.
- [11] Motin Seikh, Md.; Caignaert, V.; Lebedev, O. I.; Raveau, B. *Solid State Commun.*, **2014**, *180*, 52.
- [12] Yang, E. C.; Liu, Z. Y.; Shi, X. J.; Liang, Q. Q.; Zhao, X. J. *Inorg. Chem.*, **2010**, *49*, 7969.
- [13] Franco, D. G.; Fuertes, V. C.; Blanco, M. C.; Fernández-Díaz, M. T.; Sánchez, R. D.; Carbonio, R. E. *J. Solid State Chem.*, **2012**, *194*, 385.

- [14] Wang, Y. Q.; Yue, Q.; Qi, Y.; Wang, K.; Sun, Q.; Gao, E. Q. *Inorg. Chem.*, **2013**, 52, 4259.
- [15] Enderle, M.; Mukherjee, C.; Fåk B.; Kremer, R. K.; Broto, J. M.; Rosner, H.; Drechsler, S.-L.; Richter, J.; Malek, J.; Prokofiev, A.; Assmus, W.; Pujol, S.; Raggazzoni, J.-L.; Rakoto, H.; Rheinstädter, M.; Rønnow, H. M. *Europhys. Lett.*, **2005**, 70, 237.
- [16] Johnson, R. D.; Radaelli, P. G.; *Annu. Rev. Mater. Res.*, **2014**, 44, 269.
- [17] Tokura, Y.; Seki, S.; Nagaosa, N. *Rep. Prog. Phys.*, **2014**, 77, 076501.
- [18] Martin, F. D.; Müller-Buschbaum, Hk. *Z. Naturforsch. B*, **1994**, 49, 355.
- [19] Martin, F. D.; Müller-Buschbaum, Hk. *Z. Naturforsch. B*, **1994**, 49, 1141.
- [20] Ranmohotti, K. G. S.; Queen, W. L.; J. P. VanDerveer, West, D.; Hwu, S.-J. *J. Chem. Crystallogr.*, **2009**, 39, 303.
- [21] Byrappa, K.; Yoshimura, M. *Handbook Of Hydrothermal Technology*, Noyes Publications, **2001**.
- [22] Ishikawa, H.; Yamaura, J.; Okamoto, Y.; Yoshida, H.; Nilsen, G. J.; Hiroia, Z. *Acta Cryst. C*, **2012**, 68, i41.
- [23] Pecquenard, B.; Zavalij, P. Y.; Whittingham, M. S. *J. Mater. Chem.*, **1998**, 8, 1255.
- [24] Belokoneva, E. L.; Dimitrova, O. V. *Crystallogr. Reports*, **2010**, 55, 230
- [25] Baes Jr., C. F.; Mesmer, R. E. *The Hydrolysis of Cations*, Wiley, New York, **1970**.
- [26] Griffith, W. P.; Wickins, T. D. *J. Chem. Soc. A*, **1966**, 1087.

## **Chapter Two**

### **Experimental Methods**

This chapter contains general information about the experimental methods utilized for this research, including synthetic methods, structure determination methods, spectroscopic measurements, and physical property measurements.

In this research, hydrothermal synthesis was used. In Table 2.1 the chemical formula and brand of all the starting materials is given. Structures were determined by powder and single crystal X-ray diffraction techniques. Scanning electron microscopy and energy dispersive X-ray spectrometry (SEM-EDX) were used for surface characterization and elemental analysis. Differential scanning calorimetry (DSC) measurements were obtained to gain understanding of the thermal behavior of the materials. Raman and infrared spectroscopy were measured to study the vibrational modes of the compounds. Physical properties such as magnetism and specific heat were investigated to learn about the underlying magnetic correlations. Universal procedures for each method will be given, as well as an introduction of the principle of this method. The following chapters discuss the findings and give specific parameters or modifications in the procedure.

## **2.1 Hydrothermal Synthesis.**

### **2.1.1 Introduction to Hydrothermal Synthesis.**

Hydrothermal synthesis is a synthetic technique in which one conducts reactions in aqueous solutions at high temperatures and high vapor pressures. The term 'hydrothermal' originates from geology; it was first proposed by Sir Roderick Murchison in 1855, to describe how water acts in the earth's crust to form various minerals. [1] There are many minerals, including natural single crystals, that form in the presence of water and elements at elevated pressure and temperature.

Despite the fact that hydrothermal techniques have been applied in various fields and been tremendously successful, scientists still disagree about its definition. Morey and Niggli (1913) gave the first definition of hydrothermal synthesis as "...in the hydrothermal method the components are subjected to the action of water, at temperatures generally near though often considerably above the critical temperature of water (~370 °C) in closed bombs, and therefore, under the corresponding high pressures developed by such solutions." [2] However, most publications indicate that the supercritical conditions for hydrothermal synthesis are rarely reached in application. [3-8] Thus, the majority of scientists define the hydrothermal method in a general way as "any heterogenous chemical reaction in the presence of a solvent (whether aqueous or nonaqueous) above room temperature and at pressure greater than 1 atm in a closed system". [1]

The hydrothermal technique has been developed and applied to many different aspects of science and technology [1-8]. In this research, the hydrothermal synthesis method was



utilized for growing single crystals by taking advantage of the solubility of compounds in hot water under high pressure. The reactions were performed in a steel pressure vessel called an autoclave. A Teflon liner, which was filled with reactants as well as water, was loaded into the autoclave.

#### 2.1.2 Synthesis Conditions.



Figure 2.1. *Left*: Stainless steel autoclave. *Right*: Teflon liner.

Table 2.1. List of all chemical used for the synthesis of compounds.

Chemical Name	Formula	FW (g/mol)	Brand
Acetic Acid, Glacial	CH <sub>3</sub> COOH	60.05	Macron Fine Chemicals
Ammonium hydroxide	NH <sub>3</sub> ·H <sub>2</sub> O	35.04	14.8M, EMD
Ammonium metavanadate	NH <sub>4</sub> VO <sub>3</sub>	116.98	ICN Pharmaceuticals, Inc.
Barium Acetate	Ba(Ac) <sub>2</sub>	255.42	Strem Chemicals
Cesium carbonate	Cs <sub>2</sub> CO <sub>3</sub>	325.82	Alfa Aesar
Cobalt (II) acetate	Co(Ac) <sub>2</sub>	177.02	Matheson Coleman & Bell
Copper (II) acetate monohydrate	Cu(Ac) <sub>2</sub> ·H <sub>2</sub> O	199.65	Sigma Aldrich
Copper (II) bromide	CuBr <sub>2</sub>	223.37	Alfa Aesar
Copper (II) chloride	CuCl <sub>2</sub>	134.45	Alfa Aesar
Ethanol	C <sub>2</sub> H <sub>5</sub> OH	46.07	Decon Labs, Inc
Iron (III) chloride hexahydrate	FeCl <sub>3</sub> ·6H <sub>2</sub> O	270.30	Alfa Aesar
Lithium chloride	LiCl	42.39	J.T. Baker Chemical CO. or Alfa Aesar
Magnesium powder	Mg	24.31	Aldrich
Manganese (II) acetate tetrahydrate	Mn(Ac) <sub>2</sub> ·4H <sub>2</sub> O	245.09	Sigma
Manganese (II) chloride	MnCl <sub>2</sub>	125.84	Aldrich
Manganese (III) acetate dihydrate	Mn(Ac) <sub>3</sub> ·2H <sub>2</sub> O	268.13	Alfa Aesar
Oxalic acid	H <sub>2</sub> C <sub>2</sub> O <sub>4</sub>	90.03	GFS Chemicals
Vanadium (V) oxide	V <sub>2</sub> O <sub>5</sub>	181.88	Alfa Aesar

Teflon-lined stainless steel autoclaves (Model KLS series, Fuzhou Keleisi Test Equipment Co., Ltd, China) were used to conduct all experiments, see Figure 2.1. The

reaction conditions were controlled to be under 240 °C and less than 10 MPa. Total solution volume did not exceed 80% of the inner volume. In general, the reactions were started at room temperature and the temperature was increased by 1 °C per minute until the target temperature was reached. Once the target temperature was reached, the temperature was held for three days. A typical cooling procedure is to slowly cool the autoclave to 120 °C as a rate of 6 °C per hour. Finally, the temperature was immediately set to room temperature. The products obtained were washed with distilled water and ethanol several times. A furnace (Binder: forced convection FD 53-UL, 1.9 cu.ft.) was used for all conducted synthesis unless otherwise stated.

## **2.2 Structure Determination Methods.**

### **2.2.1 Introduction to X-ray Diffraction.**

In the crystal structure, atoms are arranged in a periodically ordered pattern in three dimensions. The discovery of X-rays by W.C. Röntgen in 1895 [9] was a significant achievement in being able to study translation symmetry. Since X-rays have a wavelength similar to the spacing of atomic planes, X-ray diffraction is an effective tool to obtain information about the arrangement of atoms in a unit cell and to determine the crystal structure. [10]

X-rays are electromagnetic radiation that upon interaction with condensed matter are scattered by electrons. These waves interfere with each other. Constructive interference, which occurs due to interaction with periodic arrays of electrons, generates diffraction

patterns. The geometry of the diffraction gives us information about the electron density distribution on a crystal lattice.

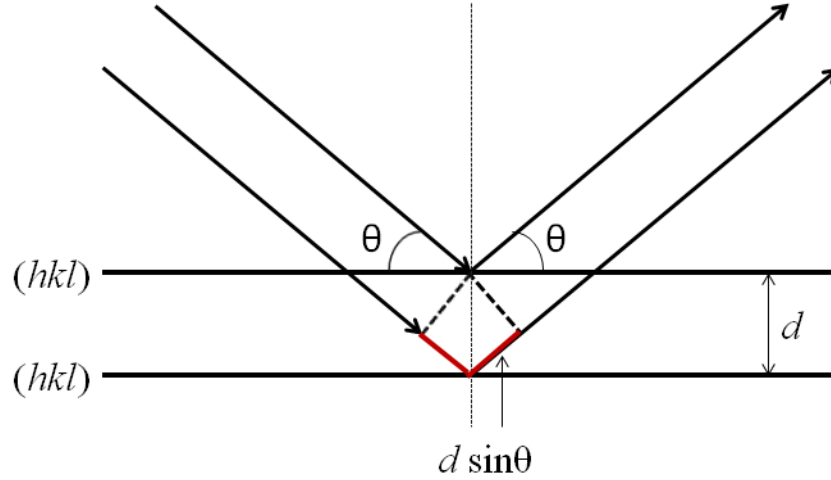


Figure 2.2. Geometrical illustration of Bragg's law. [11]

The geometry of the diffraction by a lattice was first given by the Laue equations:

$$\begin{aligned} a(\cos\psi_1 - \cos\phi_1) &= h\lambda \\ b(\cos\psi_2 - \cos\phi_2) &= k\lambda \\ c(\cos\psi_3 - \cos\phi_3) &= l\lambda \end{aligned} \quad (2.1)$$

where  $\lambda$  is the wavelength of the X-rays, the integers  $h$ ,  $k$ , and  $l$  are Miller indices representing planes in reciprocal lattice,  $a$ ,  $b$ ,  $c$  are the dimensions of the unit cell, and  $\psi_{1-3}$  and  $\phi_{1-3}$  are the angles that the incident and diffracted beams, respectively, which form with the parallel rows of atoms in three independent directions. [11] Diffraction peaks can only be observed when all three conditions (Equation 2.1) are satisfied at the same time. The Laue equations are useful to describe the geometry of single crystal X-ray diffraction.

A useful equation for obtaining the conditions for powder diffraction is Braggs' law:

$$n\lambda = 2d \sin\theta \quad (2.2)$$

where  $n$  is an integer,  $\lambda$  is the wavelength of the X-rays,  $d$  is the interplanar spacing, and  $\theta$  is the angle between the incident beam and lattice plane, also called the Bragg angle. [12] As shown in figure 2.2, only those diffracted X-ray beams that fulfill (2.2) can be observed under a  $2\theta$  angle.

### 2.2.2 Selection of a Single Crystal for X-ray Diffraction Studies.

Single crystals were selected using a Leica MZ16 optical microscope. Furthermore, Photos of magnified crystals with polarized light were taken using an Olympus BX 41-P polarizing microscope equipped with an Olympus DP12 microscope digital camera system.

### 2.2.3 Single Crystal X-ray Diffraction.

Single crystal X-ray diffraction data were collected to structurally characterize the compounds. Crystals were taken from the bulk of each sample and immersed in Paratone-N oil (Hampton Research) to clean off any residues such as powders. Under a microscope, a couple of crystals were selected and mounted on the tip of a glass fiber which was placed on a brass pin and mounted on a goniometer. Data was collected by a curved imaging plate area detector on a Rigaku Rapid II instrument (Mo  $K\alpha$  radiation with  $\lambda = 0.71075 \text{ \AA}$ ) or by an APEX II CCD Detector on a Bruker AXS instrument (Mo  $K\alpha$  radiation with  $\lambda = 0.71073 \text{ \AA}$ ) at room temperature. For the Rigaku instrument, the

program CrystalClear [13] was used to determine the unit cell parameters, absorption correction, and data reductions. For the Bruker instrument, the program SAINT [14] was used to determine the unit cell parameters, and MULTISCAN [15] implemented in the WinGX [16] platform was used for the absorption correction. The structures were solved by direct methods and refined by Difference-Fourier Synthesis (SHELX97 or 2013) [17]. The final structure solutions were checked by applying the program system PLATON [18]. The program Diamond [19] was used to illustrate the crystal structures.

#### 2.2.4 Powder X-ray Diffraction.

A PANalytical X'Pert Pro Diffractometer (with  $\lambda$  Cu  $K\alpha_1$  = 1.540562 Å and  $K\alpha_2$  = 1.544389 Å) was used to collect diffraction patterns to confirm the phase purity and structure model of the compounds. Each sample was ground into fine powder in an agate mortar and placed on a PW1817/32 zero background silicon crystal sample holder. Data were collected on the powder samples using a 57 minute scan in the  $2\theta$  range of 10 - 100°. Lattice constants were refined by profile-matching (Lebail fit) methods using the program Full-prof. [20]

### **2.3 Scanning Electron Microscopy (SEM) and Energy Dispersive X-ray Spectrometry (EDX).**

The scanning electron microscope (SEM) technique is used to image and analyze bulk samples. SEM uses electrons generated by a thermionic, Schottky, or field-emission cathode. The electrons are then accelerated through a voltage difference between cathode

and anode. The focused beam of electrons interacts with atoms in the sample producing secondary electrons. The secondary electrons are detected and generate a high resolution image providing information for surface characterization. [21, 22] Chemical analysis of the crystals, by means of SEM-EDX, was performed at the Texas Center for Superconductivity at the University of Houston (T<sub>C</sub>SUH). Crystals were selected and placed on a carbon disk by using adhesive carbon tape. In order to minimize electron charging effects, the samples were coated with a thin film of carbon. The coating was performed in a vacuum at  $9.5 \times 10^{-5}$  torr, using a Ladd Research Industries carbon evaporator. Subsequently, the carbon disk was attached to a brass sample holder. This was inserted into a pre-chamber of the instrument and the vacuum was pumped to approximately  $10^{-4}$  Pa. The analysis was carried out at approximately  $9 \times 10^{-5}$  Pa and the SEM data was recorded on a Jeol JSM 8330 F scanning electron microscope equipped with an energy dispersive spectrometer (EDS) using a silicon drift X-ray detector (SDD) by means of a 15 kV accelerating voltage and a 12  $\mu$ A emission current from a cold-field emission gun alongside an EDAX analyzer. The ratio of the heavy elements was analyzed using the TEAM<sup>TM</sup> EDS software Suite. The normal instrumental error is usually below 5%.

## **2.4 Differential Scanning Calorimetry.**

Differential scanning calorimetry (DSC) is used to measure the change of the difference in the heat flow rate between a sample and an inert reference sample while their temperatures are controlled by the preset program. [23] The output is a curve of heat flow

rate (mW) as a function of time (t) or temperature (T). Since the DSC works at constant pressure, the heat flow rate is equivalent to the enthalpy changes:

$$(dq/dt)_p = dH/dt \quad (2.3)$$

The difference in the heat flow rate between the sample (s) and the reference (r) is:

$$\Delta(dH/dt) = (dH/dt)_s - (dH/dt)_r \quad (2.4)$$

In an endothermic process, such as phase transitions, heat is absorbed by the sample, thus a higher heat flow rate goes to the sample to maintain the same temperature as the reference. Therefore,  $\Delta(dH/dt)$  is positive. In an exothermic process, such as crystallization, the opposite happens. [23] DSC measurements were performed using a Mettler Toledo Gas Controller GC 200 Star System. The crystals were ground into a fine powder and approximately 5-10 mg evenly placed into a 40  $\mu$ L aluminum pan. The pan was then covered with an aluminum lid and sealed. The lid was perforated in the center. An empty aluminum pan with a perforated lid was used as a reference. Liquid nitrogen was used as the cooling source with a flow rate of 80 mL/minute. The temperature for the measurements was set according to the individual sample specifications, within the range of -150  $^{\circ}$ C – 500  $^{\circ}$ C at a rate of 20  $^{\circ}$ C/minute.



## 2.5 Vibrational Spectroscopy.

### 2.5.1 Introduction to Vibrational Spectroscopy.

In crystallography, point groups are used to describe the molecular symmetry and crystal structure of a compound. The assigned molecular point group, determined from the symmetry elements, can be used to predict the spectroscopic behavior of the compound.

The complex motions of molecular vibrations are the result of the superposition of a number of relatively simple vibrational motions known as normal modes of vibration. [24]

The number of normal modes in a given molecule is determined by the number of atoms in the molecule. For a Cartesian coordinate system, an atom has three degrees of motional freedom, which are along the x, y, or z direction. The displacements occurring in these three directions are independent of each other. So a total of  $3N$  degrees of freedom are obtained, where  $N$  is the number of atoms in the molecule. For linear molecules, three of these degrees of freedom arise from translations along the axes, and two are the result of molecular rotations. For non-linear molecules, there are three degrees of translational freedom and three degrees of rotational freedom for the entire molecule. Thus,  $3N-6$  degrees of freedom remain to be normal modes related to vibrational motions in a non-linear molecule. A linear molecule is different because the rotation of the molecule about the molecular axis cannot occur since all atoms lie on the same axis. So in the special case of a linear molecule with  $N$  atoms there are  $3N-5$  normal modes of vibration.

The entire set of  $3N$  normal modes can be transformed according to the irreducible representations of the molecular point group, because the  $3N$  Cartesian displacement vectors may be used as the basis for a reducible representation. The character table

directly gives the symmetry types of the normal modes, by which we can identify the genuine modes of vibration of a molecule and the non-genuine modes of translation and rotation. [24]

From this character table, the symmetry types of normal modes also tell us their activities with respect to Raman and infrared. The Raman active species are assigned by the change of the components of the tensor of polarizability, while the infrared active vibrations respond to a change in the dipole moment. An important part of molecular symmetry concerns molecules which have a center of symmetry. There is a rule for these special molecules, that is: a vibration which is symmetric with regard to the center of symmetry is forbidden in the infrared spectrum, whereas a vibration which is antisymmetric to the center of symmetry is forbidden in the Raman spectrum. [25]

The motions that characterize normal modes of vibration in a molecule can be symmetric stretching, asymmetric stretching, bending, and deformation (including rocking, wagging, and twisting). The vibrational spectrum of a molecule is composed of different bands representing active vibrations. The spectrum depends on the masses of the atoms in the molecule, the strength of their chemical bonds, and the atomic arrangement. [26] The expression which relates these to the vibrational frequency is Hooke's law:

$$\nu = \frac{1}{2\pi c} \sqrt{\frac{K}{\mu}} \quad (2.5)$$

where  $c$  is the velocity of light,  $K$  is the force constant of the bond between atoms A and B, and  $\mu$  is the reduced mass of atoms A and B of masses  $M_A$  and  $M_B$ , and the relationship between them is given by the following equation:

$$\mu = \frac{M_A M_B}{M_A + M_B} \quad (2.6)$$

The simple model of a small molecule is widely used to interpret vibrational spectroscopy. However, it is very difficult to predict the vibrational spectra of a complex molecule that has a three-dimensional structure, and in which a large number of atoms are present. [27] To obtain this information, calculations (density functional theory (DFT)) based on the determined structural model were used. [28] This method can be used to confirm a structure model by comparing experimental spectroscopic data to the calculated phonon data. This method is much more precise than comparing the data to the already known spectroscopic data of fragments with similar point groups, because the total modes per unit cell are derived.

### 2.5.2 Vibrational Spectroscopy of Vanadates.

This work contains two different vanadates,  $[\text{VO}_4]^{3-}$  and  $[\text{V}_2\text{O}_7]^{4-}$ . To characterize their vibrational modes and to predict the vibrational spectrum bands, their individual symmetry must be taken into consideration.

The  $[\text{VO}_4]^{3-}$  unit, is tetrahedral of  $T_d$  symmetry and characterized by four vibrational modes presented by this irreducible representation [29]:

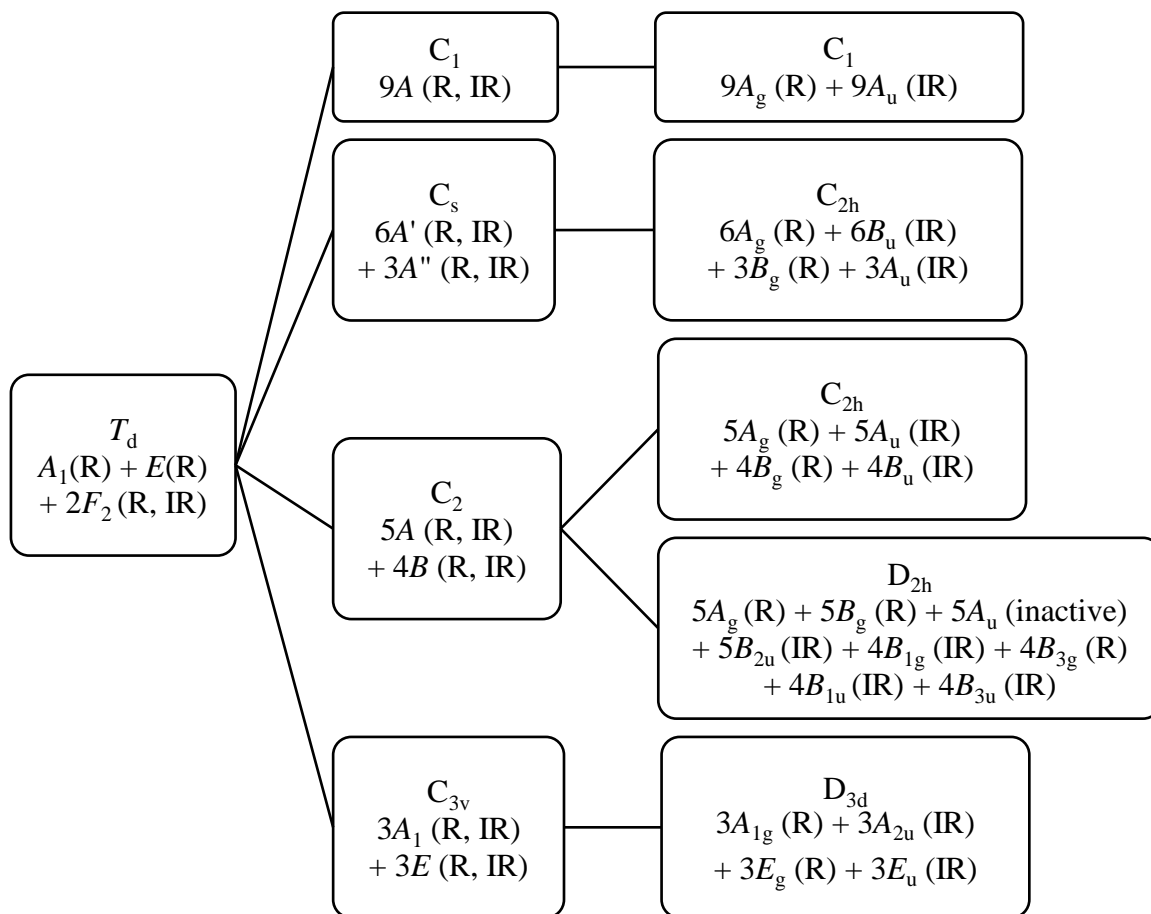
$$\Gamma = A_1(\text{R}) + E(\text{R}) + 2F_2(\text{R}, \text{IR}) \quad (2.7)$$

Through symmetry lowering to  $C_{3v}$ ,  $C_2$ ,  $C_s$ , or  $C_1$ , the degeneracy is removed and all modes become both Raman and infrared active. The vanadate unit possesses various symmetries in different synthetic compounds and crystalline minerals. For each individual case, the factor group analysis is required to generate the irreducible

representation from one of the above basic point groups, see Table 2.2. The pyrovanadate unit ( $[\text{V}_2\text{O}_7]^{4-}$ ) is more complicated since stretching and bending within the dimer unit will occur at both terminal and bridging O. [32-36] The V–O–V bridging angle has also been studied to gain understanding about its influence on the difference in frequency between asymmetric and symmetric V–O–V bridge stretching. [36-38]

The rest of the structure other than the vanadate group will also affect the vibrational modes in a compound. The Bilbao database [39] is a very useful tool to study the vibrational modes of compounds. Using a cif file as an input, detailed information on the vibrational modes is automatically generated.

Table 2.2. Factor group analysis of the  $[\text{VO}_4]$  unit. [29-31]



### 2.5.3 Infrared Spectroscopy.

Infrared spectra originate from transitions between two vibrational levels of a molecule, in the electronic ground state. [40] Infrared refers to the part of electromagnetic spectrum which has a lower frequency than the visible region and higher frequency than the microwave region. (Figure 2.3) Frequency is related to the energy of the waves given by the Bohr equation:

$$E=h\nu \quad (2.8)$$

where  $h$  is the Planck constant ( $h = 6.626 \times 10^{-34}$  J·s). The velocity of a wave is a constant:

$$c = \lambda\nu \quad (2.9)$$

The wavelength,  $\lambda$ , is inversely proportional to the frequency and energy. A customary unit for wavelength is  $\mu\text{m}$  and wavenumber in  $\text{cm}^{-1}$  is used to express frequency. By combining these relations, the following equation is introduced:

$$\bar{\nu} (\text{cm}^{-1}) = 10^4/\lambda (\mu\text{m}) \quad (2.10)$$

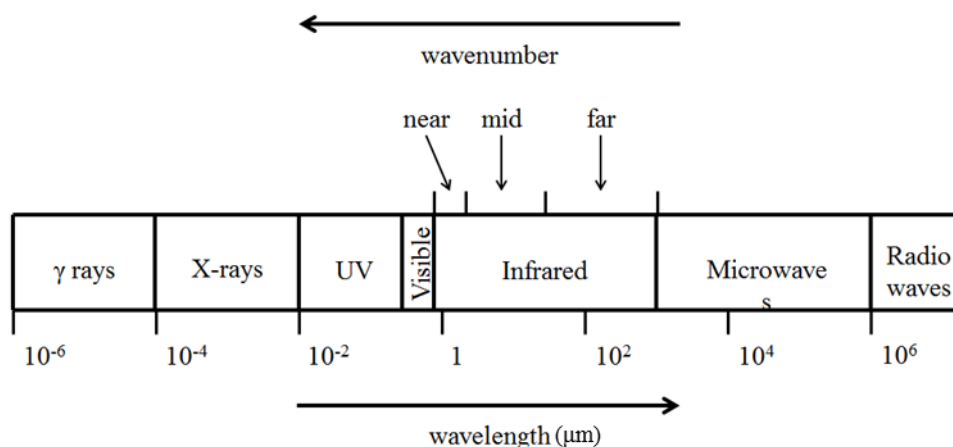


Figure 2.3. The electromagnetic spectrum. [41]

The infrared spectrum covers wavenumbers from roughly 13000 to  $10 \text{ cm}^{-1}$ , or wavelengths from 0.78 to 1000  $\mu\text{m}$ . [42] It is often divided into three regions; the near, mid, and far infrared. (see Figure 2.3) The regions can vary depending on different publications. Nevertheless, the pure vibrational spectra concerned in our research are

observed in the range between  $375\text{ cm}^{-1}$  and  $4000\text{ cm}^{-1}$ , which is within the mid infrared region. [40]

#### 2.5.4 Raman Spectroscopy.

Raman spectra originate from the electronic polarizability caused by excitation via ultraviolet or visible light. [40] This phenomenon was first observed by Dr. C. V. Raman in 1928. [43] It is based on photons interacting with the molecule and the resulting scattering. Thus, there is no need for the photon to have an energy match the difference between two energy levels of the molecule as infrared spectroscopy requires. The scattered photons are collected at an angle to the incident light beam. [27]

When the sample is irradiated with a monochromatic light source, there are two ways that the photons can be scattered by the atoms: elastic scattering and inelastic scattering. If only the electron cloud is distorted, the photons will be scattered with very small frequency changes, which is elastic scattering. For molecules this is also called Rayleigh scattering. However, if vibrational motion is involved, energy will be transferred from the incident photon to the molecule or the reverse. In this case, the scattering is inelastic. The energy difference between the scattered photon and the incident photon is one vibrational unit.

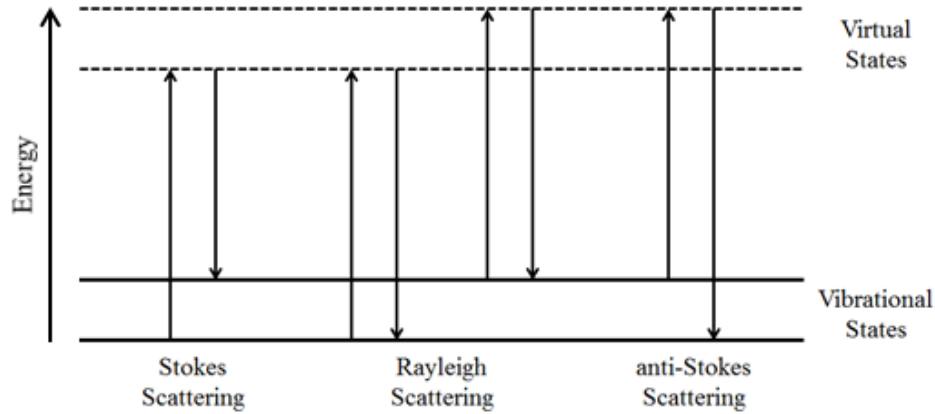


Figure 2.4. Energy level diagram for Raman scattering; (1) Stokes scattering, (2) Rayleigh scattering, (3) anti-Stokes scattering.

There are two possible types of Raman scattering, Stokes and anti-Stokes, which depend on the direction of the energy flow. For Stokes scattering, part of the incident photon energy is transformed into vibrational energy, resulting in lower scattered photon energy, and therefore a lower frequency light is observed. In the case of anti-Stokes scattering, the incident photon absorbs energy from vibrational motion of an atom, resulting in higher scattered photon energy, leading to a higher frequency light. The energy difference between the Rayleigh and Raman scattered lights can be used to measure the vibrational energy by comparing their difference in frequency. Therefore the wavenumbers of the Stokes or anti-Stokes shifts are directly equal to the vibrational energies of the solid materials. [25, 27, 44] The different types of scattering are compared in Figure 2.4.



### 2.5.5 Instrumentation of Infrared and Raman Spectroscopy.

Infrared spectroscopy was used to confirm the phase purity and to check for any residual starting materials. Furthermore, it was employed to study the V-O, *M*-O (*M* is a transition metal atom), and O-H displacements in comparison with the DFT data. All infrared spectra were collected on finely ground powder samples in an argon filled glove box on an Alpha-P Infrared Spectrometer in reflectance mode.

Raman spectroscopy measurements were performed on single crystal samples or powder samples at room temperature by Dr. Alexander Litvinchuk at the Texas Center for Superconductivity using a Horiba Jobin Yvon T 6400 spectrometer equipped with an optical microscope and a liquid nitrogen cooled CCD detector. The crystals were either placed on glass slides which had grooves carved in them or on flat thin indium plates to help mount the crystals with different orientations. In some cases for the needle-shaped crystals, glass fibers were used to orient the crystals. Polarized Raman data were measured only for crystals with regular shapes. The scattering spectra were collected using an Ar<sup>+</sup> green ( $\lambda = 514.5$  nm, 2.41 eV) or a He-Ne red ( $\lambda = 632$  nm, 1.96 eV) excitation line. In order to minimize heating of the sample, the incident laser power was kept below 1.0 mW. The laser spot had a diameter of  $\approx 2$   $\mu\text{m}$ .

## 2.6 Physical Properties.

### 2.6.1 Introduction to Magnetism.

A magnetic moment,  $M$ , is acquired by a sample of a magnetic compound in an external magnetic field,  $H$ .  $M$  is related to  $H$  through:

$$\partial M / \partial H = \chi \quad (2.11)$$

where  $\chi$  is the temperature dependent magnetic susceptibility,  $\chi(T)$ . In our research, the molar magnetic moment and molar magnetic susceptibility were usually used. When the magnetic field is weak enough,  $\chi$  is independent of  $H$ , so that the equation can be written as:

$$M = \chi H \quad (2.12)$$

In principle,  $\chi$  is the sum of two contributions:

$$\chi = \chi^D + \chi^P \quad (2.13)$$

where  $\chi^D$  and  $\chi^P$  represent the negative diamagnetic and positive paramagnetic susceptibilities, respectively. In our actual data processing, a diamagnetic correction was made based on Pascal's constants [45], by subtracting the sum of the diamagnetic contributions of all cations and anions in the molecular formula from the measured susceptibility. Since the diamagnetic susceptibility is negative, the measured susceptibility was corrected by adding a small positive value. In later chapters, diamagnetic susceptibility is subtracted for all susceptibility data and  $\chi$  refers to the corrected paramagnetic susceptibility. [46]

Consider a paramagnet with multiple ions. Magnetic moments are coupled to each other and such an internal interaction is called an exchange field. [47] The simplest situation in

molecular magnetism is that any kind of coupling between ground and excited states per magnetic ion may be neglected. In this case, the Curie law is established:

$$\chi = \frac{C}{T} \quad (2.14)$$

where  $T$  is the temperature in Kelvin, and  $C$  is the Curie constant which depends on the spin multiplicity of the ground state. [46] Interatomic coupling leads to a spontaneous ordering of the magnetic moments below some critical temperature,  $T_c$ . The Curie-Weiss law best describes the observed susceptibility variation in the paramagnetic region above  $T_c$ . It is expressed by the following equation:

$$\chi = \frac{C}{T - \Theta} \quad (2.15)$$

where  $\Theta$  is the Weiss constant.  $T_c$  indicates the transition temperature from order to disorder. By plotting  $1/\chi$  vs  $T$ , it is possible to initially judge whether a compound is ferromagnetic or antiferromagnetic, which will be discussed later. [48] The representation of an approximate quantum mechanical exchange interaction is given by exchange field:

$$U = -2JS_i \cdot S_j \quad (2.16)$$

where  $U$  is the energy of interaction, and  $J$  is the exchange integral. The coefficients relate to the overlap of the charge distributions between two atoms or ions and denoted  $i$  and  $j$ . This equation corresponds to the Heisenberg model. [47]

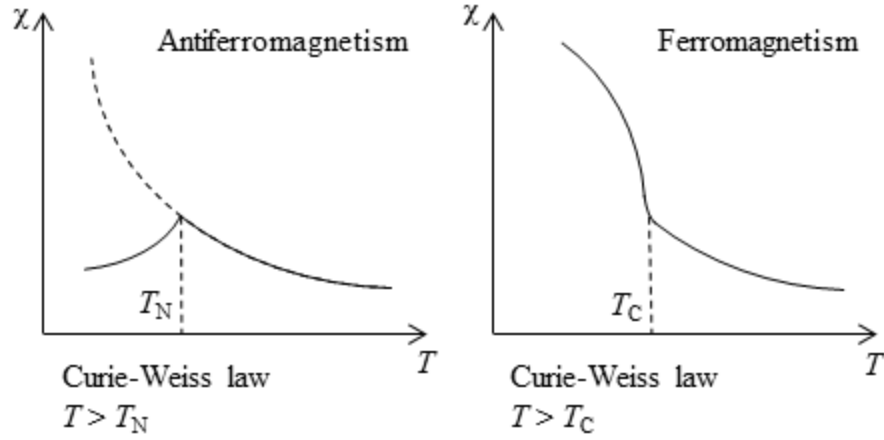


Figure 2.5. Temperature dependent magnetic susceptibility in an antiferromagnetic compound and a ferromagnetic compound [47].

There are different ordered arrangements of electron spins. If the exchange integral  $J$  is positive, ferromagnetic coupling results. A ferromagnet has a spontaneous magnetic moment arising from all electron spins aligning in the same direction, parallel to each other below a transition temperature, Curie temperature,  $T_c$ , even in an applied magnetic field of zero. Above the transition temperature, the system goes into a high temperature paramagnetic state, where spins are randomly oriented. If the exchange integral,  $J$ , is negative, the spins are antiferromagnetically coupled and ordered in an antiparallel arrangement. Two situations can arise for antiferromagnets. Either the coupled spins have equal moments leading to a net moment of zero for the substance which is antiferromagnetic, or the coupled spins have unequal moments so that there is a net magnetic moment of the substance which is ferrimagnetic. [47, 48] The transition temperature of an antiferromagnet is called the Néel temperature.

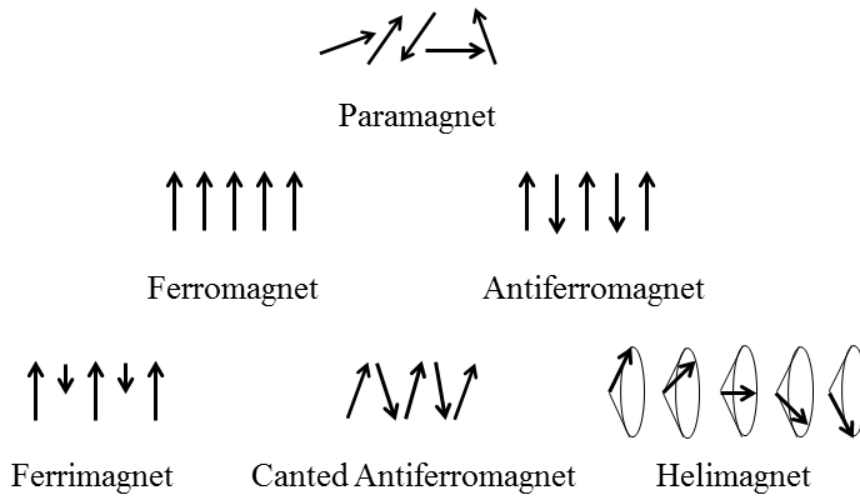


Figure 2.6. Possible ordering of electron spins.

A special case of antiferromagnetism is canted antiferromagnetism or parasitic ferromagnetism [48]. It can be accounted for by the canting of antiparallel spins. If both spins are canted in the same direction, it will result in a small net magnetic moment along this direction. However, if the canting of the spins cancel one another due to the symmetry, there will be no net moment observed. [48] Helimagnetism is an even more complicated spin arrangement resulting from the competition between ferromagnetic and antiferromagnetic coupling, which is often observed in frustrated magnetic systems. [47]

### 2.6.2 Introduction to Specific Heat ( $C_p$ ).

Specific heat or molar heat capacity is an intensive physical property, which is a characteristic of the material. The corresponding extensive property is the heat capacity. The specific heat is defined as the amount of heat required to increase the temperature per

unit quantity (mass or mole) of a pure substance by one Kelvin. Assuming a substance of mass,  $m$ , possessing a specific heat,  $C$ , to change the substance's temperature by  $\Delta T$ , the amount of heat,  $Q$ , absorbed or released is represented by the equation:

$$Q = Cm \Delta T \quad (2.17)$$

This relationship does not apply when a phase transition is encountered. Usually the specific heat,  $C_p$ , is measured at constant pressure. The specific heat includes the lattice part (phonons) as well as contribution from other terms. We are concerned with the magnetic part ( $C_m$ ). The magnetic material (ferromagnet, antiferromagnet, or ferrimagnet) shows a phase transition from the 3D ordered phase at low temperature to the disordered paramagnetic phase at high temperature above the Curie or Néel temperature. The specific measurement provides us with information about the magnetic phase transition. [49] The compounds discussed later do not undergo structural phase transitions at low temperature and, therefore, all anomalies observed originate from the magnetic contribution.

### 2.6.3 Magnetic Measurement.

Magnetic measurements were carried out on a Physical Property Measurement System (PPMS, Quantum Design) from 2 - 300 K in applied fields up to 8 T. Susceptibility data were obtained in field-cooled (FC) and zero-field-cooled (ZFC) mode. Crystals were ground into powder and pressed thin pellets for sample preparation and approximately 5 - 15 mg of the compound were wrapped in non-magnetic cling film and placed into a

plastic capsule for the measurement. All data were corrected for diamagnetic contributions.

#### 2.6.4 Specific Heat Measurement.

Specific heat measurements were also carried out on PPMS from 2 - 300 K in applied fields up to 8 T. Crystals were ground into powder for sample preparation. The same pellet used for magnetic measurement was sintered and annealed. Part of the pellet, which weighed about 4 - 6 mg was then placed into the instrument. To obtain the magnetic contribution to the total specific heat, the data was corrected by subtracting the phonon contribution. A convenient way to account for the lattice part is to use non-magnetic isotypic derivatives. The zero-field data of a non-magnetic compound with isotropic structure type was calibrated by a  $C_p/T$  or  $C_p$  max factor and shifted accordingly in temperature to use as a baseline representing the phonon contribution.

## 2.7 References

- [1] Byrappa, K.; Yoshimura, M. *Handbook Of Hydrothermal Technology*, Noyes Publications, **2001**.
- [2] Morey, G. W.; Niggli, P.; *J. Am. Chem. Soc.*, **1913**, 35, 1086.
- [3] Laudise, R. A. *The Growth of Single Crystals*, Prentice-Hall, Englewood Cliffs, NJ, **1970**.
- [4] Rabenau, A. *Angew. Chem. Int. Ed. Engl.*, **1985**, 24, 1026.
- [5] Lobachev, A. N. *Crystallization Processes under Hydrothermal Conditions*, Consultants Bureau, New York, **1973**.
- [6] Roy, R. *J. Solid State Chem.*, **1994**, 111, 11.
- [7] Byrappa, K. *Hydrothermal Growth of Crystals*, Pergamon Press, Oxford, UK, **1992**.
- [8] Brown, P. W.; Constantz, B. *Hydroxyapatite and Related Materials*, CRC Press, Inc., **1994**.
- [9] Heilbron, J. L. *Physica Scripta. T*, **1996**, 61, 60.
- [10] Suryanarayana, C.; Norton, M. G. *X-ray Diffraction: A Practical Approach*, Springer, **1998**.
- [11] Pecharsky, V. K.; Zavalij, P. Y. *Fundamentals of Powder Diffraction and Structural characterization of Material*, Springer, **2003**.
- [12] Giacovazzo, C. *et al. Fundamentals of Crystallography*, Oxford University Press, **1992**.
- [13] Rigaku, *CrystalClear*, Rigaku Corporation, Tokyo, Japan, **2011**.



- [14] Bruker, *SAINT*, Bruker AXS Inc., Madison, WI, USA, **2002-2014**
- [15] Blessing, R. H. *Acta Crystallogr. A*, **1995**, *51*, 33.
- [16] Farrugia, L. J. *WinGX*, Vers. 2013.3, *J. Appl. Cryst.*, **2012**, *45*, 849.
- [17] Sheldrick, G. M. *Acta Crystallogr. A*, **2008**, *64*, 112.
- [18] Spek, A.L. *J. Appl. Cryst.*, **2003**, *36*, 7; Spek, A. L. *Acta Cryst. D*, **2009**, *65*, 148.
- [19] Brandenburg, K. *Diamond*, Vers. 3.2i, Crystal Impact GbR, Bonn, Germany, **1997-2012**.
- [20] Rodriguez-Cavajal, J. Program *FullProf*, Vers. 2.05, Laboratoire Léon Brillouin CEA-CNRS, Gif-sur-Yvette, Cedex, France, **2011**.
- [21] Reimer, L. *Scanning Electron Microscopy: Physics of Image Formation and Microanalysis*. Springer, **1998**.
- [22] Egerton, R. F. *Physical Principles of Electron Microscopy: An Introduction to TEM, SEM, and AEM*. Springer, **2005**.
- [23] Höhne, G.; Hemminger, W. F.; Flammersheim, H.-J. *Differential Scanning Calorimetry*, Springer, **2003**.
- [24] Cotton, F. A. *Chemical Applications of Group Theory*, Wiley, **1990**.
- [25] Schrader, B. *Infrared and Raman Spectroscopy: Methods and Applications*, VCH, **1995**.
- [26] Harris, D. C.; Bertolucci, M. D. *Symmetry and Spectroscopy: An Introduction to Vibrational and Electronic Spectroscopy*, Oxford University Press, **1978**.
- [27] Smith, E.; Dent, G. *Modern Raman Spectroscopy - A Practical Approach*, Wiley, **2005**.

- [28] Clark, S. J.; Segall, M. D.; Pickard, C. J.; Hasnip, P. J.; Probert, W. J.; Refson, K.; Payne, M. C. *Z. Kristallogr.*, **2005**, 220, 567.
- [29] Frost, R. L.; Palmer, S. J.; Cejka, J.; Sejkora, J.; Plasil, J.; Bahfenne, S.; Keeffe, E. C.; *J. Raman Spectrosc.*, **2011**, 42, 1701.
- [30] Frost, R. L.; Henry, D. A.; Weier, M. L.; Martens, W. *J. Raman Spectrosc.*, **2006**, 37, 722.
- [31] Baran, E. J.; Aymonino, P. J. *J. Molec. Struc.*, **1972**, 11, 453.
- [32] Hezel, A.; Ross, S.D. *Spectrochim. Acta A*, **1967**, 23, 1583.
- [33] Brown, R.G.; Ross, S.D. *Spectrochim. Acta A*, **1972**, 28, 1263.
- [34] Frost, R. L.; Erickson, K. L.; Weier, M. L.; Carmody, O. *Spectrochim. Acta A*, **2005**, 61, 829.
- [35] de Waal, D.; Hutter, C. *Mater. Res. Bull.*, **1994**, 29, 843.
- [36] Pedregosa, J. C.; Barah, E. J.; Aymonin, P. J. *Z. anorg. Chem.*, **1974**, 404, 308.
- [37] Brown, R.G. Ph.D. Thesis, London, **1970**.
- [38] Baran, E. J. *J. Mol. Struct.*, **1978**, 48, 441.
- [39] Aroyo, M. I. *et al. Bulg. Chem. Commun.*, **2011**, 43, 183; Aroyo, M. I. *et al. Z. Krist.*, **2006**, 1, 15; Aroyo, M. I. *et al. Acta Cryst. A*, **2006**, 62, 115; Kroumova, *et al. Phase Transitions*, **2003**, 76, 155.
- [40] Nakamoto, K. *Infrared and Raman Spectra of Inorganic and Coordination Compounds, Part A, Theory and Applications in Inorganic Chemistry*, 6<sup>th</sup> edition, Wiley, **2009**.

- [41] Online edition for students of organic chemistry lab courses at the University of Colorado, Boulder, Department of Chemistry and Biochemistry, Chapter 15, *Infrared Spectroscopy: Theory*, **2002**.
- [42] Stuart, B. H. *Infrared Spectroscopy: Fundamentals and Applications*, Wiley, **2004**.
- [43] Gardiner, D. J.; Graves, P. R. *Practical Raman Spectroscopy*, Springer-Verlag, **1989**.
- [44] Weber, W. H.; Merlin, R. *Raman Scattering in Materials Science*, Springer, **2000**.
- [45] Bain, G. A.; Berry, J. F. *J. Chem. Educ.*, **2008**, 85, 532.
- [46] Kahn, O. *Molecular Magnetism*, Wiley-VCH, **1993**.
- [47] Kittel, C. *Introduction to Solid State Physics*, Wiley, New York, **2005**.
- [48] Goodenough, J. B. *Magnetism and the Chemical Bond*, Wiley, New York, **1963**.
- [49] Chaplot, S. L.; Mittal, R.; Choudhury, N. *Thermodynamic Properties of Solids: Experiment and Modeling*, Wiley, **2010**.

## Chapter Three

### Synthesis, Crystal Structures, Lattice Dynamics, and Magnetic Properties of $\text{Ba}_2\text{XCu}(\text{OH})[\text{V}_2\text{O}_7]$ with $X = \text{Cl}, \text{Br}$

#### 3.1 Introduction.

Salt-inclusion vanadates, such as  $\text{KBa}_2\text{Cl}[\text{V}_2\text{O}_7]$ , [1]  $\text{KBaClCu}[\text{V}_2\text{O}_7]$ , [2] or  $\text{Ba}_5\text{Cl}_2[\text{V}_2\text{O}_7]_2$  [3] are rare and have so far mainly been obtained by flux-melt methods. Recently, classical solid state synthesis methods have been employed to obtain salt-inclusion type of compounds containing phosphates, [4, 5] arsenates, [6, 7] silicates, [8, 9] and various vanadates. [1-3, 7, 10-14] These compounds containing other transition metals are interesting due to their potential function as batteries or catalysts and their magnetic properties. [13, 14]

Chlorovanadates have been reported [1-3, 8-14] and can be regarded as either salt-inclusion or oxide-halide intergrowth compounds. It is not common that halides and oxides are integrated into one compound. The most recent achievement for these compounds is the discovery of  $\text{Ba}_5\text{Cl}_2[\text{V}_2\text{O}_7]_2$ , [3] an alkaline-earth chlorovandate which exhibits a structure composed of a  $\frac{2}{\infty}[\text{BaCl}]$  extended salt lattice of the BN-type structure with the pseudo-hexagonal windows occupied by  $[\text{V}_2\text{O}_7]^{4-}$  units at the center.

Most of the salt-inclusion vanadates are synthesized by high temperature solid-state reactions applying flux methods. Here, we report two novel isotypic compounds ( $\text{Ba}_2\text{XCu}(\text{OH})[\text{V}_2\text{O}_7]$  with  $X = \text{Cl}, \text{Br}$ ) synthesized by hydrothermal synthesis, which

exhibit the structural feature of a  $\frac{2}{\infty}[\text{Ba}_2\text{X}]^{3+}$  layer. The magnetic transition metal,  $\text{Cu}^{2+}$  is coordinated by hydroxide ions and divanadate groups. Such a complex structure is unexpected and intriguing with regard to exhibiting interesting physical properties. Furthermore, the structure type of the title compound is significantly different from that of  $\text{KBaClCu}[\text{V}_2\text{O}_7]$  where connectivity between  $\text{Cu}^{2+}$  to both anionic sublattices ( $\text{Cl}^-$  and  $[\text{V}_2\text{O}_7]^{4-}$ ) is established. [2]

### 3.2 Synthesis of Single Crystals of $\text{Ba}_2\text{XCu}(\text{OH})[\text{V}_2\text{O}_7]$ , $\text{X} = \text{Cl}, \text{Br}$ .

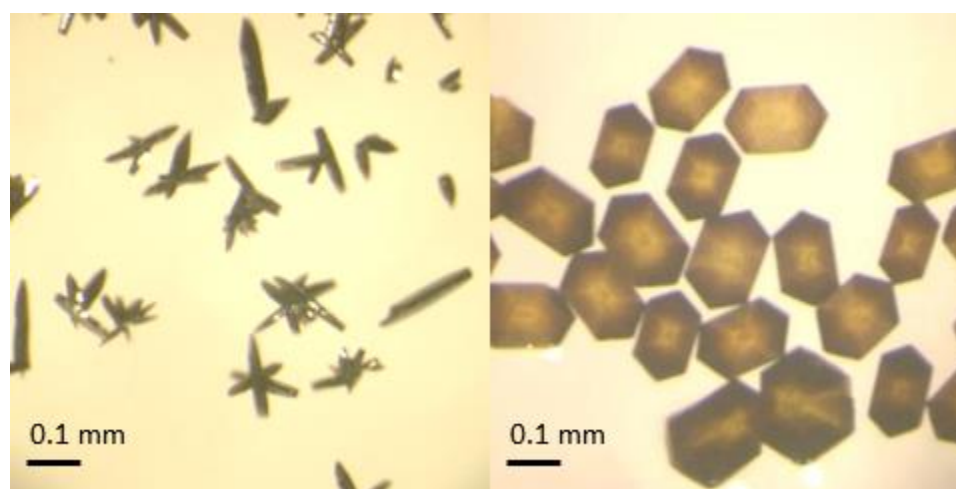


Figure 3.1. Photos of magnified crystals. *Left:*  $\text{Ba}_2\text{ClCu}(\text{OH})[\text{V}_2\text{O}_7]$ . *Right:*  $\text{Ba}_2\text{BrCu}(\text{OH})[\text{V}_2\text{O}_7]$ .

Single crystals of  $\text{Ba}_2\text{ClCu}(\text{OH})[\text{V}_2\text{O}_7]$  were synthesized by hydrothermal methods using 1.0 mmol of  $\text{NH}_4\text{VO}_3$ , 1.5 mmol of  $\text{CuCl}_2$ , 1.0 mmol of  $\text{Ba}(\text{Ac})_2$ , and 5.0 mmol of  $\text{LiCl}$  as starting materials in a molar ratio of 1 : 1.5 : 1:5. Instead of mixing all of the starting materials directly, we first dissolve the  $\text{NH}_4\text{VO}_3$  in concentrated  $\text{NH}_3\cdot\text{H}_2\text{O}$  while gently

heating ( $\sim 60\text{ }^{\circ}\text{C}$ ) and stirring. The rest of the starting materials were easily dissolved in distilled water. All solutions were then mixed together in Teflon-lined stainless steel autoclaves. Drops of concentrated  $\text{NH}_3\cdot\text{H}_2\text{O}$  were used to adjust the pH of the system to 9 - 10. The total volume of the reaction mixture was 20 ml and 26 ml Teflon-lined Parr containers were used. Typical reactions were carried out at  $220\text{ }^{\circ}\text{C}$  for 3 - 4 days. Crystals of  $\text{Ba}_2\text{BrCu}(\text{OH})[\text{V}_2\text{O}_7]$  are synthesized by replacing the  $\text{CuCl}_2$  and  $\text{LiCl}$  by the respective bromide.

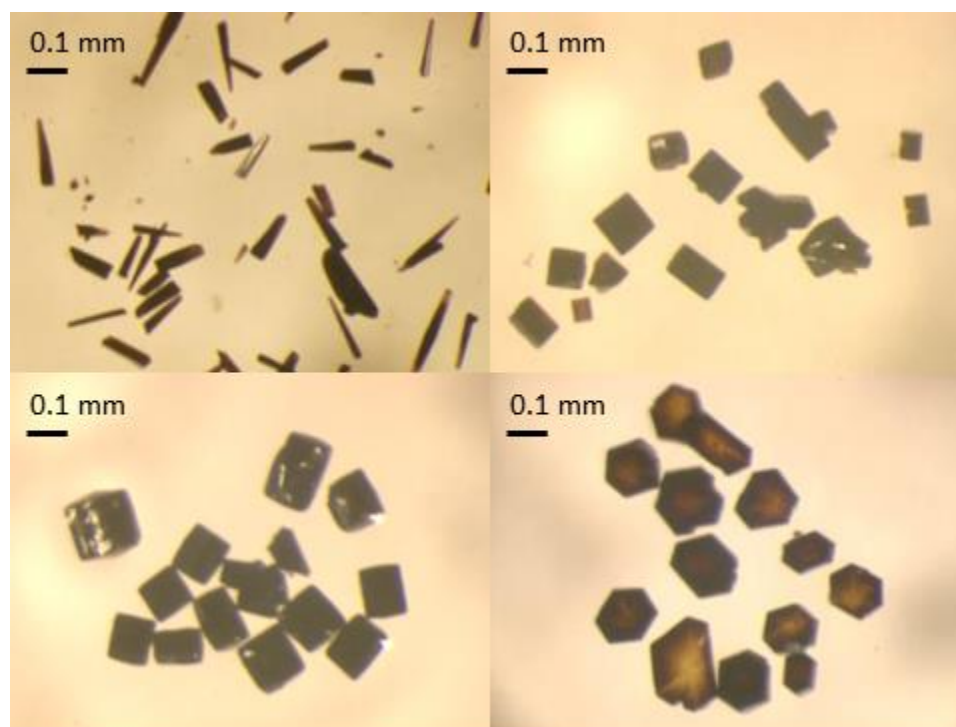


Figure 3.2. Morphologies of  $\text{Ba}_2\text{BrCu}(\text{OH})[\text{V}_2\text{O}_7]$  crystals grown at different pH values. Crystals were synthesized at initial pH = 7.8 (*top left*), 8.5 (*top right*), 9.1 (*bottom left*), 9.8 (*bottom right*).

The dark green precipitate was collected, washed with distilled water several times, and then dried naturally in the hood overnight. The main product of the olive crystals were needle shaped in the case of  $\text{Ba}_2\text{ClCu}(\text{OH})[\text{V}_2\text{O}_7]$  and of different morphologies for  $\text{Ba}_2\text{BrCu}(\text{OH})[\text{V}_2\text{O}_7]$ . The pH value has been shown to affect the morphologies of the crystals, as previously reported for hydrothermal synthesis routes. [15, 16] We conducted a series of reactions under different pH values for  $\text{Ba}_2\text{BrCu}(\text{OH})[\text{V}_2\text{O}_7]$ . As the pH increases, the crystal shape changes from needle, to rectangular, square and hexagonal.

### 3.3 Scanning Electron Microscopy-Energy Dispersive X-ray Spectroscopy (SEM-EDX) of $\text{Ba}_2\text{XCu}(\text{OH})[\text{V}_2\text{O}_7]$ , $\text{X} = \text{Cl}, \text{Br}$ .

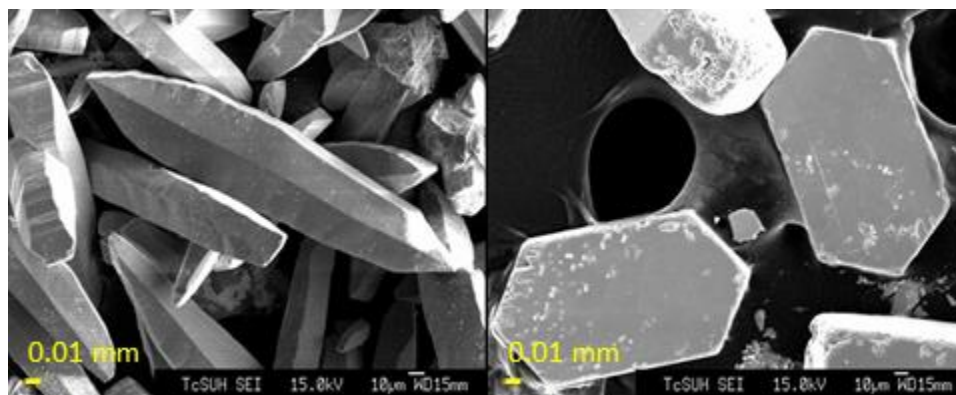


Figure 3.3. SEM pictures of carbon-coated samples indicating the morphology of the crystals:  $\text{Ba}_2\text{ClCu}(\text{OH})[\text{V}_2\text{O}_7]$  (*left*),  $\text{Ba}_2\text{BrCu}(\text{OH})[\text{V}_2\text{O}_7]$  (*right*).

The morphology of crystals are investigated by SEM. (Figure 3.3) The  $\text{Ba}_2\text{ClCu}(\text{OH})[\text{V}_2\text{O}_7]$  crystals are needle-shaped with sharp long edges and layers stacked

along the long edge, whereas the  $\text{Ba}_2\text{ClCu}(\text{OH})[\text{V}_2\text{O}_7]$  crystals synthesized at  $\text{pH} \approx 10$  are elongated hexagonal plate-shaped crystals.

Table 3.1. Atomic composition for  $\text{Ba}_2\text{XCu}(\text{OH})[\text{V}_2\text{O}_7]$ ,  $X = \text{Cl}, \text{Br}$ .

<b><math>\text{Ba}_2\text{ClCu}(\text{OH})[\text{V}_2\text{O}_7]</math></b>	<b>Ba</b>	<b>Cl</b>	<b>Cu</b>	<b>V</b>
Average, atomic%	38(1)	21(2)	18(2)	33(1)
Stoichiometry	2.3	1.3	1.1	2.0
<b><math>\text{Ba}_2\text{BrCu}(\text{OH})[\text{V}_2\text{O}_7]</math></b>	<b>Ba</b>	<b>Br</b>	<b>Cu</b>	<b>V</b>
Average, atomic%	35(2)	19(4)	13(2)	32(3)
Stoichiometry	2.2	1.2	0.8	2.0

Energy Dispersive X-ray (EDX) analysis of several crystals confirmed the composition ratio Ba/X/Cu/V of 2 : 1 : 1 : 2 with an average observed atomic-% of 38(1) Ba; 21(2) Cl; 18(2) Cu; 33(1) V from 11 measured spots for  $\text{Ba}_2\text{ClCu}(\text{OH})[\text{V}_2\text{O}_7]$  (Table 3.8 in the supplemental material) and 35(2) Ba; 19(4) Br; 13(2) Cu; 32(3) V from 14 measured spots for  $\text{Ba}_2\text{BrCu}(\text{OH})[\text{V}_2\text{O}_7]$  (Table 3.9 in the supplemental material), respectively.  $\text{BaX}_2$ ,  $X = \text{Cl}, \text{Br}$ , and Cu as well as V metal were used as standards. The calculated stoichiometry (Table 3.1) for both  $\text{Ba}_2\text{XCu}(\text{OH})[\text{V}_2\text{O}_7]$ ,  $X = \text{Cl}, \text{Br}$  compounds support the structure models solved and refined from our single crystal X-ray data.



### 3.4 Single Crystal X-ray Diffraction of $\text{Ba}_2\text{XCu}(\text{OH})[\text{V}_2\text{O}_7]$ , $X = \text{Cl}, \text{Br}$ .

Crystals were measured on Rigaku instruments. A needle-shaped crystal was selected from the  $\text{Ba}_2\text{ClCu}(\text{OH})[\text{V}_2\text{O}_7]$  batch and a hexagonal plate-shaped crystal was selected from the  $\text{Ba}_2\text{BrCu}(\text{OH})[\text{V}_2\text{O}_7]$  batch. Single crystal data sets for  $\text{Ba}_2\text{XCu}(\text{OH})[\text{V}_2\text{O}_7]$ ,  $X = \text{Cl}, \text{Br}$  were collected. The unit cell parameters were initially determined for monoclinic with the unique  $\beta$  angle around  $115^\circ$  and  $a$  and  $c$  are almost equal. The reflection conditions are not clear, and PLATON suggests the orthorhombic space group *Pnma* unambiguously for both  $\text{Ba}_2\text{ClCu}(\text{OH})[\text{V}_2\text{O}_7]$  and  $\text{Ba}_2\text{BrCu}(\text{OH})[\text{V}_2\text{O}_7]$  compounds. Unindexed peaks of the general pattern indicates a possible twinning problem. The H-refinement is not achievable due to the residual electron density. The R values indicate a problematic structure probably due to stacking disorder or crystal twinning problems. The crystal structure was refined as Chapter Two. The crystallographic details of the crystal data for  $\text{Ba}_2\text{XCu}(\text{OH})[\text{V}_2\text{O}_7]$ ,  $X = \text{Cl}, \text{Br}$  are listed in Table 3.2. Fractional atomic coordinates and isotropic or equivalent isotropic displacement parameters are listed in S2 and selected interatomic distances and angles for both structures are listed in S3, S4, respectively, in the supplemental material.

Table 3.2. Crystal data and details of the structure determination for Ba<sub>2</sub>XCu(OH)[V<sub>2</sub>O<sub>7</sub>],  
X = Cl, Br. (refined with twin law: a rotation with respect to *a* axis)

Formula	Ba <sub>2</sub> ClCuV <sub>2</sub> O <sub>8</sub>	Ba <sub>2</sub> BrCuV <sub>2</sub> O <sub>8</sub>
Mass/Formula unit ( <i>M<sub>r</sub></i> )	603.55 g mol <sup>-1</sup>	648.01 g mol <sup>-1</sup>
Crystal system	orthorhombic	orthorhombic
Space group	<i>Pnma</i> , <i>Z</i> = 4	<i>Pnma</i> , <i>Z</i> = 4
Lattice constants	<i>a</i> = 15.1085(2) Å <i>b</i> = 6.0802(1) Å <i>c</i> = 9.6152(2) Å	<i>a</i> = 15.193(1) Å <i>b</i> = 6.1110(1) Å <i>c</i> = 9.6658(2) Å
Volume	883.28(2) Å <sup>3</sup>	897.43(6) Å <sup>3</sup>
Density	4.539 g/cm <sup>3</sup>	4.796 g/cm <sup>3</sup>
F (000)	1144	1144
Temperature	293K	293K
Crystal size	0.10 × 0.05 × 0.04 mm	0.16 × 0.10 × 0.04 mm
Range	θ <sub>max</sub> = 30.051°; θ <sub>min</sub> = 2.511°	θ <sub>max</sub> = 34.980°; θ <sub>min</sub> = 3.334°
Data set	-21 < <i>h</i> < 21 -8 < <i>k</i> < 8 -13 < <i>l</i> < 13	-24 < <i>h</i> < 23 -9 < <i>k</i> < 9 -15 < <i>l</i> < 15
<i>R</i> <sub>int</sub>	0.0364	0.0305
Measured/Unique reflections	17443/1143	14620/2286
Parameter refined	68	78
<i>R</i> <sub>1</sub> , <i>wR</i> <sub>2</sub> , GooF	0.1349, 0.3094, 1.306	0.1091, 0.2575, 1.290
μ (Mo Kα)	13.503 mm <sup>-1</sup>	17.445 mm <sup>-1</sup>
( <i>T</i> <sub>min</sub> , - <i>T</i> <sub>max</sub> )	0.856 - 1.000	0.494 - 1.000
BASF	0.01808, 0.01455, 0.01396	0.01364, 0.00515, 0.00875

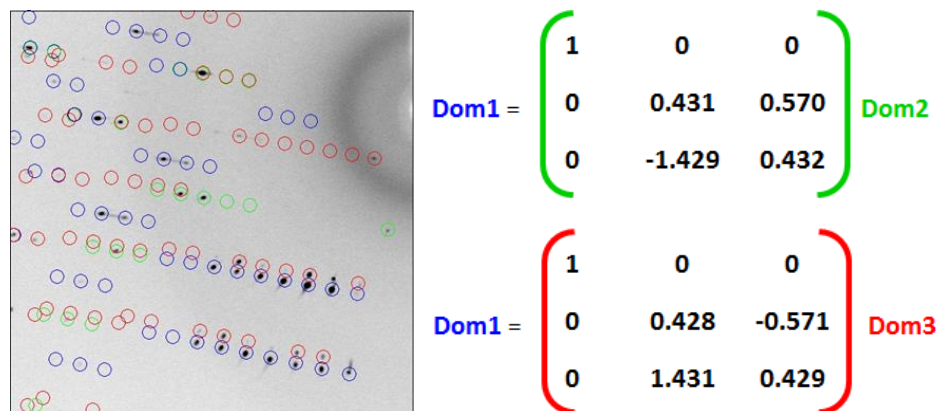


Figure 3.4. *Left:* Image of reflections for  $\text{Ba}_2\text{ClCu}(\text{OH})[\text{V}_2\text{O}_7]$  showing three domains circled by different colors. The main domain is Domain 1 (blue). *Right:* Matrices representing the orientations of the other two domains as related to Domain 1. Domain 2 (green) is clockwise rotated by  $64.46^\circ$ , with respect to  $a$  axis, and Domain 3 (red) is counterclockwise rotated by  $64.64^\circ$  with respect to  $a$  axis.

Crystal data of  $\text{Ba}_2\text{ClCu}(\text{OH})[\text{V}_2\text{O}_7]$  show that one unit cell cannot index all reflections. At least three domains indexed for the same unit cell are distinguished utilizing the TwinSolve software integrated in *CrystalClear-SM Expert 2.0 r15* (Rigaku, 2011). Figure 3.4 is shown here as an example, different domains are circled in different colors. Domain 1 (blue) is the major component. Reflections circled by green and red are somewhat too close to the reflections belonging to Domain 1, which indicates a twinning problem. The orientation of the additional two domains can be expressed as a function of Domain 1, with a rotation of approximately  $64.5^\circ$  with respect to  $a$  axis, either clockwise or counterclockwise.

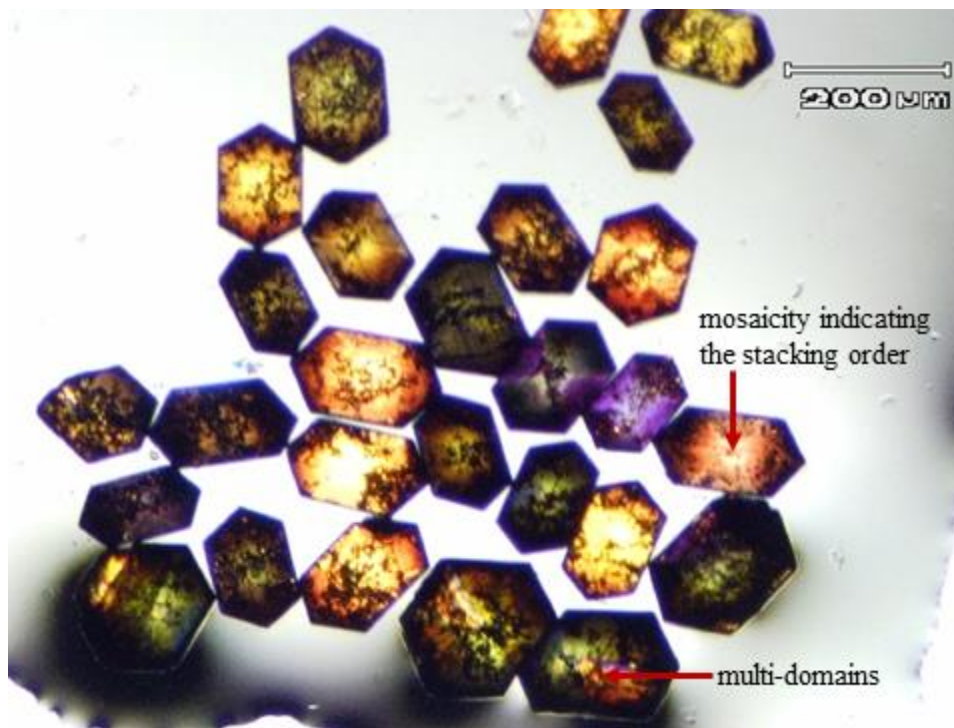


Figure 3.5. Photos of magnified  $\text{Ba}_2\text{BrCu}(\text{OH})[\text{V}_2\text{O}_7]$  crystals under polarized light.

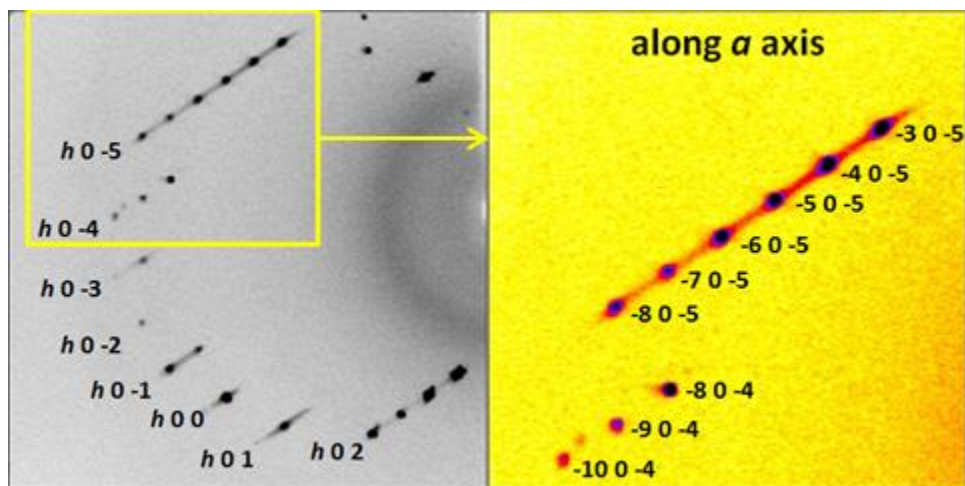


Figure 3.6. *Left*: Image of reflections for  $\text{Ba}_2\text{BrCu}(\text{OH})[\text{V}_2\text{O}_7]$  showing streaks between unique reflections. *Right*: Indexed reflections showing the orientation of the streaks.

On the other hand, a microscope with polarized light was used to help selecting suitable single crystals for  $\text{Ba}_2\text{BrCu}(\text{OH})[\text{V}_2\text{O}_7]$  [17] See Figure 3.5, crystals with a regular shape and single color were selected for single X-ray diffraction measurements. Domains of  $\text{Ba}_2\text{BrCu}(\text{OH})[\text{V}_2\text{O}_7]$  structure are indistinguishable. However, some continuous streaks were found in between unique reflections for the crystal structure of  $\text{Ba}_2\text{BrCu}(\text{OH})[\text{V}_2\text{O}_7]$  indicating the stacking faults. [18] Moreover all the streaks are along the  $a$  axis. (Figure 3.6)

Table 3.3. Integral reflection conditions for  $Pnma$  (No. 62).

Types of reflections	$hkl$	$0kl$	$h0l$	$hk0$	$h00$	$0k0$	$00l$
Reflection conditions	-	$k+l = 2n$	-	$h = 2n$	$h = 2n$	$k = 2n$	$l = 2n$

The extinction rules for the reflections of  $Pnma$  (No. 62) space group are listed in Table 3.3. Systematic absence violations were found for both crystal data sets and can be eliminated by applying the same twin law derived from  $\text{Ba}_2\text{ClCu}(\text{OH})[\text{V}_2\text{O}_7]$  data.  $\text{Ba}_2\text{BrCu}(\text{OH})[\text{V}_2\text{O}_7]$  has much smaller relative batch scale factors (BASF) for each component compared with  $\text{Ba}_2\text{ClCu}(\text{OH})[\text{V}_2\text{O}_7]$ . The domains in  $\text{Ba}_2\text{BrCu}(\text{OH})[\text{V}_2\text{O}_7]$  structure are indistinguishable, a possible pseudo-merohedral [19] twinning may occur in this case.

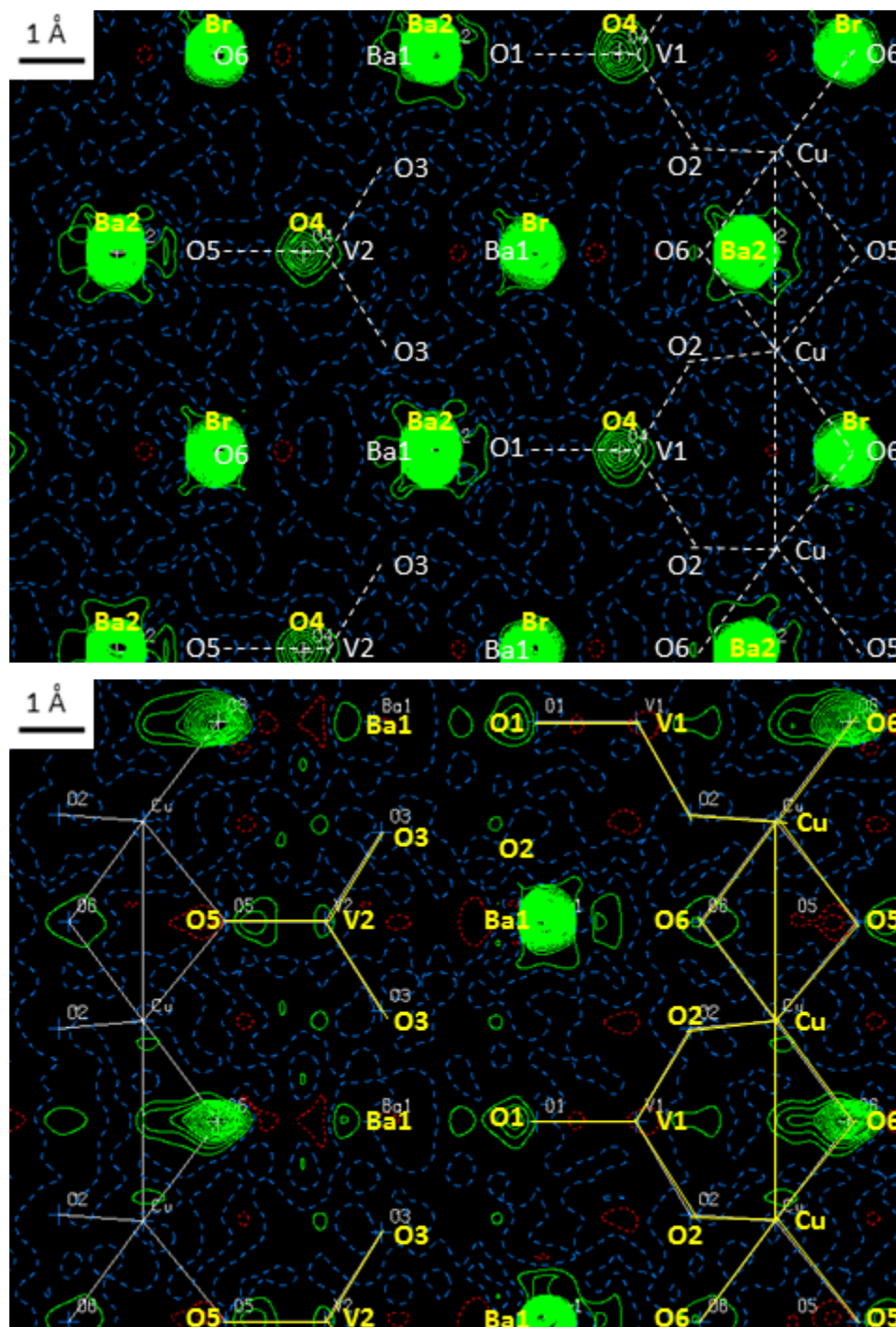


Figure 3.7.  $2F_o - F_c$  electron density maps of  $\text{Ba}_2\text{BrCu}(\text{OH})[\text{V}_2\text{O}_7]$  generated from crystal data (*bc* plane). *Top*: Ba-Br pseudo-honeycomb type of arrangement. *Bottom*: Cu–O chains connected to  $[\text{V}_2\text{O}_7]$ . Peaks (green), holes (red).

The R values are not much improved by applying the twin law, which may be attributed to the stacking faults. In Figure 3.7, the  $2F_o - F_c$  electron density maps of  $\text{Ba}_2\text{BrCu}(\text{OH})[\text{V}_2\text{O}_7]$  crystal data are obtained from PLATON. Here, we show the maps in the  $bc$  planes which are perpendicular to the stacking orientation ( $a$  axis). The heavy atoms of Ba2 and Br form pseudo-honeycomb 2D lattices with out-of-plane Ba1 atoms connected to Br. The  $[\text{V}_2\text{O}_7]$  dimers are in the center of the honeycombs. (Figure 3.7 - top) In between the 2D lattices, the  $[\text{V}_2\text{O}_7]$  dimers connect to Cu-O chains via two terminal O atoms. Notice that the sticking-out Ba1 and O6 atoms are at the same level with respect to the  $a$  axis. (Figure 3.7 - bottom) The rotation of the  $[\text{V}_2\text{O}_7]$  dimer with respect to Ba-Br lattice will shift the orientation of connected Cu-O chain. Thus, the Ba1 and O6 positions might overlap, which can explain the residual electron density observed around O6.

### 3.5 Powder X-ray Diffraction and Refinement of $\text{Ba}_2\text{XCu}(\text{OH})[\text{V}_2\text{O}_7]$ , $X = \text{Cl}, \text{Br}$ .

Powder refinement data for  $\text{Ba}_2\text{XCu}(\text{OH})[\text{V}_2\text{O}_7]$  ( $X = \text{Cl}, \text{Br}$ ) is shown in Figure 3.8. The tiny extra peaks in the  $\text{Ba}_2\text{BrCu}(\text{OH})[\text{V}_2\text{O}_7]$  refinement are identified as a small portion of impurity of  $\text{Ba}_2\text{V}_2\text{O}_7$ . The results of the refinements confirm our structural model with  $Pnma$  space group, see Table 3.4.



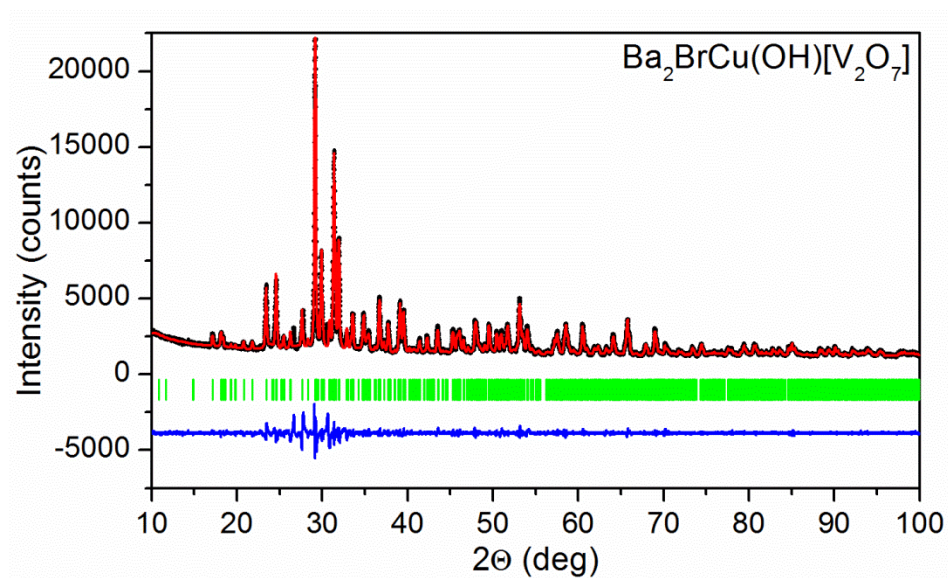
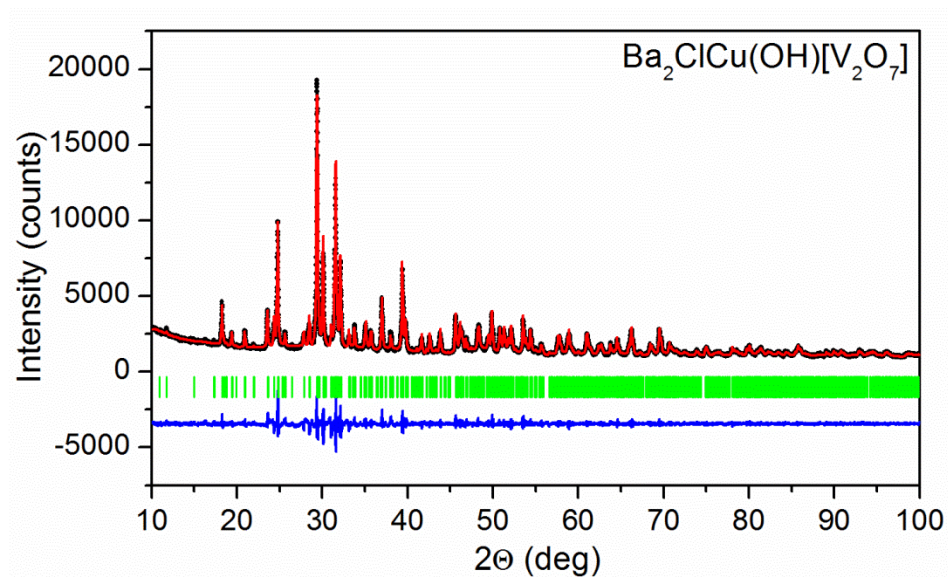


Figure 3.8. Powder refinement data for  $\text{Ba}_2\text{ClCu}(\text{OH})[\text{V}_2\text{O}_7]$  (*left*);  $\text{Ba}_2\text{BrCu}(\text{OH})[\text{V}_2\text{O}_7]$  (*right*). Observed (red), calculated (black), Bragg positions (green) and difference (blue).



Table 3.4. Powder refinement results of  $\text{Ba}_2\text{XCu}(\text{OH})[\text{V}_2\text{O}_7]$ ,  $X = \text{Cl}, \text{Br}$ , orthorhombic space group  $Pnma$  ( $Z = 4$ ).

<b>Formula</b>	$\text{Ba}_2\text{ClCu}(\text{OH})[\text{V}_2\text{O}_7]$	$\text{Ba}_2\text{BrCu}(\text{OH})[\text{V}_2\text{O}_7]$
<b>Unit Cell (<math>\text{\AA}</math>)</b>	$a = 15.0889(2)$	$a = 15.1942(3)$
	$b = 6.0710(1)$	$b = 6.1182(1)$
	$c = 9.6076(1)$	$c = 9.6616(1)$
<b>Volume (<math>\text{\AA}^3</math>)</b>	880.10(2)	898.15(2)
$\chi^2$	4.63	6.11
$R_{\text{Bragg}}$	1.226	1.109
<b>RF-factor</b>	0.6767	0.7520

### 3.6 Crystal Structure Description and Discussion for $\text{Ba}_2\text{XCu}(\text{OH})[\text{V}_2\text{O}_7]$ , $X = \text{Cl}, \text{Br}$ .

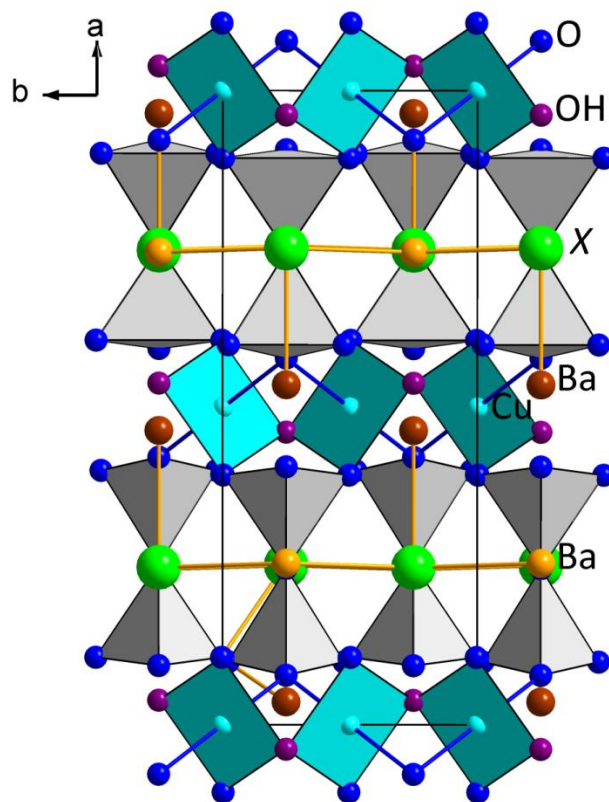


Figure 3.9. Projection of the crystal structure of  $\text{Ba}_2\text{XCu}(\text{OH})[\text{V}_2\text{O}_7]$ ,  $X = \text{Cl}, \text{Br}$ .

Figure 3.9 shows the unit cell of the structure model of  $\text{Ba}_2\text{XCu}(\text{OH})[\text{V}_2\text{O}_7]$  with  $X = \text{Cl}$  or  $\text{Br}$ . It contains multi-anions and the structure is stacked with both oxide and halide layers along  $a$  axis. Overall, the crystal structure can be divided into three features:  $\frac{2}{\infty}[\text{Ba}_2\text{X}]^{3+}$  layers,  $[\text{V}_2\text{O}_7]^{4-}$  dimers and  $\frac{1}{\infty}[\text{CuO}_{2/2}(\text{OH})_{2/2}\text{O}_{2/1}]^{5-}$  chains.

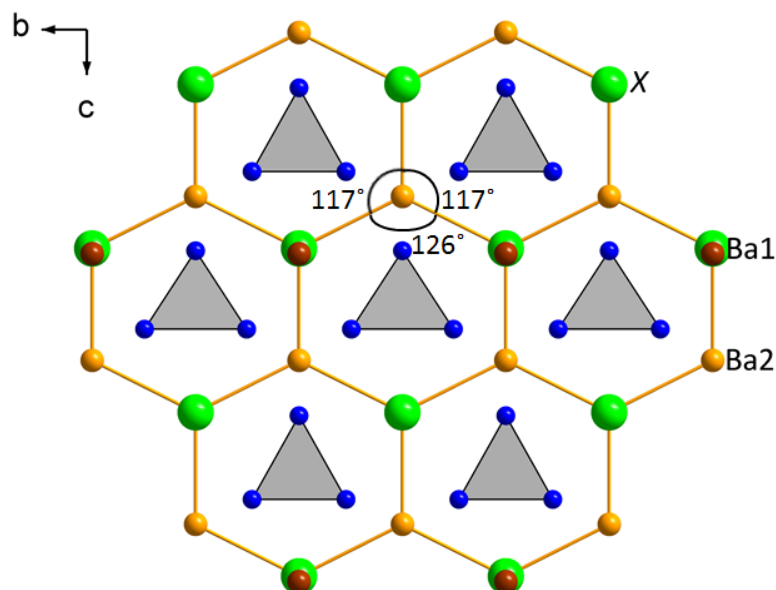


Figure 3.10. Projection of the intergrown  $\frac{2}{3}[\text{Ba}_2\text{X}]^{3+}$  layer with the  $[\text{V}_2\text{O}_7]^{4-}$  in the center of a pseudo-honeycomb type of arrangement in  $\text{Ba}_2\text{XCu}(\text{OH})[\text{V}_2\text{O}_7]$ ,  $\text{X} = \text{Cl}, \text{Br}$ .

Table 3.5 Distances and angles for Ba–X bonds.

$\text{Ba}_2\text{XCu}(\text{OH})[\text{V}_2\text{O}_7]$	$\text{X} = \text{Cl}$	$\text{X} = \text{Br}$
X–Ba1	3.186(8) Å	3.268(2) Å
X–Ba2 (×2)	3.409(4) Å	3.415(1) Å
X–Ba2'	3.265(8) Å	3.308(2) Å
Ba2–X–Ba2 (×2)	116.9(1)°	116.51(3)°
Ba2–X–Ba2'	126.2(2)°	126.97(7)°

The main symmetry of the  $\text{Ba}_2\text{XCu}[\text{V}_2\text{O}_7](\text{OH})$  type of structures is determined by the arrangement of the  $\frac{2}{3}[\text{Ba}_2\text{X}]^{3+}$  layers. (Figure 3.10) Three  $\text{Ba}^{2+}$  and three  $\text{X}^-$  ions form a slightly distorted hexagonal ring with interior angles quite close to  $120^\circ$  ( $117^\circ$ ,  $117^\circ$ ,

126°), see Table 3.5, and this is extended into an infinite plane with an alternating arrangement (BN-structure type analogy). Each  $X^-$  is connected to an extra out-of plane  $Ba^{2+}$  ion (Ba1). The  ${}^2_\infty[Ba_2X]^{3+}$  layers maintain the whole structure as a framework. Each hexagon contains one centered  $[V_2O_7]^{4-}$  dimer. As shown in Figure 3.11, the  ${}^2_\infty[Ba_2X]^{3+}$  framework is weakly coupled to the  $[V_2O_7]^{4-}$  dimer. Thus there is no restriction for the rotation of  ${}^2_\infty[Ba_2X]^{3+}$  and  $[V_2O_7]^{4-}$ . The orientation of layers might be altered.

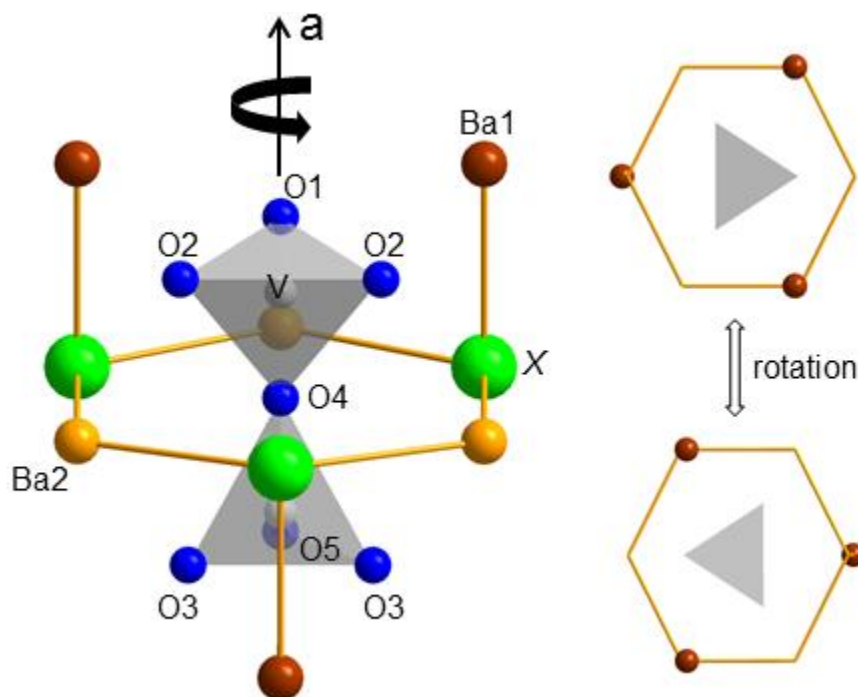


Figure 3.11. Perspective view of  $[V_2O_7]^{4-}$  in the center of distorted hexagonal ring of  ${}^2_\infty[Ba_2X]^{3+}$  layer indicating a freedom of rotation between the  $[V_2O_7]^{4-}$  dimer and the  ${}^2_\infty[Ba_2X]^{3+}$  layer.

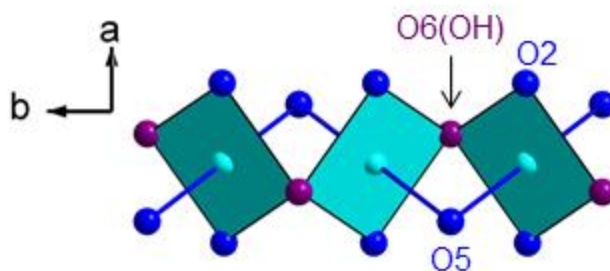


Figure 3.12. Perspective view of the  $\frac{1}{\infty}[\text{CuO}_{2/2}(\text{OH})_{2/2}\text{O}_{2/1}]^{5-}$  chain in  $\text{Ba}_2\text{XCu}(\text{OH})[\text{V}_2\text{O}_7]$ ,  $X = \text{Cl}, \text{Br}$ .

Table 3.6. Cu–O distances and Cu–O–Cu angles of  $\text{Ba}_2\text{XCu}(\text{OH})[\text{V}_2\text{O}_7]$ ,  $X = \text{Cl}$  or  $\text{Br}$ , referring to Figure 3.12.

$\text{Ba}_2\text{XCu}(\text{OH})[\text{V}_2\text{O}_7]$	$X = \text{Cl}$	$X = \text{Br}$
Cu–O6(OH)	1.99(2) Å	1.989(9) Å
Cu–O2	2.09(2) Å	2.056(9) Å
Cu–O5	2.29(2) Å	2.35(1) Å
Cu–O6(OH)–Cu	99(1)°	100.4(6)°
Cu–O5–Cu	83.1(8)°	81.1(4)°

The  $[\text{V}_2\text{O}_7]^{4-}$  dimer group as shown in Figure 3.11 is connected to  $\text{Cu}^{2+}$  in a bridging fashion between two  $\text{Cu}^{2+}$  sites resulting in the formation of  $\frac{1}{\infty}[\text{CuO}_{2/2}(\text{OH})_{2/2}\text{O}_{2/1}]^{5-}$  which corner-share two O-atoms and two terminal O-atoms. The C.N. for  $\text{Cu}^{2+}$  is complemented by two  $(\text{OH})^-$  groups. The distorted octahedra centered by  $\text{Cu}^{2+}$  are connected to each other via edge-sharing and form a trans  $\frac{1}{\infty}[\text{CuO}_{2/2}(\text{OH})_{2/2}\text{O}_{2/1}]^{5-}$  chain (Figure 3.12). Within the chain, the octahedra are connected by edge-sharing. Cu–O distances and

bridging Cu–O–Cu angles are investigated and listed in Table 3.6. Within the colored plaquette, four Cu–O distances including Cu–O6(OH) distances are similar. While the Cu–O5 bonds perpendicular to the plaquette are much longer.

The structure is built up along the  $a$  axis by  $\frac{2}{\infty}[\text{Ba}_2\text{X}]^{3+}$  layers. These layers are connected via  $[\text{V}_2\text{O}_7]^{4-}$  dimers to the  $\frac{1}{\infty}[\text{CuO}_{2/2}(\text{OH})_{2/2}\text{O}_{2/1}]^{5-}$  chains, and these connections are weak and loose. For example, the Ba1 ions stick out of the pseudo-honeycomb Ba- $X$  plane into the interlayer spaces which are not occupied by the  $\frac{1}{\infty}[\text{CuO}_{2/2}(\text{OH})_{2/2}\text{O}_{2/1}]^{5-}$  chains.

### 3.7 Spectroscopy for $\text{Ba}_2\text{XCu}(\text{OH})[\text{V}_2\text{O}_7]$ , $X = \text{Cl}, \text{Br}$ .

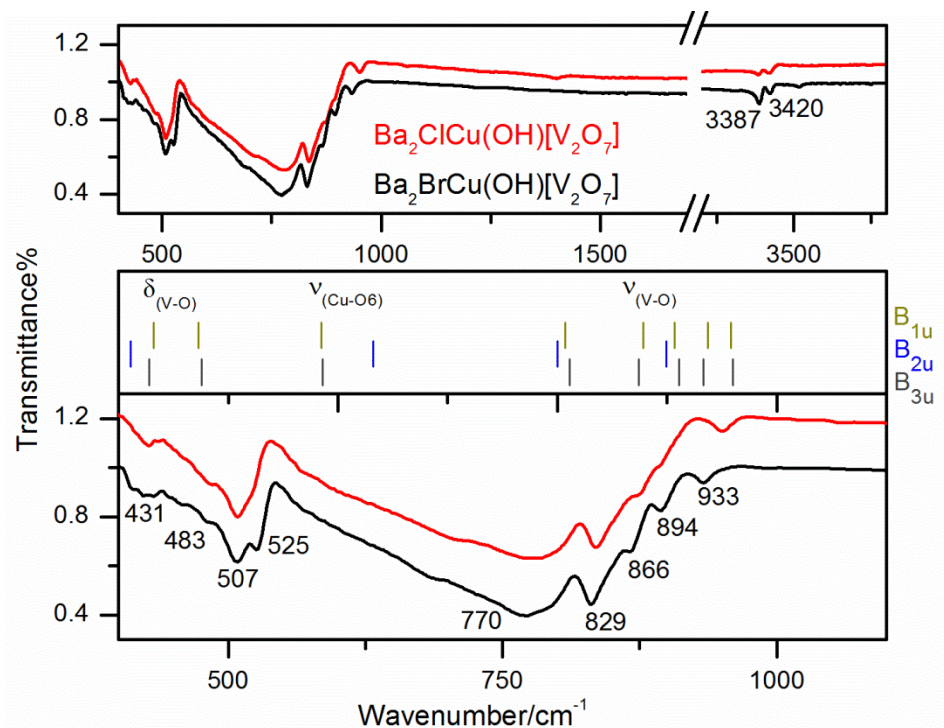


Figure 3.13. Experimental MIR-spectra and calculated displacements for  $\text{Ba}_2\text{XCu}(\text{OH})[\text{V}_2\text{O}_7]$ ,  $X = \text{Cl}, \text{Br}$ .

Infrared and Raman spectroscopy were used to study the lattice dynamics. Since there are 56 atoms excluding H atoms within one unit cell, the total number of normal modes will be  $56 \times 3 = 168$ . All expected IR and Raman active modes are:  $\Gamma_{\text{total}} = 24A_g (\text{RA}) + 18A_u (\text{inactive}) + 15B_{1g} (\text{RA}) + 27B_{1u} (\text{IR}) + 24B_{2g} (\text{RA}) + 18B_{2u} (\text{IR}) + 15B_{3g} (\text{RA}) + 27B_{3u} (\text{IR})$ . The Density Functional Theory (DFT) method is used to calculate the frequencies for all the modes. Comparing the Raman and IR data to the DFT data helps us to evaluate the structure model previously obtained from the single crystal X-ray diffraction data.

Comparing the two compounds of  $X = \text{Cl}$  and  $\text{Br}$ , almost the same mid-infrared (MIR) spectra are observed, see Figure 3.13. The modes at  $3387 \text{ cm}^{-1}$  and  $3420 \text{ cm}^{-1}$  can be assigned as the O-H stretching modes, and these are supposed to be split for an orthorhombic structure. As reported for natural minerals, e.g.  $\text{Cu}_2(\text{OH})_3\text{Cl}$ , the  $\text{OH}^-$  stretching modes of hydroxide bonded to  $\text{Cu}^{2+}$  have frequencies ranging from  $3315 \text{ cm}^{-1}$  to  $3450 \text{ cm}^{-1}$ , [20] and in our case the modes are found in this energy range. On the other hand, the  $\text{OH}^-$  stretching modes of a “free” hydroxide ion are found at  $\sim 3550 \text{ cm}^{-1}$  as observed for  $\text{NaOH}$  [21, 22] and  $\text{Na}_5\text{FeO}_3(\text{OH})$  [23].

Table 3.7. Assignments of MIR-spectra for  $\text{Ba}_2\text{BrCu}(\text{OH})[\text{V}_2\text{O}_7]$  compared with DFT data.

Fundamental assignments for isolated $[\text{V}_2\text{O}_7]^{4-}(\text{aq})$ ( $\text{cm}^{-1}$ )		Assignments based on DFT data	DFT ( $\text{cm}^{-1}$ )	Experimental ( $\text{cm}^{-1}$ )	$\Delta v_{\text{cal-exp}}$ ( $\text{cm}^{-1}$ )
		$\nu(\text{OH})$		3420, 3387	
$\nu(\text{VO}_3)(\text{sym})$	877	$\nu(\text{VO}_3)$	960, 958	933	26
$\nu(\text{VO}_3)(\text{asym})$	850	$\nu(\text{VO}_3)$ and $\nu(\text{VOV})$	937, 933	894	41
		$\nu(\text{VO}_3)$ and $\delta(\text{VO}_3)$	911, 907, 899	866	40
		$\nu(\text{VO}_3)$ and $\nu(\text{VOV})$	878, 874	829	47
$\nu(\text{VOV})(\text{asym})$	810	$\nu(\text{VOV})$	811, 807, 800	770	36
		$\delta(\text{Cu-O6})$	632	525	107
		$\delta(\text{Cu-O6})$	586, 585	507	78
$\nu(\text{VOV})(\text{sym})$	503	$\nu(\text{VOV})$ and $\delta(\text{VOV})$	477, 473	483	
		$\delta(\text{Cu-O2})$	432, 428, 411	410 - 440	



Assignments for  $\text{Ba}_2\text{BrCu}(\text{OH})[\text{V}_2\text{O}_7]$  are referenced in the range between 700 and 950  $\text{cm}^{-1}$  as V-O stretching; around 525  $\text{cm}^{-1}$  as Cu-O6 stretching; and below 500  $\text{cm}^{-1}$  can be assigned as V-O deformation modes, see Table 3.7. Compared with the fundamental vibrational modes for the  $[\text{V}_2\text{O}_7]^{4-}$  in aqueous solution, [24] assignments for the  $[\text{V}_2\text{O}_7]^{4-}$  in our compounds are much more complicated, but in good agreement with the general trend. Experimental and theoretical data match well in energies, except for the prominent blue shifts for the Cu-O6 stretching modes. This can be explained by the fact that hydrogen has not been considered in the structure model used for the DFT calculation, because we were unable to localize the H-positions in our structural model. An “over-charged” Cu cation (formally  $\text{Cu}^{3+}$ ) results and increases the frequency of the Cu-O6 stretching modes by  $\sim 100 \text{ cm}^{-1}$ . Thus, it is conceivable that the H atom is localized on the O6 atom (OH-group), which then results in  $\text{Cu}^{2+}$ , see also the magnetic property measurements. Cu-O6 displacements are isolated from the pyrovanadate group (Figure 3.14). Further details are given in the supplemental material. (S5)

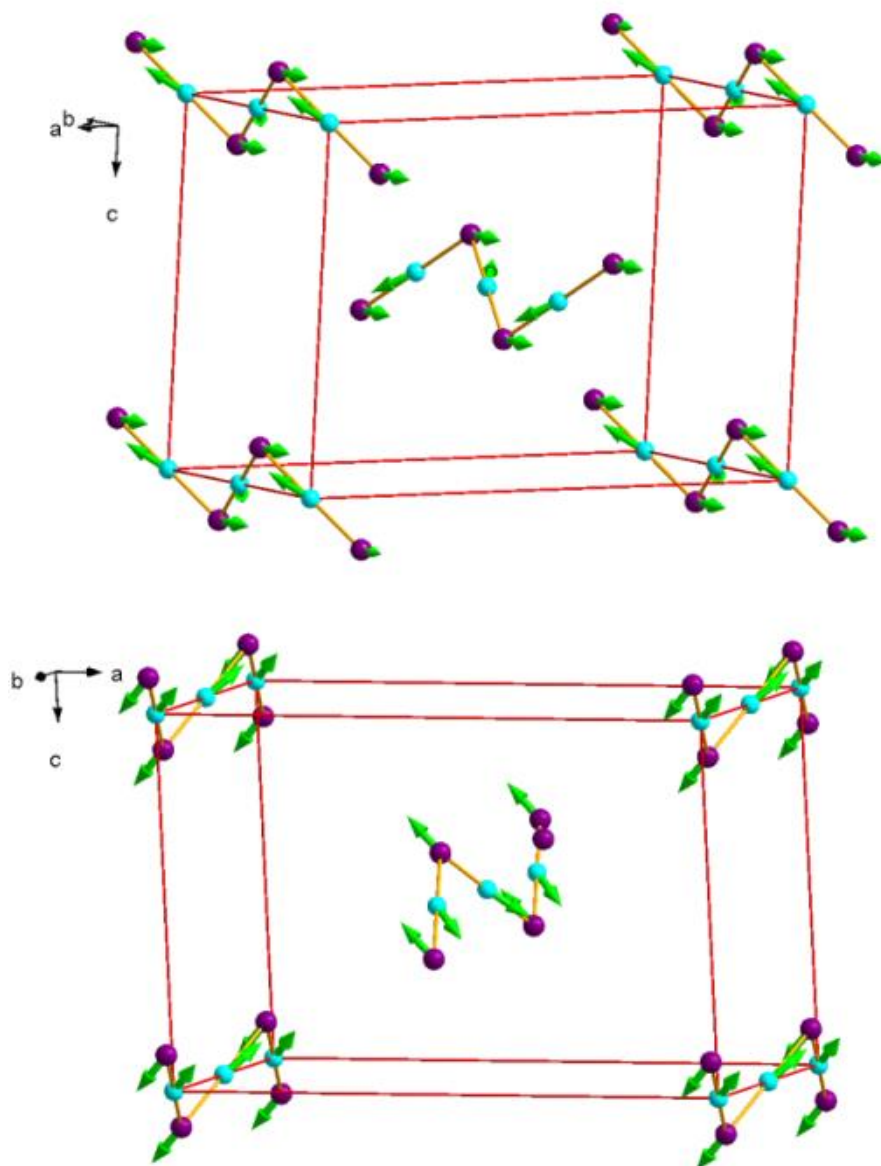


Figure 3.14. Vibrational patterns of  $\text{Ba}_2\text{BrCu}(\text{OH})[\text{V}_2\text{O}_7]$  IR modes from DFT calculations related to Cu-O6 displacements. *Left*:  $B_{2u}$  at  $632\text{ cm}^{-1}$ , *Right*:  $B_{3u}$  at  $586\text{ cm}^{-1}$ . Cu (cyan), O (purple).

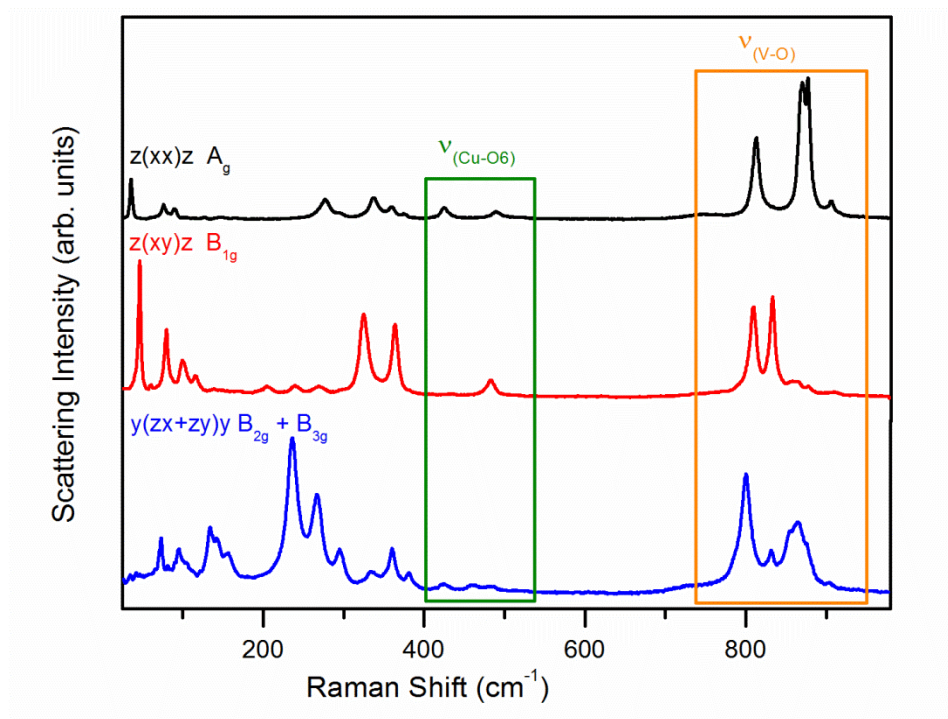


Figure 3.15. Polarized single crystal Raman data for  $\text{Ba}_2\text{BrCu}(\text{OH})[\text{V}_2\text{O}_7]$ .

The Raman data of  $\text{Ba}_2\text{BrCu}(\text{OH})[\text{V}_2\text{O}_7]$  reveals the number of peaks (based on the high intensity  $A_g$  modes) expected from the DFT calculations, see Figure 3.15. In summary, the experimental and theoretical data are in good agreement with an overall blue shift of  $60 \text{ cm}^{-1}$  for the high energy region. This further confirms the accuracy of the structure model derived from the single crystal X-ray diffraction data. All high frequency Raman modes are shown in the supplementary material. It is noteworthy, that we do not find the proposed empirical relation between  $\text{V-O}^{\text{bridging}}$  versus  $\text{V-O}^{\text{terminal}}$  modes linked to the bridging angle of the  $[\text{V}_2\text{O}_7]^{4-}$  unit. [25] Our lattice dynamic calculations indicate a rather surprising result of mixed  $\text{V-O}^{\text{bridging}}$  and  $\text{V-O}^{\text{terminal}}$  modes at high energies. (Figure 3.16)

More Raman displacements as obtained from our theoretical work are presented in the supplementary material. (S5)

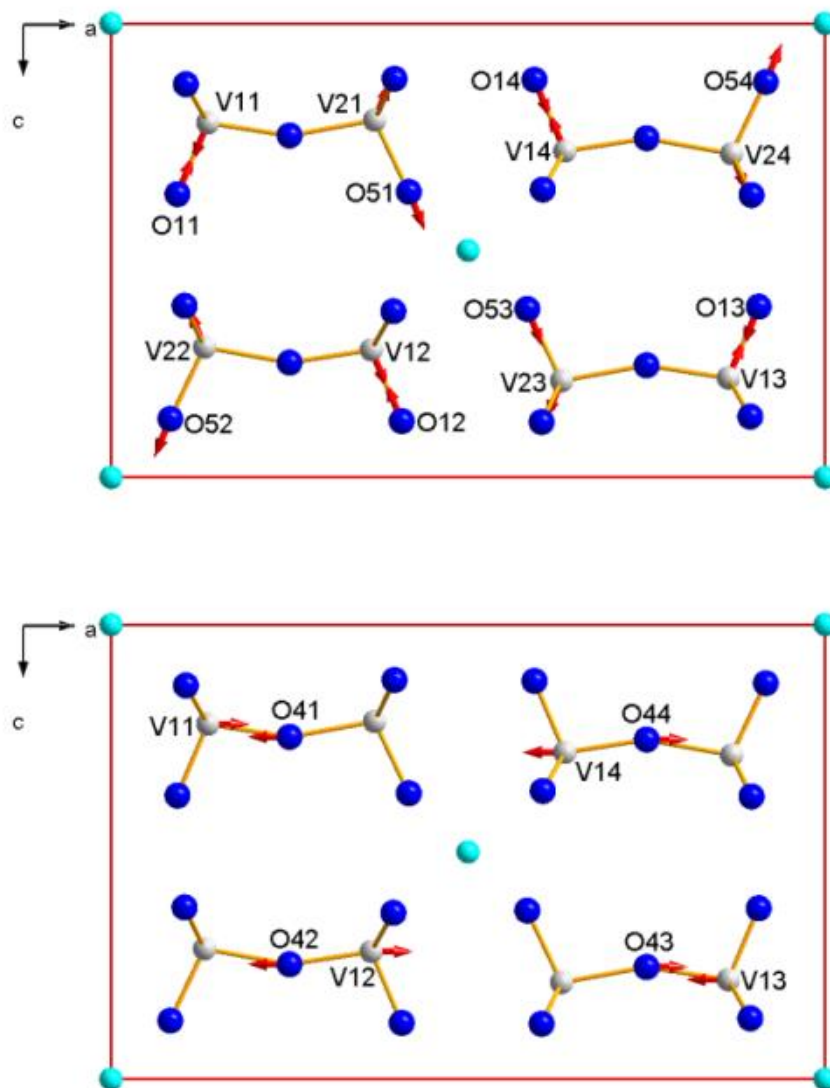


Figure 3.16. Vibrational patterns of two  $\text{Ba}_2\text{BrCu}(\text{OH})[\text{V}_2\text{O}_7]$  Raman modes from DFT calculations. *Left*:  $A_g$  at  $976\text{ cm}^{-1}$ , *Right*:  $B_{2g}$  at  $946\text{ cm}^{-1}$ .

### 3.8 Physical Properties of $\text{Ba}_2\text{XCu}(\text{OH})[\text{V}_2\text{O}_7]$ , $X = \text{Cl, Br}$ .

The magnetic properties originate from the presence of  $\text{Cu}^{2+}$  ( $d^9$ ) located within the  ${}^1_{\infty}[\text{CuO}_{2/2}(\text{OH})_{2/2}\text{O}_{2/1}]^{5-}$  chain present in the structure. The magnetic active orbital for an elongated CuO6-entity is the  $d_{x^2-y^2}$  orbital, which is indicated by the plaquette depiction in Figure 3.12. Based on the Goodenough-Kanamori rules, [26] the Cu-O6-Cu bridging angle, which is  $\sim 100^\circ$ , should yield antiferromagnetic (AFM) exchange interactions. Therefore, we will evaluate our data within the quasi one-dimensional  $S = 1/2$  Heisenberg AFM model. [27]

The magnetization,  $M(H)$ , at 2 K of both compounds is shown in Figure 3.17. We use the Brillouin function [27] to determine the defect of concentration assuming its contribution is paramagnetic ( $S = 1/2$ ,  $g = 2.18$  (Cl) and 2.16 (Br), respectively). A fit of the low temperature magnetization measurement is shown in Figure 3.16 with the magnetization of a Heisenberg 1D-AFM  $S = 1/2$  chain considered to be linear in field dependence at small fields, for  $H \ll J_{\text{AFM}}$ . We find the defect concentration of the paramagnetic impurity to be 8% and 5% for  $X = \text{Cl}$  and Br, respectively. Note that the twinning problem, encountered while solving the crystal structures, might add to the presence of defects.

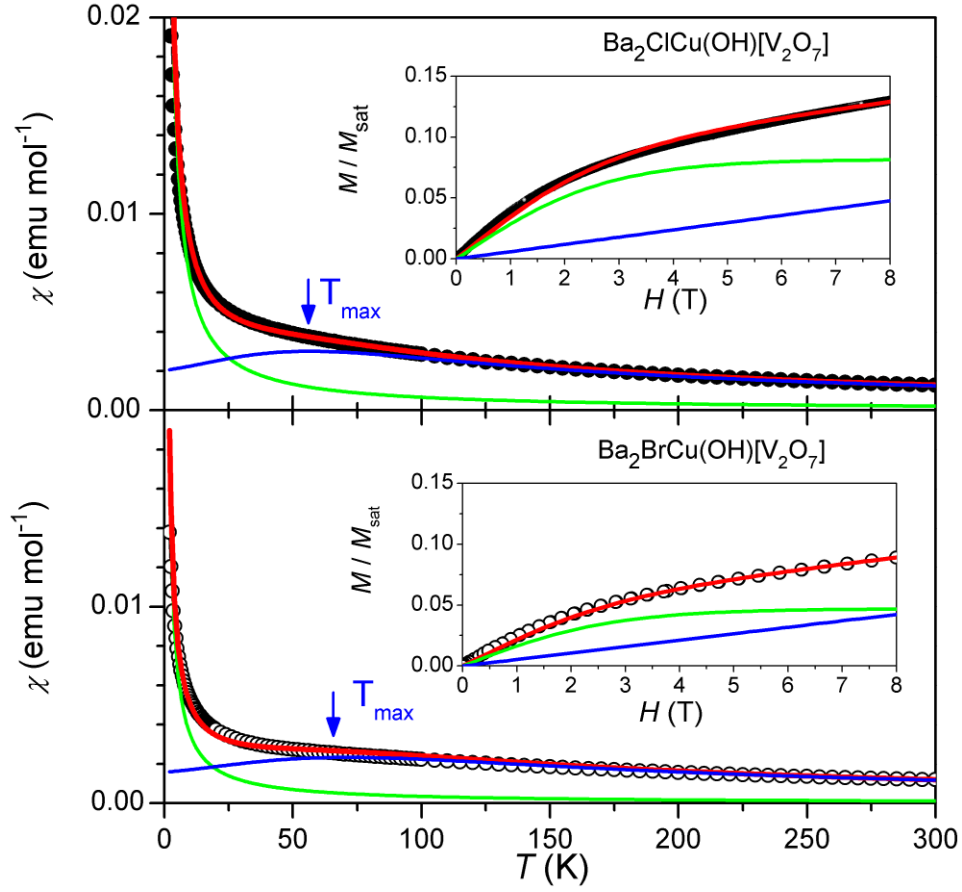


Figure 3.17. *Insets:* The field dependent magnetization data measured at 2 K for  $\text{Ba}_2\text{XCu}(\text{OH})[\text{V}_2\text{O}_7]$ ,  $X = \text{Cl}$  (bullets) or  $\text{Br}$  (circles) with an overall fit (red) to Brillouin function [27] for  $S = 1/2$  for the determination of the defect concentration (green) and to the assumed linear behavior in  $H$  for an AFM chain compound (blue), see text. (*Main panels*) The measured susceptibility in applied fields of 1 T (ZFC) for  $\text{Ba}_2\text{XCu}(\text{OH})[\text{V}_2\text{O}_7]$ ,  $X = \text{Cl}$  or  $\text{Br}$ . The fit (red) of the experimental data is given by the combination of AFM chain (blue) and a defect (green) contribution.

For the susceptibility data (Figure 3.17) of  $\text{Ba}_2\text{XCu}(\text{OH})[\text{V}_2\text{O}_7]$ , we see a significant difference from a Curie or Curie-Weiss type of behavior. For a typical AFM,  $\chi(T)$  is

expected to show a maximum and a continuous decrease while approaching 0 K. Here, we observe a Curie-tail that can be attributed to defects (see magnetization above), which is a common feature for small spin systems and low-dimensional features, here a 1D-AFM. According to the shape of this tail, the defects lead to a partial paramagnetic behavior obeying the Curie law [27]:

$$\chi^{\text{defects}} = C/T \quad (3.1)$$

Consequently, we account for these paramagnetic impurities by using the respective percentages for the Curie-paramagnetic part of the susceptibility. Hence, the temperature dependent susceptibility,  $\chi(T)$ , is composed of two components: defects (8% or 5%) and the remaining 92% or 95% related to the  $S = 1/2$  AFM chain (abbreviated B. F.).

$$\chi^{\text{fit}} = \chi^{\text{B. F.}} + \chi^{\text{defects}} \quad (3.2)$$

We have calculated and plotted two contributions separately and give the sum as a fit to the experimental data (Figure 3.17). For the uniform AFM-Heisenberg chain, the Bonner-Fisher model [28] is used with the  $g$  value as given above and the antiferromagnetic coupling constant,  $J$ , with  $J_{\text{Cl}} = 87$  K for  $X = \text{Cl}$  and  $J_{\text{Br}} = 110$  K for  $X = \text{Br}$ .

$$\chi^{\text{B. F.}} = \frac{0.25 + 0.07497x + 0.075235x^2}{1.0 + 0.9931x + 0.172135x^2 + 0.757825x^3} \quad (3.3)$$

$$x = |J|k_{\text{B}}T$$

Taking a closer look where  $\chi$  reaches  $T_{\text{max}}$  for the AFM chain model, the theoretical relationship of  $T_{\text{max}}/J_{\text{AFM}} = 0.641$  is obeyed.  $J_{\text{AFM}}$  for  $X = \text{Br}$  is larger than that for  $X = \text{Cl}$ .

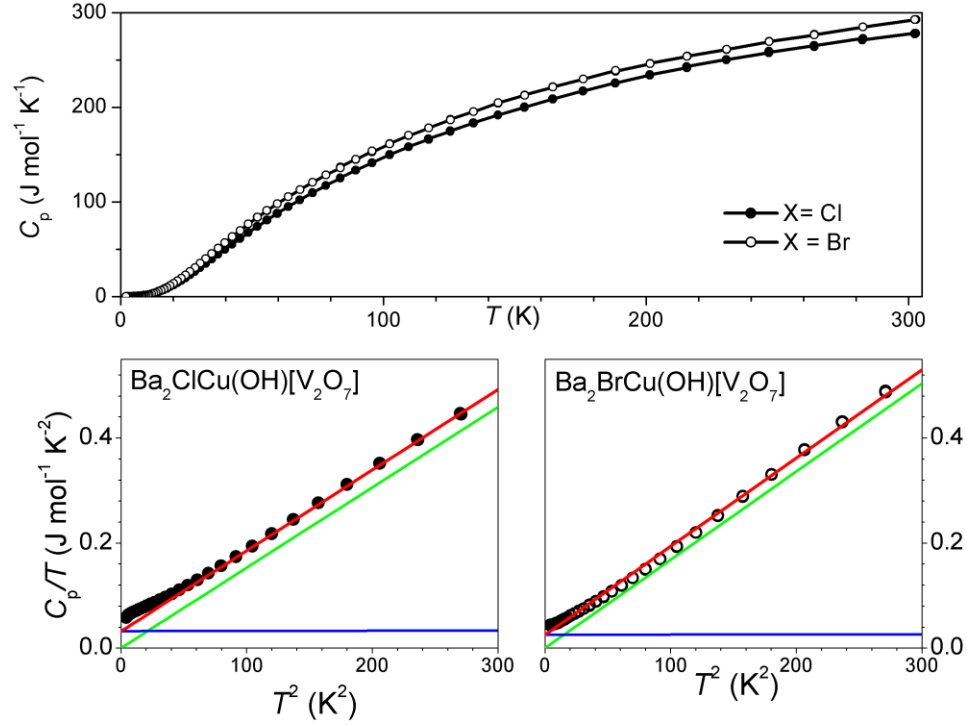


Figure 3.18. *Top panel:* The total specific heat data measured in zero-field is given. *Bottom panels:*  $C_p/T$  versus  $T^2$  for  $\text{Ba}_2\text{XCu(OH)[V}_2\text{O}_7]$ ,  $X = \text{Cl}$  (black bullets) and  $\text{Br}$  (black circles) at low temperatures. The fits (red) to the experimental data are composed of the phonon (green) and magnetic (blue) contributions at low temperatures.

Specific heat measurements were also conducted to provide further information. The total specific heat,  $C_p(T)$  is given in Figure 3.18. No anomaly indicative of magnetic long range order (3D) is observed which provides further support for the realization of a uniform quasi 1D-AFM Heisenberg system. [29] Considering the Debye model, [30] which predicts, at very low temperatures, a dependency of the phonon contribution to the total specific heat,  $C_p(T)$ , to be proportional to  $T^3$ , we plot  $C_p(T)/T$  versus  $T^2$  (Figure 3.18). Then the phonon contributions become linear in  $T^2$  and pass through the origin at very



low temperatures. The green curve represents the simulated  $C_{\text{phonon}}/T$  vs.  $T^2$  with the slope obtained from the linear fit of the appropriate range in the experimental data. The magnetic part of the specific heat ( $C_m(T) = AT$  at low temperatures) can then be attributed to the offset (constant value, A, related to  $J_{\text{AFM}}$ ) within the high temperature series expansions for the specific heat of a spin  $S$  antiferromagnetic uniform Heisenberg chain, as reported by Johnston *et al.* in 2000: [31]

$$\frac{C(T)}{Nk_B} = \frac{x^2}{3t^2} \left[ 1 + \sum_{n=1}^{\infty} \frac{c_n(x)}{t^n} \right] \quad (3.4)$$

$$x = S(S+1), t = k_B T/J$$

where  $N$  is the number of spins,  $c_n(x)$  is a numerical function of  $S$ . The best fit is achieved for  $J_{\text{AFM}} = 87$  K for  $X = \text{Cl}$  and  $J_{\text{AFM}} = 110$  K for  $X = \text{Br}$  which is consistent with our results from the magnetization measurements. This confirms the  $S = 1/2$  Heisenberg quasi 1D-AFM properties of these compounds.

### 3.9 Conclusions.

Two new compounds with an unprecedented type of structure have been successfully synthesized by application of hydrothermal methods. Crystals have been grown with different morphologies in the pH range between 8 and 10. We found evidence of stacking faults for both compounds as well as twinning for both needle-shaped  $\text{Ba}_2\text{ClCu}(\text{OH})[\text{V}_2\text{O}_7]$  crystals and elongated hexagonal plate-shaped  $\text{Ba}_2\text{BrCu}(\text{OH})[\text{V}_2\text{O}_7]$  crystals. Lattice dynamics were studied to confirm the structure model solved from the single X-ray data. The magnetic  $\text{Cu}^{2+}$  ions are linked to chains which can be described by the theory of a quasi 1D  $S = 1/2$  Heisenberg AFM references, Confirmation is obtained

from both magnetic and specific heat measurements. Furthermore, increasing the size of the halide ion (here:  $\text{Cl}^-$  to  $\text{Br}^-$ ) leads to the expansion of cell parameters. This structural difference impacts the magnetic behavior of  $\text{Ba}_2\text{ClCu}(\text{OH})[\text{V}_2\text{O}_7]$  and  $\text{Ba}_2\text{BrCu}(\text{OH})[\text{V}_2\text{O}_7]$  and finds its manifestation in the increasing value of the coupling parameter  $J_{\text{AFM}}$ .

### 3.10 References.

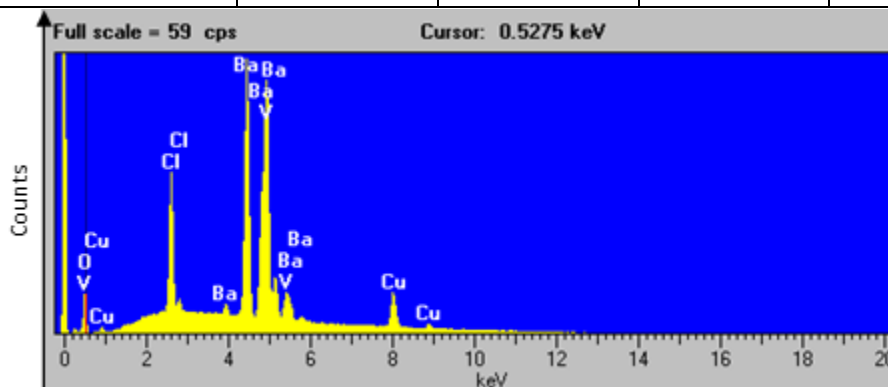
- [1] Martin, F. D.; Müller-Buschbaum, Hk. *Z. Naturforsch. B*, **1994**, *49*, 355.
- [2] Martin, F. D.; Müller-Buschbaum, Hk. *Z. Naturforsch. B*, **1994**, *49*, 1141.
- [3] Ranmohotti, K. G. S.; Queen, W. L.; J. P. VanDerveer, West, D.; Hwu, S.-J. *J. Chem. Crystallogr.*, **2009**, *39*, 303.
- [4] Müller, A.; Reuter, H.; Dillinger, S. *Angew. Chem. Int. Ed. Engl.*, **1995**, *34*, 2328.
- [5] Huang, Q.; Hwu, S.-J. *Inorg. Chem.*, **2003**, *42*, 655.
- [6] Hwu, S.-J.; Ulutagay-Kartin, M.; Clayhold, J. A.; Mackay, R.; Wardojo, T. A.; O'Connor, C. J.; Krawiec, M. *J. Am. Chem. Soc.*, **2002**, *124*, 12404.
- [7] Banks, E.; Greenblatt, M.; Post, H.; *Inorg. Chem.*, **1970**, *9*, 2259.
- [8] Mo, X.; Hwu, S.-J. *Inorg. Chem.*, **2003**, *42*, 3978.
- [9] Mo, X.; Ferguson, E.; Hwu, S.-J. *Inorg. Chem.*, **2005**, *44*, 3121.
- [10] Aia, M. A.; Lubin, P. *J. Electrochem. Soc.*, **1966**, *113*, 1331.
- [11] Albrecht, C.; Cohen, S.; Mayer, I.; Reinen, D. *J. Solid State Chem.*, **1993**, *107*, 218.
- [12] Queen, W. L.; West, J. P.; Hudson, J.; Hwu, S.-J.; VanDerveer, D. G.; Zarzyczny, M. C.; Pavlick, R. A. *Angew. Chem. Int. Ed.*, **2008**, *47*, 3791.
- [13] Mahjoor, P.; Lattur, S. E. *Inorg. Chem.*, **2010**, *49*, 4486.
- [14] Queen, W. L.; West, J. P.; Hudson, J.; Hwu, S.-J. *Inorg. Chem.*, **2011**, *50*, 11064.
- [15] Lan, X.; Zhang, J.; Gao, H.; Wang, T. *CrystEngComm*, **2011**, *13*, 633.
- [16] Zakhharova, G. S.; Täschner, Ch.; Kolb, T.; Jähne, C.; Leonhardt, A.; Büchner, B.; Klingeler, R. *Dalton Trans.*, **2013**, *42*, 4897.

- [17] Chandra, N.; Ravi Acharya, K.; Moody, P. C. E. *Acta Cryst. D*, **1999**, 55, 1750.
- [18] Yamada, Y.; Kitsuda, K.; Nohdo, S.; Ikeda, N. *Phys. Rev. B*, **2000**, 62, 12167.
- [19] Dauter, Z. *Acta Cryst. D*, **2003**, 59, 2004.
- [20] Lutz, H.D. *Structure and Bonding*, **1995**, 82, 81.
- [21] Beckenkamp, K.; Lutz, H. D. *J. Molec. Struct.*, **1992**, 270, 393.
- [22] Busing, W. R. *J. Chem. Phys.*, **1955**, 23, 933.
- [23] Gheorghe, D. E.; Litvinchuk, A. P.; Möller, A. Z. *Anorg. Allg. Chem.*, **2012**, 638, 2087.
- [24] Griffith, W. P.; Wickins, T. D. *J. Chem. Soc. A*, **1966**, 1087.
- [25] Baran, E. J. *J. Mol. Struct.*, **1978**, 48, 441.
- [26] Goodenough, J. B. *Magnetism and the Chemical Bond*, Interscience, New York, **1963**.
- [27] Kahn, O. *Molecular Magnetism*, Wiley-VCH, **1993**.
- [28] Bonner, J.C.; Fisher, M. E. *Phys. Rev. A*, **1964**, 135, 640.
- [29] Mermin, N. D.; Wagner, H. *Phys. Rev. Lett.*, **1966**, 17, 1133.
- [30] Debye, P.; *Annalen der Physik (Leipzig)*, **1912**, 39, 789.
- [31] Johnston, D.C.; Kremer, R. K.; Troyer, M.; Wang, X.; Klümper, A.; Bud'ko, S. L.; Panchula, A. F.; Canfield, P. C. *Phys. Rev. B*, **2000**, 61, 9558.

### 3.11 Supplemental Material.

S-1: Table 3.8. Atomic composition for Ba<sub>2</sub>ClCu(OH)[V<sub>2</sub>O<sub>7</sub>].

Elements	V	Cu	Cl	Ba
Position 1, Atomic %	29.18	14.96	21.09	34.75
Position 2, Atomic %	29.48	16.81	19.49	34.21
Position 3, Atomic %	29.59	16.69	20.28	33.42
Position 4, Atomic %	30.54	22.55	14.63	32.27
Position 5, Atomic %	30.24	20.35	16.52	32.89
Position 6, Atomic %	29.84	15.88	19.71	34.57
Position 7, Atomic %	28.84	15.38	20.87	34.89
Position 8, Atomic %	30.06	14.35	19.96	35.62
Position 9, Atomic %	30.31	15.41	18.05	36.23
Position 10, Atomic %	29.59	16.63	19.20	34.56
Position 11, Atomic %	29.69	15.63	20.71	33.96
Elements	V	Cu	Cl	Ba
Average, atomic %	33(1)	18(2)	21(2)	38(1)
Stoichiometry	2.0	1.1	1.3	2.3

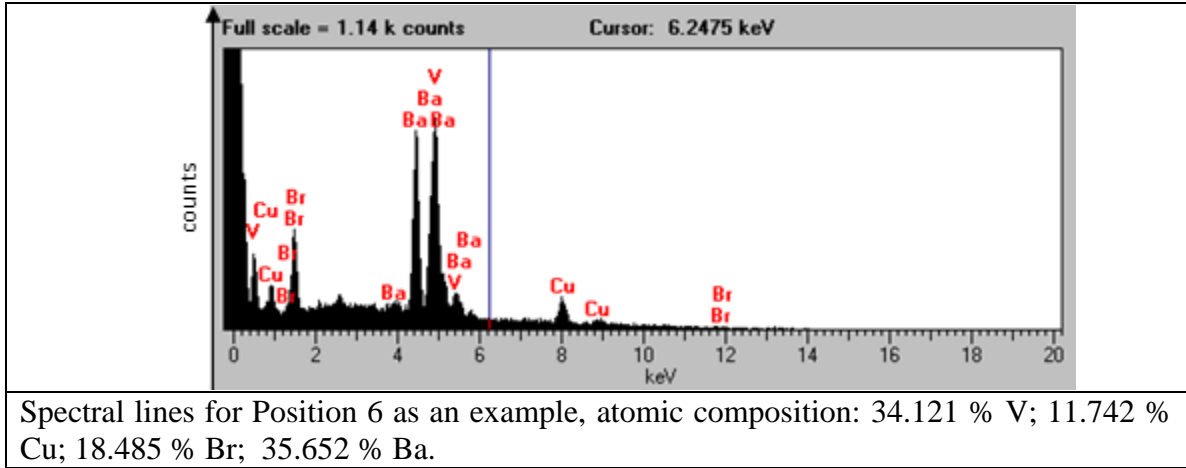


Spectral lines for Position 1 as an example, atomic composition: 29.18 % V; 14.96 % Cu; 21.09 % Cl; 34.75 % Ba.

S-1: Table 3.9. Atomic composition for Ba<sub>2</sub>BrCu(OH)[V<sub>2</sub>O<sub>7</sub>].

Elements	<b>V</b>	<b>Cu</b>	<b>Br</b>	<b>Ba</b>
Position 1, Atomic %	30.863	14.035	19.388	35.714
Position 2, Atomic %	31.961	11.487	19.428	37.124
Position 3, Atomic %	32.415	10.848	22.934	33.803
Position 4, Atomic %	29.048	18.095	19.817	33.039
Position 5, Atomic %	32.932	10.935	22.064	34.069
Position 6, Atomic %	34.121	11.742	18.485	35.652
Position 7, Atomic %	31.368	13.391	19.990	35.251
Position 8, Atomic %	31.668	13.980	18.498	35.855
Position 9, Atomic %	32.143	12.532	21.619	33.706
Position 10, Atomic %	41.293	14.389	6.041	38.277
Position 11, Atomic %	31.941	11.827	21.414	34.818
Position 12, Atomic %	32.678	13.619	18.000	35.704
Position 13, Atomic %	29.378	10.708	21.376	38.538
Position 14, Atomic %	31.807	14.993	21.570	31.631
Elements	<b>V</b>	<b>Cu</b>	<b>Br</b>	<b>Ba</b>
Average, atomic %	32(3)	13(2)	19(4)	35(2)
Stoichiometry	2.0	0.8	1.2	2.2

Table 3.9. Continued.



Standard deviations were calculated based on the equation  $\sigma = \sqrt{\frac{\sum(x-\bar{x})^2}{n}}$ , where  $\sigma$  = standard deviation,  $\Sigma$  = sum of,  $x$  = each value in the data set,  $\bar{x}$  = mean value of the data set.  $n$  = number of values in the data set.

S-2: Table 3.10. Fractional atomic coordinates and isotropic or equivalent isotropic displacement parameters ( $\text{\AA}^2$ ) for  $\text{Ba}_2\text{ClCu}(\text{OH})[\text{V}_2\text{O}_7]$ .

Atom	Wyckoff site	<i>x</i>	<i>y</i>	<i>z</i>	$U_{\text{iso}}^*/U_{\text{eq}}$
Ba1	<i>4c</i>	0.0380(1)	0.7500	0.3657(2)	0.0126(4)
Ba2	<i>4c</i>	0.2509(1)	0.7500	0.0477(2)	0.0110(4)
Cl	<i>4c</i>	0.2516(5)	0.2500	0.8873(8)	0.014(1)
V1	<i>4c</i>	0.1361(3)	0.2500	0.2207(5)	0.0064(9)
V2	<i>4c</i>	0.3698(3)	0.2500	0.2157(5)	0.0049(9)
Cu	<i>4a</i>	0.0000	0.0000	0.0000	0.0102(7)
O1	<i>4c</i>	0.091(2)	0.2500	0.376 (3)	0.013(3)
O2	<i>8d</i>	0.108(1)	0.015(3)	0.137(2)	0.011(2)
O3	<i>8d</i>	0.397(1)	0.475(3)	0.122(2)	0.011(2)
O4	<i>4c</i>	0.251(2)	0.2500	0.250(3)	0.014(4)
O5	<i>4c</i>	0.081(2)	0.7500	−0.125(3)	0.013(3)
O6	<i>4c</i>	0.038(2)	0.2500	−0.120(3)	0.014*



S-2: Table 3.11. Fractional atomic coordinates and isotropic or equivalent isotropic displacement parameters ( $\text{\AA}^2$ ) for  $\text{Ba}_2\text{BrCu}(\text{OH})[\text{V}_2\text{O}_7]$ .

Atom	Wyckoff site	<i>x</i>	<i>y</i>	<i>z</i>	$U_{\text{iso}}^*/U_{\text{eq}}$
Ba1	<i>4c</i>	0.03478(7)	0.7500	0.3645(1)	0.0130(2)
Ba2	<i>4c</i>	0.24968(7)	0.7500	0.0426(1)	0.0119(2)
Br	<i>4c</i>	0.2505(1)	0.2500	0.8849(2)	0.0146(3)
V1	<i>4c</i>	0.1353(2)	0.2500	0.2189(3)	0.0064(4)
V2	<i>4c</i>	0.3691(2)	0.2500	0.2130(3)	0.0064(4)
Cu	<i>4a</i>	0.0000	0.0000	0.0000	0.0107(4)
O1	<i>4c</i>	0.0917(8)	0.2500	0.377(1)	0.011(2)
O2	<i>8d</i>	0.1050(6)	0.017(1)	0.134(1)	0.011(1)
O3	<i>8d</i>	0.3972(6)	0.474(2)	0.123(1)	0.016(2)
O4	<i>4c</i>	0.2512(9)	0.2500	0.246(2)	0.016(2)
O5	<i>4c</i>	0.0837(9)	0.7500	−0.130(2)	0.017(3)
O6	<i>4c</i>	0.036(1)	0.2500	−0.119(2)	0.017*

S-3: Table 3.12. Selected interatomic distances (Å) for Ba<sub>2</sub>ClCu(OH)[V<sub>2</sub>O<sub>7</sub>].

Ba1—O6 <sup>i</sup>	2.62(2)	V1—O2 <sup>iv</sup>	1.695(2)
Ba1—O3 <sup>ii</sup>	2.71(2)	V1—O2	1.695(2)
Ba1—O3 <sup>iii</sup>	2.71(2)	V1—O4	1.76(3)
Ba1—O2 <sup>iv</sup>	2.92(2)	V2—O3 <sup>iv</sup>	1.691(2)
Ba1—O2 <sup>v</sup>	2.92(2)	V2—O3	1.691(2)
Ba1—O3 <sup>vi</sup>	2.98(2)	V2—O5 <sup>vii</sup>	1.70(3)
Ba1—O3 <sup>vii</sup>	2.98(2)	V2—O4	1.83(2)
Ba1—O1 <sup>v</sup>	3.145(6)	Cu—O6	1.99(2)
Ba1—O1	3.145(6)	Cu—O6 <sup>xvi</sup>	1.99(2)
Ba1—O1 <sup>viii</sup>	3.16(2)	Cu—O2 <sup>xvi</sup>	2.09(2)
Ba1—Cl <sup>ix</sup>	3.186(8)	Cu—O2	2.09(2)
Ba2—O2 <sup>iv</sup>	2.835(2)	Cu—O5 <sup>i</sup>	2.29(2)
Ba2—O2 <sup>v</sup>	2.835(2)	Cu—O5 <sup>xv</sup>	2.29(2)
Ba2—O4 <sup>ix</sup>	2.87(2)	O1—Ba2 <sup>vii</sup>	2.90(2)
Ba2—O3 <sup>x</sup>	2.859(2)	O1—Ba1 <sup>xv</sup>	3.145(6)
Ba2—O3	2.859(2)	O1—Ba1 <sup>viii</sup>	3.16 (2)
Ba2—O1 <sup>ix</sup>	2.90(2)	O5—V2 <sup>ix</sup>	1.70(3)
Ba2—O5	3.05(2)	O5—Cu <sup>xviii</sup>	2.29(2)
Ba2—Cl <sup>ix</sup>	3.266(8)	O5—Cu <sup>v</sup>	2.29(2)
Ba2—Cl <sup>xi</sup>	3.409(4)	O2—Ba2 <sup>xv</sup>	2.84(2)
Ba2—Cl <sup>xii</sup>	3.409(4)	O2—Ba1 <sup>xv</sup>	2.92(2)
Cl—Ba1 <sup>vii</sup>	3.186(8)	O3—Ba1 <sup>xix</sup>	2.71(2)
Cl—Ba2 <sup>vii</sup>	3.265(8)	O3—Ba1 <sup>ix</sup>	2.98(2)

Table 3.12. Continued.

Cl—Ba2 <sup>xiii</sup>	3.409(4)	O4—Ba2 <sup>vii</sup>	2.87(2)
Cl—Ba2 <sup>xiv</sup>	3.409(4)	O6—Cu <sup>xviii</sup>	1.99(2)
V1—O1	1.64(3)	O6—Ba1 <sup>i</sup>	2.62(2)

S-3: Table 3.13. Selected interatomic distances (Å) for Ba<sub>2</sub>BrCu(OH)[V<sub>2</sub>O<sub>7</sub>].

Ba1—O6 <sup>i</sup>	2.60(2)	V1—O2	1.710(9)
Ba1—O3 <sup>ii</sup>	2.688(9)	V1—O2 <sup>iv</sup>	1.710(9)
Ba1—O3 <sup>iii</sup>	2.688(9)	V1—O4	1.78(1)
Ba1—O2 <sup>iv</sup>	2.961(9)	V2—O3	1.68(1)
Ba1—O2 <sup>v</sup>	2.961(9)	V2—O3 <sup>iv</sup>	1.679(9)
Ba1—O3 <sup>vi</sup>	3.03(1)	V2—O5 <sup>vii</sup>	1.68(2)
Ba1—O3 <sup>vii</sup>	3.03(1)	V2—O4	1.82(1)
Ba1—O1 <sup>viii</sup>	3.15(1)	Cu—O6 <sup>xvi</sup>	1.989(9)
Ba1—O1 <sup>v</sup>	3.178(3)	Cu—O6	1.989(9)
Ba1—O1	3.178(3)	Cu—O2 <sup>xvi</sup>	2.056(9)
Ba1—Br <sup>ix</sup>	3.268(2)	Cu—O2	2.056(9)
Ba2—O4 <sup>ix</sup>	2.87(2)	Cu—O5 <sup>i</sup>	2.35(1)
Ba2—O2 <sup>iv</sup>	2.874(9)	Cu—O5 <sup>xv</sup>	2.35(1)
Ba2—O2 <sup>v</sup>	2.874(9)	O1—Ba2 <sup>vii</sup>	2.89(1)
Ba2—O1 <sup>ix</sup>	2.89(1)	O1—Ba1 <sup>viii</sup>	3.15(1)
Ba2—O3 <sup>x</sup>	2.91(1)	O1—Ba1 <sup>xv</sup>	3.178(3)
Ba2—O3	2.91(1)	O2—Ba2 <sup>xv</sup>	2.874(9)

Table 3.13. Continued.

Ba2—O5	3.02(1)	O2—Ba1 <sup>xv</sup>	2.961(9)
Ba2—Br <sup>ix</sup>	3.308(2)	O3—Ba1 <sup>xix</sup>	2.688(9)
Ba2—Br <sup>xi</sup>	3.415(1)	O3—Ba1 <sup>ix</sup>	3.03(1)
Ba2—Br <sup>xii</sup>	3.415(1)	O4—Ba2 <sup>vii</sup>	2.87(2)
Br—Ba1 <sup>vii</sup>	3.268(2)	O5—V2 <sup>ix</sup>	1.68(2)
Br—Ba2 <sup>vii</sup>	3.308(2)	O5—Cu <sup>xviii</sup>	2.35(1)
Br—Ba2 <sup>xiii</sup>	3.415(1)	O5—Cu <sup>v</sup>	2.35(1)
Br—Ba2 <sup>xiv</sup>	3.415(1)	O6—Cu <sup>xviii</sup>	1.989(9)
V1—O1	1.67(1)	O6—Ba1 <sup>i</sup>	2.60(2)

Symmetry codes: (i)  $-x, -y+1, -z$ ; (ii)  $x-1/2, y, -z+1/2$ ; (iii)  $x-1/2, -y+3/2, -z+1/2$ ; (iv)  $x, -y+1/2, z$ ; (v)  $x, y+1, z$ ; (vi)  $-x+1/2, y+1/2, z+1/2$ ; (vii)  $-x+1/2, -y+1, z+1/2$ ; (viii)  $-x, -y+1, -z+1$ ; (ix)  $-x+1/2, -y+1, z-1/2$ ; (x)  $x, -y+3/2, z$ ; (xi)  $x, y, z-1$ ; (xii)  $x, y+1, z-1$ ; (xiii)  $x, y, z+1$ ; (xiv)  $x, y-1, z+1$ ; (xv)  $x, y-1, z$ ; (xvi)  $-x, -y, -z$ ; (xvii)  $-x, y-1/2, -z$ ; (xviii)  $-x, y+1/2, -z$ ; (xix)  $x+1/2, y, -z+1/2$ .

S-4: Table 3.14. Selected angles (°) for Ba<sub>2</sub>ClCu(OH)[V<sub>2</sub>O<sub>7</sub>].

O6 <sup>i</sup> —Ba1—O3 <sup>ii</sup>	72.4(5)	O4 <sup>ix</sup> —Ba2—O1 <sup>ix</sup>	55.9(7)
O6 <sup>i</sup> —Ba1—O3 <sup>iii</sup>	72.4(5)	O3—Ba2—O1 <sup>ix</sup>	60.4(5)
O3 <sup>ii</sup> —Ba1—O3 <sup>iii</sup>	76.2(7)	O2 <sup>iv</sup> —Ba2—O5	61.5(5)
O6 <sup>i</sup> —Ba1—O2 <sup>iv</sup>	58.6(5)	O2 <sup>v</sup> —Ba2—O5	61.5(5)
O3 <sup>ii</sup> —Ba1—O2 <sup>iv</sup>	88.6(4)	O4 <sup>ix</sup> —Ba2—O5	56.6(7)
O3 <sup>iii</sup> —Ba1—O2 <sup>iv</sup>	131.0(5)	O3 <sup>x</sup> —Ba2—O5	141.6(4)
O6 <sup>i</sup> —Ba1—O2 <sup>v</sup>	58.6(5)	O3—Ba2—O5	141.6(4)
O3 <sup>ii</sup> —Ba1—O2 <sup>v</sup>	131.0(5)	O1 <sup>ix</sup> —Ba2—O5	112.4(6)
O3 <sup>iii</sup> —Ba1—O2 <sup>v</sup>	88.6(4)	Cl <sup>ix</sup> —Ba2—Cl <sup>xi</sup>	116.9(1)
O2 <sup>iv</sup> —Ba1—O2 <sup>v</sup>	67.0(7)	Cl <sup>ix</sup> —Ba2—Cl <sup>xii</sup>	116.9(1)
O6 <sup>i</sup> —Ba1—O3 <sup>vi</sup>	152.4(3)	Cl <sup>xi</sup> —Ba2—Cl <sup>xii</sup>	126.2(2)
O3 <sup>ii</sup> —Ba1—O3 <sup>vi</sup>	120.3(3)	Ba1 <sup>vii</sup> —Cl—Ba2 <sup>vii</sup>	86.9(2)
O3 <sup>iii</sup> —Ba1—O3 <sup>vi</sup>	86.5(5)	Ba1 <sup>vii</sup> —Cl—Ba2 <sup>xiii</sup>	91.9(2)
O2 <sup>iv</sup> —Ba1—O3 <sup>vi</sup>	139.1(4)	Ba2 <sup>vii</sup> —Cl—Ba2 <sup>xiii</sup>	116.9(1)
O2 <sup>v</sup> —Ba1—O3 <sup>vi</sup>	104.4(5)	Ba1 <sup>vii</sup> —Cl—Ba2 <sup>xiv</sup>	91.9(2)
O6 <sup>i</sup> —Ba1—O3 <sup>vii</sup>	152.4(3)	Ba2 <sup>vii</sup> —Cl—Ba2 <sup>xiv</sup>	116.9(1)
O3 <sup>ii</sup> —Ba1—O3 <sup>vii</sup>	86.5(5)	Ba2 <sup>xiii</sup> —Cl—Ba2 <sup>xiv</sup>	126.2(2)
O3 <sup>iii</sup> —Ba1—O3 <sup>vii</sup>	120.3(3)	O1—V1—O2 <sup>iv</sup>	108.9(7)
O2 <sup>iv</sup> —Ba1—O3 <sup>vii</sup>	104.4(5)	O1—V1—O2	108.9(7)
O2 <sup>v</sup> —Ba1—O3 <sup>vii</sup>	139.1(4)	O2 <sup>iv</sup> —V1—O2	115(1)
O3 <sup>vi</sup> —Ba1—O3 <sup>vii</sup>	54.6(6)	O1—V1—O4	105(1)
O6 <sup>i</sup> —Ba1—O1 <sup>v</sup>	98.0(5)	O2 <sup>iv</sup> —V1—O4	109.1(7)
O3 <sup>ii</sup> —Ba1—O1 <sup>v</sup>	142.6(5)	O2—V1—O4	109.1(7)

Table 3.14. Continued.

O3 <sup>iii</sup> —Ba1—O1 <sup>v</sup>	66.6(5)	O3 <sup>iv</sup> —V2—O3	108(1)
O2 <sup>iv</sup> —Ba1—O1 <sup>v</sup>	117.7(6)	O3 <sup>iv</sup> —V2—O5 <sup>vii</sup>	112.1(7)
O2 <sup>v</sup> —Ba1—O1 <sup>v</sup>	53.0(6)	O3—V2—O5 <sup>vii</sup>	112.1(7)
O3 <sup>vi</sup> —Ba1—O1 <sup>v</sup>	56.4(6)	O3 <sup>iv</sup> —V2—O4	109.6(7)
O3 <sup>vii</sup> —Ba1—O1 <sup>v</sup>	109.5(6)	O3—V2—O4	109.6(7)
O6 <sup>i</sup> —Ba1—O1	98.0(5)	O5 <sup>vii</sup> —V2—O4	105(1)
O3 <sup>ii</sup> —Ba1—O1	66.6(5)	O6—Cu—O6 <sup>xvi</sup>	180
O3 <sup>iii</sup> —Ba1—O1	142.6(5)	O6—Cu—O2 <sup>xvi</sup>	83.6(8)
O2 <sup>iv</sup> —Ba1—O1	53.0(6)	O6 <sup>xvi</sup> —Cu—O2 <sup>xvi</sup>	96.4(8)
O2 <sup>v</sup> —Ba1—O1	117.7(6)	O6—Cu—O2	96.4(8)
O3 <sup>vi</sup> —Ba1—O1	109.5(6)	O6 <sup>xvi</sup> —Cu—O2	83.6(8)
O3 <sup>vii</sup> —Ba1—O1	56.4(6)	O2 <sup>xvi</sup> —Cu—O2	180
O1 <sup>v</sup> —Ba1—O1	150.3(8)	O6—Cu—O5 <sup>i</sup>	87.2(7)
O6 <sup>i</sup> —Ba1—O1 <sup>viii</sup>	116.1(7)	O6 <sup>xvi</sup> —Cu—O5 <sup>i</sup>	92.8(7)
O3 <sup>ii</sup> —Ba1—O1 <sup>viii</sup>	58.6(5)	O2 <sup>xvi</sup> —Cu—O5 <sup>i</sup>	86.7(8)
O3 <sup>iii</sup> —Ba1—O1 <sup>viii</sup>	58.6(5)	O2—Cu—O5 <sup>i</sup>	93.3(8)
O2 <sup>iv</sup> —Ba1—O1 <sup>viii</sup>	144.5(3)	O6—Cu—O5 <sup>xv</sup>	92.8(7)
O2 <sup>v</sup> —Ba1—O1 <sup>viii</sup>	144.5(3)	O6 <sup>xvi</sup> —Cu—O5 <sup>xv</sup>	87.2(7)
O3 <sup>vi</sup> —Ba1—O1 <sup>viii</sup>	63.5(5)	O2 <sup>xvi</sup> —Cu—O5 <sup>xv</sup>	93.3(8)
O3 <sup>vii</sup> —Ba1—O1 <sup>viii</sup>	63.5(5)	O2—Cu—O5 <sup>xv</sup>	86.7(8)
O1 <sup>v</sup> —Ba1—O1 <sup>viii</sup>	97.6(4)	O5 <sup>i</sup> —Cu—O5 <sup>xv</sup>	180(1)
O1—Ba1—O1 <sup>viii</sup>	97.6(4)	Ba2 <sup>vii</sup> —O1—Ba1 <sup>xv</sup>	103.1(5)
O2 <sup>iv</sup> —Ba2—O2 <sup>v</sup>	69.3(6)	Ba1—O1—Ba1 <sup>xv</sup>	150.3(8)

Table 3.14. Continued.

O2 <sup>iv</sup> —Ba2—O4 <sup>ix</sup>	107.3(5)	Ba2 <sup>vii</sup> —O1—Ba1 <sup>viii</sup>	93.4(7)
O2 <sup>v</sup> —Ba2—O4 <sup>ix</sup>	107.3(5)	Ba1—O1—Ba1 <sup>viii</sup>	82.4(4)
O2 <sup>iv</sup> —Ba2—O3 <sup>x</sup>	147.9(4)	Ba1 <sup>xv</sup> —O1—Ba1 <sup>viii</sup>	82.4(4)
O2 <sup>v</sup> —Ba2—O3 <sup>x</sup>	100.5(4)	Cu <sup>xviii</sup> —O5—Cu <sup>v</sup>	83.1(8)
O4 <sup>ix</sup> —Ba2—O3 <sup>x</sup>	104.8(5)	Ba2 <sup>xv</sup> —O2—Ba1 <sup>xv</sup>	100.9(5)
O2 <sup>iv</sup> —Ba2—O3	100.5(4)	Ba1 <sup>xix</sup> —O3—Ba2	104.9(5)
O2 <sup>v</sup> —Ba2—O3	147.9(4)	Ba1 <sup>xix</sup> —O3—Ba1 <sup>ix</sup>	93.5(5)
O4 <sup>ix</sup> —Ba2—O3	104.8(5)	Ba2—O3—Ba1 <sup>ix</sup>	108.5(5)
O3 <sup>x</sup> —Ba2—O3	71.6(6)	V1—O4—V2	161(2)
O2 <sup>iv</sup> —Ba2—O1 <sup>ix</sup>	143.3(4)	Cu <sup>xviii</sup> —O6—Cu	99(1)
O2 <sup>v</sup> —Ba2—O1 <sup>ix</sup>	143.3(4)		

S-4: Table 3.15. Selected angles (°) for Ba<sub>2</sub>BrCu(OH)[V<sub>2</sub>O<sub>7</sub>].

O6 <sup>i</sup> —Ba1—O3 <sup>ii</sup>	73.8(3)	O2 <sup>iv</sup> —Ba2—O1 <sup>ix</sup>	143.8(2)
O6 <sup>i</sup> —Ba1—O3 <sup>iii</sup>	73.8(3)	O2 <sup>v</sup> —Ba2—O1 <sup>ix</sup>	143.8(2)
O3 <sup>ii</sup> —Ba1—O3 <sup>iii</sup>	77.7(4)	O4 <sup>ix</sup> —Ba2—O3 <sup>x</sup>	105.6(3)
O6 <sup>i</sup> —Ba1—O2 <sup>iv</sup>	57.5(3)	O2 <sup>iv</sup> —Ba2—O3 <sup>x</sup>	146.7(3)
O3 <sup>ii</sup> —Ba1—O2 <sup>iv</sup>	88.3(3)	O2 <sup>v</sup> —Ba2—O3 <sup>x</sup>	100.3(2)
O3 <sup>iii</sup> —Ba1—O2 <sup>iv</sup>	131.3(3)	O1 <sup>ix</sup> —Ba2—O3 <sup>x</sup>	60.3(3)
O6 <sup>i</sup> —Ba1—O2 <sup>v</sup>	57.5(3)	O4 <sup>ix</sup> —Ba2—O3	105.6(3)
O3 <sup>ii</sup> —Ba1—O2 <sup>v</sup>	131.3(3)	O2 <sup>iv</sup> —Ba2—O3	100.3(2)
O3 <sup>iii</sup> —Ba1—O2 <sup>v</sup>	88.3(3)	O2 <sup>v</sup> —Ba2—O3	146.7(3)

Table 3.15. Continued.

O2 <sup>iv</sup> —Ba1—O2 <sup>v</sup>	66.8(4)	O1 <sup>ix</sup> —Ba2—O3	60.3(3)
O6 <sup>i</sup> —Ba1—O3 <sup>vi</sup>	153.1(2)	O3 <sup>x</sup> —Ba2—O3	70.8(4)
O3 <sup>ii</sup> —Ba1—O3 <sup>vi</sup>	120.7(2)	O4 <sup>ix</sup> —Ba2—O5	56.2(4)
O3 <sup>iii</sup> —Ba1—O3 <sup>vi</sup>	86.8(3)	O2 <sup>iv</sup> —Ba2—O5	62.0(3)
O2 <sup>iv</sup> —Ba1—O3 <sup>vi</sup>	138.3(2)	O2 <sup>v</sup> —Ba2—O5	62.0(3)
O2 <sup>v</sup> —Ba1—O3 <sup>vi</sup>	104.4(3)	O1 <sup>ix</sup> —Ba2—O5	113.0(3)
O6 <sup>i</sup> —Ba1—O3 <sup>vii</sup>	153.05(2)	O3 <sup>x</sup> —Ba2—O5	142.1(2)
O3 <sup>ii</sup> —Ba1—O3 <sup>vii</sup>	86.8(3)	O3—Ba2—O5	142.1(2)
O3 <sup>iii</sup> —Ba1—O3 <sup>vii</sup>	120.7(2)	Br <sup>ix</sup> —Ba2—Br <sup>xi</sup>	116.52(3)
O2 <sup>iv</sup> —Ba1—O3 <sup>vii</sup>	104.4(3)	Br <sup>ix</sup> —Ba2—Br <sup>xii</sup>	116.52(3)
O2 <sup>v</sup> —Ba1—O3 <sup>vii</sup>	138.3(2)	Br <sup>xi</sup> —Ba2—Br <sup>xii</sup>	126.97(6)
O3 <sup>vi</sup> —Ba1—O3 <sup>vii</sup>	53.8(4)	Ba1 <sup>vii</sup> —Br—Ba2 <sup>vii</sup>	86.58(5)
O6 <sup>i</sup> —Ba1—O1 <sup>viii</sup>	118.1(4)	Ba1 <sup>vii</sup> —Br—Ba2 <sup>xiii</sup>	91.76(4)
O3 <sup>ii</sup> —Ba1—O1 <sup>viii</sup>	59.3(3)	Ba2 <sup>vii</sup> —Br—Ba2 <sup>xiii</sup>	116.51(3)
O3 <sup>iii</sup> —Ba1—O1 <sup>viii</sup>	59.3(3)	Ba1 <sup>vii</sup> —Br—Ba2 <sup>xiv</sup>	91.76(4)
O2 <sup>iv</sup> —Ba1—O1 <sup>viii</sup>	144.8(2)	O3—V2—O5 <sup>vii</sup>	111.1(4)
O2 <sup>v</sup> —Ba1—O1 <sup>viii</sup>	144.8(2)	O3 <sup>iv</sup> —V2—O5 <sup>vii</sup>	111.1(4)
O3 <sup>vi</sup> —Ba1—O1 <sup>viii</sup>	63.6(3)	O3—V2—O4	110.0(4)
O3 <sup>vii</sup> —Ba1—O1 <sup>viii</sup>	63.6(3)	O3 <sup>iv</sup> —V2—O4	110.0(4)
O6 <sup>i</sup> —Ba1—O1 <sup>v</sup>	98.5(2)	O5 <sup>vii</sup> —V2—O4	105.2(7)
O3 <sup>ii</sup> —Ba1—O1 <sup>v</sup>	144.3(3)	O6 <sup>xvi</sup> —Cu—O6	180.0
O3 <sup>iii</sup> —Ba1—O1 <sup>v</sup>	66.8(3)	O6 <sup>xvi</sup> —Cu—O2 <sup>xvi</sup>	96.5(5)
O2 <sup>iv</sup> —Ba1—O1 <sup>v</sup>	117.4(3)	O6—Cu—O2 <sup>xvi</sup>	83.5(5)



Table 3.15. Continued.

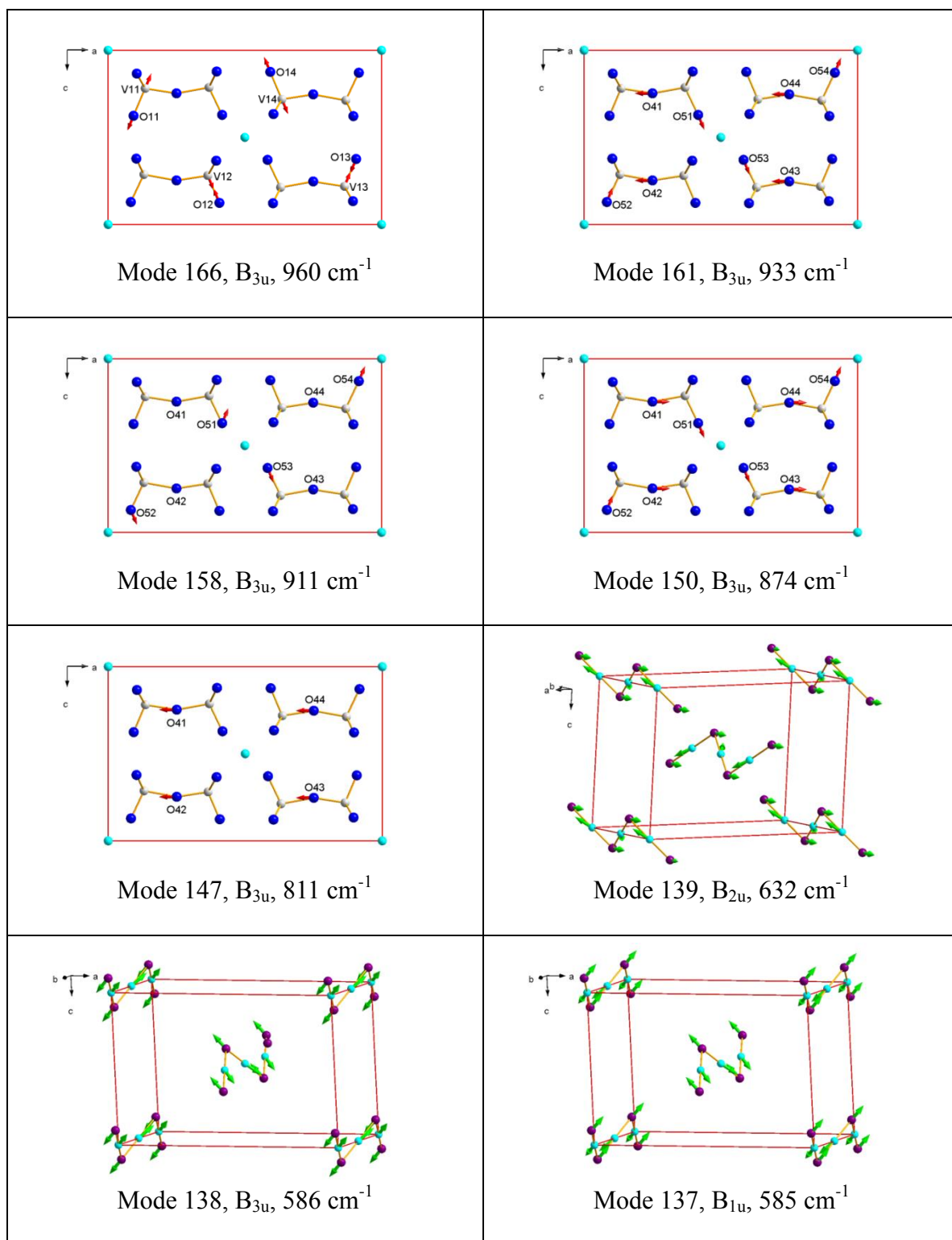
O2 <sup>v</sup> —Ba1—O1 <sup>v</sup>	53.3(3)	O6 <sup>xvi</sup> —Cu—O2	83.5(5)
O3 <sup>vi</sup> —Ba1—O1 <sup>v</sup>	55.9(3)	O6—Cu—O2	96.5(5)
O3 <sup>vii</sup> —Ba1—O1 <sup>v</sup>	108.0(3)	O2 <sup>xvi</sup> —Cu—O2	180.0
O1 <sup>viii</sup> —Ba1—O1 <sup>v</sup>	97.7(2)	O6 <sup>xvi</sup> —Cu—O5 <sup>i</sup>	92.4(4)
O6 <sup>i</sup> —Ba1—O1	98.5(2)	O6—Cu—O5 <sup>i</sup>	87.6(4)
O3 <sup>ii</sup> —Ba1—O1	66.8(3)	O2 <sup>xvi</sup> —Cu—O5 <sup>i</sup>	87.1(4)
O3 <sup>iii</sup> —Ba1—O1	144.4(3)	O2—Cu—O5 <sup>i</sup>	92.9(4)
O2 <sup>iv</sup> —Ba1—O1	53.3(3)	O6 <sup>xvi</sup> —Cu—O5 <sup>xv</sup>	87.6(4)
O2 <sup>v</sup> —Ba1—O1	117.4(3)	O6—Cu—O5 <sup>xv</sup>	92.4(4)
O3 <sup>vi</sup> —Ba1—O1	108.0(3)	O2 <sup>xvi</sup> —Cu—O5 <sup>xv</sup>	92.9(4)
O3 <sup>vii</sup> —Ba1—O1	55.9(3)	O2—Cu—O5 <sup>xv</sup>	87.1(4)
O1 <sup>viii</sup> —Ba1—O1	97.7(2)	O5 <sup>i</sup> —Cu—O5 <sup>xv</sup>	180.0(8)
O1 <sup>v</sup> —Ba1—O1	148.1(4)	Ba2 <sup>vii</sup> —O1—Ba1 <sup>viii</sup>	94.1(3)
O4 <sup>ix</sup> —Ba2—O2 <sup>iv</sup>	107.6(3)	Ba2 <sup>vii</sup> —O1—Ba1 <sup>xv</sup>	104.4(2)
O4 <sup>ix</sup> —Ba2—O2 <sup>v</sup>	107.6(3)	Ba1 <sup>viii</sup> —O1—Ba1 <sup>xv</sup>	82.3(2)
O2 <sup>iv</sup> —Ba2—O2 <sup>v</sup>	69.1(3)	Ba2 <sup>vii</sup> —O1—Ba1	104.4(2)
O4 <sup>ix</sup> —Ba2—O1 <sup>ix</sup>	56.7(4)	Ba1 <sup>viii</sup> —O1—Ba1	82.3(2)
Ba2 <sup>vii</sup> —Br—Ba2 <sup>xiv</sup>	116.51(3)	Ba1 <sup>xv</sup> —O1—Ba1	148.1(4)
Ba2 <sup>xiii</sup> —Br—Ba2 <sup>xiv</sup>	126.97(7)	Ba2 <sup>xv</sup> —O2—Ba1 <sup>xv</sup>	101.2(3)
O1—V1—O2	109.6(4)	Ba1 <sup>xix</sup> —O3—Ba2	104.4(3)
O1—V1—O2 <sup>iv</sup>	109.6(4)	Ba1 <sup>xix</sup> —O3—Ba1 <sup>ix</sup>	93.2(3)
O2—V1—O2 <sup>iv</sup>	113.0(6)	Ba2—O3—Ba1 <sup>ix</sup>	107.8(3)
O1—V1—O4	105.0(7)	V1—O4—V2	162(1)

Table 3.15. Continued.

O2—V1—O4	109.7(4)	Cu <sup>xviii</sup> —O5—Cu <sup>v</sup>	81.1(4)
O2 <sup>iv</sup> —V1—O4	109.7(4)	Cu <sup>xviii</sup> —O6—Cu	100.4(6)
O3—V2—O3 <sup>iv</sup>	109.3(7)		

Symmetry codes: (i)  $-x, -y+1, -z$ ; (ii)  $x-1/2, y, -z+1/2$ ; (iii)  $x-1/2, -y+3/2, -z+1/2$ ; (iv)  $x, -y+1/2, z$ ; (v)  $x, y+1, z$ ; (vi)  $-x+1/2, y+1/2, z+1/2$ ; (vii)  $-x+1/2, -y+1, z+1/2$ ; (viii)  $-x, -y+1, -z+1$ ; (ix)  $-x+1/2, -y+1, z-1/2$ ; (x)  $x, -y+3/2, z$ ; (xi)  $x, y, z-1$ ; (xii)  $x, y+1, z-1$ ; (xiii)  $x, y, z+1$ ; (xiv)  $x, y-1, z+1$ ; (xv)  $x, y-1, z$ ; (xvi)  $-x, -y, -z$ ; (xvii)  $-x, y-1/2, -z$ ; (xviii)  $-x, y+1/2, -z$ ; (xix)  $x+1/2, y, -z+1/2$ .

S-5: Figure 3.19. Depiction of selected IR active modes in BaBrCu(OH)[V<sub>2</sub>O<sub>7</sub>].



S-5: Figure 3.20. Depiction of selected Raman active modes in BaBrCu(OH)[V<sub>2</sub>O<sub>7</sub>].

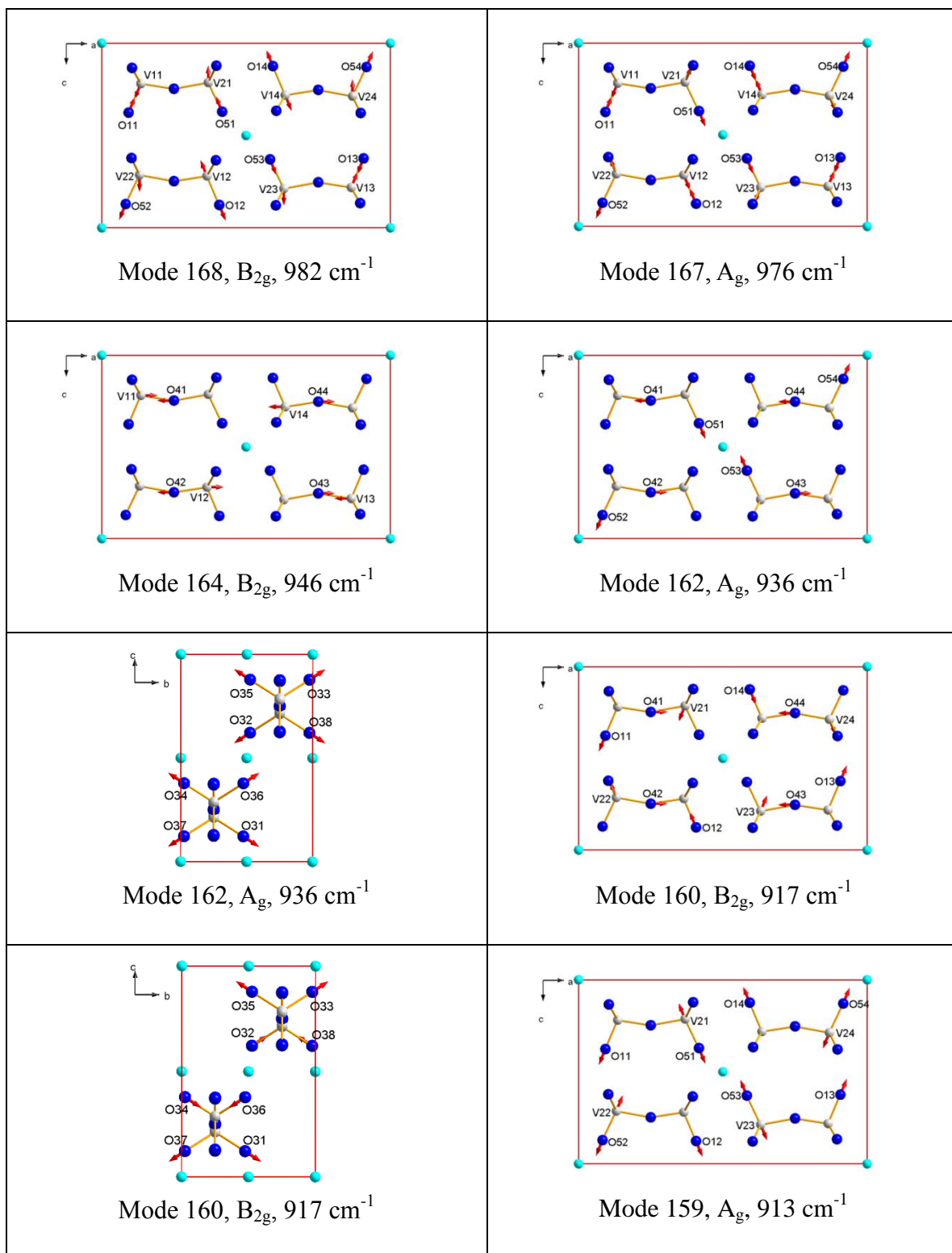


Figure 3.20. Continued.

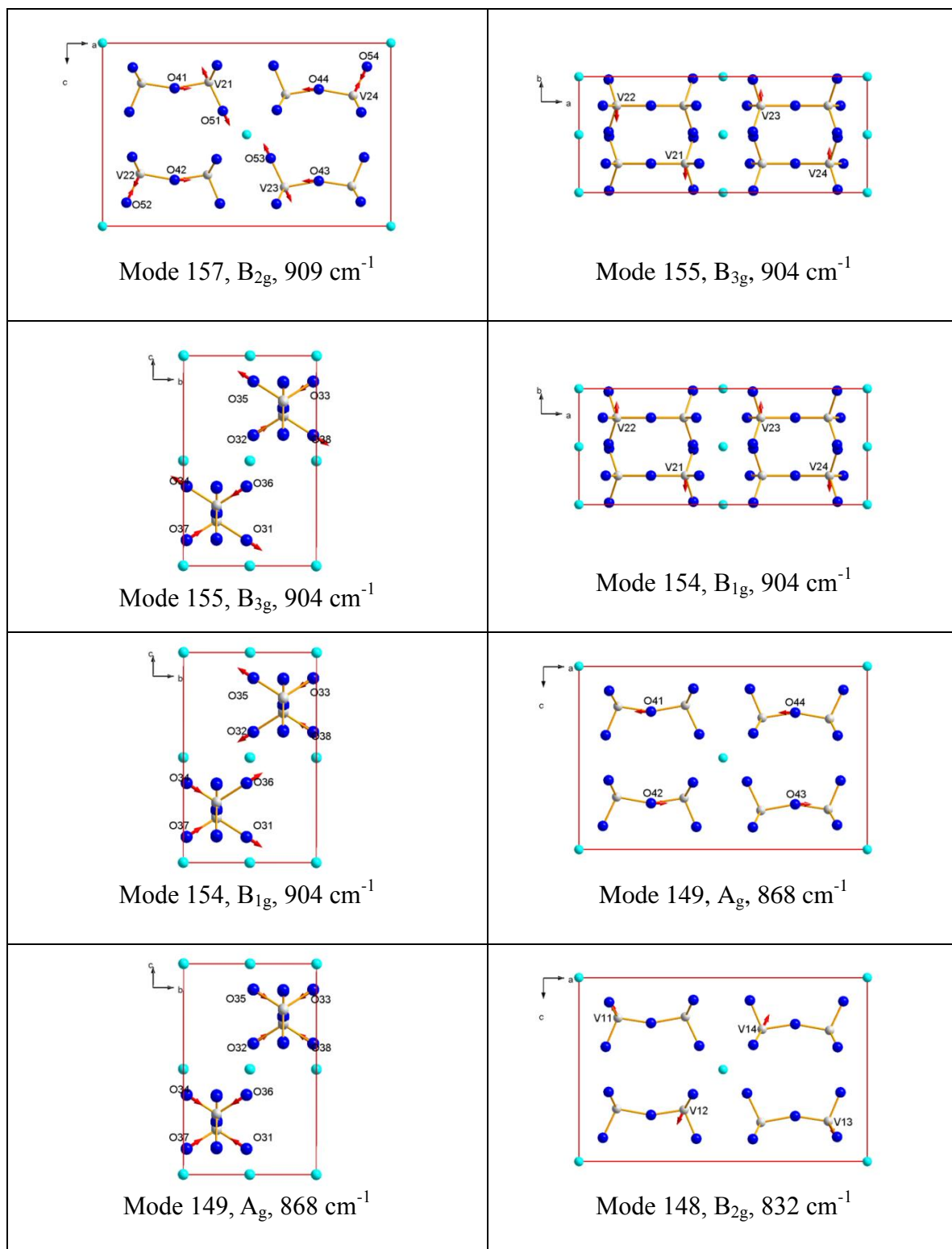
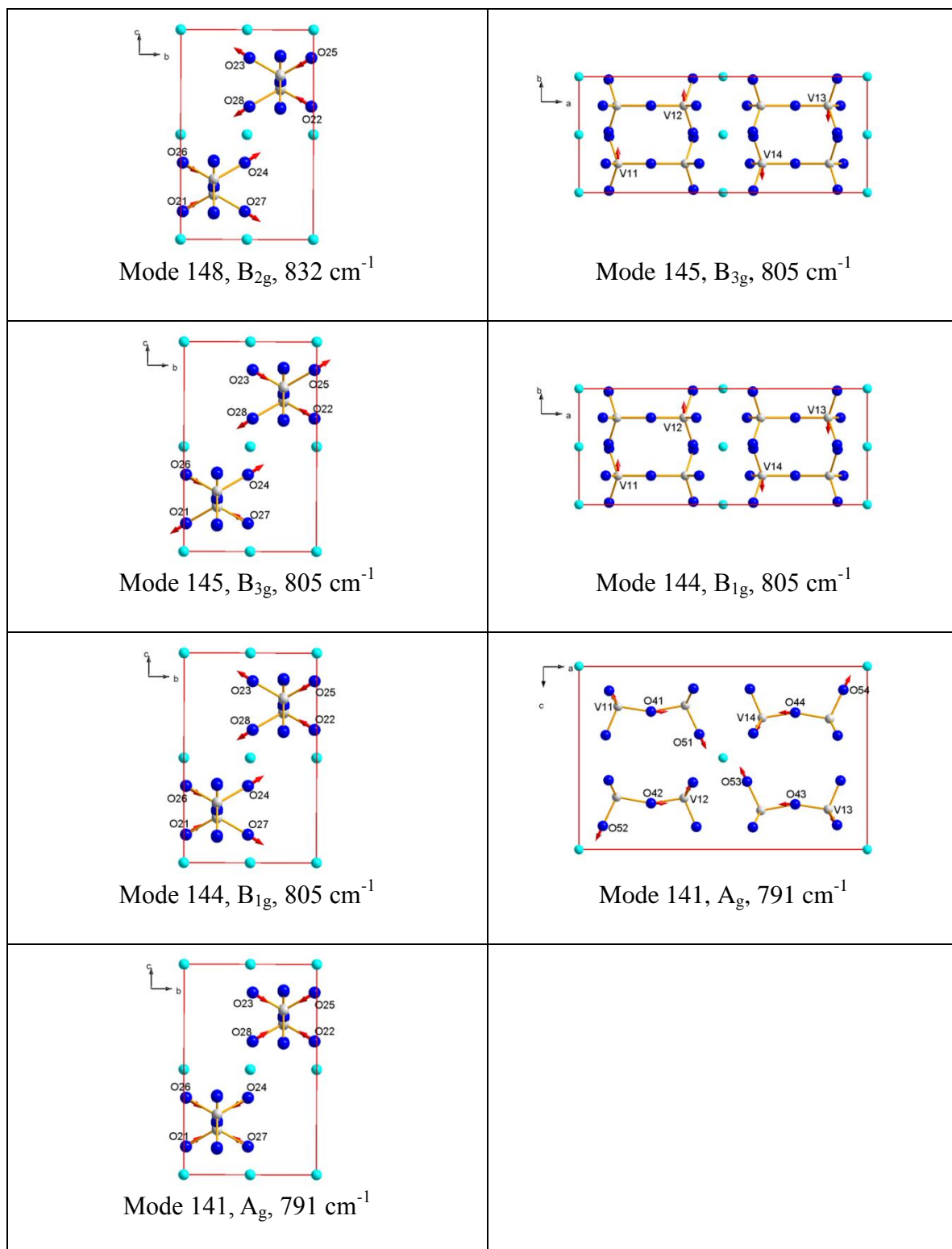


Figure 3.20. Continued.



## Chapter Four

### Synthesis, Crystal Structures, and Physical Properties of $M_2(\text{OH})[\text{VO}_4]$ with

$$M = \text{Mn, Cu}^*$$

#### 4.1 Introduction.

In the previous chapter, two isotypic compounds  $\text{Ba}_2\text{XCu}(\text{OH})[\text{V}_2\text{O}_7]$ ,  $X = \text{Cl, Br}$  were synthesized and discussed. The initial idea for this chapter was replacing the out-of-plane Ba fully or partially by alkali metal cations. Such vandadates have been reported to be obtained by solid-state methods, e.g.  $\text{KBa}_2\text{Cl}[\text{V}_2\text{O}_7]$  [1] and  $\text{KBaClCu}[\text{V}_2\text{O}_7]$ . [2] In the presence of CsCl our hydrothermal synthesis approach either lead to  $\text{CsV}_3\text{O}_8$  [3] or  $\text{BaV}_2\text{O}_6$  [4] and  $\text{Cu}_2(\text{OH})[\text{VO}_4]$ . In 2003, Wu *et al.* reported blue  $\text{Cu}_2(\text{OH})[\text{VO}_4]$  crystallizing in the space group  $Pnma$ . [5] Our results of the structure refinement of orange crystals of  $\text{Cu}_2(\text{OH})[\text{VO}_4]$  indicated a new polymorph with the space group  $P2_12_12_1$ . Unfortunately, in 2014, Zhang *et al.* published the revised structure and gave magnetic data as well. [6] We also obtained from similar synthesis methods  $\text{Mn}_2(\text{OH})[\text{VO}_4]$  crystallizing in the centrosymmetric space group  $Pnma$ , [7] isotypic with  $\text{Cu}_2(\text{OH})[\text{VO}_4]$  Wu *et al.* (2003), [5]  $\text{Zn}_2(\text{OH})[\text{VO}_4]$  Wang *et al.* (1998), [8] and  $\text{Zn}_{1.86}\text{Cd}_{0.14}(\text{OH})[\text{VO}_4]$  Dordevic *et al.* (2010), [9] Interestingly,  $\text{Ni}_2(\text{OH})[\text{VO}_4]$  also crystallizes in the acentric space group  $P2_12_12_1$  as noted by Wang *et al.* (1998). [8]

\*Part of this chapter has been previously published: Sun, K.; Möller, A. *Acta Crystallogr. E*, **2014**, 70, i33.

The family of transition metal vanadates,  $M_2(\text{OH})[\text{VO}_4]$  were all synthesized by hydrothermal methods as single crystals. [5-9] So far, magnetic properties [6] and potential application as cathode materials [8] have been reported.

#### 4.2 Synthesis of Single Crystals of $M_2(\text{OH})[\text{VO}_4]$ with $M = \text{Mn}, \text{Cu}$ .

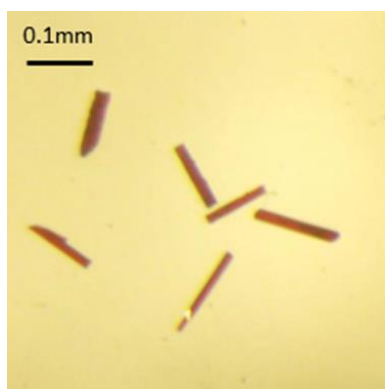


Figure 4.1. Photo of magnified  $\text{Mn}_2(\text{OH})[\text{VO}_4]$  crystals.

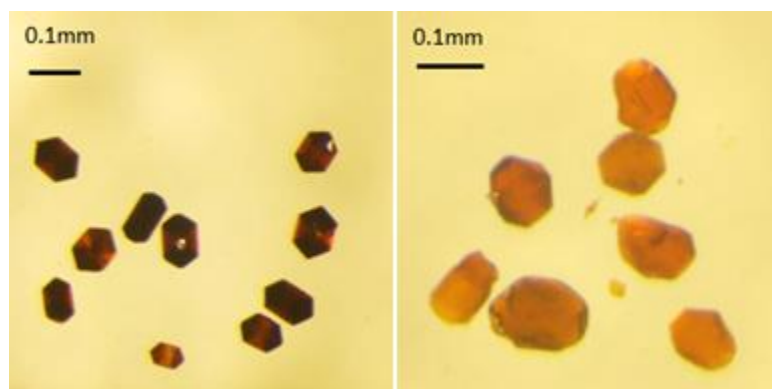


Figure 4.2. Photos of magnified  $\text{Cu}_2(\text{OH})[\text{VO}_4]$  crystals from two different reactions.

*Left:* dark orange hexagonal plate-shaped crystals of  $\text{Cu}_2(\text{OH})[\text{VO}_4]$  from reaction i).

*Right:* orange plate-shaped crystals of  $\text{Cu}_2(\text{OH})[\text{VO}_4]$  from reaction ii).



$\text{Mn}_2(\text{OH})[\text{VO}_4]$  and  $\text{Cu}_2(\text{OH})[\text{VO}_4]$  were both synthesized by hydrothermal methods. For  $\text{Mn}_2(\text{OH})[\text{VO}_4]$ , we used  $\text{H}_2\text{V}_3\text{O}_8$  as a starting material.  $\text{H}_2\text{V}_3\text{O}_8$  was obtained by reacting 0.5 mmol  $\text{V}_2\text{O}_5$ , 0.5 mmol  $\text{H}_2\text{C}_2\text{O}_4$  and 20 mL distilled water in a 26 ml Teflon-lined stainless steel autoclave at 180 °C for 2 days according to [10]. The product is a blue green solid in a blue solution. Powder XRD shows the major phase is  $\text{H}_2\text{V}_3\text{O}_8$  (see S-1 in the supplemental material). 1.75 mmol  $\text{Mn}(\text{Ac})_2 \cdot 4\text{H}_2\text{O}$  and 5 mmol  $\text{LiCl}$  were immediately added to the solution containing  $\text{H}_2\text{V}_3\text{O}_8$  as a precipitate. Drops of concentrated  $\text{NH}_3 \cdot \text{H}_2\text{O}$  were used to adjust the pH to 9.1. The entire mixture was sealed in a 26 ml Teflon-lined stainless steel autoclave and kept in a furnace at 220 °C for 3 days, then slowly cooled down to room temperature as discussed in Chapter Two. The final product was washed with distilled water and ethanol alcohol several times. Red needle-shaped crystals of  $\text{Mn}_2(\text{OH})[\text{VO}_4]$  and dark block-shaped crystals of  $\text{Mn}_7(\text{OH})_3[\text{VO}_4]_4$  (discussed in Chapter Six) were obtained.

Single crystals of  $\text{Cu}_2(\text{OH})[\text{VO}_4]$  were synthesized by two different reactions: i) 0.5 mmol  $\text{NH}_4\text{VO}_3$ , 1.0 mmol  $\text{Cu}(\text{Ac})_2 \cdot \text{H}_2\text{O}$ , and 10 mL distilled water; ii) 0.5 mmol  $\text{NH}_4\text{VO}_3$ , 1.0 mmol  $\text{CuCl}_2$ , 10 mL distilled water. Drops of concentrated  $\text{NH}_3 \cdot \text{H}_2\text{O}$  were used to adjust the pH to around 9 in each case. Each mixture was sealed in 12 ml Teflon-lined stainless steel autoclave, kept in the furnace at 220 °C for three days, and cooled as described in Chapter Two. The final products were washed with distilled water and ethanol alcohol several times.  $\text{Cu}_2(\text{OH})[\text{VO}_4]$  precipitated as i) dark orange hexagonal plate-shaped crystals (Figure 4.2 - left) and dark block-shaped crystals and ii) orange plate-shaped crystals (Figure 4.2 - right). Single crystal data of  $\text{Cu}_2(\text{OH})[\text{VO}_4]$  were

collected and solved for a crystal from each of reaction i) and ii). The dark orange hexagonal plate-shaped crystals were  $\text{Cu}_2(\text{OH})[\text{VO}_4]$  i), but the majority of solid products were dark block-shaped crystals of  $\text{Cu}_2\text{O}$ . Unlike the reported results, [5, 6] phase-pure products could not be obtained in the presence of  $\text{Cu}(\text{Ac})_2$  under basic conditions.  $\text{Cu}_2\text{O}$  seems to be a preferred product for such reaction conditions. Pure samples of  $\text{Cu}_2(\text{OH})[\text{VO}_4]$  were only obtained by the modified reaction ii) using  $\text{CuCl}_2$  instead of  $\text{Cu}(\text{Ac})_2 \cdot \text{H}_2\text{O}$ .

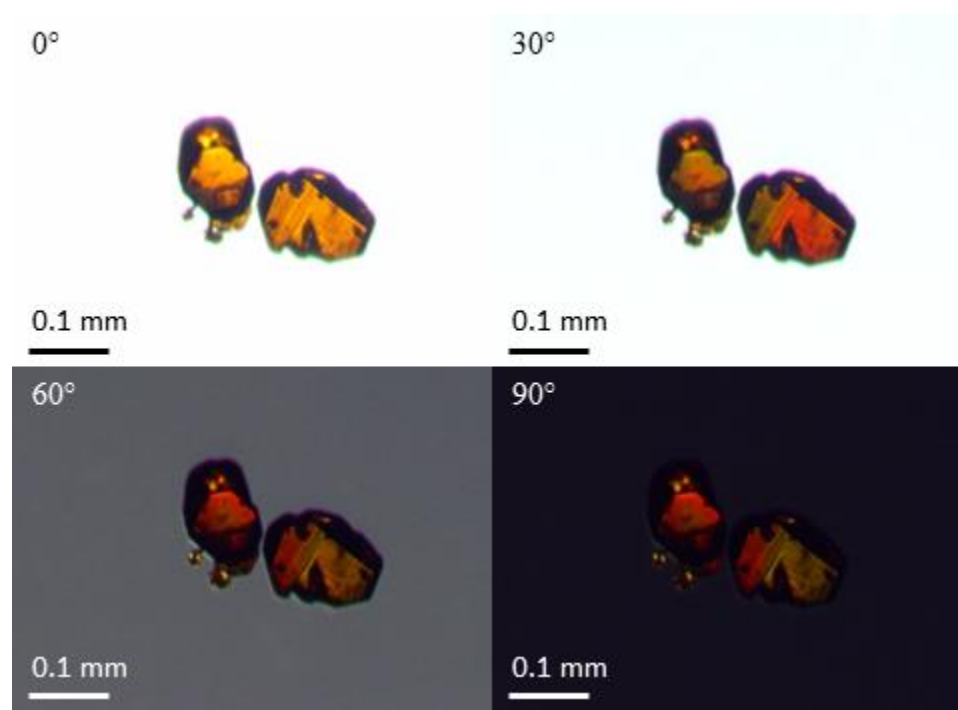


Figure 4.3. Polarized photos of magnified  $\text{Cu}_2(\text{OH})[\text{VO}_4]$  crystals.

Photos of magnified crystals with polarized light were taken. (Figure 4.3) From our observation, the crystals presented different colors under different angles and showed

weak colors under cross-polarized light (90°). This result indicates an acentric space group.

#### **4.3 Single Crystal X-ray Diffraction of $M_2(\text{OH})[\text{VO}_4]$ with $M = \text{Mn}, \text{Cu}$ .**

Single crystal data were collected on a Rigaku instrument. A red needle-shaped crystal was selected for  $\text{Mn}_2(\text{OH})[\text{VO}_4]$  and a dark orange hexagonal plate-shaped crystal ii) was selected for  $\text{Cu}_2(\text{OH})[\text{VO}_4]$ . The crystal structures were solved and refined as described in Chapter Two. Hydrogen atom positions were found from difference Fourier maps and were refined by restricting the O-H distance (DFIX command) and using the ride-on option for the isotropic displacements with  $U_{\text{iso}}(\text{H}) = 1.5 \times U_{\text{eq}}(\text{O})$ . For the final refinement the AFIX command was applied. Platon suggests an acentric structure for  $\text{Cu}_2(\text{OH})[\text{VO}_4]$ . The Flack parameter is 0.49 indicating twinning for  $\text{Cu}_2(\text{OH})[\text{VO}_4]$ , with the twinning component with respect to the  $b$  axis. Systematic absence violations vanish after applying the twinning commands (“TWIN 0 0 -1 -1 0 0 0 -1 0 4” and “BASF 0.00147 0.00086 0.49401”). The details of crystal data for  $M_2(\text{OH})[\text{VO}_4]$  with  $M = \text{Mn}, \text{Cu}$  are listed in Table 4.1.

Fractional atomic coordinates and isotropic or equivalent isotropic displacement parameters are listed in S-2 and selected interatomic distances and angles for  $M_2(\text{OH})[\text{VO}_4]$  with  $M = \text{Mn}, \text{Cu}$  are listed in S-3, and S-4, respectively, in the supplemental material.

Table 4.1. Crystal data and details of the structure determination for  $M_2(\text{OH})[\text{VO}_4]$ ,  
 $M = \text{Mn, Cu}$ .

Formula	$\text{Mn}_2(\text{OH})[\text{VO}_4]$	$\text{Cu}_2(\text{OH})[\text{VO}_4]$
Mass/Formula unit ( $M_r$ )	241.83 g mol <sup>-1</sup>	259.03 g mol <sup>-1</sup>
Crystal system	orthorhombic	orthorhombic
Space group	$Pnma$ , $Z = 8$	$P2_12_12_1$ , $Z = 8$
Lattice constants	$a = 14.911(1) \text{ \AA}$ $b = 6.1225(3) \text{ \AA}$ $c = 9.1635(5) \text{ \AA}$	$a = 6.0564(1) \text{ \AA}$ $b = 8.5581(2) \text{ \AA}$ $c = 14.954(1) \text{ \AA}$
Volume	836.57(8) Å <sup>3</sup>	775.10(6) Å <sup>3</sup>
Density	3.840 g/cm <sup>3</sup>	4.439 g/cm <sup>3</sup>
F (000)	912	976
Temperature	293K	293K
Crystal size	0.14 × 0.02 × 0.02 mm	0.12 × 0.08 × 0.02 mm
Range	$\theta_{\text{max}} = 33.13^\circ$ ; $\theta_{\text{min}} = 3.52^\circ$	$\theta_{\text{max}} = 28.0^\circ$ ; $\theta_{\text{min}} = 3.4^\circ$
Data set	-22 < h < 22 -9 < k < 9 -13 < l < 14	-8 < h < 8 -11 < k < 11 -19 < l < 19
$R_{\text{int}}$	0.0459	0.041
Measured/Unique reflections	11657/1715	7210/1854
Parameter refined	92	148
$R_1$ , $wR_2$ , GooF	0.0449, 0.0613, 1.356	0.053, 0.139, 1.13
$\mu$ (Mo $K_\alpha$ )	8.036 mm <sup>-1</sup>	13.13 mm <sup>-1</sup>
( $T_{\text{min}}$ , $-T_{\text{max}}$ )	0.777 - 1.000	0.350 - 0.811
BASF	-	0.49401

#### 4.4 Powder X-ray Diffraction and Refinement of $\text{Cu}_2(\text{OH})[\text{VO}_4]$ .

A refinement of the power X-ray diffraction pattern of  $\text{Mn}_2(\text{OH})[\text{VO}_4]$  is not available since the product was not single phased, see above. The powder X-ray diffraction pattern of  $\text{Cu}_2(\text{OH})[\text{VO}_4]$  was collected to confirm the phase purity and the structure model. The sample was prepared by grinding crystals into a fine powder. Powder refinement data for  $\text{Cu}_2(\text{OH})[\text{VO}_4]$  are shown in Figure 4.4. The results of the refinements are listed below in Table 4.2.

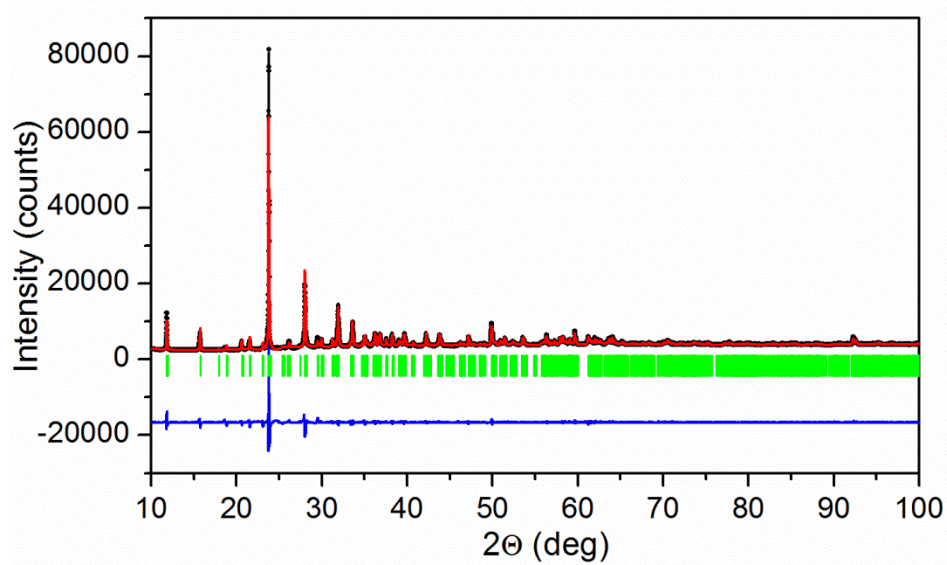


Figure 4.4. Powder refinement data for  $\text{Cu}_2(\text{OH})[\text{VO}_4]$ . Observed (black), calculated (red), Bragg positions (green) and difference (blue).

Table 4.2. Powder refinement results for  $\text{Cu}_2(\text{OH})[\text{VO}_4]$ , orthorhombic space group  $P2_12_12_1$ .

<b>Formula</b>	$\text{Cu}_2(\text{OH})[\text{VO}_4]$
<b>Unit Cell (<math>\text{\AA}</math>)</b>	$a = 6.0536(1)$
	$b = 8.5544(2)$
	$c = 14.9565(1)$
<b>Volume (<math>\text{\AA}^3</math>)</b>	774.52(2)
$\chi^2$ , $R_{\text{Bragg}}$ , <b>RF-factor</b>	10.7, 1.65, 1.32

#### 4.5 Crystal Structure Description and Discussion for $M_2(\text{OH})[\text{VO}_4]$ with $M = \text{Mn}$ , $\text{Cu}$ .

$\text{Mn}_2(\text{OH})[\text{VO}_4]$  crystallizes in the centrosymmetric space group  $Pnma$ , while the structure of  $\text{Cu}_2(\text{OH})[\text{VO}_4]$  was determined as acentric  $P2_12_12_1$ . The structural features of  $\text{Mn}_2(\text{OH})[\text{VO}_4]$  will be discussed first and then followed by the discussion of  $\text{Cu}_2(\text{OH})[\text{VO}_4]$ .

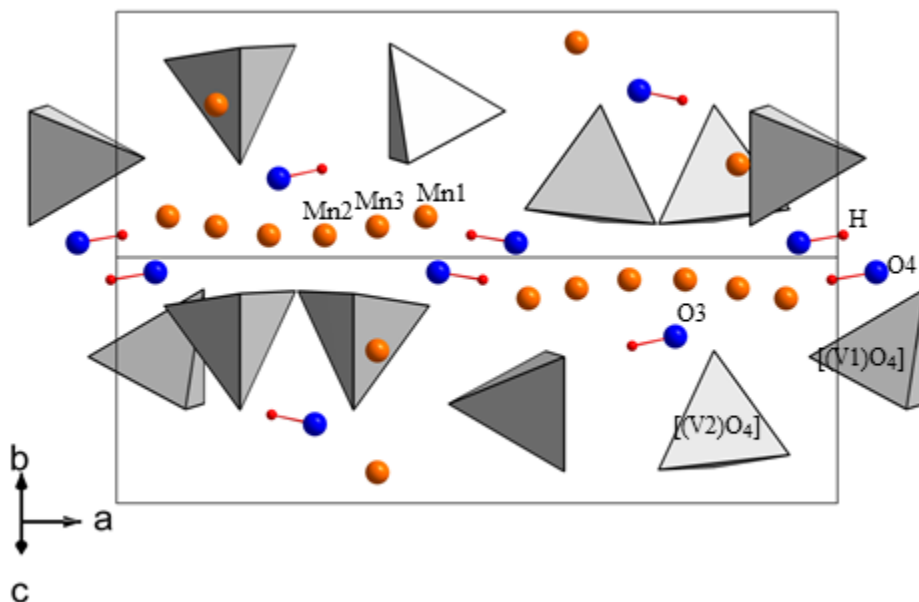


Figure 4.5. A projection of the crystal of  $\text{Mn}_2(\text{OH})[\text{VO}_4]$  along  $[011]$ .

The crystal structure of  $\text{Mn}_2(\text{OH})[\text{VO}_4]$  contains three  $\text{Mn}^{2+}$  ions and two  $[\text{VO}_4]^{3-}$  units which are crystallographically independent. (Figure 4.5) The H-atoms are linked to O3 and O4. Hydroxide ions are exclusively bonded to Mn-atoms. Mn1 and Mn2 occupy a  $4c$

position, respectively, with *m*. site symmetry, whereas Mn3 is located on a general *8d* position with lower site symmetry.

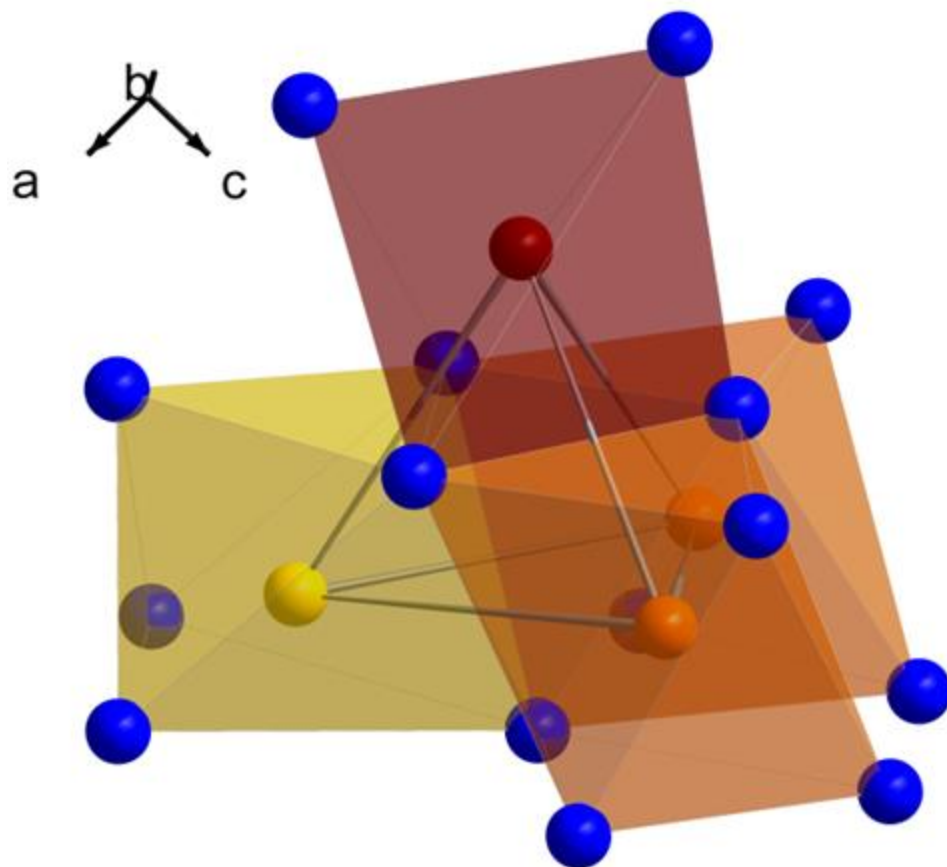


Figure 4.6. Polyhedral representations of  $\text{Mn}_2(\text{OH})[\text{VO}_4]$ , Mn1 (red), Mn2 (yellow) and Mn3 (orange).

The coordination environment of Mn1 is represented by a distorted trigonal-bipyramid, while Mn2 and Mn3 are found in an octahedral coordination. The four Mn-centered polyhedra (including Mn1, Mn2, and two symmetry-related Mn3 polyhedra) connect to each other via the edges. Mn1 connects to Mn2 and two Mn3 only via the edges of a



single trigonal face. Mn2 shares four common edges with Mn3 on two trans-faces as well as a single edge with Mn1. Mn3 connects to symmetry related Mn3 positions via trans-edges along [010] to two Mn2 and only one Mn1. The four Mn atoms form a Mn<sub>4</sub> tetrahedral building unit, see in Figure 4.6.

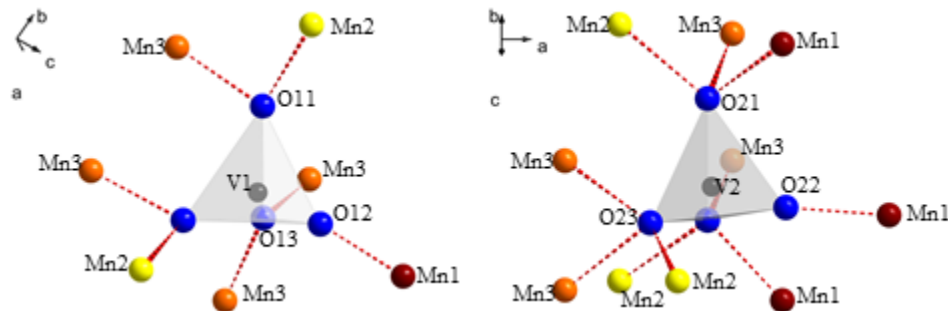


Figure 4.7. The second coordination spheres around V atoms linked via O atoms. *Left:* V1. *Right:* V2.

Figure 4.7 depicts two  $[\text{VO}_4]^{3-}$  units with  $C_{2v}$  point group symmetry. Each V atom and two O per tetrahedron are located on a mirror plane. The other two O per  $[\text{VO}_4]$  unit are found on a general position, respectively. V1 is coordinated by O11 (8d), O12 (4c), and O13 (4c). Mn2 and Mn3 are linked via O11 whereas O13 connects to two Mn3. O12 connects solely to Mn1. However, the second coordination sphere around V2 is dissimilar with respect to O21 (8d) connecting to Mn1, Mn2, and Mn3 as well as O23 (4c) linked to Mn2 and two Mn3. Again O22 (4c) connects only to Mn1.

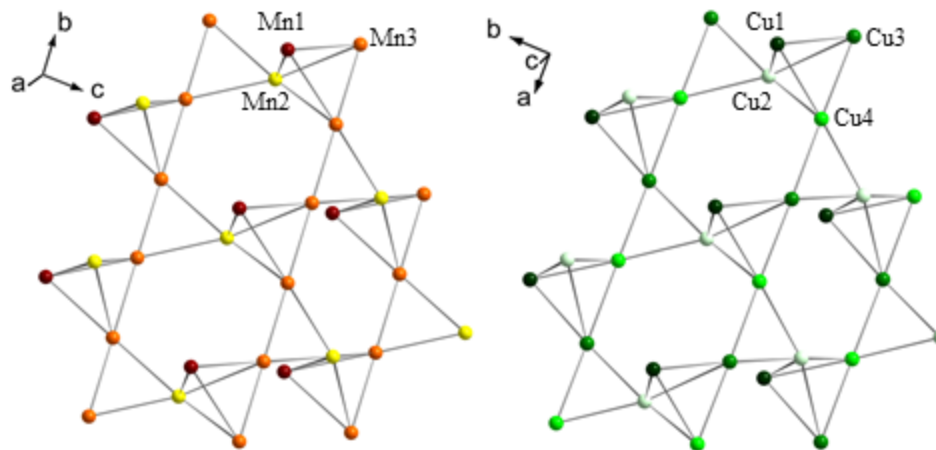


Figure 4.8. The  $M$ - $M$  connectivity per layer with each connecting line representing a link exclusively via edge-sharing. *Left:*  $\text{Mn}_2(\text{OH})[\text{VO}_4]$ . *Right:*  $\text{Cu}_2(\text{OH})[\text{VO}_4]$ .

In Figure 4.8 the Mn–Mn connectivity is shown. The layers resemble a corrugated kagome-like geometry with triangular and hexagonal entities based on the Mn2 and Mn3 connectivities. Mn1 is capping every other triangular unit and thus considered as out-of-plane. Per unit cell two of these layers are present which are linked through Mn–O–V–O–Mn bridges into a three-dimensional framework.

For acentric  $\text{Cu}_2(\text{OH})[\text{VO}_4]$ , four Cu positions result with alternating Cu3/Cu4 connectivity along the  $a$ -axis. Note the difference in standard settings for the orthorhombic space groups  $Pnma$  and  $P2_12_12_1$ .

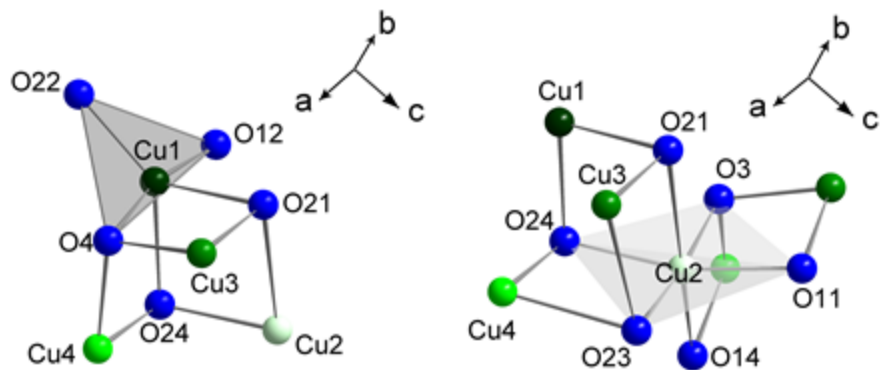


Figure 4.9. Cu-O and Cu-O-Cu connectivity of  $\text{Cu}_2(\text{OH})[\text{VO}_4]$ . *Left*: Cu1. *Right*: Cu2.

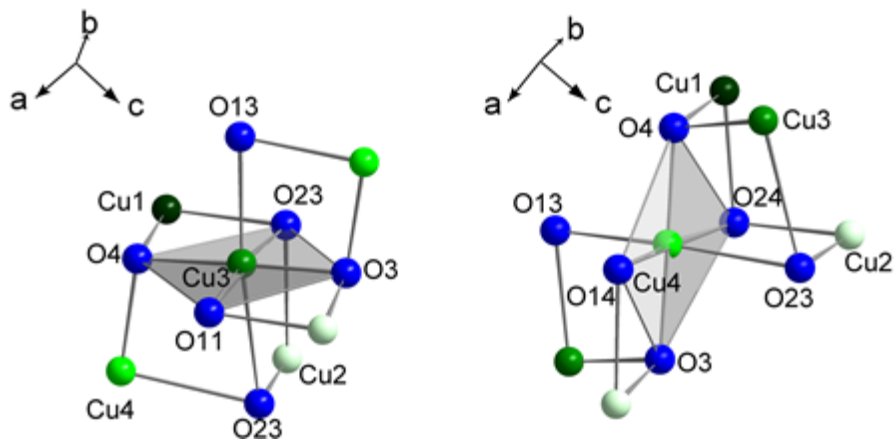


Figure 4.10. Cu-O and Cu-O-Cu connectivity of  $\text{Cu}_2(\text{OH})[\text{VO}_4]$ . *Left*: Cu3. *Right*: Cu4.

In Figure 4.10 the respective connectivity between adjacent Cu-atoms is shown. The four Cu centered polyhedra are connected exclusively via edge-sharing. Due to the Jahn-Teller effect [11] present in the case of  $\text{Cu}^{2+}$  with a  $d^9$  configuration, the axial Cu-O distances within an octahedron are elongated. Here the shorter equatorial Cu-O distances are represented by the colored polyhedra, see Figure 4.9 and 4.10. These plaquettes represent the  $d_{x^2-y^2}$  magnetic orbital as well and are thus important for the magnetic properties. Cu1

Based on the investigation of Cu–O–Cu connectivity and the consideration of relevant magnetic orbitals in space, we propose the magnetic exchange pathways via edges and corners for Cu<sub>2</sub>(OH)[VO<sub>4</sub>] in Figure 4.11. The Cu<sub>2</sub> and Cu<sub>3</sub> magnetic orbitals form edge-shared dimers and connect to Cu<sub>4</sub> via corners. These three Cu are coupled on a 2D lattice. In Figure 4.12, the ladder type of magnetic arrangement is depicted. Cu<sub>3</sub> and Cu<sub>4</sub> are coupled forming the legs with the bridging feature (rungs) associated with Cu<sub>2</sub>. As mentioned above, Cu<sub>1</sub> is located in the terminal position. The magnetic coupling to the

2D lattice is unknown and might be referred to as a “loose end member” within the tetrahedral entity or linked to the legs.

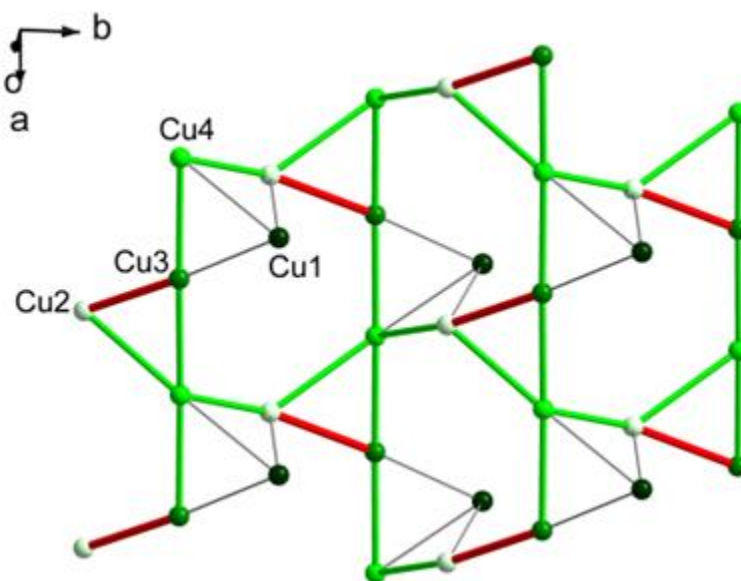


Figure 4.12. Ladder type magnetic arrangement along [100] for  $\text{Cu}_2(\text{OH})[\text{VO}_4]$ , corner-sharing (green), dimers (red), and end member (grey).

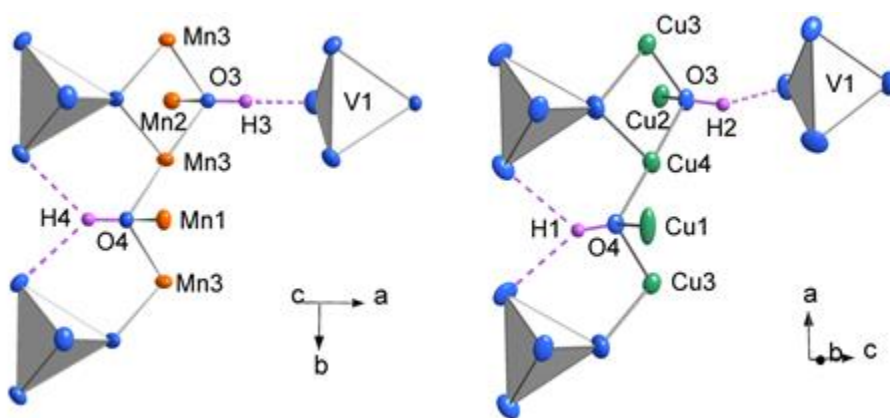


Figure 4.13. Hydrogen bonding for  $M_2(\text{OH})[\text{VO}_4]$  with  $M = \text{Mn}, \text{Cu}$ . *Left:*  $\text{Mn}_2(\text{OH})[\text{VO}_4]$ . *Right:*  $\text{Cu}_2(\text{OH})[\text{VO}_4]$ . Ellipsoids are of 75% probability.

In Figure 4.13, the two hydroxide groups of  $\text{Mn}_2(\text{OH})[\text{VO}_4]$  are of *m*. point group symmetry with direct and bifurcated  $\text{O}^{\text{D}}\cdots\text{O}^{\text{A}}$  contacts, respectively. (Table 4.3) The mirror plane is perpendicular to *b*-axis. The two hydroxide groups of  $\text{Cu}_2(\text{OH})[\text{VO}_4]$  are very similar, but due to the reduced symmetry, asymmetric and bending is evident. (Table 4.4)

Table 4.3. Interatomic distances and angles for O-donor ( $\text{O}^{\text{D}}$ ) and O-acceptor ( $\text{O}^{\text{A}}$ ) contacts for  $\text{Mn}_2(\text{OH})[\text{VO}_4]$  (*Pnma*).

$\text{O}^{\text{D}}\text{-H}\cdots\text{O}^{\text{A}}$	$\text{O}^{\text{D}}\text{-H}$ (Å)	$\text{H}\cdots\text{O}^{\text{A}}$ (Å)	$\text{O}^{\text{D}}\cdots\text{O}^{\text{A}}$ (Å)	$\text{O}^{\text{D}}\text{-H}\cdots\text{O}^{\text{A}}$ (°)
O3-H3 $\cdots$ O12	0.96	1.79	2.734(4)	165
O4-H4 $\cdots$ O11 <sup>i</sup>	0.97	2.39	3.161(3)	137
O4-H4 $\cdots$ O11 <sup>ii</sup>	0.97	2.39	3.161(3)	137

Symmetry codes: (i)  $x-1/2, y, -z+1/2$ ; (ii)  $x-1/2, -y+1/2, -z+1/2$ .

Table 4.4. Interatomic distances and angles for O-donor ( $\text{O}^{\text{D}}$ ) and O-acceptor ( $\text{O}^{\text{A}}$ ) contacts for  $\text{Cu}_2(\text{OH})[\text{VO}_4]$  (*P2<sub>1</sub>2<sub>1</sub>2<sub>1</sub>*).

$\text{O}^{\text{D}}\text{-H}\cdots\text{O}^{\text{A}}$	$\text{O}^{\text{D}}\text{-H}$ (Å)	$\text{H}\cdots\text{O}^{\text{A}}$ (Å)	$\text{O}^{\text{D}}\cdots\text{O}^{\text{A}}$ (Å)	$\text{O}^{\text{D}}\text{-H}\cdots\text{O}^{\text{A}}$ (°)
O3-H3 $\cdots$ O12	0.94	1.79	2.6233(2)	146
O4-H4 $\cdots$ O11	0.98	2.48	3.2081(2)	131
O4-H4 $\cdots$ O14	0.98	2.45	3.3224(2)	148

Based on the evaluation of the *M*–O–*M* connectivities, the difference in the second coordination sphere between the  $[\text{V1O}_4]$  and  $[\text{V2O}_4]$  units, and the two independent

positions found for hydroxide groups, the more informative structure-related formula should be presented as  $M_4(\text{OH})_2[\text{VO}_4]_2$  with  $Z = 4$  per unit cell. Distances of Mn–O are found to be in the narrow range of 2.0 - 2.3 Å for  $\text{Mn}_4(\text{OH})_2[\text{VO}_4]_2$ . Strong distortion occurs for  $\text{Cu}_4(\text{OH})_2[\text{VO}_4]_2$  with axial Cu–O distances of  $\sim 2.3 - 2.4$  Å and equatorial Cu–O distances of 1.9 - 2.1 Å.

#### 4.6 Physical Properties of $\text{Cu}_2(\text{OH})[\text{VO}_4]$ .

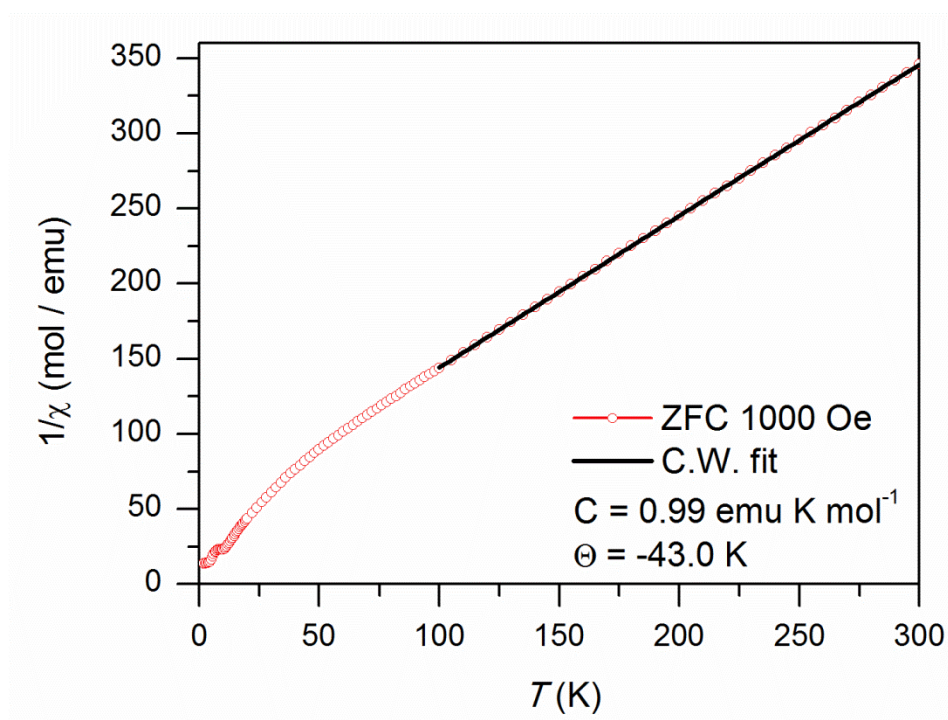


Figure 4.14. Inverse susceptibility data for  $\text{Cu}_2(\text{OH})[\text{VO}_4]$  with a fit to the Curie-Weiss law.

We first look at the inverse susceptibility at 0.1 T (Figure 4.14) The high temperature region of  $1/\chi(T)$  above 100 K is fitted linearly to a Curie-Weiss law. The Curie constant  $C$

derived from the slope of a linear fit is  $0.99 \text{ emu K mol}^{-1}$  which is larger than the theoretical value of  $0.75 \text{ emu K mol}^{-1}$  for the sum of two paramagnetic  $\text{Cu}^{2+}$  ( $S = 1/2$ ) per formula with  $g = 2.0$ . This is not unexpected for orbital contributions for  $\text{Cu}^{2+}$  and well in line with typical larger  $g$ -values for octahedral Cu-complexes. The Weiss temperature,  $\Theta$  is found to be around  $-43 \text{ K}$ , indicating strong antiferromagnetic interactions. The Curie constant and Weiss temperature observed are quite similar to the data published by Zhang *et al.* [6]

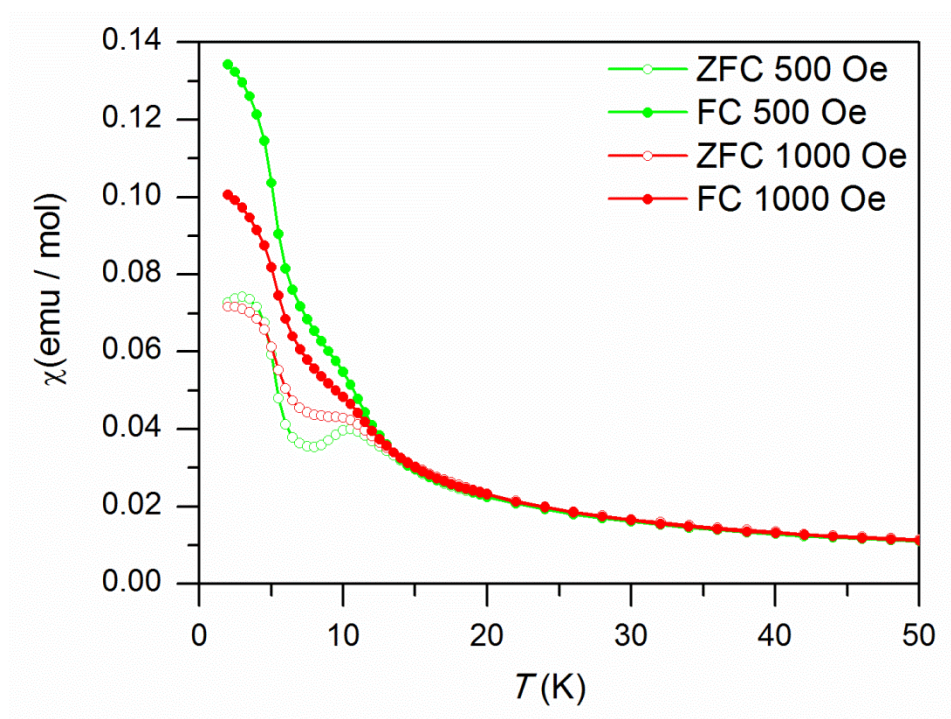


Figure 4.15. Susceptibility data for  $\text{Cu}_2(\text{OH})[\text{VO}_4]$  below 50 K.

The  $\chi(T)$  data in the low temperature range, below 50 K, are plotted in Figure 4.15. The splitting between ZFC and FC is observed below 11 K and decreases with increasing



applied field. These observations indicate possible ferrimagnetic or canted antiferromagnetic correlations in the low temperature range. An additional feature at around 5 K is evident.

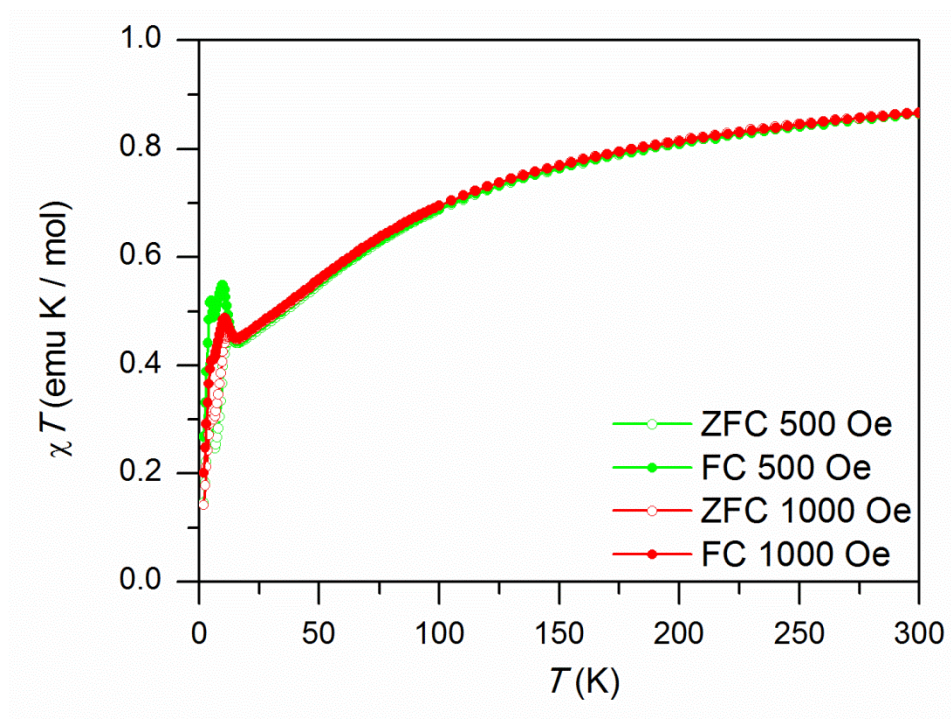


Figure 4.16. Susceptibility ( $\chi T(T)$ ) data for  $\text{Cu}_2(\text{OH})[\text{VO}_4]$ .

In Figure 4.16 we present the  $\chi T(T)$  data. At 300 K, the value of  $\chi T$  reaches a plateau at  $0.87 \text{ emu K mol}^{-1}$  which matches the two paramagnetic  $\text{Cu}^{2+}$  ( $S = 1/2$ ) per formula with a calculated  $g^{\text{eff}} = 2.15$ , which is similar to those  $g$ -values obtained for  $\text{Ba}_2\text{XCu}(\text{OH})[\text{V}_2\text{O}_7]$  in Chapter Three. The dominant antiferromagnetic short-range correlations at high temperatures are evidenced by a gradual slope below 250 K. At low temperatures ferromagnetic correlations contribute to the ferrimagnetic long-range order at  $T_C \approx 11 \text{ K}$ .

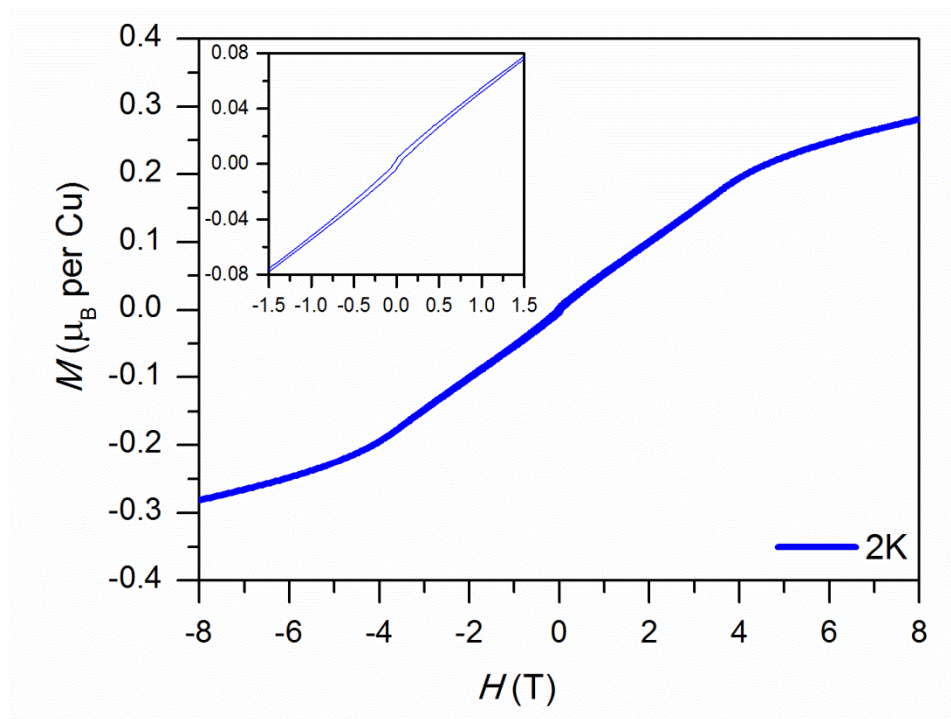


Figure 4.17. Magnetization data for  $\text{Cu}_2(\text{OH})[\text{VO}_4]$ :  $M(H)$  per Cu data at 2 K.

The magnetization data at 2 K,  $M(H)$ , were measured up to 8 T and plotted in units of  $\mu_B$  per Cu in Figure 4.17. A very narrow hysteresis loop is found up to 1.5 T, see the inset. Above 4 T, the magnetization approaches a value of 0.28  $\mu_B$  at 8 T, which is close to the one third of the saturated moment for one  $\text{Cu}^{2+}$  ( $S = 1/2$ ) with  $M_S = 1 \mu_B$ . The reduced magnetization from the expected value of 1  $\mu_B$  in the low temperature suggests strong antiferromagnetic contributions.

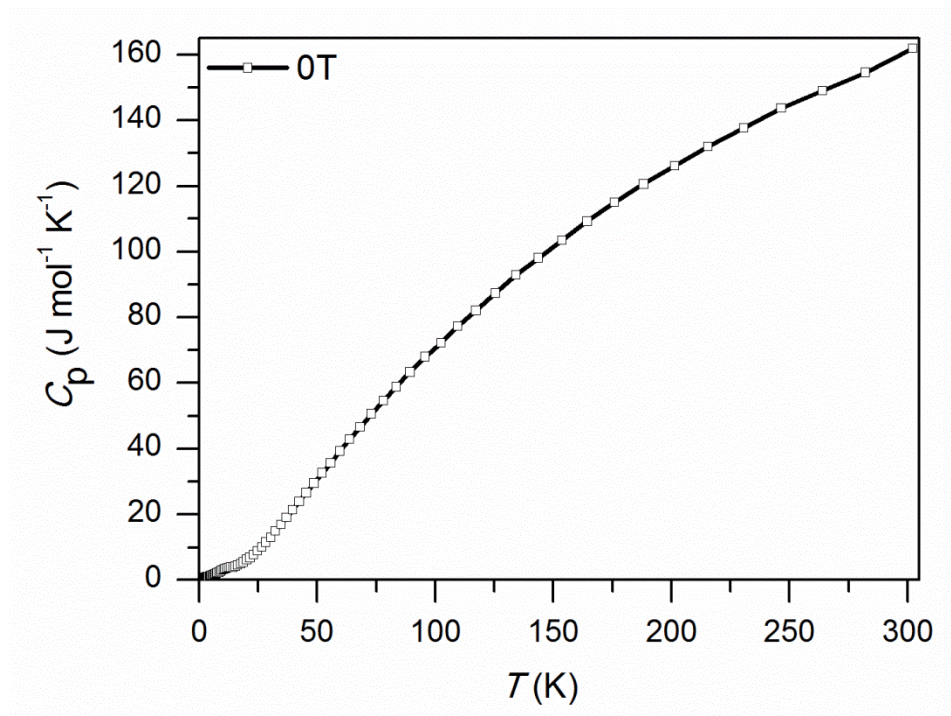


Figure 4.18. Total specific heat data for  $\text{Cu}_2(\text{OH})[\text{VO}_4]$  at zero field.

The measured total specific heat,  $C_p(T)$ , for  $\text{Cu}_2(\text{OH})[\text{VO}_4]$  in zero applied field is given in Figure 4.18. At low temperature an anomaly is observed at  $T_C = 10.2 \text{ K}$ , see also Figure 4.17.

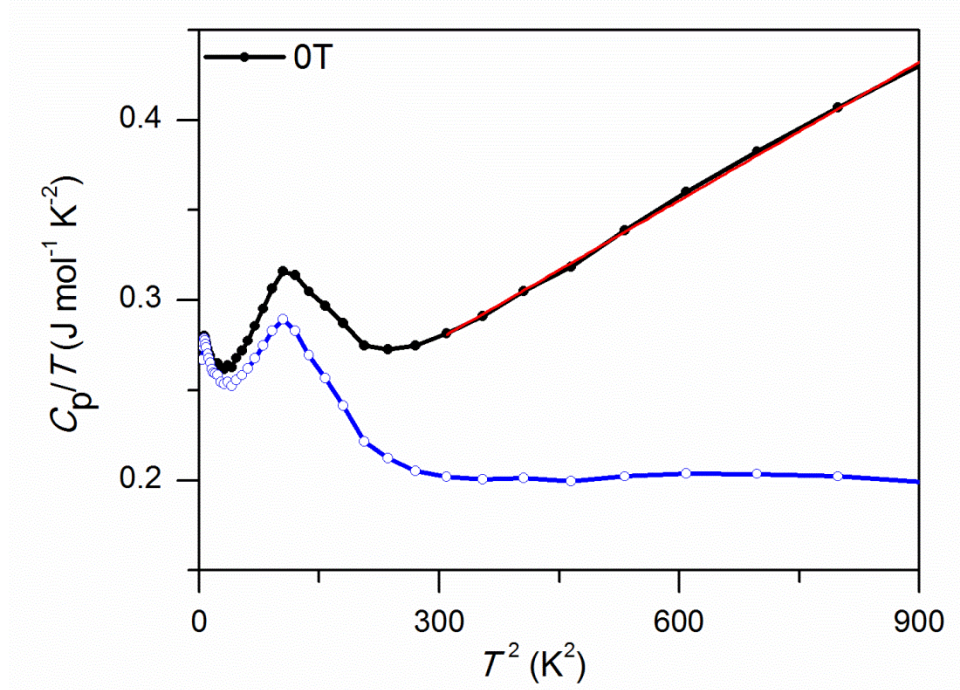


Figure 4.19. The total and magnetic specific heat,  $C_p(T)/T$  (black),  $C_m(T)/T$  (blue) below 30 K. The red line represents the fit to the data between 17 K and 30 K.

In Figure 4.19  $C_p/T$  is plotted versus  $T^2$ . The specific heat data in the range of 17 K to 30 K can be fitted to the equation  $C_p(T) = AT^2 + BT^3$ . Based on the Debye model, [12] the phonon contribution,  $C_L(T)$ , to the total specific heat,  $C_p(T)$ , is proportional to  $T^3$  at low temperatures. Thus, the  $BT^3$  term can be assigned to the phonon contribution with  $B$  related to the Debye-temperature,  $\Theta_D$ , by the number of atoms per formula unit,  $n$  (here: nine atoms). From equation  $B = 12\pi^4 Rn/(5\Theta_D^3)$  ( $R$  is the gas constant) [13] we obtain  $\Theta_D = 408.5$  K in a good agreement with Zhang *et al.* [6] The  $AT^2$  term relates to the magnetic short-range order of a 2D lattice, compare the layered structure given above.



The magnetic part of the specific heat then can be obtained by subtracting the phonon contribution from the total specific heat data.

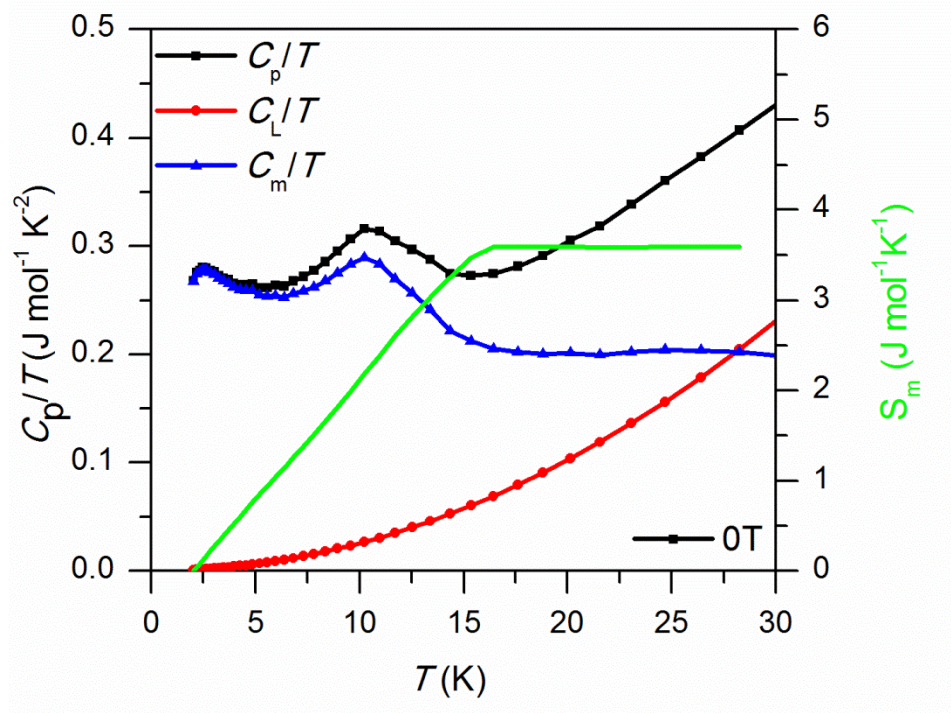


Figure 4.20. The magnetic part of the specific heat,  $C_p(T)/T$  (black),  $C_m(T)/T$  (blue)  $C_L(T)/T$  (red) for  $\text{Cu}_2(\text{OH})[\text{VO}_4]$  and the associated entropy,  $S_m(T)$  (green), below 17 K.

In Figure 4.20, we plotted the  $C_p(T)/T$  per  $\text{Cu}_2(\text{OH})[\text{VO}_4]$  data with respect to the magnetic and phonon contribution.  $S_m(T)$  is obtained by integrating  $C_m(T)/T$  and given for the temperature range from 2 K to 17 K. Within the range of the anomaly (6 - 17 K) the magnetic entropy amounts to  $2.5 \text{ J mol}^{-1} \text{ K}^{-1}$ , which is comparable with the reported value of  $2.39 \text{ J mol}^{-1} \text{ K}^{-1}$  given by Zhang *et al.* [6] Note that there are in fact four different Cu positions in the structure,  $\text{Cu}_4(\text{OH})_2[\text{VO}_4]_2$ . Then  $\sim 5.0 \text{ J mol}^{-1} \text{ K}^{-1}$  of the magnetic

entropy released for the  $\lambda$ -anomaly, which is close to the value of  $R \ln(2S + 1)$  for the  $S = 1/2$  system. This result suggests the  $\lambda$ -anomaly is related to one Cu ( $S = 1/2$ ) out of four per structural formula unit. One might relate this finding to a “loose end” or terminal magnetic species attached to the present 2D lattice, Cu1. Tentatively, one might assign this to the structural feature of the terminal Cu1, which provides a weakly coupled moment inducing long-range order.

#### 4.7 Conclusions.

Single crystals of  $M_2(\text{OH})[\text{VO}_4]$  with  $X = \text{Mn}, \text{Cu}$  were synthesized via hydrothermal methods. We determined the crystal structure of  $\text{Mn}_2(\text{OH})[\text{VO}_4]$  in the centrosymmetric space group  $Pnma$ . [7] The acentric  $\text{Cu}_2(\text{OH})[\text{VO}_4]$  polymorph was confirmed to crystallize in the space group  $P2_12_12_1$  in agreement with Zhang *et al.* [6] Additionally, we found unreported twinning for the  $\text{Cu}_2(\text{OH})[\text{VO}_4]$ , which interestingly has the same value as the ambiguous Flack-parameter reported by Zhang *et al* [6]. It should be noted that the twinning proposed here might be considered to be an intrinsic property and yet not fully understood. Our powder diffraction data is in line with this twinned structure solution, whereas the comparison of the “untwinned” structure model gives an unsatisfactory intensity mismatch for our data and the presented diffractogram by Zhang *et al* [6]. We furthermore discussed the Hydrogen bonding in comparison between  $\text{Mn}_2(\text{OH})[\text{VO}_4]$  and  $\text{Cu}_2(\text{OH})[\text{VO}_4]$ . The magnetic properties of  $\text{Cu}_2(\text{OH})[\text{VO}_4]$  are determined and confirm the results reported by Zhang *et al.* [6] Here we propose based on an analysis of relevant magnetic orbitals a connectivity pattern to understand the underlying antiferromagnetic

short-range correlations within the layer. From the magnetic part of the specific heat the release of magnetic entropy is found close to a  $S=1/2$  system for the relevant entity based on structure considerations of  $\text{Mn}_4(\text{OH})_2[\text{VO}_4]_2$ .

#### 4.8 References.

- [1] Martin, F. D.; Müller-Buschbaum, Hk. *Z. Naturforsch. B*, **1994**, 49, 355.
- [2] Martin, F. D.; Müller-Buschbaum, Hk. *Z. Naturforsch. B*, **1994**, 49, 1141.
- [3] Oka, Y.; Yao, Takeshi; Yamamoto, N. *Mater. Res. Bull.*, **1997**, 32, 1201.
- [4] Yao, T.; Oka, Yoshio.; Yamamoto, N. *Inorg. Chim. Acta.*, **1995**, 238, 165.
- [5] Wu, C.; Lu, C.; Zhuang, H.; Huang, J. *Eur. J. Inorg. Chem.*, **2003**, 2867.
- [6] Zhang, S.-Y.; He, Z.-Z.; Yang, M.; Guoa, W.-B.; Tang, Y.-Y. *Dalton Trans.*, **2014**, 43, 3521.
- [7] Sun, K.; Möller, A. *Acta Crystallogr. E*, **2014**, 70, i33.
- [8] Wang, X.; Liu, L.; Jacobson, A. J. *Z. Anorg. Allg. Chem.*, **1998**, 624, 1977.
- [9] Đorević, T., Stojanović, J.; Karanović, L. *Acta Cryst. E*, **2010**, 66, i79.
- [10] Oka, Y.; Yao, T.; Yamamoto, N. *J. Solid State Chem.*, **1990**, 89, 372.
- [11] Englman, R. *Jahn-Teller Effect in Molecules and Crystals*, John Wiley & Sons Ltd, **1972**.
- [12] Debye, P.; *Annalen der Physik (Leipzig)*, **1912**, 39, 789.
- [13] Kittel, C. *Introduction to Solid State Physics*, Wiley, New York, **2005**.



#### 4.9 Supplemental Material.

S-1:

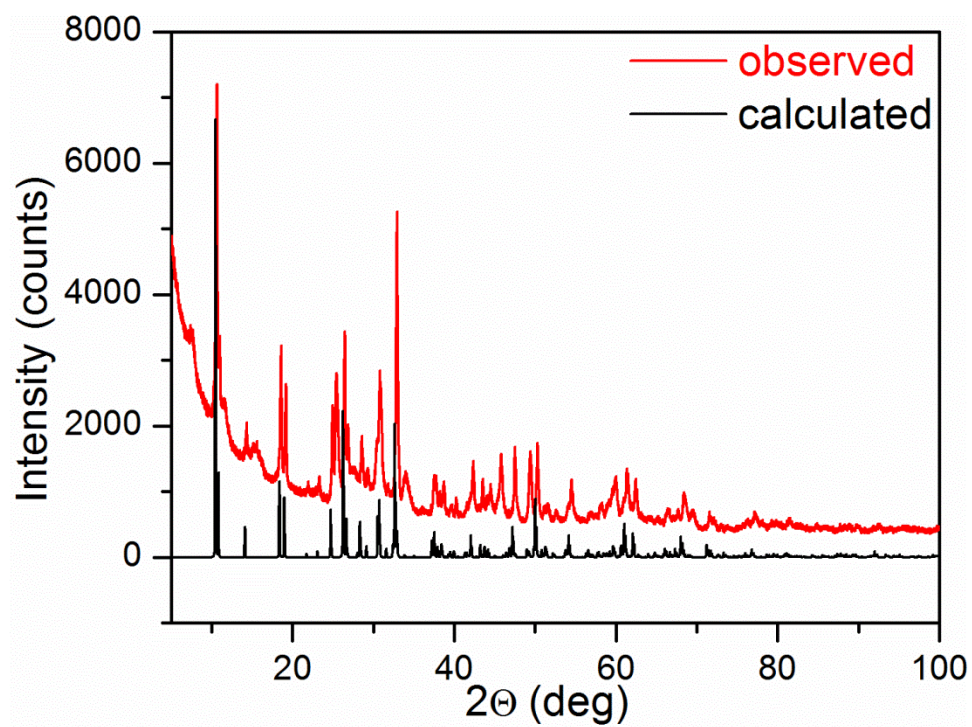


Figure 4.21. Powder XRD data for  $\text{H}_2\text{V}_3\text{O}_8$ . Observed (red), calculated (black).

S-2: Table 4.5. Fractional atomic coordinates and isotropic or equivalent isotropic displacement parameters ( $\text{\AA}^2$ ) for  $\text{Mn}_2(\text{OH})[\text{VO}_4]$  (*Pnma*).

	<i>Wyckoff</i>	<i>x</i>	<i>y</i>	<i>z</i>	$U_{\text{iso}}^*/U_{\text{eq}}$
Mn1	<i>4c</i>	0.07126(4)	0.2500	0.08355(7)	0.0116(1)
Mn2	<i>4c</i>	0.28875(4)	0.2500	0.15984(6)	0.0105(1)
Mn3	<i>8d</i>	0.36181(3)	0.00226(7)	−0.12336(5)	0.01003(9)
V1	<i>4c</i>	0.42573(4)	0.7500	0.18749(7)	0.0072(1)
V2	<i>4c</i>	0.16571(4)	0.7500	0.02724(7)	0.0069(1)
O11	<i>8d</i>	0.3790(1)	0.5171(3)	0.1122(2)	0.0134 (4)
O12	<i>4c</i>	0.0956(2)	0.2500	−0.1322(3)	0.0170 (6)
O13	<i>4c</i>	0.4610(2)	0.2500	−0.1544(3)	0.0137 (6)
O21	<i>8d</i>	0.17131(1)	−0.0131(3)	0.1339(2)	0.0111 (4)
O22	<i>4c</i>	−0.0666(2)	0.2500	0.0537(4)	0.0189 (6)
O23	<i>4c</i>	0.2522(2)	0.2500	0.3867(3)	0.0082 (5)
O3	<i>4c</i>	0.2751(2)	0.2500	−0.0716(3)	0.0100 (5)
H3	<i>4c</i>	0.2151(2)	0.2500	−0.110(5)	0.015*
O4	<i>4c</i>	0.0539(2)	0.2500	0.3099(3)	0.0106 (5)
H4	<i>4c</i>	−0.008(2)	0.2500	0.341(5)	0.016*

S-2: Table 4.6. Fractional atomic coordinates and isotropic or equivalent isotropic displacement parameters ( $\text{\AA}^2$ ) for  $\text{Cu}_2(\text{OH})[\text{VO}_4]$  ( $P2_12_12_1$ ).

	<i>Wyckoff</i>	<i>x</i>	<i>y</i>	<i>z</i>	$U_{\text{iso}}^*/U_{\text{eq}}$
Cu1	4 <i>a</i>	0.2250(3)	0.6632(1)	0.07317(6)	0.0240(3)
Cu2	4 <i>a</i>	0.7360(2)	0.1022(1)	0.21500(6)	0.0129(2)
Cu3	4 <i>a</i>	0.9693(2)	0.3779(1)	0.13632(7)	0.0128(3)
Cu4	4 <i>a</i>	0.47631(2)	0.3802(1)	0.13971(7)	0.0127(3)
V1	4 <i>a</i>	0.2162(2)	0.0622(1)	0.07988(8)	0.0100(3)
V2	4 <i>a</i>	0.2720(2)	0.2223(1)	0.34436(8)	0.0101(3)
O11	4 <i>a</i>	−0.027(1)	0.1480(8)	0.1216(5)	0.018(1)
O12	4 <i>a</i>	0.228(1)	−0.1286(6)	0.1122(4)	0.017(1)
O13	4 <i>a</i>	0.216(1)	0.0755(8)	−0.0311(4)	0.021(1)
O14	4 <i>a</i>	0.445(1)	0.1539(8)	0.1215(5)	0.019(1)
O21	4 <i>a</i>	0.037(1)	0.1075(8)	0.3318(4)	0.018(1)
O22	4 <i>a</i>	0.279(1)	0.2918(6)	0.4476(4)	0.020(1)
O23	4 <i>a</i>	0.253(1)	0.3786(6)	0.2712(4)	0.014(1)
O24	4 <i>a</i>	0.517(1)	0.1086(8)	0.3242(4)	0.015(1)
O3	4 <i>a</i>	0.730(1)	0.3278(6)	0.2150(3)	0.012(1)
H3	4 <i>a</i>	0.7079	0.3749	0.2713	0.018*
O4	4 <i>a</i>	0.226(1)	0.4357(6)	0.0621(4)	0.012(1)
H4	4 <i>a</i>	0.2032	0.4037	0.0000	0.017*

S-3: Table 4.7. Selected Interatomic Distances (Å) for Mn<sub>2</sub>(OH)[VO<sub>4</sub>] (*Pnma*).

Mn1—O12	2.010(3)	Mn2—O3	2.131(3)	Mn3—O3	2.049(2)
Mn1—O22	2.074(3)	Mn2—O23	2.149(3)	Mn3—O4 <sup>ii</sup>	2.083(2)
Mn1—O4	2.091(3)	Mn2—O11	2.162(2)	Mn3—O13	2.137(2)
Mn1—O21 <sup>i</sup>	2.243(2)	Mn2—O11 <sup>i</sup>	2.162(2)	Mn3—O11 <sup>i</sup>	2.177(2)
Mn1—O21	2.243(2)	Mn2—O21	2.391(2)	Mn3—O21 <sup>ii</sup>	2.279(2)
V1—O12 <sup>iii</sup>	1.683(3)	V1—O11	1.731(2)		
V1—O13 <sup>iv</sup>	1.717(3)	V1—O11 <sup>v</sup>	1.731(2)		
V2—O22 <sup>vi</sup>	1.654(3)	V2—O21 <sup>i</sup>	1.751(2)		
V2—O21 <sup>vii</sup>	1.751(2)	V2—O23 <sup>viii</sup>	1.777(3)		

Symmetry codes: (i)  $x, -y+1/2, z$ ; (ii)  $-x+1/2, -y, z-1/2$ ; (iii)  $x, -y-1/2, z$ ; (iv)  $-x+1/2, -y+1, z+1/2$ ; (v)  $-x+1, -y+1, -z$ ; (vi)  $x, -y+3/2, z$ ; (vii)  $-x, -y+1, -z$ ; (viii)  $x, y+1, z$ ; (ix)  $-x+1/2, -y+1, z-1/2$ ; (x)  $x, y-1, z$ ; (xi)  $-x+1/2, -y, z+1/2$ ; (xii)  $-x+1/2, y+1/2, z+1/2$ .

S-3: Table 4.8. Selected Interatomic Distances (Å) for Cu<sub>2</sub>(OH)[VO<sub>4</sub>] (*P*2<sub>1</sub>2<sub>1</sub>2<sub>1</sub>).

Cu1—O12 <sup>i</sup>	1.875(5)	Cu2—O23 <sup>vi</sup>	1.926(5)	Cu3—O3	1.916(6)
Cu1—O22 <sup>ii</sup>	1.917(6)	Cu2—O3	1.931(5)	Cu3—O4 <sup>vii</sup>	1.975(6)
Cu1—O4	1.954(5)	Cu2—O11 <sup>vii</sup>	2.041(7)	Cu3—O11 <sup>vii</sup>	1.980(7)
Cu1—O21 <sup>iii</sup>	2.185(7)	Cu2—O24	2.103(6)	Cu3—O21 <sup>iv</sup>	2.022(7)
Cu1—O24 <sup>iv</sup>	2.238(7)	Cu2—O14	2.293(7)	Cu3—O13 <sup>viii</sup>	2.234(6)
Cu1 <sup>ix</sup> —O12	1.875(5)	Cu2 <sup>v</sup> —O11	2.041(7)	Cu3 <sup>v</sup> —O11	1.980(7)
Cu1 <sup>xi</sup> —O22	1.917(6)	Cu2 <sup>iv</sup> —O23	1.926(5)	Cu3 <sup>x</sup> —O13	2.234(6)
Cu1 <sup>vi</sup> —O24	2.238(7)	Cu2—O23 <sup>vi</sup>	1.926(5)	Cu3 <sup>vi</sup> —O21	2.022(7)
Cu1 <sup>xii</sup> —O21	2.185(7)	Cu2—O3	1.931(5)	Cu3 <sup>v</sup> —O4	1.975(6)
Cu4—O3	1.957(6)	V1—O13	1.664(6)	V2—O22	1.655(6)
Cu4—O14	1.965(7)	V1—O12	1.704(5)	V2—O23	1.732(5)
Cu4—O4	1.965(6)	V1—O14	1.710(7)	V2—O21	1.737(7)
Cu4—O24 <sup>iv</sup>	2.028(7)	V1—O11	1.760(6)	V2—O24	1.801(7)
Cu4—O13 <sup>viii</sup>	2.210(7)				
Cu4—O23	2.387(6)				
Cu4 <sup>x</sup> —O13	2.210(6)				
Cu4 <sup>vi</sup> —O24	2.028(7)				

Symmetry codes: (i)  $x, y+1, z$ ; (ii)  $-x+1/2, -y+1, z-1/2$ ; (iii)  $-x, y+1/2, -z+1/2$ ; (iv)  $-x+1, y+1/2, -z+1/2$ ; (v)  $x-1, y, z$ ; (vi)  $-x+1, y-1/2, -z+1/2$ ; (vii)  $x+1, y, z$ ; (viii)  $x+1/2, -y+1/2, -z$ ; (ix)  $x, y-1, z$ ; (x)  $x-1/2, -y+1/2, -z$ ; (xi)  $-x+1/2, -y+1, z+1/2$ ; (xii)  $-x, y-1/2, -z+1/2$ .

S-4: Table 4.9. Selected angles (°) for Mn<sub>2</sub>(OH)[VO<sub>4</sub>] (*Pnma*).

O12—Mn1—O22	92.8(1)	O4 <sup>ii</sup> —Mn3—O21 <sup>ii</sup>	82.29(9)
O12—Mn1—O4	176.7(1)	O13—Mn3—O21 <sup>ii</sup>	90.0(1)
O22—Mn1—O4	90.5(1)	O11 <sup>i</sup> —Mn3—O21 <sup>ii</sup>	174.06(7)
O12—Mn1—O21 <sup>i</sup>	94.73(8)	O11 <sup>i</sup> —Mn3—O23 <sup>ii</sup>	90.60(9)
O22—Mn1—O21 <sup>i</sup>	133.34(5)	O21 <sup>ii</sup> —Mn3—O23 <sup>ii</sup>	84.16(8)
O4—Mn1—O21 <sup>i</sup>	82.99(7)	O12 <sup>iv</sup> —V1—O13 <sup>v</sup>	111.1(2)
O12—Mn1—O21	94.73(8)	O12 <sup>iv</sup> —V1—O11	108.39(9)
O22—Mn1—O21	133.34(5)	O13 <sup>v</sup> —V1—O11	109.04(9)
O4—Mn1—O21	82.99(7)	O12 <sup>iv</sup> —V1—O11 <sup>vi</sup>	108.39(9)
O21 <sup>i</sup> —Mn1—O21	91.8(1)	O13 <sup>v</sup> —V1—O11 <sup>vi</sup>	109.04(9)
O3—Mn2—O23	159.8(1)	O11—V1—O11 <sup>vi</sup>	110.9(1)
O3—Mn2—O11	81.85(7)	O22 <sup>vii</sup> —V2—O21 <sup>viii</sup>	107.05(9)
O23—Mn2—O11	110.69(7)	O22 <sup>vii</sup> —V2—O21 <sup>i</sup>	107.05(9)
O3—Mn2—O11 <sup>i</sup>	81.85 (7)	O21 <sup>viii</sup> —V2—O21 <sup>i</sup>	111.9(1)
O23—Mn2—O11 <sup>i</sup>	110.69 (7)	O22 <sup>vii</sup> —V2—O23 <sup>ix</sup>	106.9(2)
O11—Mn2—O11 <sup>i</sup>	98.3(1)	O21 <sup>viii</sup> —V2—O23 <sup>ix</sup>	111.82(8)
O3—Mn2—O21	80.28(7)	O21 <sup>i</sup> —V2—O23 <sup>ix</sup>	111.82(8)
O23—Mn2—O21	84.84(7)	Mn2—O11—Mn3 <sup>i</sup>	94.93(8)
O11—Mn2—O21	160.92(7)	Mn3—O13—Mn3 <sup>i</sup>	90.4(1)
O11 <sup>i</sup> —Mn2—O21	85.76(7)	Mn1—O21—Mn3 <sup>xi</sup>	92.06(7)
O3—Mn2—O21 <sup>i</sup>	80.28(7)	Mn1—O21—Mn2	91.37(7)
O23—Mn2—O21 <sup>i</sup>	84.84(7)	Mn3 <sup>xi</sup> —O21—Mn2	92.42(7)
O11—Mn2—O21 <sup>i</sup>	85.76(7)	Mn2—O23—Mn3 <sup>xi</sup>	98.57(9)

Table 4.9. Continued.

O11 <sup>i</sup> —Mn2—O21 <sup>i</sup>	160.92(7)	Mn2—O23—Mn3 <sup>xii</sup>	98.57(9)
O21—Mn2—O21 <sup>i</sup>	84.7(1)	Mn3 <sup>xi</sup> —O23—Mn3 <sup>xii</sup>	84.45 (9)
O3—Mn3—O4 <sup>ii</sup>	176.1(1)	Mn3 <sup>i</sup> —O3—Mn3	95.5(1)
O3—Mn3—O13	86.67(8)	Mn3 <sup>i</sup> —O3—Mn2	99.8(1)
O4 <sup>ii</sup> —Mn3—O13	94.01(8)	Mn3—O3—Mn2	99.8(1)
O3—Mn3—O11 <sup>i</sup>	83.40(9)	Mn3 <sup>xii</sup> —O4—Mn3 <sup>xi</sup>	95.7(1)
O4 <sup>ii</sup> —Mn3—O11 <sup>i</sup>	100.35(9)	Mn3 <sup>xii</sup> —O4—Mn1	102.5(1)
O13—Mn3—O11 <sup>i</sup>	95.1(1)	Mn3 <sup>xi</sup> —O4—Mn1	102.5(1)
O3—Mn3—O21 <sup>ii</sup>	93.88(9)		

Symmetry codes: (i)  $x, -y+1/2, z$ ; (ii)  $-x+1/2, -y, z-1/2$ ; (iii)  $x, -y-1/2, z$ ; (iv)  $-x+1/2, -y+1, z+1/2$ ; (v)  $-x+1, -y+1, -z$ ; (vi)  $x, -y+3/2, z$ ; (vii)  $-x, -y+1, -z$ ; (viii)  $x, y+1, z$ ; (ix)  $-x+1/2, -y+1, z-1/2$ ; (x)  $x, y-1, z$ ; (xi)  $-x+1/2, -y, z+1/2$ ; (xii)  $-x+1/2, y+1/2, z+1/2$ .

S-4: Table 4.10. Selected angles (°) for Cu<sub>2</sub>(OH)[VO<sub>4</sub>] (*P*2<sub>1</sub>2<sub>1</sub>2<sub>1</sub>).

O12 <sup>i</sup> —Cu1—O22 <sup>ii</sup>	96.5(3)	O3—Cu4—O13 <sup>viii</sup>	87.0(2)
O12 <sup>i</sup> —Cu1—O4	166.7(2)	O14—Cu4—O13 <sup>viii</sup>	97.5(3)
O22 <sup>ii</sup> —Cu1—O4	96.8(2)	O4—Cu4—O13 <sup>viii</sup>	91.7(2)
O12 <sup>i</sup> —Cu1—O21 <sup>iii</sup>	90.6(3)	O24 <sup>iv</sup> —Cu4—O13 <sup>viii</sup>	91.0(2)
O22 <sup>ii</sup> —Cu1—O21 <sup>iii</sup>	132.3(3)	O3—Cu4—O23	88.2(2)
O4—Cu1—O21 <sup>iii</sup>	80.8(3)	O14—Cu4—O23	93.1(3)
O12 <sup>i</sup> —Cu1—O24 <sup>iv</sup>	88.8(3)	O4—Cu4—O23	93.0(2)
O22 <sup>ii</sup> —Cu1—O24 <sup>iv</sup>	136.2(3)	O24 <sup>iv</sup> —Cu4—O23	78.3(2)
O4—Cu1—O24 <sup>iv</sup>	81.2(2)	O13 <sup>viii</sup> —Cu4—O23	168.0(2)
O21 <sup>iii</sup> —Cu1—O24 <sup>iv</sup>	90.9(2)	O13—V1—O12	110.4(3)
O23 <sup>vi</sup> —Cu2—O3	173.8(2)	O13—V1—O14	109.5(4)
O23 <sup>vi</sup> —Cu2—O11 <sup>vii</sup>	103.9(3)	O12—V1—O14	107.7(3)
O3—Cu2—O11 <sup>vii</sup>	79.7(3)	O13—V1—O11	108.9(3)
O23 <sup>vi</sup> —Cu2—O24	88.0(2)	O12—V1—O11	109.5(3)
O3—Cu2—O24	87.8(3)	O14—V1—O11	110.9(3)
O11 <sup>vii</sup> —Cu2—O24	165.8(3)	Cu3 <sup>v</sup> —O11—Cu2 <sup>v</sup>	96.1(3)
O23 <sup>vi</sup> —Cu2—O14	106.4(2)	Cu4—O14—Cu2	91.8(3)
O3—Cu2—O14	78.0(2)	Cu4 <sup>x</sup> —O13—Cu3 <sup>x</sup>	84.4(2)
O11 <sup>vii</sup> —Cu2—O14	95.0(3)	O22—V2—O23	108.3(3)
O24—Cu2—O14	89.1(3)	O22—V2—O21	108.9(3)
O3—Cu3—O4 <sup>vii</sup>	176.2(2)	O23—V2—O21	108.3(3)
O3—Cu3—O11 <sup>vii</sup>	81.6(2)	O22—V2—O24	109.3(3)
O4 <sup>vii</sup> —Cu3—O11 <sup>vii</sup>	100.2(2)	O23—V2—O24	111.5(3)



Table 4.10. Continued.

O3—Cu3—O21 <sup>iv</sup>	93.3(2)	O21—V2—O24	110.5(3)
O4 <sup>vii</sup> —Cu3—O21 <sup>iv</sup>	84.6(2)	Cu2 <sup>iv</sup> —O23—Cu4	93.6(2)
O11 <sup>vii</sup> —Cu3—O21 <sup>iv</sup>	172.7(3)	Cu3 <sup>vi</sup> —O21—Cu1 <sup>xii</sup>	92.5(3)
O3—Cu3—O13 <sup>viii</sup>	87.3(2)	Cu4 <sup>vi</sup> —O24—Cu2	99.8(3)
O4 <sup>vii</sup> —Cu3—O13 <sup>viii</sup>	95.8(2)	Cu4 <sup>vi</sup> —O24—Cu1 <sup>vi</sup>	90.3(3)
O11 <sup>vii</sup> —Cu3—O13 <sup>viii</sup>	96.1(3)	Cu2—O24—Cu1 <sup>vi</sup>	95.7(3)
O21 <sup>iv</sup> —Cu3—O13 <sup>viii</sup>	88.8(3)	Cu1—O4—Cu4	101.2(3)
O3—Cu4—O14	86.0(2)	Cu1—O4—Cu3 <sup>v</sup>	101.5(3)
O3—Cu4—O4	178.6(2)	Cu4—O4—Cu3 <sup>v</sup>	102.4(2)
O14—Cu4—O4	94.7(3)	Cu3—O3—Cu2	102.1(3)
O3—Cu4—O24 <sup>iv</sup>	93.0(2)	Cu3—O3—Cu4	100.9(2)
O14—Cu4—O24 <sup>iv</sup>	171.3(3)	Cu2—O3—Cu4	104.1(3)
O4—Cu4—O24 <sup>iv</sup>	86.5(2)		

Symmetry codes: (i)  $-x, y+1/2, -z+3/2$ ; (ii)  $x, y+1, z$ ; (iii)  $x+1, y, z$ ; (iv)  $x+1, y+1, z$ ; (v)  $-x, y-1/2, -z+3/2$ ; (vi)  $x+1/2, -y+1/2, -z+1$ ; (vii)  $-x-1/2, -y+1, z-1/2$ ; (viii)  $-x-1, y-1/2, -z+3/2$ ; (ix)  $x-1, y, z$ ; (x)  $x-1, y-1, z$ ; (xi)  $x, y-1, z$ ; (xii)  $x-1/2, -y+1/2, -z+1$ ; (xiii)  $-x-1/2, -y+1, z+1/2$ ; (xiv)  $-x-1, y+1/2, -z+3/2$ .

## Chapter Five

### Synthesis, Crystal Structures, and Physical Properties of a Unique Canted

#### Antiferromagnet: $\text{BaMn}_9[\text{VO}_4]_6(\text{OH})_2^*$

##### 5.1 Introduction.

Magnetic materials with unique structural features often give rise to unusual magnetic behavior. Recently, multiferroics have drawn much attention because they exhibit magnetic ordering with a spontaneous electric polarization. [1-5] Related compounds were obtained through a solid-state approach guided by theoretical work. [4] Examples are transition metal oxides such as  $\text{CaBaCo}_4\text{O}_7$  (noncollinear ferrimagnet), [6, 7]  $\text{RbFe}[\text{MoO}_4]_2$ , [8, 9] or  $\text{A} \text{Ag}_2\text{Fe}[\text{VO}_4]_2$  with  $\text{A} = \text{K}$  or  $\text{Rb}$  ( $120^\circ$  chiral and helical magnetic order), [10] and  $\text{Cu}_2\text{OSeO}_3$  (skyrmion phase). [11-13]

In Chapter Three, barium copper vanadates,  $\text{Ba}_2\text{XCu}(\text{OH})[\text{V}_2\text{O}_7]$ ,  $\text{X} = \text{Cl}, \text{Br}$ , were reported. Here, a novel barium manganese vanadate,  $\text{BaMn}_9[\text{VO}_4]_6(\text{OH})_2$ , was also obtained by hydrothermal synthesis. There are not many compounds with the composition of  $\text{Ba}^{2+}\text{--Mn}^{2+}\text{--}[\text{VO}_4^{3-}]$  or  $\text{Mn}^{2+}\text{--}[\text{VO}_4^{3-}]\text{--}(\text{OH}^-)$  reported. Examples are  $\text{BaMn}[\text{VO}_4]_2$ , [14, 15] or  $\text{BaAg}_2\text{Mn}[\text{VO}_4]_2$ , [16, 17] and  $\text{Mn}_2(\text{OH})[\text{VO}_4]$ , [18]  $\text{Mn}_{7-2/3z}(\text{OH})_3[\text{VO}_4]_{4-2z}[\text{V}_2\text{O}_7]_z$  with  $z \approx 0.199(3)$ , [19] or  $\text{PbMn}[\text{VO}_4](\text{OH})$ . [20] Comparing these compounds,  $\text{BaMn}_9[\text{VO}_4]_6(\text{OH})_2$  stands out because it contains vanadate and hydroxide anions as well as being a Mn-rich compound.  $\text{CaMn}_7\text{O}_{12}$ , a

\*This chapter has been previously published: Sun, K.; Livinchuk, A. P.; Tapp, J.; Lorenz, B. Möller, A. *Inorg. Chem.*, DOI: 10.1021/ic502266k.

perovskite-type material exhibits giant polarization and magneto-orbital helices. [21, 22]  $\text{BaMn}_9[\text{VO}_4]_6(\text{OH})_2$  crystallizes in a cubic structure and symmetry restrained equilateral triangles consist of magnetic ions. This structure feature in combination with being an antiferromagnet causes the so-called geometrical frustration, pertaining to the typical multiferroics with either  $\text{Mn}^{2+}$  or  $\text{Fe}^{3+}$  ions ( $S = 5/2$ ). [4, 5] Thus,  $\text{BaMn}_9[\text{VO}_4]_6(\text{OH})_2$  was selected as a unique canted antiferromagnet to study potential magneto-dielectric coupling or even multiferroic properties.

Previously, only the structure of the natural mineral nabiasite,  $\text{BaMn}_9[(\text{V},\text{As})\text{O}_4]_6(\text{OH})_2$  was reported. [23] In our work, hydrothermal synthesis, re-determined crystal structure, the spectroscopic properties, and physical properties are studied and structure-property relationships are discussed.

## **5.2 Synthesis of Single Crystals of $\text{BaMn}_9[\text{VO}_4]_6(\text{OH})_2$ .**

Single crystals of  $\text{BaMn}_9[\text{VO}_4]_6(\text{OH})_2$  were synthesized by hydrothermal methods using 0.5 mmol of  $\text{NH}_4\text{VO}_3$ , 0.75 mmol of  $\text{MnCl}_2$ , 0.5 mmol of  $\text{Ba}(\text{Ac})_2$  and 2.5 mmol of  $\text{LiCl}$  as starting materials in a molar ratio of 1:1.5:1:5. All starting materials were then mixed together with distilled water in a Teflon liner. Drops of concentrated  $\text{NH}_3 \cdot \text{H}_2\text{O}$  were used to adjust the pH of the system strictly between 7.8 and 8.2. The total volume of the aqueous solution was 10 ml and 12 ml Teflon-lined stainless steel autoclave was used. The reaction was carried out at 220 °C for 3 - 4 days and cooled with a standard cooling procedure as we discussed in Chapter Two.

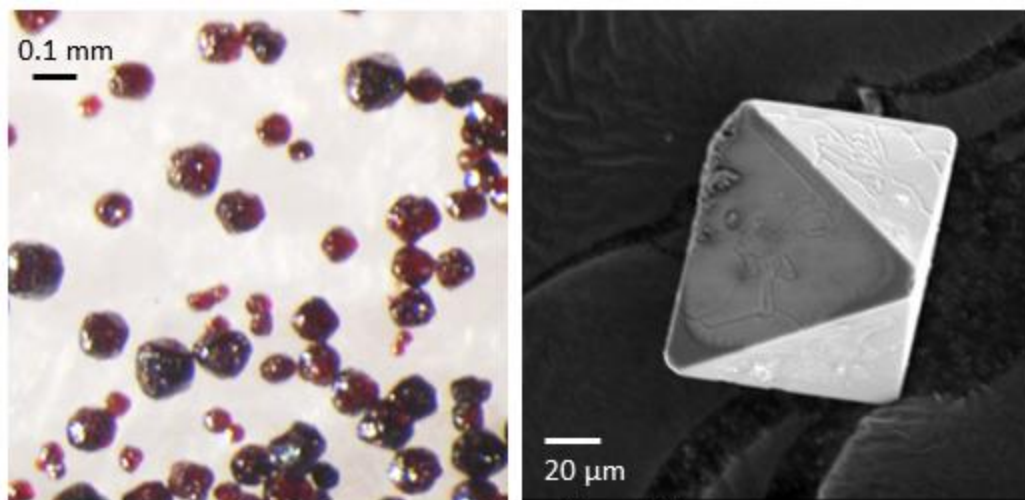


Figure 5.1. *Left:* Photo of magnified  $\text{BaMn}_9[\text{VO}_4]_6(\text{OH})_2$  crystals. *Right:* SEM picture of the carbon-coated sample showing one octahedral block-shaped crystal of  $\text{BaMn}_9[\text{VO}_4]_6(\text{OH})_2$ .

The final pH of the mother liquid dropped below 4, indicating that the crystalline product contains hydroxide. The dark red crystals were collected by filtering, washed with distilled water several times, and then dried naturally in the hood overnight. The crystals were block-shaped with a diameter of approximately 0.1 mm on average as shown in Figure 5.1 - left.

Photos of magnified crystals with polarized light were taken. From our observation, weak red spots were still shown under cross-polarized light ( $90^\circ$ ). However, no polarization is expected for a cubic centrosymmetric structure, which is supposed to lead to complete extinction. This result indicates a possible accentric space group.

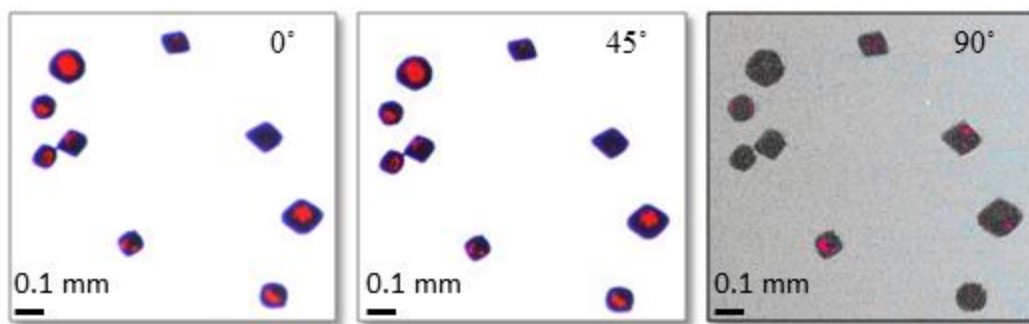


Figure 5.2. Photos with polarized light under different angles of magnified  $\text{BaMn}_9[\text{VO}_4]_6(\text{OH})_2$  crystals. From left to right, angles are  $0^\circ$ ,  $45^\circ$ , and  $90^\circ$ .

### 5.3 Scanning Electron Microscopy-Energy Dispersive X-ray Spectroscopy (SEM-EDX) of $\text{BaMn}_9[\text{VO}_4]_6(\text{OH})_2$ .

Table 5.1. Atomic composition for  $\text{BaMn}_9[\text{VO}_4]_6(\text{OH})_2$ .

$\text{BaMn}_9[\text{VO}_4]_6(\text{OH})_2$	Ba	Mn	V
Stoichiometry	1.0(1)	9.2(4)	5.8(2)

Energy Dispersive X-ray (EDX) analysis confirmed the composition ratio Ba/Mn/V of 1 : 9 : 6 based on average values from 22 measured spots. (Table 5.5 in the supplemental material) The SEM picture in Figure 5.1 - right shows the octahedral shape of a carbon-coated crystal. The calculated stoichiometry is shown in Table 5.1.

#### 5.4 Single Crystal X-ray Diffraction of $\text{BaMn}_9[\text{VO}_4]_6(\text{OH})_2$ .

Crystals were measured on a Bruker instrument. A dark red block-shaped crystal was selected. The structure was refined in both acentric space group  $P2_13$  and centrosymmetric space group  $Pa\bar{3}$ . The H atoms were refined using the AFIX 3 command and the ride-on constraint  $U_{\text{iso}}(\text{H}) = -1.5 \times U_{\text{aniso}}(\text{O})$ . For the refinement in  $P2_13$  the temperature factors of (pseudo-) symmetry related atoms were coupled by using EADP command to minimize correlation effects. Consequently, the number of refined independent parameters was reduced from 128 to 87. Structures were refined as described in Chapter 2. The specific crystallographic data and details are listed in Table 5.2. fractional atomic coordinates as well as isotropic or equivalent isotropic displacement parameters are listed in S-2, and selected interatomic distances and angles for both structure solutions are listed in S-3 and S-4 in the supplemental material.

The structure refinement as shown does not provide obvious evidence to determine which one of the two is the true space group. We used first principle calculations [24, 25] to determine the difference in energy between the two space groups. However, the total calculated difference between the two structure models of  $Pa\bar{3}$  and  $P2_13$  is 48 meV per unit cell (176 atoms), which is negligible. The centrosymmetric one of  $Pa\bar{3}$  is only slightly lower than the other one in energy. For simplicity reasons, we will discuss the crystal structure in the structure description section based on  $Pa\bar{3}$ .

Table 5.2. Crystal Data and Details of the Structure Determination for  $\text{BaMn}_9[\text{VO}_4]_6(\text{OH})_2$ .

Formula	$\text{BaMn}_9[\text{VO}_4]_6(\text{OH})_2$	
Mass/Formula unit ( $M_r$ )	1355.46 g mol <sup>-1</sup>	
Crystal system	cubic	
Space group	$Pa\bar{3}$	$P2_13$
Z	4	
Lattice constant	$a = 12.8417(2) \text{ \AA}$	
Volume	2117.7(1) Å <sup>3</sup>	
Density	4.251 g/cm <sup>3</sup>	
F (000)	2516	
$\mu$ (Mo K $\alpha$ )	9.61 mm <sup>-1</sup>	
Temperature	293K	
Crystal size	0.12 × 0.10 × 0.10 mm	
Range	$\theta_{\text{max}} = 28.326^\circ$ ; $\theta_{\text{min}} = 2.747^\circ$	$\theta_{\text{max}} = 28.326^\circ$ ; $\theta_{\text{min}} = 2.243^\circ$
Data set	$-17 < h < 13$ , $-16 < k < 17$ , $-14 < l < 17$	
$R_{\text{int}}$	0.044	
Measured reflections	11735	
Rejected reflections	807	none
Unique reflections	891	1555
Parameter refined	65	87
$R_1$ , $wR_2$ , GooF	0.018, 0.050, 1.25	0.022, 0.063, 1.15
( $T_{\text{min}}$ , $-T_{\text{max}}$ )	0.2081 - 0.3363	0.2084 - 0.3381

### 5. 5 Powder X-ray Diffraction and Refinement of $\text{BaMn}_9[\text{VO}_4]_6(\text{OH})_2$ .

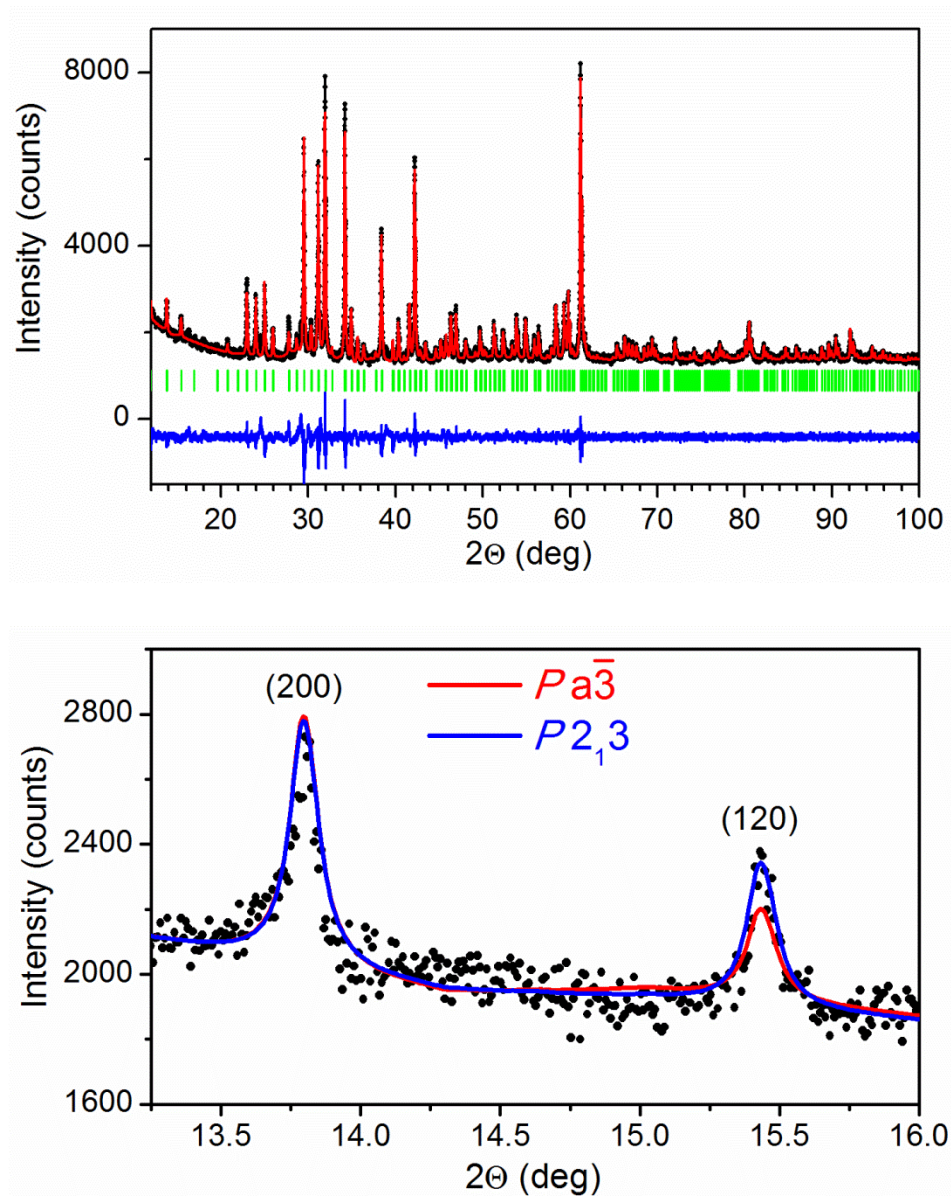


Figure 5.3. *Top*: Powder refinement data for  $\text{BaMn}_9[\text{VO}_4]_6(\text{OH})_2$ . Observed (black), calculated (red), Bragg positions (green) and difference (blue). *Bottom*: Difference in calculated intensities for the (120) reflection. Experimental data (black circles).



Table 5.3. Powder refinement results for  $\text{BaMn}_9[\text{VO}_4]_6(\text{OH})_2$ , Both space groups of  $Pa\bar{3}$  and  $P2_13$  are listed separately.

Space group	$Pa\bar{3}$	$P2_13$
Unit Cell (Å)	$a = 12.83629(5)$	$a = 12.83624(5)$
$\chi^2$ , $R_{\text{Bragg}}$ , $R_{\text{F}}$ -factor	3.31, 2.26, 1.96	3.23, 2.42, 2.24

Powder X-ray diffraction patterns were collected to confirm the phase purity and the structure model of the compounds. The sample was ground into fine powder from crystals. Powder refinement data for  $\text{BaMn}_9[\text{VO}_4]_6(\text{OH})_2$  are shown in Figure 5.3. The results of the refinements are listed in Table 5.3.

## 5.6 Crystal Structure Description and Discussion for $\text{BaMn}_9[\text{VO}_4]_6(\text{OH})_2$ .

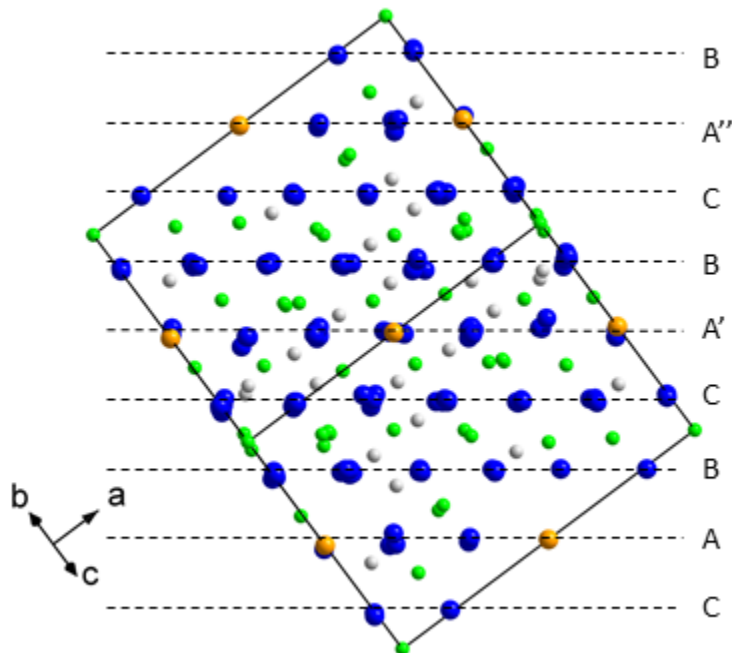


Figure 5.4. Unit cell of  $\text{BaMn}_9[\text{VO}_4]_6(\text{OH})_2$  with dashed lines showing the close-packing layers. Color theme: Ba (orange), Mn (green), V (grey), O (blue), H atoms not shown here.

The crystal structure of  $\text{BaMn}_9[\text{VO}_4]_6(\text{OH})_2$  can be described as a cubic close-packed (ccp) arrangement packed by  $\text{O}^{2-}$  anions and  $\text{Ba}^{2+}$  cations, which have similar ionic radii (stacking sequence  $\text{ABCA'BCA''BCA}\dots$ ). B and C layers, as labeled in Figure 5.4, contain only O atoms, while layers of A, A' or A'' consist of O and Ba atoms. Ba atoms are isolated from each other. As shown in Figure 5.5, Ba is located in a cube-octahedral

site with the coordination number of twelve. All the Ba atoms are isolated within the layer. The interatomic distance of Ba–O is approximately 3.0 Å on average. (Table 5.4)

Table 5.4. Selected Interatomic Distances and  $\text{O}^{\text{donor}}\text{--H}\cdots\text{O}^{\text{acceptor}}$  angle for  $\text{BaMn}_9[\text{VO}_4]_6(\text{OH})_2$  ( $Pa\bar{3}$ ).

Ba—O11 ( $\times 6$ )	2.857(2) Å	Mn1—O12 ( $\times 3$ )	2.144(1) Å
Ba—O12 ( $\times 6$ )	3.165(2) Å	Mn1—O14 ( $\times 3$ )	2.162(2) Å
V1—O11	1.679(2) Å	Mn2—O13 ( $\times 6$ )	2.172(2) Å
V1—O14	1.721(2) Å	Mn3—O1	2.119(1) Å
V1—O12	1.732(2) Å	Mn3—O11	2.123(2) Å
V1—O13	1.769(2) Å	Mn3—O13	2.167(1) Å
O1—H1	0.95 Å	Mn3—O14	2.176(2) Å
H1 $\cdots$ O14	2.46 Å	Mn3—O12	2.204(2) Å
O1 $\cdots$ O14 ( $\times 3$ )	3.179(3) Å	Mn3—O13'	2.452(1) Å
O1—H1 $\cdots$ O14	132°		

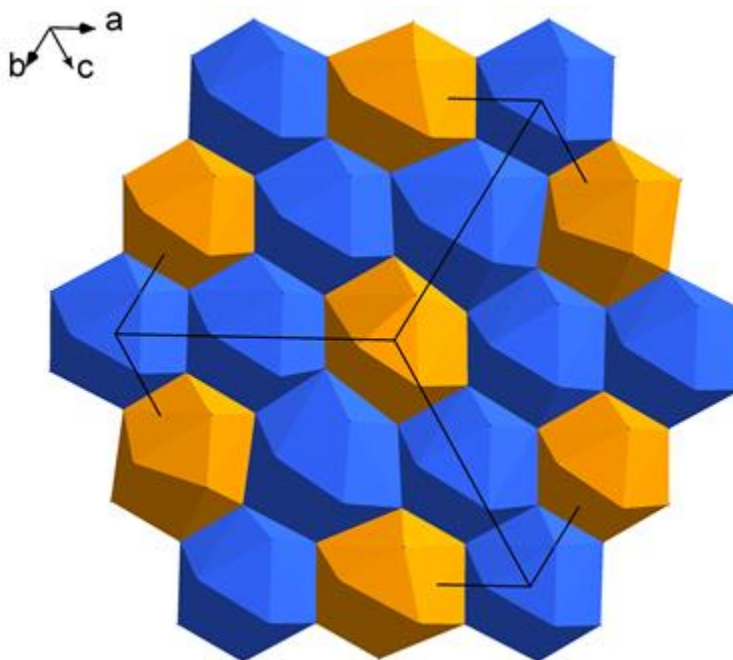


Figure 5.5. Close-packing arrangement (Ba/O): polyhedral for layer A central atoms are depicted. Color theme: Ba (orange), O (blue).

The ccp arrangement leaves octahedral and tetrahedral sites in between these packing layers. Mn atoms partially fill the octahedral sites and the tetrahedral voids are partially occupied by V atoms. The average interatomic distances,  $\text{Mn-O} \approx 2.18 \text{ \AA}$  and  $\text{V-O} = 1.73 \text{ \AA}$  are typical for  $\text{Mn}^{2+}$  and  $\text{V}^{5+}$  in their respective coordination spheres, see also Table 5.4 for selected distances. Mn3 is found in the center of a severely distorted octahedron with quite large deviation of Mn–O distances. The longest Mn–O is  $2.452(1) \text{ \AA}$ , much larger than the average. The distortion is caused by the hydroxide in the coordination sphere around Mn3. On the other hand, Mn1 and Mn2 have almost equal Mn–O distances and close to orthogonal O–Mn–O arrangement for  $O_h$  symmetry.

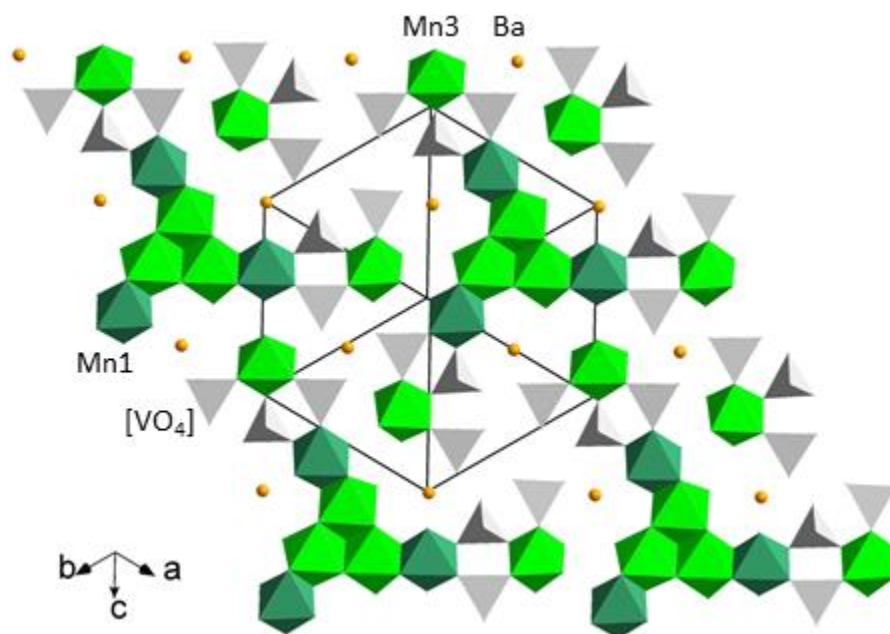


Figure 5.6. Occupancy of  $\text{O}_h$  (Mn) and  $\text{T}_d$  (V) sites in  $\text{BaMn}_9[\text{VO}_4]_6(\text{OH})_2$  adjacent to A-type layers.

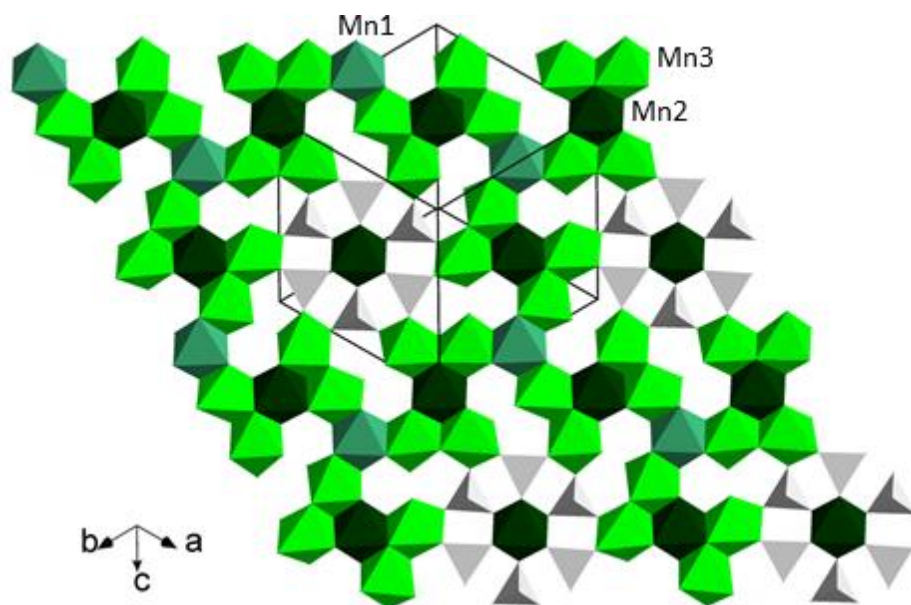


Figure 5.7. Occupancy of  $\text{O}_h$  (Mn) and  $\text{T}_d$  (V) sites in  $\text{BaMn}_9[\text{VO}_4]_6(\text{OH})_2$  adjacent to pure O-packing B and C layers.

As discussed, Mn and V atoms partially occupy the voids between the packing layers. The occupancy of both octahedral and tetrahedral sites differ for the sites adjacent to A-type layers with mixed O/Ba composition from those between exclusively O-contained ones (layers of B and C), see Figure 5.6 and 5.7. For the former,  $\text{Ba}^{2+}$  cations lead to unoccupied adjacent sites, leaving 25% octahedral sites occupied by Mn-centered polyhedra. As shown in Figure 5.6, fragments of edge-shared  $[\text{Mn}_{1,3}\text{O}_6]$ -polyhedra occur with the Mn(1)–Mn(3) distances of 3.05 Å. These fragments further connect via corners (O11) to  $[\text{VO}_4]$ -tetrahedra which provide a bridge to seemingly isolated Mn3-centered octahedra. This corner-shared O11 is exclusively connected to Mn3 in a terminal position. On the other hand, 50% occupancy of octahedral sites for Mn atoms is found for layers in between B and C. Here the Mn2 site with *Oh* symmetry are found either at isolated locations separated through exclusive connectivity to  $[\text{VO}_4]$ -tetrahedra, or are connected by edge-sharing to Mn3. The Mn2–Mn3 distances for neighboring octahedra are 3.22 Å. Overall, the structure forms a three-dimensional network with complex connectivity of edge-shared  $[\text{MnO}_6]$ -octahedra.

It is noteworthy that two interesting structural features are found for the Mn-O connectivity of this unique cubic structure (Figure 5.8). The first one is the centered isolated triangle Mn1–(Mn3)<sub>3</sub>, which is linked exclusively by O atoms from the  $[\text{VO}_4]$ -tetrahedra. (Figure 5.8 - left) The second feature is a double-cube consisting of (Mn3)<sub>3</sub>–Mn2–(Mn3)<sub>3</sub> entities. Again, the connectivity of Mn2–Mn3 involves only O from the  $[\text{VO}_4]$ -unit, See Figure 5.8 - right. Also notice that the  $\text{OH}^-$  group is capping three Mn3 atoms.

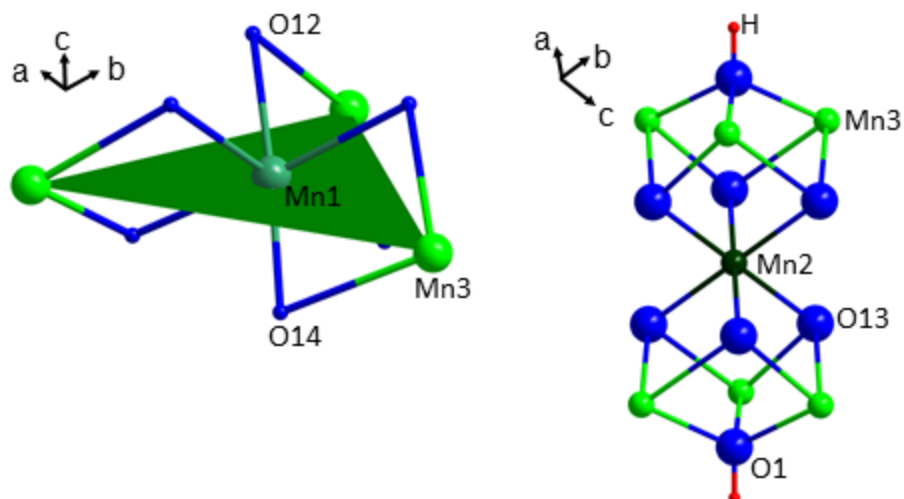


Figure 5.8. The two features of Mn–O–Mn connectivity with the center of Mn1 and Mn2.  
*Left:* centered triangle. *Right:* double-cube.

### 5.7 Spectroscopy for BaMn<sub>9</sub>[VO<sub>4</sub>]<sub>6</sub>(OH)<sub>2</sub>.

Infrared and Raman spectra are shown in Figure 5.9 and Figure 5.10, respectively. Stretching vibrational modes are found around 400 cm<sup>-1</sup> for Mn–O, in a similar region to the Cu–O stretching mode for Ba<sub>2</sub>XCu(OH)[V<sub>2</sub>O<sub>7</sub>], X = Cl, Br. The V–O stretching modes occur in the typical region around 700–900 cm<sup>-1</sup>. As shown in Table 5.4, the [VO<sub>4</sub>]<sup>3-</sup> units in the BaMn<sub>9</sub>[VO<sub>4</sub>]<sub>6</sub>(OH)<sub>2</sub> structure have a local symmetry of C<sub>1</sub>. It is expected to exhibit four fundamental V–O stretching modes, which should be both infrared and Raman active. [26] In the Raman spectrum, four significant bands are observed at 762 cm<sup>-1</sup>, 804 cm<sup>-1</sup>, 866 cm<sup>-1</sup>, and 879 cm<sup>-1</sup>. The highest intensity mode occurs at 804 cm<sup>-1</sup> and does not occur in the corresponding region in the infrared spectrum. Therefore, it can be assigned to the symmetric V–O stretching vibrational

mode. The mode at  $762\text{ cm}^{-1}$  in the Raman is found to be the most intensive mode in the infrared at  $760\text{ cm}^{-1}$ . The mode at  $866\text{ cm}^{-1}$  is seen as a shoulder in the infrared and showing moderate polarization in the Raman. The highest energy mode at  $879\text{ cm}^{-1}$  only occurs in cross-polarization (HV) in the Raman, whereas in the infrared a strong band is observed at  $877\text{ cm}^{-1}$ . Thus, we assign the three latter modes to the asymmetric V–O stretching vibrational modes. In the Raman spectra, there are two other weak bands observed in the low frequency region. The mode at  $\approx 322\text{ cm}^{-1}$  relates to the bending vibrations of the vanadate. The mode at  $\approx 200\text{ cm}^{-1}$  belongs to the lattice. Overall, the Raman mode frequencies are in excellent agreement with the non-polarized Raman spectrum reported earlier for the mineral nabiasite. [23]

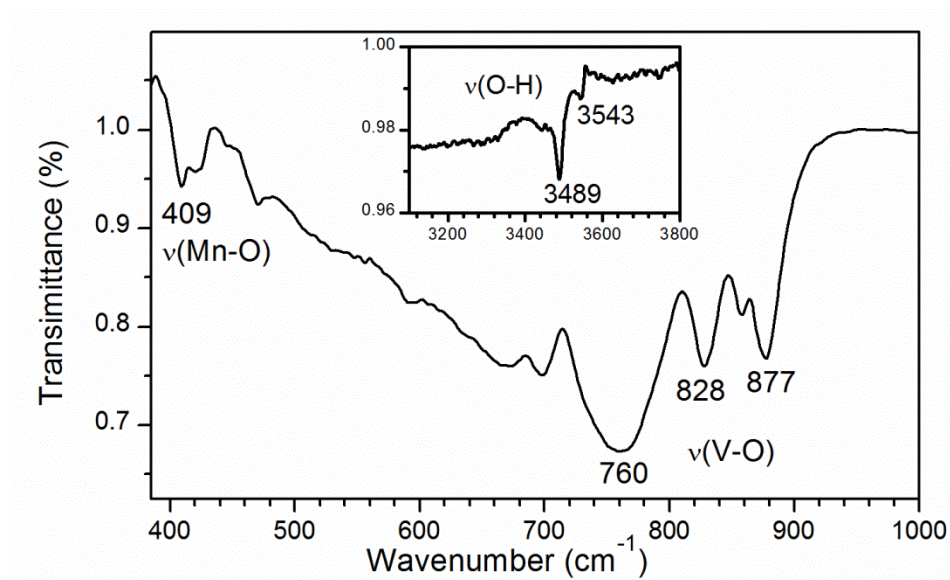


Figure 5.9. IR-spectrum for  $\text{BaMn}_9[\text{VO}_4]_6(\text{OH})_2$  in the spectral region of Mn–O and V–O stretching vibrations, *v.* *Inset:* In- and out-of phase O–H modes.



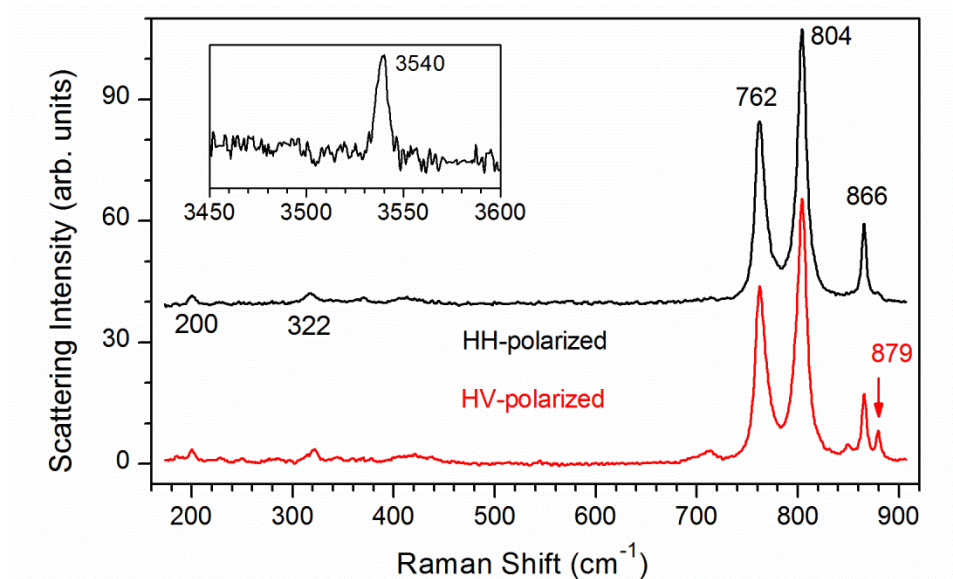


Figure 5.10. Single crystal Raman-spectrum for  $\text{BaMn}_9[\text{VO}_4]_6(\text{OH})_2$  for parallel (HH) and crossed (HV) polarizations of incident and scattered light. *Inset*: In-phase O–H mode.

Around  $3500\text{ cm}^{-1}$  is the typical region for O–H stretching and we found evidence of this in both infrared and Raman spectra. The vibrations of the hydroxide are observed at 3489 and  $3543\text{ cm}^{-1}$  in the infrared. Similar values have been reported for volborthite,  $\text{Cu}_3\text{V}_2\text{O}_7(\text{OH})_2 \cdot 2\text{H}_2\text{O}$ . [27] The red-shift of the stronger IR-mode (tentatively assigned to an out-of phase displacement) is often taken as an indicator for hydrogen bonding. [28] In comparison, typical “free”  $\text{OH}^-$  ions exhibit vibrations around  $3556\text{ cm}^{-1}$ . [29–31] Considering the geometric information (Table 5.4) and the relative red-shift,  $\Delta\nu(\text{O–H}) \approx -67\text{ cm}^{-1}$ , the interaction between the proton of the hydroxide and the vanadate is weak and dominantly of electrostatic origin. The  $\nu(\text{O–H})$  mode with higher frequency is detected also in the Raman and consequently assigned to an in-phase displacement.

## 5.8 Physical Properties of $\text{BaMn}_9[\text{VO}_4]_6(\text{OH})_2$ .

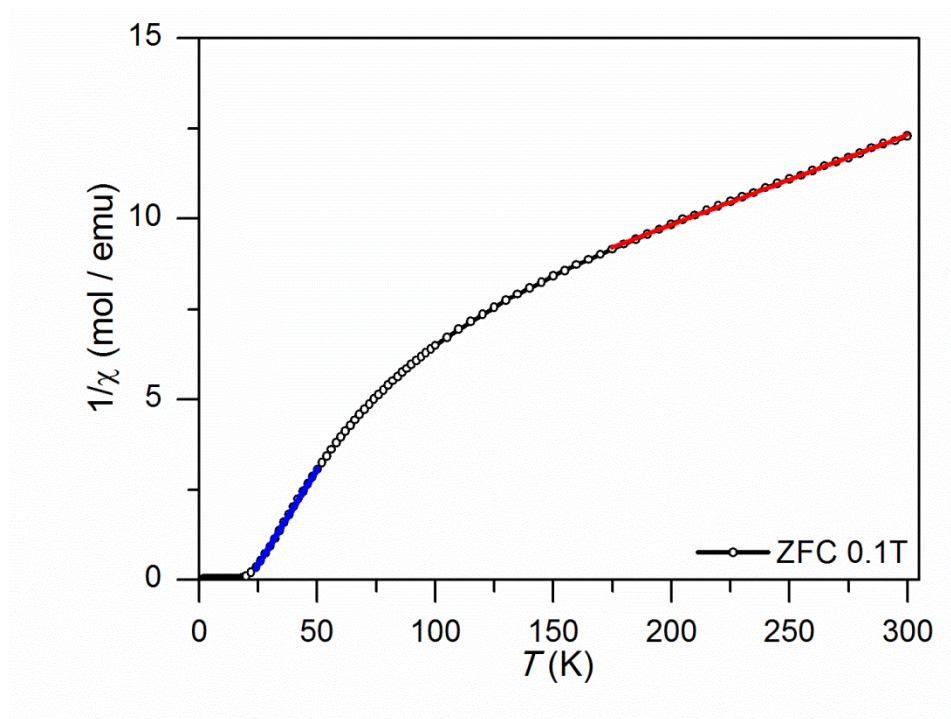


Figure 5.11. Inverse susceptibility data for  $\text{BaMn}_9[\text{VO}_4]_6(\text{OH})_2$  with fits the Curie–Weiss law.

There are in total nine magnetic Mn ions per unit cell of  $\text{BaMn}_9[\text{VO}_4]_6(\text{OH})_2$ . We first look at the inverse susceptibility. (Figure 5.11) The high temperature region of  $1/\chi(T)$  is fitted linearly to a Curie-Weiss law above 175 K. The Curie constant  $C^{\text{HT}}$  derived from the slope of a linear fit is  $40.11 \text{ emu K mol}^{-1}$  which matches the effective moment equivalent to the sum of nine paramagnetic  $\text{Mn}^{2+}$  per formula with  $S = 5/2$ . The calculated  $C^{\text{HT}}$  is  $39.39 \text{ emu K mol}^{-1}$ . The Weiss temperature,  $\Theta^{\text{HT}}$  is found from the intersection to be around  $-195 \text{ K}$ , indicating strong antiferromagnetic interactions.

Absence of an anomaly in the high temperature region around 200 K further confirms the presence of antiferromagnet short range order. At low temperature a gradual change occurs in  $1/\chi(T)$ . Another linear region is observed from 25 K to 50 K. Fitting of this range gives  $C^{LT} = 9.44 \text{ emu K mol}^{-1}$ , which is equivalent to two  $\text{Mn}^{2+}$  of  $S = 5/2$ .  $\Theta^{LT}$  is found around 20 K. This positive intersection indicates that ferromagnetic types of interactions occur at low T and lead to long range order at  $T_c \approx 20 \text{ K}$ . Based on these observations,  $\text{BaMn}_9[\text{VO}_4]_6(\text{OH})_2$  can be classified as a complicated case of either a ferrimagnet or a canted antiferromagnet.

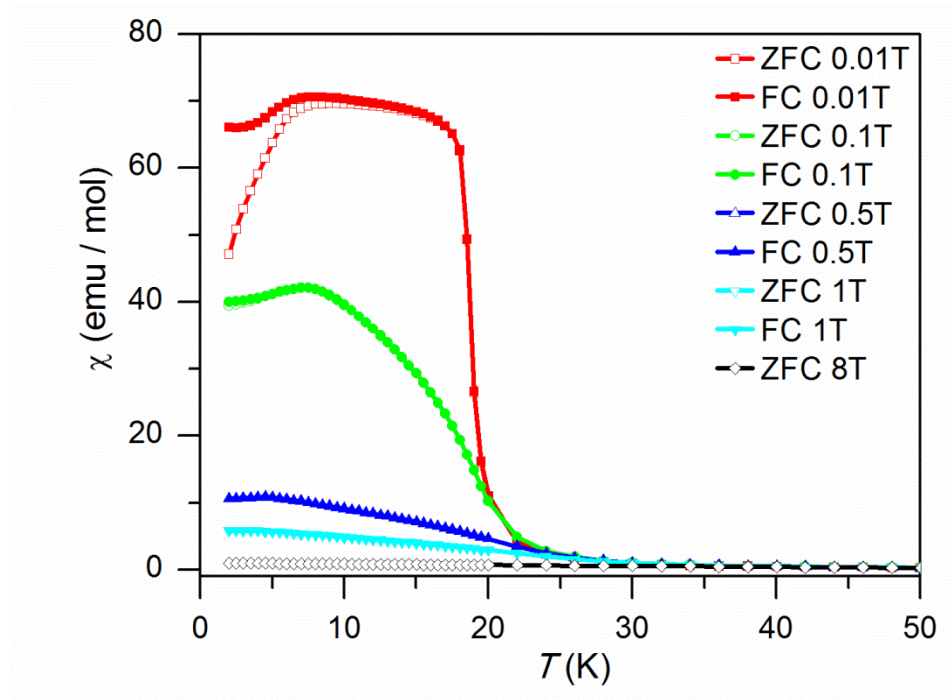


Figure 5.12. Susceptibility data for  $\text{BaMn}_9[\text{VO}_4]_6(\text{OH})_2$  at various fields.

Figure 5.12 shows the low temperature range (below 50 K) of the  $\chi(T)$  data at various fields for ZFC and FC up to 8 T. The splitting between ZFC and FC is only observed for the low field 0.01 T below 10 K, vanishing immediately after the maximum is reached. At 0.1 T, the data show almost no splitting between ZFC and FC, and the maximum shifts to a lower temperature around 7.5 K. The maximum keeps shifting to lower temperature and also decreases quickly with increasing applied field, indicating increasing antiferromagnetic correlations. These observations provide evidence for competing ferromagnetic and antiferromagnetic correlations in the low temperature range.

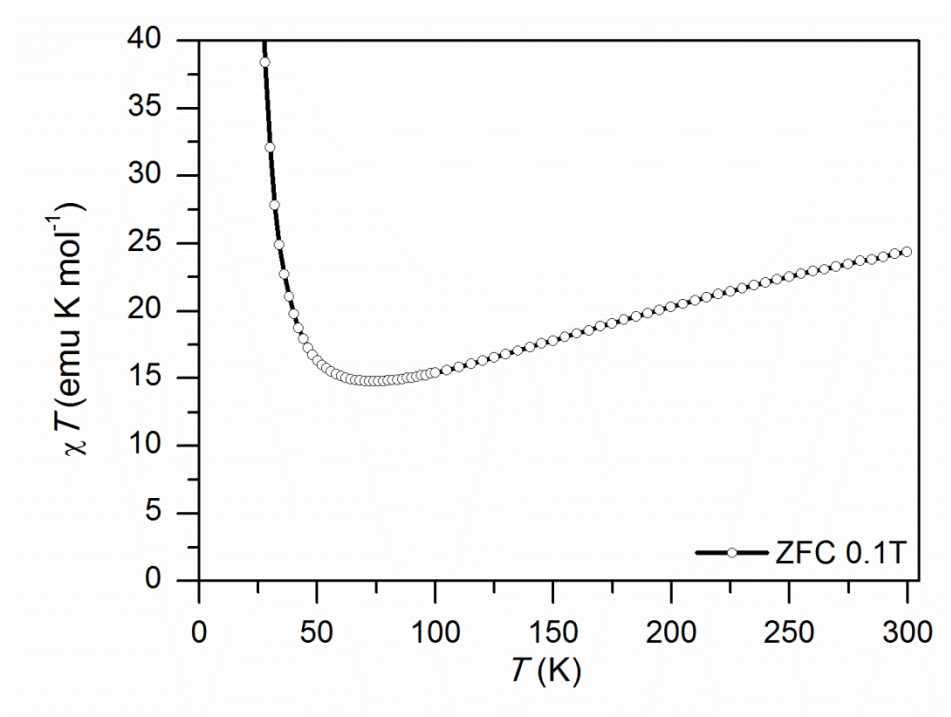


Figure 5.13. Susceptibility ( $\chi T(T)$ ) data for  $\text{BaMn}_9[\text{VO}_4]_6(\text{OH})_2$  at 0.1 T.

In Figure 5.13 we present the  $\chi T(T)$  for ZFC at 0.1 T, which is taken out from Figure 5.14 with a larger temperature range. Around 70 K, the dip shows that the dominant antiferromagnetic correlation starts to turn to the major ferromagnetic correlations. The value of  $\chi T$  at this temperature is approximately  $14.7 \text{ emu K mol}^{-1}$ , which is close to the calculated value ( $13.1 \text{ emu K mol}^{-1}$ ) of  $\chi T$  for an effective spin system of  $S^{\text{eff}} = 15/2$ . This is one third of the paramagnetic value considering all nine  $\text{Mn}^{2+}$  with the spin system of  $S = 45/2$ .

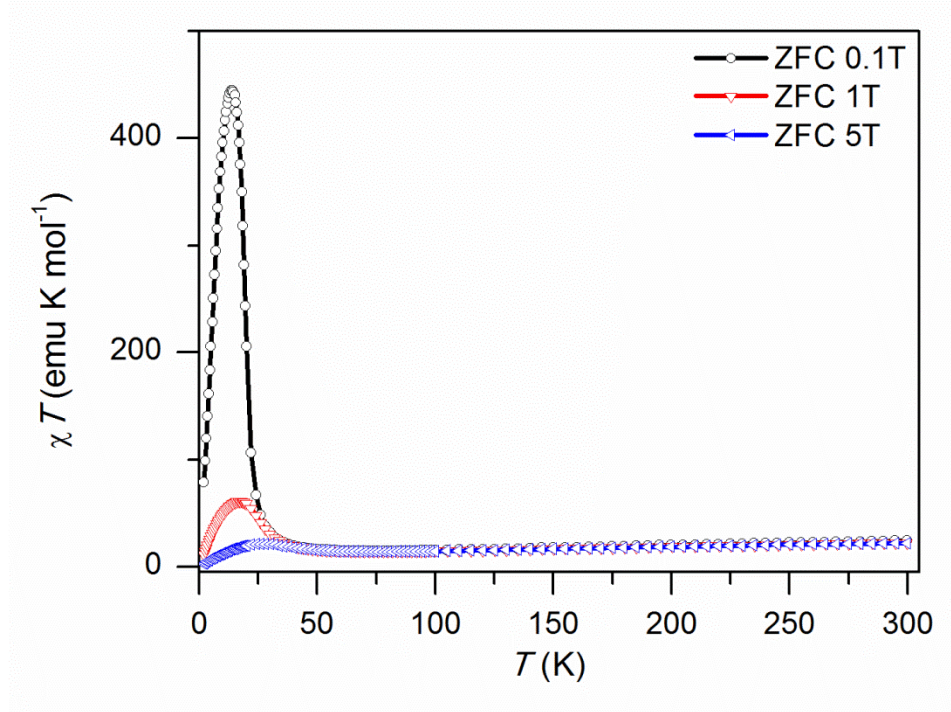


Figure 5.14. Susceptibility ( $\chi T(T)$ ) data for  $\text{BaMn}_9[\text{VO}_4]_6(\text{OH})_2$  at various fields.

The magnetization data,  $M(H)$ , were measured up to 8 T and are shown in Figure 5.15. With increasing temperature, the slope becomes linear and the magnetic moment is

reduced significantly as seen from 20 K to 40 K. It reveals the strong antiferromagnetic correlations above  $T_C \approx 20$  K. Below  $T_C$ , The steep onset increase upon applied fields indicates predominantly ferromagnetic interactions. The change of the magnetic moment becomes gradual at around 0.15 T (2 K data), from  $\approx 7 \mu_B$  to  $\approx 12.7 \mu_B$  up to 8 T reaching a plateau above 4 T. The magnetic moment of  $12.7 \mu_B$  at the highest field is far below the expected saturated moment for nine  $Mn^{2+}$  with  $M_s = 9 \times 5 \mu_B = 45 \mu_B$ . Nevertheless, it is approximately one third ( $15 \mu_B$ ) of the expected saturated moment, which matches the effective spin system with  $S^{eff} = 15/2$  at the low temperature range as discussed for the  $\chi T(T)$  plot. Furthermore, the reduction from the expected value of  $15 \mu_B$  in the low temperature range suggests there is still some competing antiferromagnetic contribution counteracting the moment. This canted antiferromagnetic ground state of  $BaMn_9[VO_4]_6(OH)_2$  could be attributed to the frustration caused by the magnetic ion arrangement in the structure.



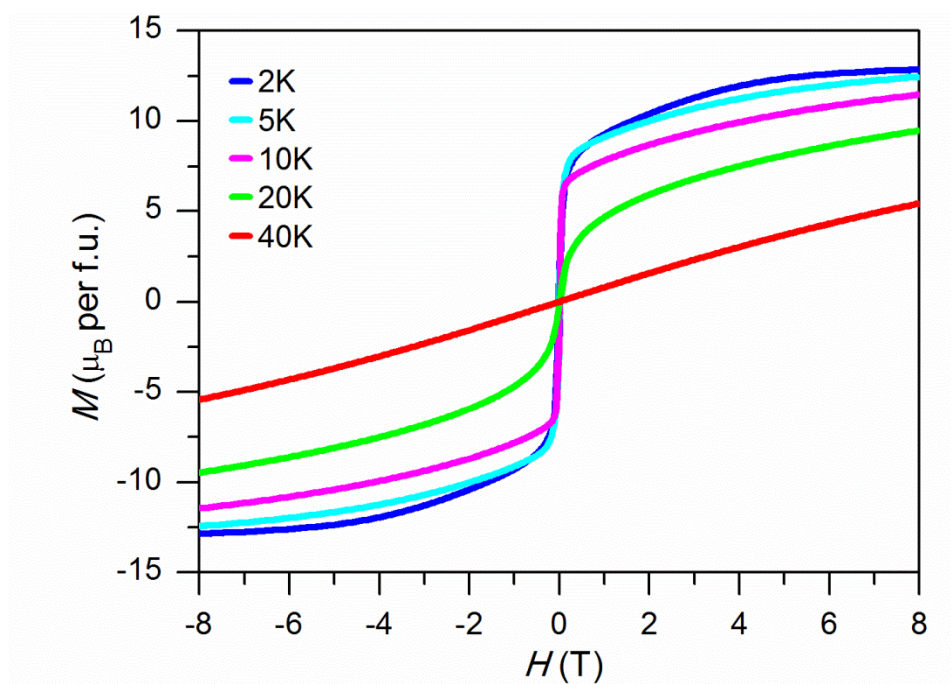


Figure 5.15. Magnetization data for  $\text{BaMn}_9[\text{VO}_4]_6(\text{OH})_2$  at various temperatures.

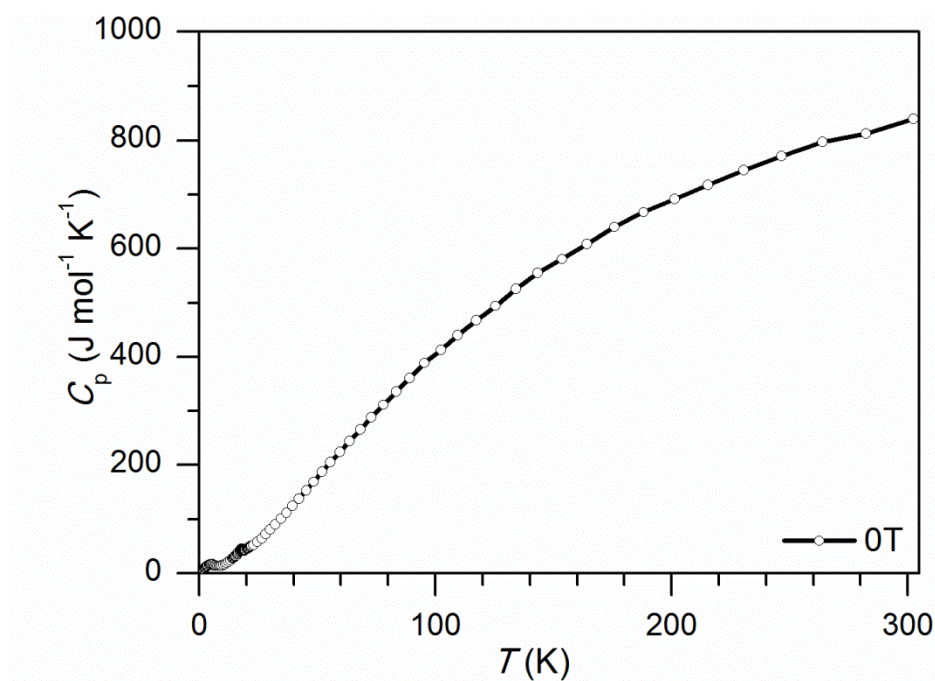


Figure 5.16. Total specific heat data for  $\text{BaMn}_9[\text{VO}_4]_6(\text{OH})_2$  at zero field.

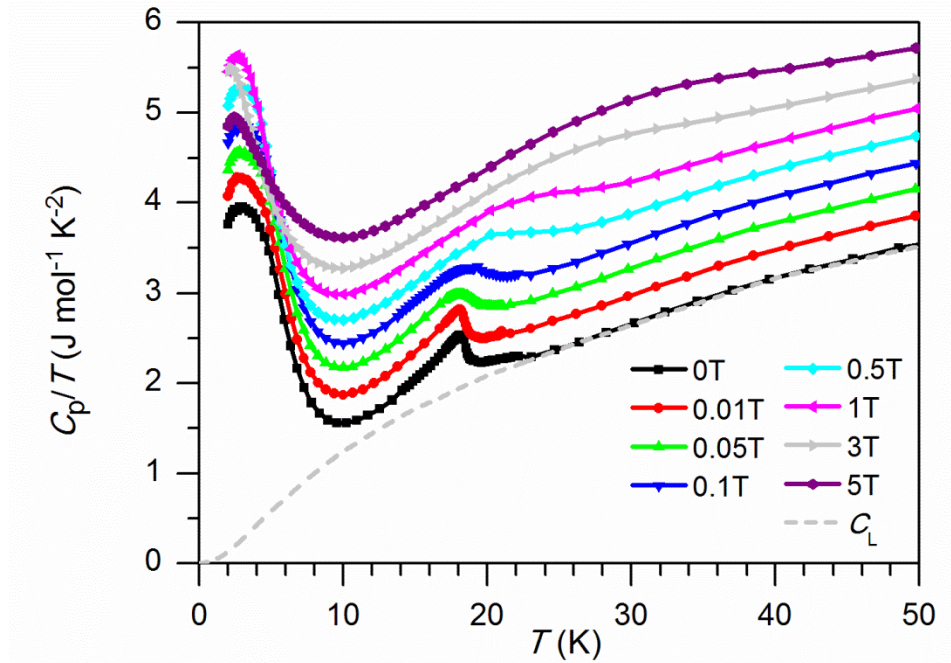


Figure 5.17. Specific heat data for  $\text{BaMn}_9[\text{VO}_4]_6(\text{OH})_2$ : low temperature  $C_p(T)/T$  data for various applied fields (data offset:  $0.5 \text{ J mol}^{-1} \text{ K}^{-2}$  per increasing applied field). The dashed line represents the fitted lattice contribution,  $C_L(T)/T$ .

In Figure 5.16, The measured specific heat,  $C_p(T)$ , for  $\text{BaMn}_9[\text{VO}_4]_6(\text{OH})_2$  in zero applied field is given. At low temperature an anomaly is observed at  $T_C = 18.3 \text{ K}$  ( $H = 0 \text{ T}$ ). For better observation, a set of  $C_p/T(T)$  data are plotted in Figure 5.17 for the range of 0 K to 50 K. It shows the anomalies broaden, shift to higher temperature, and quickly vanish as the applied field increases (above  $H = 0.1 \text{ T}$ ). Therefore, the associated heat also shifts to the higher temperature upon increasing field which confirms the origin of the ferromagnetic interaction. Another feature of the  $C_p/T(T)$  data is the onset additional contribution occurring below 10 K with a maximum around 3 K. Above  $H = 0.1 \text{ T}$  this feature decreases, smears out, and shifts to higher temperature where it adds to the broad



bump at higher temperatures. Note that above 50 K all measurements under different fields follow the same temperature dependence as the zero-field measurement. Thus, the magnetic part of the specific heat below 50K is constant for all fields measured and subject to significant fluctuations.

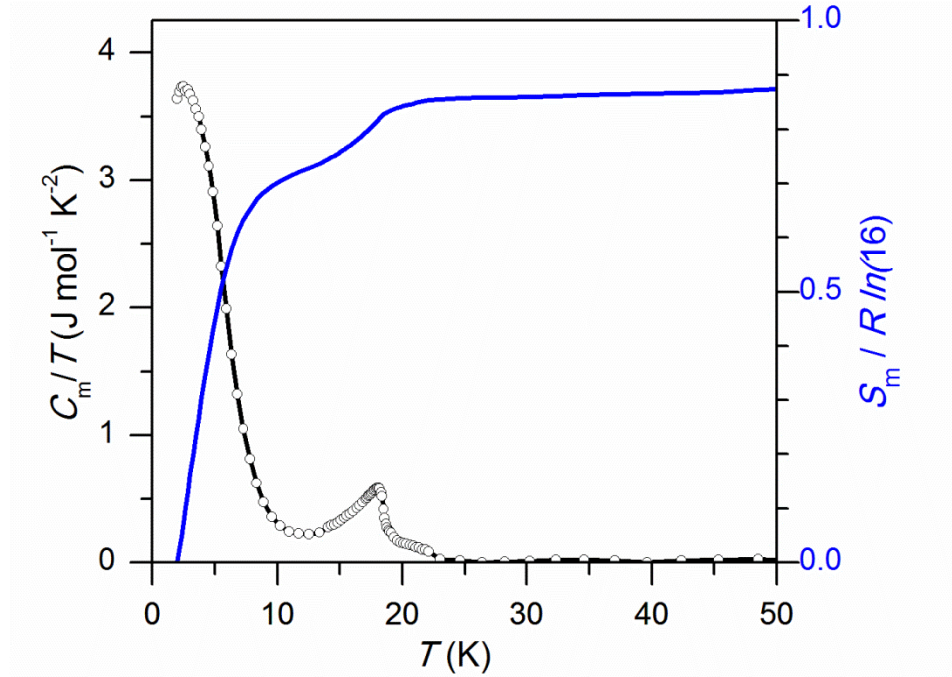


Figure 5.18. The magnetic part of the specific heat,  $C_m(T)/T$  for  $\text{BaMn}_9[\text{VO}_4]_6(\text{OH})_2$  at zero fields (black) and the associated entropy,  $S_m(T)$ , (blue).

In Figure 5.18, we show the magnetic part of the specific heat,  $C_m(T)$ , and the associated magnetic entropy,  $S_m(T)$ .  $C_m(T)/T$  is derived from the  $C_p(T)/T$  data by subtracting a baseline. This baseline represents the lattice contribution,  $C_L(T)/T$ . In our first approximation, the short-range magnetic contributions are neglected for the high temperature region, which are expected to range well beyond 300 K. Then the baseline

can be obtained from fitting a smooth curve to the temperature region from 30 K to 300 K and extrapolating the high temperature fit down to  $\approx 10$  K. The approach in the very low temperature region towards 0 K is adjusted by a Debye-law,  $C_L(T)^{LT} = bT^3$ . The magnetic entropy is given by integrating  $C_m(T)/T$ . The blue curve in Figure 5.18 shows the magnetic part of the entropy released in the temperature range from 2 K to 50 K. Note, we give  $S_m$  in units of the multiplication of  $R$  (gas constant) and  $\ln(2S^{\text{eff}}+1)$ , with  $S^{\text{eff}} = 15/2$ . Overall, approximately 90% of the associated magnetic entropy is released, which corroborates the results from the susceptibility data. At around 10 K ( $\approx 70\%$ ) a plateau in  $S_m(T)$  separates the low temperature feature with the maximum around 3 K from the area of the anomaly at around 18 K ( $\approx 20\%$ ) as discussed above.

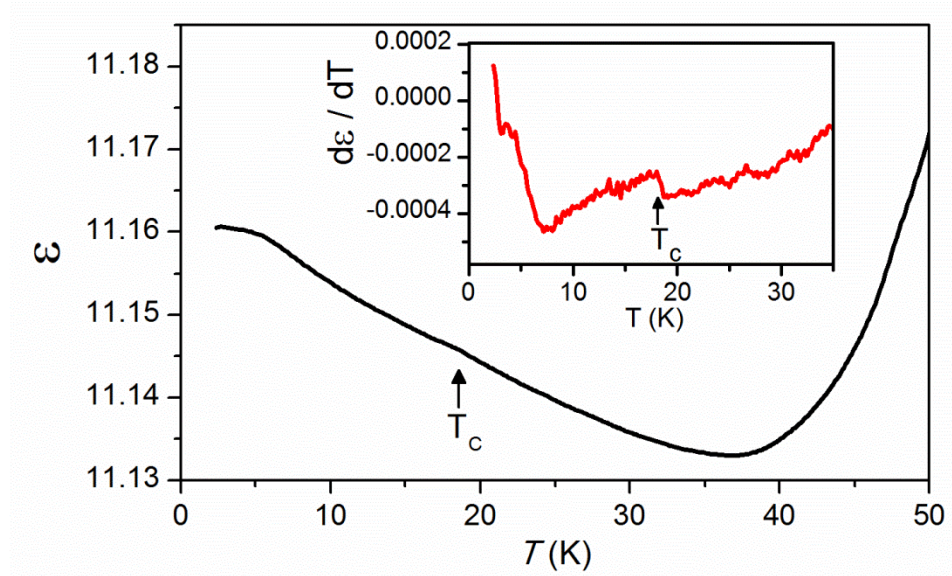


Figure 5.19. Temperature dependence of the dielectric constant for  $\text{BaMn}_9[\text{VO}_4]_6(\text{OH})_2$ .

*Inset:* Derivative of the dielectric constant indicating an anomaly at  $T_C$ .

Dielectric constants were measured by Dr. Bernd Lorenz at the Texas Center for Superconductivity on pressed powder pellets from 2 K to 50 K using the high-precision capacitance bridge AH 2500A (Anderleen-Hagerling) operating at a frequency of 1000 Hz. The capacitance was measured between two contacts made of silver paint attached to parallel faces of the pellet.

In Figure 5.19, we show the measured dielectric constant,  $\epsilon(T)$ , for  $\text{BaMn}_9[\text{VO}_4]_6(\text{OH})_2$  at temperatures below 50 K. The dielectric constant initially decreases down to  $\approx 37$  K which is a common  $T$ -dependence behavior for oxides. However, on further lowering the temperature  $\epsilon(T)$  starts to increase again. At the order transition,  $T_C \approx 18$  K, a kink is observed; see also the derivative plot shown in the inset of Figure 5.19. The change in the dielectric constant at the magnetic ordering temperature (magneto-dielectric effect) is frequently observed at magnetic transitions due to spin-lattice coupling. As polarization measurements have not been conducted due to the small crystal sizes, a ferroic-classification of the magneto-polarization coupling type cannot be confirmed here. [1, 2] Below  $\approx 10$  K the increase in  $\epsilon(T)$  slows down and  $\epsilon(T)$  has a constant value, see  $d\epsilon(T)/dT$ . It is interesting to note that  $C_m(T)$  shows the development of a low temperature feature with a maximum around 3 K in the same temperature range. One might speculate that the magnetic fluctuations evident from the magnetic specific heat and the dielectric constant are coupled. Certainly, these initial characteristics suggest that  $\text{BaMn}_9[\text{VO}_4]_6(\text{OH})_2$  presents a rather interesting and unique case which calls for further experimental studies and a theoretical microscopic picture.

## 5.9 Discussion of the Structure-Property Relationship.

In Figure 5.8, two structural features of Mn-O-Mn connectivity were discussed. The centered triangle one (Figure 5.8 - left) is associated with the dominant short-range antiferromagnetic correlations at high temperatures. The ground state of this entity is represented by a  $S^{\text{C-T}} = 10/2$  spin system which originates from an antiparallel arrangement of the central Mn1 ion surrounded by three Mn3 ions. In this situation, the three Mn3 moments are forced into a parallel orientation opposite to the center Mn1 moment. Such a fragment has received considerable attention in the field of single molecular magnets. [32-34]

The other connectivity of Mn3, except for being a member of the triangle centered with Mn1, is through sharing O1 attached with H which forms an equilateral triangle with the other two Mn3 atoms via edge sharing. Then two (Mn3)<sub>3</sub>-triangles are further capping a Mn2 above and below, respectively, see Figure 5.8 - right. Such equilateral triangles of magnetic ions are geometrically frustrated for dominant antiferromagnetic interactions.

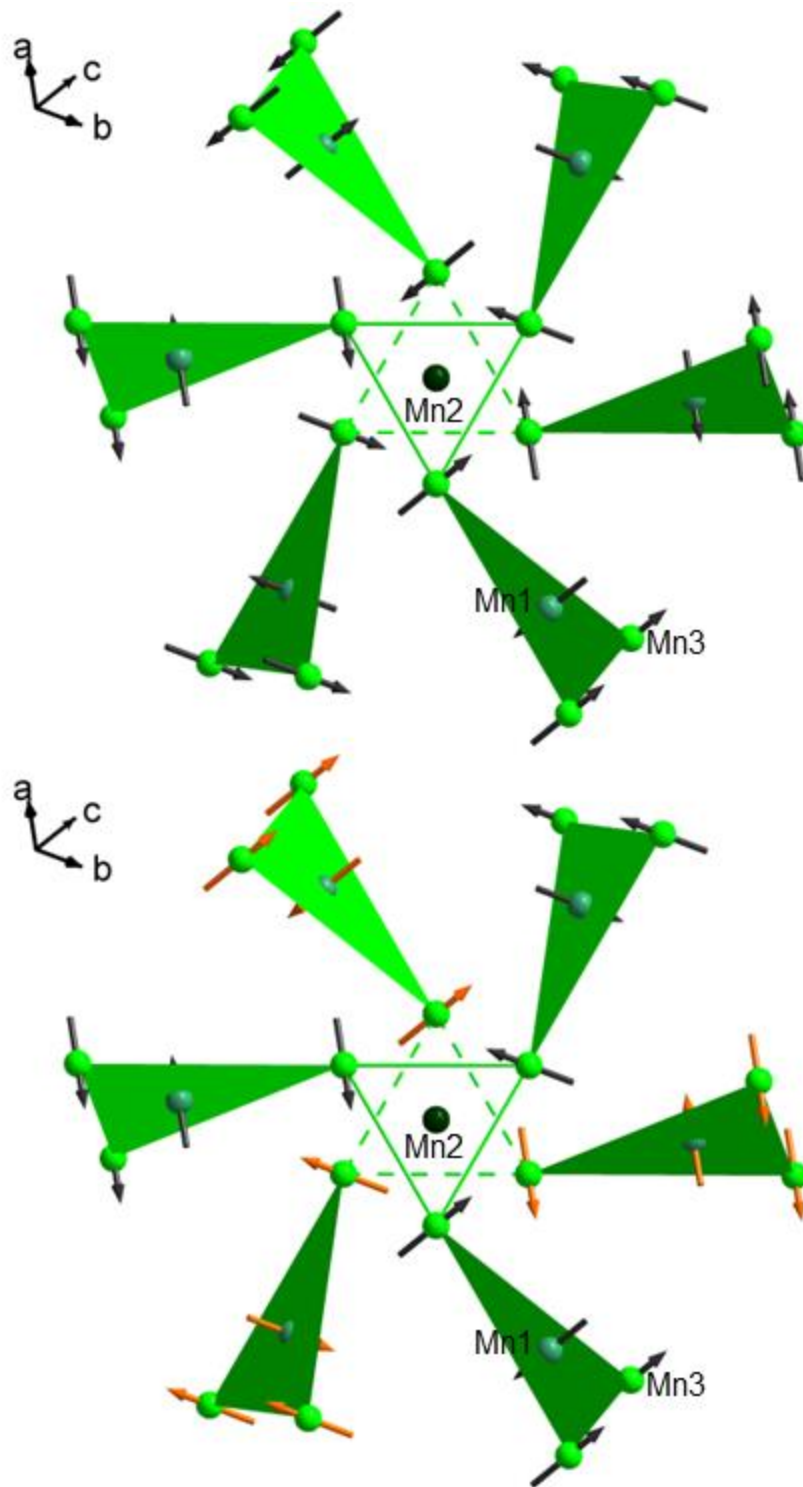


Figure 5.20. Sketch of the proposed chiral spin arrangement. *Top*: the centrosymmetric.

*Bottom*: the acentric case. Note the inverted spin-alignment (orange arrows) for the latter.

The two structure features can be combined and represent a 'paddle-wheel' structure as depicted in Figure 5.20. The angle of the magnetic moment of each Mn3 is induced by the orientation of the Mn1 centered triangle as discussed, and such an orientation is adding to the frustration. For the centrosymmetric case of  $Pa\bar{3}$ , a spiral arrangement results with canting in an out-of plane fashion on each (Mn3)<sub>3</sub>-triangle (Figure 5.20 - top). Note that inversion symmetry forces the out-of plane orientation of each (Mn3)<sub>3</sub> moment opposite to the orientation of the other (Mn3)<sub>3</sub> unit adjacent to Mn2. Thus, it is impossible to align the central Mn2 moment antiparallel to both (Mn3)<sub>3</sub>-triangles.

On the other hand, breaking of inversion symmetry (acentric structure of  $P2_13$ ) allows the two neighboring (Mn3)<sub>3</sub> (via Mn2) moments to point in the same direction. Thus, the top (Mn3)<sub>3</sub>-triangle has the Mn3 moments arranged counter-clockwise while the bottom triangle has a clockwise arrangement of Mn3 moments. (Figure 5.20 - bottom). In this case, an antiferromagnetic scenario involving Mn2 with the six Mn3 might occur, compare also to Figure 5.8 - right. However, the canting of the in-plane Mn3 moments per triangle cannot be resolved though symmetry reduction and remains chiral.

Overall, the compound consists of nine Mn<sup>2+</sup> ions per formula unit, each of the magnetic Mn<sup>2+</sup> ions with an  $S = 5/2$ . Assuming the two Mn1 and one Mn2 per formula unit are antiferromagnetically coupled to the other six Mn3 results in an effective spin of 15/2. The same  $S^{\text{eff}}$  value can be derived by  $6/3 \times S^{\text{C-T}} - S^{5/2} = 15/2$ , considering the Mn1 centered triangle as a unit ( $S^{\text{C-T}}$ ). Our data indeed show that this effective spin system is present below 50 K. Strong fluctuations persist down to low temperatures which are presumably caused by the frustrated nature of the Mn3-Mn3 interaction on the

(Mn3)<sub>3</sub>–triangle. The helical nature of the additional canting adds to the development of the ferromagnetic feature observed in the magnetic and specific heat data at  $T_C$ .

### 5.10 Conclusions.

We have synthesized and grown crystals for  $\text{BaMn}_9[\text{VO}_4]_6(\text{OH})_2$  by applying hydrothermal synthesis with a narrow starting pH range around 8.0. The crystal structure has been re-determined. Besides the space group  $Pa\bar{3}$  which was reported for the naturally occurring mineral nabiasite,  $\text{BaMn}_9[(\text{V},\text{As})\text{O}_4]_6(\text{OH})_2$ , a possible acentric space group  $P2_13$  is proposed since violations of the diffraction selection rules (single crystal X-ray data) and intensity differences (refined powder X-ray data) were found. The acentric space group is further supported by observation under polarized light, which shows spots of polarized light in cross polarization. Moreover, the dielectric constant was measured to provide clear evidence for the magneto-dielectric coupling of magnetic long-range order to the lattice around  $T_C$ . Spectroscopic measurements of infrared and Raman were discussed. Magnetic and specific measurements were conducted for this compound. Based on the rather complicated connectivity of selected structural features, competing antiferromagnetic and ferromagnetic correlations are proposed for this presumably frustrated and canted antiferromagnet.

## 5.11 References.

- [1] Eerenstein, W.; Mathur, N. D.; Scott, J. F. *Nature*, **2006**, 442, 759.
- [2] Cheong, S.-W.; Mostovoy, M. *Nature*, **2007**, 6, 13.
- [3] Tokura, Y.; Seki, S. *Adv. Mater.*, **2010**, 22, 1554.
- [4] Tokura, Y.; Seki, S.; Nagaosa, N. *Rep. Prog. Phys.*, **2014**, 77, 076501.
- [5] Johnson, R. D.; Radaelli, P. G. *Annu. Rev. Mater. Res.*, **2014**, 44, 269.
- [6] Singh, K.; Caignaert, V.; Chapon, L.; Pralong, V.; Raveau, B.; Maignan, A. *Phys. Rev. B*, **2012**, 86, 024410.
- [7] Caignaert, V.; Maignan, A.; Singh, K.; Simon, C.; Pralong, V.; Raveau, B.; Mitchell, J.; Zheng, H.; Huq, A.; Chapon, L. *Phys. Rev. B*, **2013**, 88, 174403.
- [8] Kenzelmann, M.; Lawes, G.; Harris, A. B.; Gasparovic, G.; Broholm, C.; Ramirez, A. P.; Jorge, G. A.; Jaime, M.; Park, S.; Huang, Q.; Shapiro, A. Ya.; Demianets, L. A. *Phys. Rev. Lett.*, **2007**, 98, 267205.
- [9] White, J. S.; Niedermayer, Ch.; Gasparovic, G.; Broholm, C.; Park, J. M. S.; Shapiro, A. Ya.; Demianets, L. A.; Kenzelmann, M. *Phys. Rev. B*, **2013**, 88, 060409(R).
- [10] Amuneke, N. E.; Tapp, J.; de la Cruz, C. R.; Möller, A. *Chem. Mater.*, **2014**, 26, 5930.
- [11] Seki, S.; Yu, X.; Ishiwata, S.; Tokura, Y. *Science*, **2012**, 336, 198.
- [12] Adams, T.; Chacon, A.; Wagner, M.; Bauer, A.; Brandl, G.; Pedersen, B.; Berger, H.; Lemmens, P.; Pfeiderer, C. *Phys. Rev. Lett.*, **2012**, 108, 237204.



- [13] Mochizuki, M.; Yu, X. Z.; Seki, S.; Kanazawa, N.; Koshibae, W.; Zang, J.; Mostovoy, M.; Tokura, Y.; Nagaosa, N. *Nat. Mater.*, **2014**, *13*, 241.
- [14] von Postel, M.; Müller-Buschbaum, Hk. *Z. Anorg. Allg. Chem.*, **1992**, *615*, 97.
- [15] He, Z.; Ueda, Y.; Itoh, M. *Solid State Comm.*, **2007**, *141*, 22.
- [16] Rettich, R.; Müller-Buschbaum, Hk. *Z. Naturforsch.*, **1998**, *53b*, 291.
- [17] Bratsch, M.; Tapp, J.; Litvinchuk, A. P.; Möller, A. *Inorg. Chem.*, **2014**, *53*, 4994.
- [18] Sun, K.; Möller, A. *Acta Crystallogr. E*, **2014**, *70*, i33.
- [19] Zhang, F.; Zavalij, P. Y.; Whittingham, M. S. *J. Mater. Chem.*, **1999**, *9*, 3137.
- [20] Kolitsch, U. *Acta Crystallogr. E* **2001**, *57*, i119.
- [21] Zhang, G.; Dong, S.; Yan, Z.; Guo, Y.; Zhang, Q.; Yunoki, S.; Dagotto, E.; Liu, J.-M. *Phys. Rev., B*, **2011**, *84*, 174413.
- [22] Johnson, R. D.; Chapon, L. C.; Khalyavin, D. D.; Manuel, P.; Radaelli, P. G.; Martin, C. *Phys. Rev. Lett.*, **2012**, *108*, 067201.
- [23] Bruggeru, J.; Bonin, M.; Schenk, K. J.; Meisser, N.; Berlepsch, P.; Ragu, A. *Eur. J. Mineral.*, **1999**, *11*, 879.
- [24] Perdew, J. P.; Burke, K.; Ernzerhof, M. *Phys. Rev. Lett.*, **1996**, *77*, 3865.
- [25] Clark, S. J.; Segall, M. D.; Pickard, C. J.; Hasnip, P. J.; Probert, M. J.; Refson, K.; Payne, M. C. *Z. Kristallogr.* **2005**, *220*, 567.
- [26] Nakamoto, K. *Infrared and Raman Spectra of Inorganic and Coordination Compounds, Part A, Theory and Applications in Inorganic Chemistry*, 6<sup>th</sup> edition, Wiley, **2009**.

- [27] Frost, R. L.; Palmer, S. J.; Čejka, J.; Sejkora, J.; Plášil, J.; Bahfenne, S.; Keeffe, E. C. *J. Raman Spectroscopy*, **2011**, *42*, 1701.
- [28] Steiner, T. *Angew. Chem. Int. Ed.*, **2002**, *41*, 48.
- [29] Beckenkamp, K.; Lutz, H. D. *J. Mol. Struct.*, **1992**, *270*, 393.
- [30] Lutz, H. D. *Struct. Bonding* (Berlin), **1995**, *82*, 85.
- [31] Gheorghe, D. E.; Litvinchuk, A. P.; Möller, A. *Z. Anorg. Allg. Chem.*, **2012**, *638*, 2087.
- [32] Barra, A. L.; Caneschi, A.; Cornia, A.; Fabrizi de Biani, F.; Gatteschi, D.; Sangregorio, C.; Sessoli, R.; Sorace, L. *J. Am. Chem. Soc.*, **1999**, *121*, 5302.
- [33] Gatteschi, D.; Sessoli, R.; Cornia, A. *Chem. Commun.*, **2000**, 725.
- [34] Gao, Q.; Wang, X.; Tapp, J.; Möller, A.; Jacobson, A. J. *Inorg. Chem.*, **2013**, *52*, 6610.

## 5.12 Supplemental Material.

S-1: Table 5.5. Atomic composition for BaMn<sub>9</sub>[VO<sub>4</sub>]<sub>6</sub>(OH)<sub>2</sub>.

Elements		Ba	V	Mn
Position 1	Atomic %	4.02	23.93	37.45
	Stoichiometry	1.000	5.953	9.316
Position 2	Atomic %	3.84	21.73	34.05
	Stoichiometry	1.000	5.659	8.867
Position 3	Atomic %	1.56	8.91	14.04
	Stoichiometry	1.000	5.744	9.000
Position 4	Atomic %	3.79	21.86	35.19
	Stoichiometry	1.000	5.768	9.285
Position 5	Atomic %	3.63	21	33.29
	Stoichiometry	1.000	5.785	9.171
Position 6	Atomic %	2.42	14.71	24.49
	Stoichiometry	1.000	6.079	10.11
Position 7	Atomic %	2.93	17.71	27.62
	Stoichiometry	1.000	6.044	9.427
Position 8	Atomic %	4	22.84	36.04
	Stoichiometry	1.000	5.710	9.010
Position 9	Atomic %	1.81	10.14	15.93
	Stoichiometry	1.000	5.602	8.801

Table 5.5. Continued.

Position 10	Atomic %	2.7	16.44	26.29
	Stoichiometry	1.000	6.089	9.737
Position 11	Atomic %	2.13	11.65	18.86
	Stoichiometry	1.000	5.469	8.854
Position 12	Atomic %	1.74	10.38	16.12
	Stoichiometry	1.000	5.966	9.264
Position 13	Atomic %	3.88	22.59	36.18
	Stoichiometry	1.000	5.822	9.325
Position 14	Atomic %	4.04	23.25	36.02
	Stoichiometry	1.000	5.755	8.916
Position 15	Atomic %	2.53	15.34	24.13
	Stoichiometry	1.000	6.063	9.538
Position 16	Atomic %	1.95	11.82	18.65
	Stoichiometry	1.000	6.062	9.56
Position 17	Atomic %	3.63	19.31	29.65
	Stoichiometry	1.000	5.320	8.168
Position 18	Atomic %	4.04	24.62	38.59
	Stoichiometry	1.000	6.094	9.552
Position 19	Atomic %	3	17.22	28.41
	Stoichiometry	1.000	5.740	9.470

Table 5.5. Continued.

Position 20	Atomic %	3.11	18.06	29.41
	Stoichiometry	1.000	5.807	9.457
Position 21	Atomic %	3.33	19.73	32.2
	Stoichiometry	1.000	5.979	9.758
Position 22	Atomic %	2.4	12.98	20.92
	Stoichiometry	1.000	5.410	8.717
Elements		<b>Ba</b>	<b>V</b>	<b>Mn</b>
Average Stoichiometry		1.0(1)	5.8(2)	9.2(4)
<p>Spectral lines for Position 16 as an example, atomic composition: 1.95 % Ba; 11.82 % V; 18.65 % Mn.</p>				

Standard deviation was calculated based on the equation  $\sigma = \sqrt{\frac{\sum(x-\bar{x})^2}{n}}$ , where  $\sigma$  = standard deviation,  $\Sigma$  = sum of,  $x$  = each value in the data set,  $\bar{x}$  = mean value of the data set.  $n$  = number of values in the data set.

S-2: Table 5.6. Fractional atomic coordinates and isotropic or equivalent isotropic displacement parameters ( $\text{\AA}^2$ ) for  $\text{BaMn}_9[\text{VO}_4]_6(\text{OH})_2$  ( $P\bar{a}\bar{3}$ ).

Atom	Wyckoff site	<i>x</i>	<i>y</i>	<i>z</i>	$U_{\text{iso}}^*/U_{\text{eq}}$
Ba	<i>4b</i>	1/2	0	0	0.0155(1)
Mn1	<i>8c</i>	0.32461(2)	0.32461(2)	0.32461(2)	0.0103(1)
Mn2	<i>4a</i>	1/2	0	1/2	0.0100(2)
Mn3	<i>24d</i>	0.49479(2)	0.15977(3)	0.30640(3)	0.0124(1)
V1	<i>24d</i>	0.40757(3)	0.25407(2)	0.07287(3)	0.0086(1)
O11	<i>24d</i>	0.4798(1)	0.1700(1)	0.1421(1)	0.0137(3)
O12	<i>24d</i>	0.4914(1)	0.3307(1)	0.3211(1)	0.0129(3)
O13	<i>24d</i>	0.5029(1)	-0.0070(1)	0.3311(1)	0.0113(3)
O14	<i>24d</i>	0.3275(1)	0.1565(1)	0.3329(1)	0.0122(3)
O1	<i>8c</i>	0.6552(1)	0.1552(1)	0.3448(1)	0.0121(5)
H1	<i>8c</i>	0.6979	0.1979	0.3021	0.018*

S-2: Table 5.7. Fractional atomic coordinates and isotropic or equivalent isotropic displacement parameters ( $\text{\AA}^2$ ) for  $\text{BaMn}_9[\text{VO}_4]_6(\text{OH})_2$  ( $P2_13$ ).

Atom	Wyckoff site	<i>x</i>	<i>y</i>	<i>z</i>	$U_{\text{iso}}^*/U_{\text{eq}}$
Ba	<i>4a</i>	0.00018(7)	0.00018(7)	0.00018(7)	0.0155(1)
Mn11	<i>4a</i>	-0.1748(1)	0.6748(1)	0.3252(1)	0.0103(2)
Mn12	<i>4a</i>	0.3241(1)	0.6759(1)	0.1759(1)	0.0103(2)
Mn2	<i>4a</i>	-0.0001(2)	0.0001(2)	0.5001(2)	0.0101(2)
Mn31	<i>12b</i>	0.4941(1)	0.8396(1)	0.1922(1)	0.0123(1)
Mn32	<i>12b</i>	-0.0046(1)	0.8410(1)	0.3051(1)	0.0123(1)
V1	<i>12b</i>	-0.0926(1)	0.7458(1)	0.0732(1)	0.0086(1)
V2	<i>12b</i>	0.0726(1)	0.5923(1)	0.2462(1)	0.0086(1)
O11	<i>12b</i>	-0.0185(5)	0.8314(6)	0.1417(5)	0.0136(4)
O21	<i>12b</i>	0.1426(5)	0.5217(5)	0.3286(6)	0.0136(4)
O12	<i>12b</i>	-0.1716(6)	0.8201(5)	-0.0103(5)	0.0127(4)
O22	<i>12b</i>	-0.0067(5)	0.6676(6)	0.3222(5)	0.0127(4)
O13	<i>12b</i>	-0.0096(5)	0.6676(6)	-0.0036(5)	0.0110(4)
O23	<i>12b</i>	-0.0022(5)	0.5048(5)	0.1702(6)	0.0110(4)
O14	<i>12b</i>	-0.1662(6)	0.6725(6)	0.1568(5)	0.0120(4)
O24	<i>12b</i>	0.1565(5)	0.6679(6)	0.1722(6)	0.0120(4)
O1	<i>4a</i>	0.1544(5)	0.8456(5)	0.3456(5)	0.0116(7)
H1	<i>4a</i>	0.2006	0.7994	0.2994	0.017*
O2	<i>4a</i>	0.6561(6)	0.8439(6)	0.1561(6)	0.0116(7)
H2	<i>4a</i>	0.7020	0.7980	0.2020	0.017*

S-3: Table 5.8. Selected Interatomic Distances (Å) for BaMn<sub>9</sub>[VO<sub>4</sub>]<sub>6</sub>(OH)<sub>2</sub>. (*Pa* $\bar{3}$  and *P*<sub>213</sub>)

<i>Pa</i> $\bar{3}$ (No. 205)		<i>P</i> <sub>213</sub> (No. 198)			
Ba—O11(×6)	2.857(2)	Ba—O11 (×3)	2.838(7)	Ba—O12 (×3)	3.199(8)
Ba—O12 (×6)	3.165(2)	Ba—O21 (×3)	2.876(8)	Ba—O22 (×3)	3.136(7)
Mn1—O12 (×3)	2.144(1)	Mn11—O22 (×3)	2.161(7)	Mn12—O12 (×3)	2.128(7)
Mn1—O14 (×3)	2.162(2)	Mn11—O14 (×3)	2.165(7)	Mn12—O24 (×3)	2.155(7)
Mn2—O13 (×6)	2.172(2)	Mn2—O13 (×3)	2.156(7)	Mn2—O23 (×3)	2.188(7)
Mn3—O1	2.119(1)	Mn31—O2	2.132(6)	Mn32—O1	2.107(5)
Mn3—O11	2.123(2)	Mn31—O12	2.164(8)	Mn32—O11	2.109(7)
Mn3—O12	2.204(2)	Mn31—O21	2.135(7)	Mn32—O22	2.237(8)
Mn3—O13	2.167(1)	Mn31—O13	2.210(7)	Mn32—O23	2.130(7)
Mn3—O13'	2.452(1)	Mn31—O13'	2.424(7)	Mn32—O23'	2.480(7)
Mn3—O14	2.176(2)	Mn31—O24	2.159(8)	Mn32—O14	2.189(8)
V1—O11	1.679(2)	V1—O11	1.699(7)	V2—O21	1.659(7)
V1—O14	1.721(2)	V1—O14	1.712(7)	V2—O22	1.711(7)
V1—O12	1.732(2)	V1—O12	1.758(7)	V2—O24	1.734(7)
V1—O13	1.769(2)	V1—O13	1.762(8)	V2—O23	1.770(8)
O1—H1	0.9500	O1—H1	1.0267	O2—H2	1.0211



S-4: Table 5.9. Selected angles (°) for BaMn<sub>9</sub>[VO<sub>4</sub>]<sub>6</sub>(OH)<sub>2</sub>. ( $Pa\bar{3}$  and  $P2_13$ )

$Pa\bar{3}$ (No. 205)		$P2_13$ (No. 198)			
O12—Mn1—O12 (×3)	89.15(6)	O22—Mn11— O22 (×3)	88.4(3)	O12—Mn12— O12 (×3)	89.9(3)
O12—Mn1—O14 (×3)	85.93(6)	O22—Mn11— O14 (×3)	86.0(3)	O12—Mn12— O24 (×3)	85.8(3)
O12—Mn1—O14 (×3)	91.18(6)	O22—Mn11— O14 (×3)	91.7(2)	O12—Mn12— O24 (×3)	90.3(3)
O12—Mn1—O14 (×3)	175.07(6)	O22—Mn11— O14 (×3)	174.6(3)	O12—Mn12— O24 (×3)	175.7(3)
O14—Mn1—O14 (×3)	93.76(5)	O14—Mn11— O14 (×3)	93.7(4)	O24—Mn12— O24 (×3)	94.0(4)
O13—Mn2—O13 (×6)	91.42(5)	O13—Mn2—O13 (×3)	92.2(4)	O23—Mn2—O23 (×3)	90.9(3)
O13—Mn2—O13 (×6)	88.58(5)	O13—Mn2—O23 (×3)	87.4(2)	O13—Mn2—O23 (×3)	178.2(3)
O13—Mn2—O13 (×3)	180	O13—Mn2—O23 (×3)	89.6(2)		
O1—Mn3—O11	108.73(7)	O2—Mn31—O21	108.1(3)	O1—Mn32—O11	109.3(3)
O1—Mn3—O12	91.54(5)	O2—Mn31—O12	92.0(3)	O1—Mn32—O22	90.9(3)
O1—Mn3—O13	83.80(6)	O2—Mn31—O13	83.6(3)	O1—Mn32—O23	84.0(3)
O1—Mn3—O13'	77.16(6)	O2—Mn31— O13'	78.6(3)	O1—Mn32—O23'	75.9(3)
O1—Mn3—O14	157.37(7)	O2—Mn31—O24	158.9(3)	O1—Mn32—O14	155.9(3)
O11—Mn3—O12	91.26(6)	O21—Mn31— O12	90.3(3)	O11—Mn32— O22	92.2(3)
O11—Mn3—O13	102.15(6)	O21—Mn31— O13	102.3(3)	O11—Mn32— O23	102.1(3)
O11—Mn3—O14	93.86(6)	O21—Mn31— O24	93.0(3)	O11—Mn32— O14	94.9(3)
O11—Mn3—O13'	171.49(6)	O21—Mn31— O13'	171.1(3)	O11—Mn32— O23'	171.7(3)

Table 5.9. Continued.

O12—Mn3—O13'	82.33(5)	O12—Mn31— O13'	83.6(3)	O22—Mn32— O23'	81.0(3)
O12—Mn3—O13	166.58(6)	O12—Mn31— O13	167.5(3)	O22—Mn32— O23	165.7(3)
O12—Mn3—O14	89.22(5)	O12—Mn31— O24	89.2(3)	O22—Mn32— O14	89.1(3)
O13—Mn3—O13	84.37(8)	O13—Mn31— O13	84.0(4)	O23—Mn32— O23	84.8(4)
O13—Mn3—O14	90.30(6)	O13—Mn31— O24	90.6(3)	O23—Mn32— O14	90.1(3)
O14—Mn3—O13'	80.54(5)	O24—Mn31— O13	80.6(3)	O14—Mn32— O23'	80.3(3)
O11—V1—O12	106.04(7)	O11—V1—O12	106.7(4)	O21—V2—O22	105.5(4)
O11—V1—O13	107.94(7)	O11—V1—O13	108.6(4)	O21—V2—O23	107.4(4)
O11—V1—O14	109.26(7)	O11—V1—O14	109.8(3)	O21—V2—O24	108.2(4)
O12—V1—O13	109.45(7)	O12—V1—O13	108.4(3)	O22—V2—O23	110.5(4)
O14—V1—O12	111.40(7)	O12—V1—O14	111.2(4)	O22—V2—O24	111.5(4)
O14—V1—O13	112.50(7)	O14—V1—O13	111.8(4)	O24—V2—O23	113.0(4)

## Chapter Six

### Synthesis, Crystal Structures, Lattice Dynamics and Physical Properties of

#### Dumortierite-Like Compounds: $M_{6+x}(\text{OH})_3[\text{VO}_4]_{4-2z}[\text{V}_2\text{O}_7]_z$ with

$M = \text{Mn, Co, Mg, Fe}$

#### 6.1 Introduction.

The unusual structural features of dumortierite-like minerals and their synthetic derivatives have drawn a lot of attention. [1] The structure consists of a framework of hexagonal and triangular channels formed by face-sharing dimers and columns of face-sharing octahedra. Several minerals of this class (general formula  $M_{7-x}[\text{H}_y\text{EO}_4]_4(\text{OH})_3$ ) were reported: dumortierite ( $M = \text{Al}$ ,  $E = \text{B}$ ,  $\text{Si}$ ), [2] holtite ( $M = \text{Al}$ ,  $\text{Ta}$ ,  $\text{Fe}$ ,  $E = \text{B}$ ,  $\text{Si}$ ,  $\text{Sb}$ ,  $\text{As}$ ), [3] and magnesioidumortierite ( $M = \text{Al}$ ,  $\text{Mg}$ ,  $\text{Ti}$ ,  $E = \text{Si}$ ,  $\text{B}$ ). [4] These three minerals crystallize in isotypic orthorhombic structures ( $Pmcn$  space group). Other derivatives belonging to this class have hexagonal structures with  $P6_3$  or  $P6_3mc$  space groups: Ellenbergerite ( $M = \text{Al}$ ,  $\text{Mg}$ ,  $\text{Ti}$ ,  $E = \text{Si}$ ), [5] Phospho-ellenbergerite ( $M = \text{Mg}$ ,  $\text{Fe}$ ,  $E = \text{P}$ ,  $\text{As}$ ,  $\text{C}$ ), [6] Ekatite ( $M = \text{Zn}$ ,  $\text{Fe}$ ,  $E = \text{As}$ ,  $\text{Si}$ ). [7] The dumortierite-like structure possesses two metal-cation sites and two oxoanion sites. Among these minerals, the metal-cation sites forming a kagome-like framework are usually filled by  $\text{Mg}$  or  $\text{Al}$  and with various metals. The non-fully occupied sites are associated with the isolated columns within the hexagonal channels. Also, there are several possibilities for the derivatives on the anion sites such as borates, aluminates, silicates, phosphates, arsenates,

etc. Thus, it already shows us a great potential for this structure type to be tuned for different compositions.

The synthetic compounds of this class of materials are the phosphites ( $M_{11}(\text{HPO}_3)_8(\text{OH})_6$ ,  $M = \text{Mn, Fe, Co, Ni, Zn}$ ), [8-13] phosphates ( $M_{12+x}\text{H}_{4-2x}(\text{PO}_4)_6(\text{HPO}_4)_2(\text{OH})_6$ ,  $M = \text{Co, Ni}$ ), [14] arsenates, ( $\text{Ni}_{12+x}\text{H}_{6-2x}(\text{AsO}_4)_8(\text{OH})_6$ ,  $M_{7-x}M'_6(\text{OH})_3(\text{AsO}_4\text{H}_{2/3x})_3(\text{HAsO}_4)$ ,  $M = \text{Co, Ni}$ ), [15, 16] vanadates ( $\text{Mn}_{7-2/3z}(\text{OH})_3(\text{VO}_4)_{4-2z}(\text{V}_2\text{O}_7)_z$  ( $z \sim 0.2$ ),  $\text{Mg}_{13.4}(\text{OH})_6(\text{HVO}_4)_2(\text{H}_{0.2}\text{VO}_4)_6$ , [17-19] and mixed polyoxoanions ( $\text{Zn}_7(\text{OH})_3(\text{SO}_4)(\text{VO}_4)_3$ ,  $\text{Ni}_{12+x}\text{H}_{4-2x}(\text{EO}_4)_6(\text{HPO}_4)_2(\text{OH})_6$ ,  $E = \text{P, As}$ ), [20, 21]. All of them were synthesized under hydrothermal conditions. With the presence of water, many reports attribute the charge balance by assuming protonation of complex anion groups. [8-14, 16, 18] However, only a manganese vanadate of this class with the formula,  $\text{Mn}_{7-2/3z}(\text{OH})_3(\text{VO}_4)_{4-2z}(\text{V}_2\text{O}_7)_z$  ( $z \sim 0.2$ ), was reported to have been synthesized under controlled pH-conditions. [17] The authors found mixed occupancy of  $[\text{VO}_4]^{3-}$  and  $[\text{V}_2\text{O}_7]^{4-}$  (their ratio is denoted  $z$ ) for the anion site in the triangular channels as an alternative to a protonated product formation and correlated  $z$  to the partial occupancy of the metal-cation site in the triangular channel. To balance the charge of the formula, they claimed mixed valency with  $\text{Mn}^{2+}$  and  $\text{Mn}^{3+}$ .

Here, we report a synthetic route by applying hydrothermal synthesis under controlled pH-conditions and specific vanadate concentrations for a series of dumortierite-like vanadates of a Co or Mn based framework (6 fully occupied metal sites) and doped statistically occupied columns (1 metal site,  $M = \text{Co, Mn, Fe, Mg}$  respectively). Synthesis procedures were optimized to obtain pure and single crystalline products. We have

determined the crystal structures, compared the spectroscopic data with the DFT calculations and investigated the magnetic properties.

## 6.2 Synthesis of Single Crystals of $M_{6+x}(\text{OH})_3[\text{VO}_4]_{4-2z}[\text{V}_2\text{O}_7]_z$ .

Single crystals of  $M_{6+x}(\text{OH})_3[\text{VO}_4]_{4-2z}[\text{V}_2\text{O}_7]_z$  with  $M = \text{Co}, \text{Mn}, \text{Fe}$  and  $(\text{Mg})_{6+x}(\text{OH})_{3-y}(\text{H}_2\text{O})_y[\text{VO}_4]_{4-2z}[\text{V}_2\text{O}_7]_z$  were synthesized by hydrothermal methods. The respective acetates ( $\text{Co}(\text{Ac})_2$ ,  $\text{Mn}(\text{Ac})_2 \cdot 4\text{H}_2\text{O}$ ,  $\text{Mn}(\text{Ac})_3$ ), or  $\text{FeCl}_3 \cdot 6\text{H}_2\text{O}$ , or Mg powder with 1 mL acetic acid, glacial were used as the metal source. The compounds were obtained from the metal acetate,  $\text{NH}_4\text{VO}_3$ , and LiCl as the starting materials in a molar ratio of 7 : 4 : 20. We conducted a series of reactions. The pure Co, Mn, or Mg compounds are denoted: CoII, MnII, MgII as we used only divalent metal acetates for the synthesis. The cobalt series with ‘doped’  $M' = \text{Mn}^{2+}, \text{Mn}^{3+}, \text{Fe}^{3+}$  (starting ratio  $\text{Co}^{2+} : M' = 6 : 1$ ) are denoted as CoIIMnII, CoIIMnIII, and CoIIFeII, respectively. The two manganese based compounds are MnII and MnIIMnIII (starting ratio  $\text{Mn}^{2+} : \text{Mn}^{3+} = 6 : 1$ ). All solid starting materials were mixed together and the appropriate amount of distilled water added to a Teflon liner. Drops of concentrated  $\text{NH}_3 \cdot \text{H}_2\text{O}$  were used to adjust the pH of the system to around 9.0. The total volume of the reaction mixture was 10 ml for 12 ml and 20 ml for 26 ml Teflon-lined stainless steel autoclave. The reaction was carried out at 220 °C for 3 - 4 days and with the standard cooling procedure as discussed in Chapter Two.

There are two important parameters to be controlled for the synthesis. First, we tried three different starting pH values (i) 8.0, (ii) 9.0, (iii) 10.0 for synthesizing the MnII compound

with a formal concentration of 0.05 mol/L based on  $[\text{VO}_4]^{3-}$ . The final pH of the mother liquid dropped to (i) 4.2 (ii) 5.9, but remained almost unchanged for (iii). All other reactions were conducted under condition (ii). The final pH values were found to dramatically decrease for the transition metal compounds, around 5 - 7, but remain close to the initial pH value 8.0 for the MgII compound. The decrease in pH values indicates that a significant amount of  $\text{H}^+$  was produced from the reaction and exceeded the buffer region of  $\text{NH}_3/\text{NH}_4^+$ . We selected condition (ii) 9.0 as the standard pH for the synthesis as well crystallized and phase pure products were generally obtained. See also the general synthesis introduction for the pH-dependence and the vanadate concentration.

The vanadate concentration has a great impact on the formation of products. We attempted to synthesize the MnII compound with different  $[\text{VO}_4]^{3-}$  concentrations. The pH value was fixed at 9.0. At high concentrations, the formation of  $\text{Mn}_2\text{V}_2\text{O}_7$  is observed, see Figure 6.1. The vanadate concentration of 0.1 mol/L produced almost pure  $\text{Mn}_2\text{V}_2\text{O}_7$ . Mixed phases of  $\text{Mn}_2\text{V}_2\text{O}_7$  and MnII were observed for 0.075 mol/L, and an almost pure phase of MnII obtained below 0.05 mol/L. Thus, we optimized our synthesis procedure by restricting the concentration of  $[\text{VO}_4]^{3-}$  below 0.05 mol/L with a starting pH value around 9.0. Pure compounds were produced for the Co-series under this synthetic condition. However, for the Mn-series it seems difficult to avoid small impurities of  $\text{Mn}_2\text{V}_2\text{O}_7$ . The existence of this impurity caused slight deviations concerning the Curie constant between different batches, see magnetic measurements below.

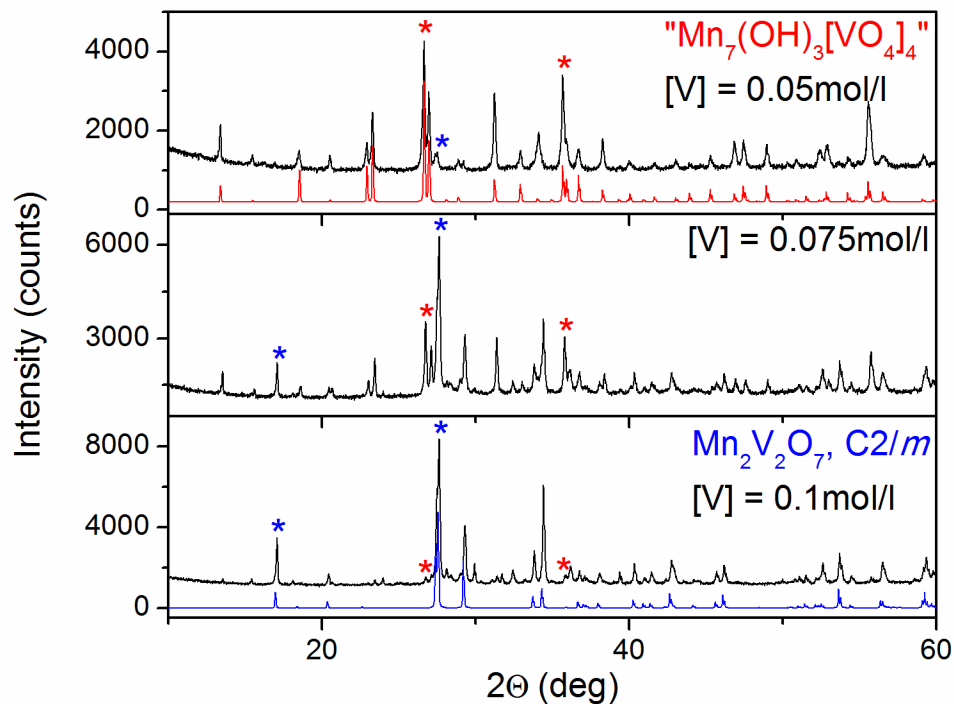


Figure 6.1. Powder XRD data for synthesis of the MnII compound with different concentrations of starting mixture based on  $[\text{VO}_4]^{3-}$ . The  $\text{Mn}_2\text{V}_2\text{O}_7$  (blue) and MnII (red) simulated powder XRD pattern are also plotted for comparison.

The needle-shaped crystals were collected by filtering, washed with distilled water several times, and then dried naturally in the hood. The crystalline products of all transition metal compounds are dark red with a metallic luster for the Co series (Figure 6.2), while the MgII crystals are transparent, see Figure 6.3.

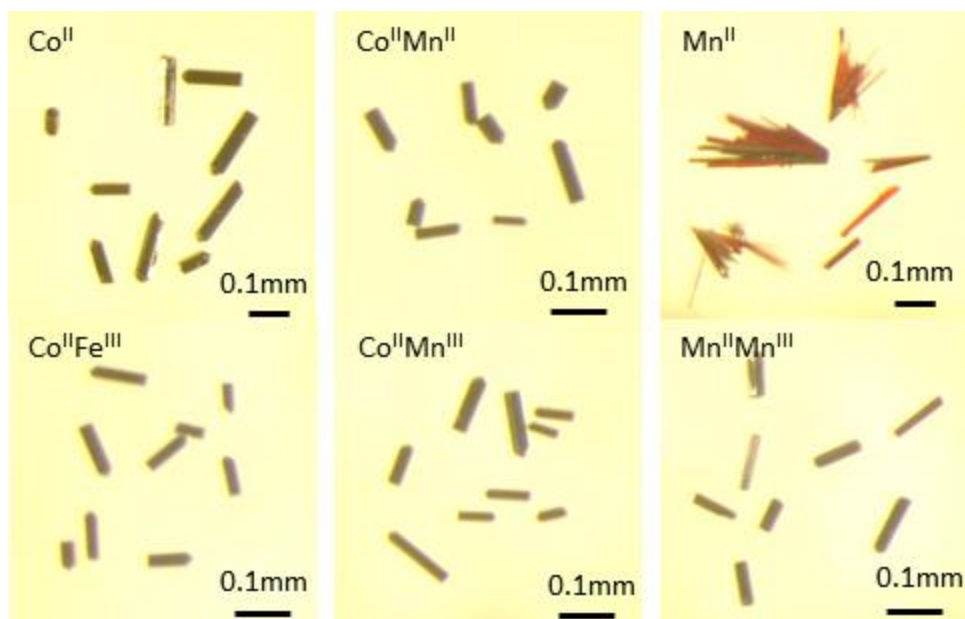


Figure 6.2. Photos of magnified crystals of all synthesized transition metal compounds ( $M_{6+x}(\text{OH})_3[\text{VO}_4]_{4-2z}[\text{V}_2\text{O}_7]_z$ ).

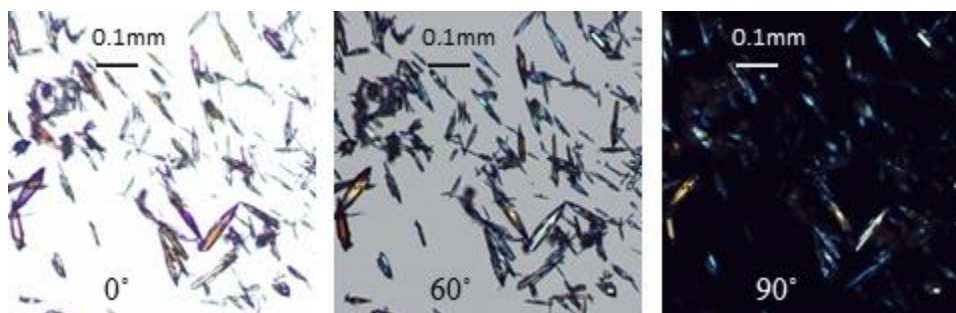


Figure 6.3. Polarized photos of magnified randomly oriented transparent crystals of  $(\text{Mg})_{6+x}(\text{OH})_{3-y}(\text{H}_2\text{O})_y[\text{VO}_4]_{4-2z}[\text{V}_2\text{O}_7]_z$ . From left to right, polarization angles are  $0^\circ$ ,  $60^\circ$ , and  $90^\circ$ .



Polarized photos of magnified crystals were taken. For an acentric structure distinct polarization is expected under the 90° cross-polarized light. The MgII compound is suitable for this observation due to its transparency, see Figure 6.3.

### 6.3 Scanning Electron Microscopy-Energy Dispersive X-ray Spectroscopy (SEM-EDX) of $M_{6+x}(\text{OH})_3[\text{VO}_4]_{4-2z}[\text{V}_2\text{O}_7]_z$ .

Energy dispersive X-ray (EDX) analysis confirmed the composition ratio  $M/\text{V}$  of 7 : 4 based on average values calculated from 6 measured spots for each compound. (S-1 in the supplemental material) The acquisition time was 300 seconds/spot. The calculated stoichiometry is shown in Table 6.1.

Table 6.1. Atomic composition for  $M_{6+x}(\text{OH})_3[\text{VO}_4]_{4-2z}[\text{V}_2\text{O}_7]_z$ .

$M_{6+x}(\text{OH})_3[\text{VO}_4]_{4-2z}[\text{V}_2\text{O}_7]_z$		$M$	$M'$	V
Stoichiometry	CoII	7.0(1)	-	4.0(1)
	CoIIMnII	5.8(2)	0.9(1)	4.0(1)
	CoIIMnIII	5.7(2)	1.0(1)	4.0(1)
	CoIIFeIII	6.0(2)	0.6(1)	4.0(1)
	MnII	7.4(2)	-	4.0(1)
	MnIIMnIII	7.5(1)	-	4.0(1)

#### 6.4 Single Crystal X-ray Diffraction of $M_{6+x}(\text{OH})_3[\text{VO}_4]_{4-2z}[\text{V}_2\text{O}_7]_z$ .

Single crystal data were collected on a Rigaku instrument. Needle-shaped crystals were selected from each sample. The title compounds were refined in the acentric space group  $P6_3mc$  with  $Z = 2$ . The occupancy of the  $M2$  site (denoted  $x$ ) and the statistical disordered  $V22$  site (denoted  $z$ ) were independently refined. The temperature factors of split positions were coupled by using the EADP command to minimize correlation effects. The H atoms were found from difference Fourier synthesis maps and refined using the ride-on constraint  $U_{\text{iso}}(\text{H}) = -1.5 \times U_{\text{aniso}}(\text{O})$ . For the final refinement the AFIX 3 command was employed. For the transition metal compounds, the hydroxide groups are associated with the O3 site. For the MgII compound, charge compensation per formula is achieved by mixed  $\text{OH}^-/\text{H}_2\text{O}$  occupancy (denoted  $y$ ) related to the O3 site. The absolute structures are evaluated by the Flack- $x$  parameter.

The crystal structure was solved and refined as described in Chapter 2. The specific crystallographic data and details are listed in Tables 6.2, 6.3, and 6.4. Fractional atomic coordinates and isotropic or equivalent isotropic displacement parameters are listed in S-2 and selected interatomic distances and angles for both structure solutions are listed in S-3 and S-4, respectively, in the supplemental material.

Table 6.2. Crystallographic data and details of the structure determination for CoII and CoIIFeIII at 293 K with 61 refined parameters. ( $Z = 2$ )

	CoII	CoIIFeIII
x	0.88(1)	0.93(2)
z	0.402(6)	0.323(8)
Formula	$\text{Co}_{6.88}\text{V}_4\text{O}_{18.60}\text{H}_3$	$\text{Co}_6\text{Fe}_{0.93}\text{V}_4\text{O}_{18.68}\text{H}_3$
$M_r$	909.77	910.83
$a$ (Å)	12.884(3)	12.8734(5)
$c$ (Å)	5.0938(5)	5.1000(3)
Volume (Å <sup>3</sup> )	732.3(3)	731.96(7)
Density (g/cm <sup>3</sup> )	4.126	4.133
F (000)	859	861
$\mu$ (Mo $K_\alpha$ ) (mm <sup>-1</sup> )	10.10	10.03
Crystal size (mm)	$0.15 \times 0.05 \times 0.05$	$0.10 \times 0.02 \times 0.02$
Range (°)	3.2 - 33.1	3.1 - 33.1
$R_{\text{int}}$	0.078	0.072
Measured reflections	10061	10527
Unique reflections	1033	1033
$R_1$ , $wR_2$ , GooF	0.051, 0.086, 1.29	0.052, 0.111, 1.30
( $T_{\text{min}}$ , $T_{\text{max}}$ )	0.775 - 1.000	0.775 - 1.000
Flack-x	0.07(2)	0.04(2)

Table 6.3. Crystallographic data and details of the structure determination for CoIIMnII and CoIIMnIII at 293 K with 61 refined parameters. ( $Z = 2$ )

	CoIIMnII	CoIIMnIII
x	0.86(2)	0.881(6)
z	0.372(7)	0.391(3)
Formula	$\text{Co}_6\text{Mn}_{0.86}\text{V}_4\text{O}_{18.60}\text{H}_3$	$\text{Co}_6\text{Mn}_{0.88}\text{V}_4\text{O}_{18.61}\text{H}_3$
$M_r$	905.89	907.22
$a$ (Å)	12.9674(8)	12.9388(3)
$c$ (Å)	5.1166(3)	5.1051(3)
Volume (Å <sup>3</sup> )	745.1(1)	740.16(6)
Density (g/cm <sup>3</sup> )	4.038	4.071
F (000)	855	856
$\mu$ (Mo $K_\alpha$ ) (mm <sup>-1</sup> )	9.68	9.77
Crystal size (mm)	$0.15 \times 0.03 \times 0.03$	$0.15 \times 0.03 \times 0.03$
Range (°)	3.1 - 34.9	3.1 - 33.1
$R_{\text{int}}$	0.082	0.027
Measured reflections	8551	10624
Unique reflections	1137	1043
$R_1$ , $wR2$ , GooF	0.053, 0.097, 1.23	0.021, 0.039, 1.29
( $T_{\text{min}}$ , $T_{\text{max}}$ )	0.724 - 1.000	0.679 - 1.000
Flack-x	0.03(2)	0.030(9)

Table 6.4. Crystallographic Data and Details of the Structure Determination for MnII, MnIIMnIII, and MgII at 293 K with 61 refined parameters. ( $Z = 2$ )

	MnII	MnIIMnIII	MgII
x	0.83(1)	0.82(1)	0.71(2)
z	0.185(8)	0.139(6)	0.275(4)
Formula	Mn <sub>6.83</sub> V <sub>4</sub> O <sub>18.82</sub> H <sub>3</sub>	Mn <sub>6.82</sub> V <sub>4</sub> O <sub>18.86</sub> H <sub>3</sub>	Mg <sub>6.71</sub> V <sub>4</sub> O <sub>18.73</sub> H <sub>4</sub>
M <sub>r</sub>	883.69	883.78	670.27
<i>a</i> (Å)	13.2233(5)	13.2102(7)	12.9099(4)
<i>c</i> (Å)	5.2679(3)	5.2630(3)	5.0895(3)
Volume (Å <sup>3</sup> )	797.71(8)	795.4(1)	734.60(6)
Density (g/cm <sup>3</sup> )	3.679	3.690	3.030
F (000)	833	833	652
$\mu$ (Mo K $\alpha$ ) (mm <sup>-1</sup> )	7.54	7.55	2.86
Crystal size (mm)	0.20 × 0.05 × 0.05	0.13 × 0.03 × 0.02	0.19 × 0.03 × 0.02
Range (°)	3.1 - 34.3	3.1 - 32.4	3.2 - 33.1
<i>R</i> <sub>int</sub>	0.076	0.051	0.053
Measured reflections	10808	10405	10328
Unique reflections	1068	1062	1034
<i>R</i> <sub>1</sub> , <i>wR</i> <sub>2</sub> , GooF	0.051, 0.098, 1.26	0.038, 0.075, 1.20	0.035, 0.067, 1.22
( <i>T</i> <sub>min</sub> , - <i>T</i> <sub>max</sub> )	0.718 - 1.000	0.791 - 1.000	0.904 - 1.000
Flack-x	0.07(2)	0.04(2)	0.01(1)

## 6.5 Powder X-ray Diffraction and Refinement of $M_{6+x}(\text{OH})_3[\text{VO}_4]_{4-2z}[\text{V}_2\text{O}_7]_z$ .

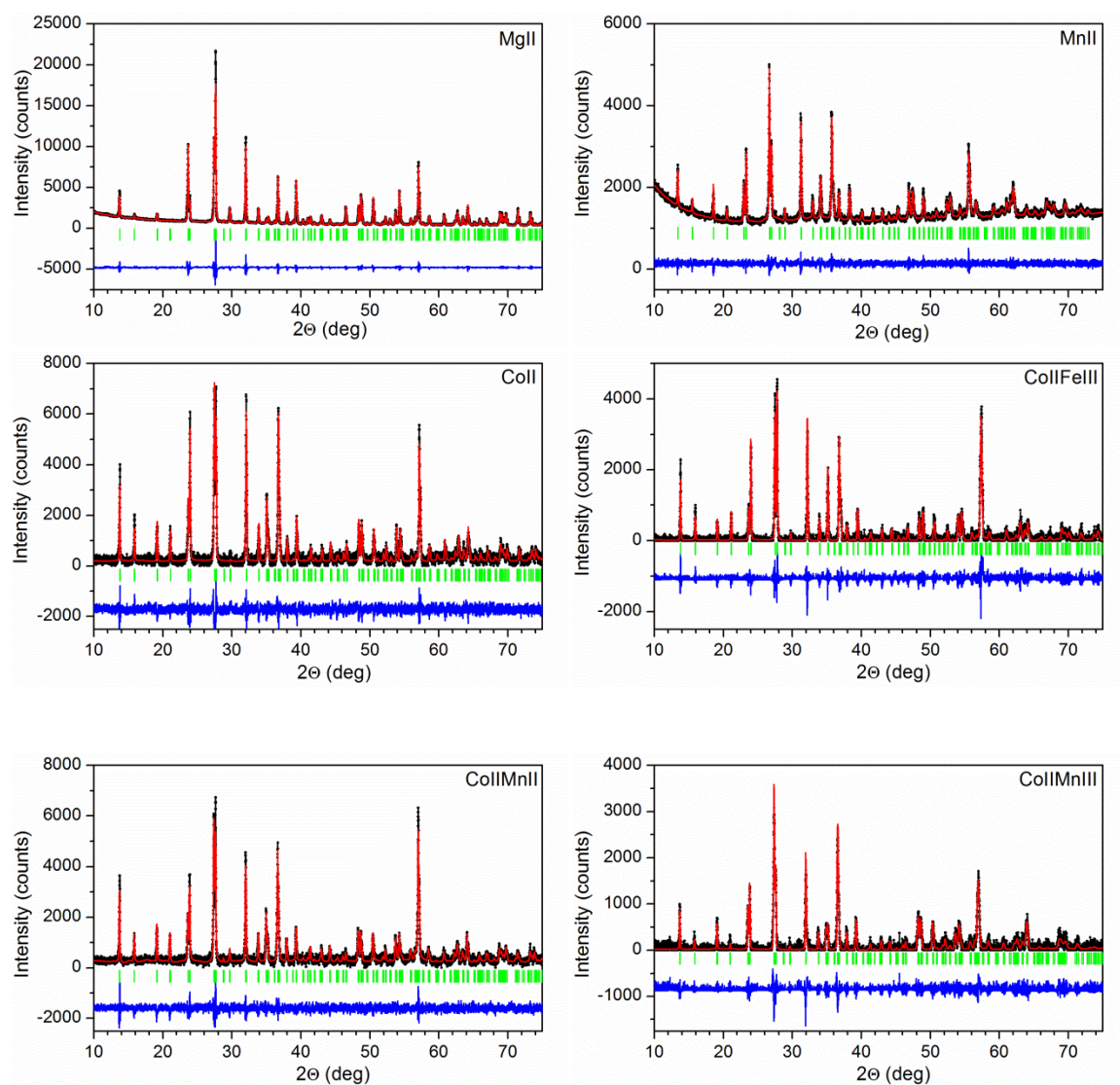


Figure 6.4. X-ray powder data for  $(M1)_6(\text{OH})_3[\text{VO}_4]_3(M2)_x\{[\text{VO}_4]_{1-2z}[\text{V}_2\text{O}_7]_z\}$ . Observed (black), calculated (red), Bragg positions (green) and difference (blue).

X-ray powder diffraction patterns were collected to confirm the phase purity and the structure model of each compound. The samples were ground into fine powders. Powder

refinement data for each compound is shown in Figure 6.4. The high background contributions to the collected intensity data for the Mn- and Co-series have been corrected for the effect of fluorescence. The members of the Co-series show similar patterns, while the relative intensities between reflections vary for different dopants. An evaluation of the lattice parameters and the occupancy factors is listed below in Table 6.5.

Table 6.5. Powder refinement results for  $M_{6+x}(\text{OH})_3[\text{VO}_4]_{4-2z}[\text{V}_2\text{O}_7]_z$  with the space group of  $P6_3mc$ .

	Unit Cell (Å)	$\chi^2$ , $R_{\text{Bragg}}$ , $R_{\text{F}}$ -factor
CoII	$a = 12.8762(3)$ , $c = 5.0859(3)$	89.7, 2.86, 3.71
CoIIMnII	$a = 12.9098(2)$ , $c = 5.0970(2)$	33.0, 1.66, 1.74
CoIIMnIII	$a = 12.9345(4)$ , $c = 5.1062(3)$	32.8, 2.75, 2.24
CoIIFeIII	$a = 12.8443(3)$ , $c = 5.1045(3)$	44.2, 3.06, 2.52
MnII	$a = 13.2153(1)$ , $c = 5.2598(1)$	1.50, 0.872, 0.754
MgII	$a = 12.90308(5)$ , $c = 5.08632(5)$	5.14, 1.06, 0.936

## 6.6 Crystal Structure Description and Discussion for $M_{6+x}(\text{OH})_3[\text{VO}_4]_{4-2z}[\text{V}_2\text{O}_7]_z$ .

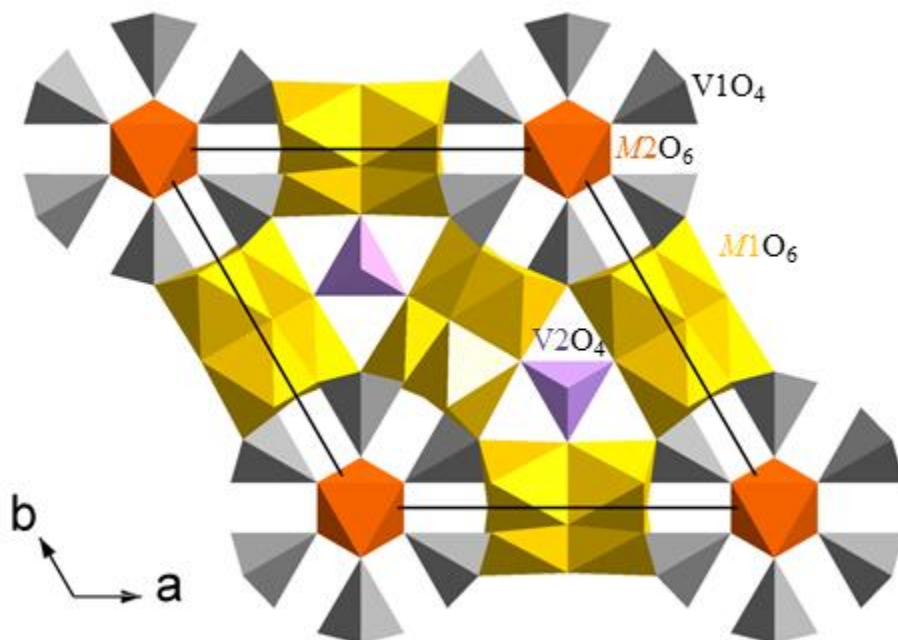


Figure 6.5. Unit cell of the idealized crystal structure of  $(M1)_6(\text{OH})_3[(V1)\text{O}_4]_3(M2)[(V2)\text{O}_4]$  in a polyhedra representation. Color theme:  $M1$  (gold),  $M2$  (orange),  $V1$  (grey),  $V2$  (lavender), O and H atoms are not shown here.

A projection of the idealized crystal structure of  $(M1)_6(\text{OH})_3[(V1)\text{O}_4]_3(M2)[(V2)\text{O}_4]$  is shown in Figure 6.5. There are two  $M$ - and two  $V$ - independent sites, respectively. The coordination environment is octahedral for  $M$  and tetrahedral for  $V$ . All  $M$ -O are found within the expected range based on the ionic radii and all  $V$ -O distances are comparable to typical interatomic distances in vanadates. (Table 6.6)



Table 6.6. Selected Interatomic Distances (Å) for  $M_{6+x}(\text{OH})_3[\text{VO}_4]_{4-2z}[\text{V}_2\text{O}_7]_z$ .

	MgII	CoII	CoIIFeIII	CoIIMnII	CoIIMnIII	MnII	MnIIMnIII
$M1\text{--O}$	2.09(7)	2.10(8)	2.10(9)	2.11(8)	2.11(8)	2.18(9)	2.18(9)
$M2\text{--O}$	2.11(2)	2.10(1)	2.09(1)	2.13(1)	2.12(1)	2.18(1)	2.18(1)
$V1\text{--O}$	1.72(2)	1.72(2)	1.73(1)	1.72(2)	1.72(1)	1.72(1)	1.72(1)
$V21\text{--O}$	1.71(2)	1.74(3)	1.73(4)	1.74(3)	1.73(2)	1.71(2)	1.71(1)
$V22\text{--O}$	1.80(9)	1.79(8)	1.73(3)	1.79(7)	1.82(5)	1.86(9)	1.88(9)
$M1\text{--}M1$	2.86	2.87	2.86	2.89	2.88	3.00	3.00
$M1\text{--}M1'$	3.07	3.06	3.06	3.07	3.07	3.20	3.20
$M2\text{--}M2$	2.55	2.55	2.55	2.56	2.55	2.63	2.63

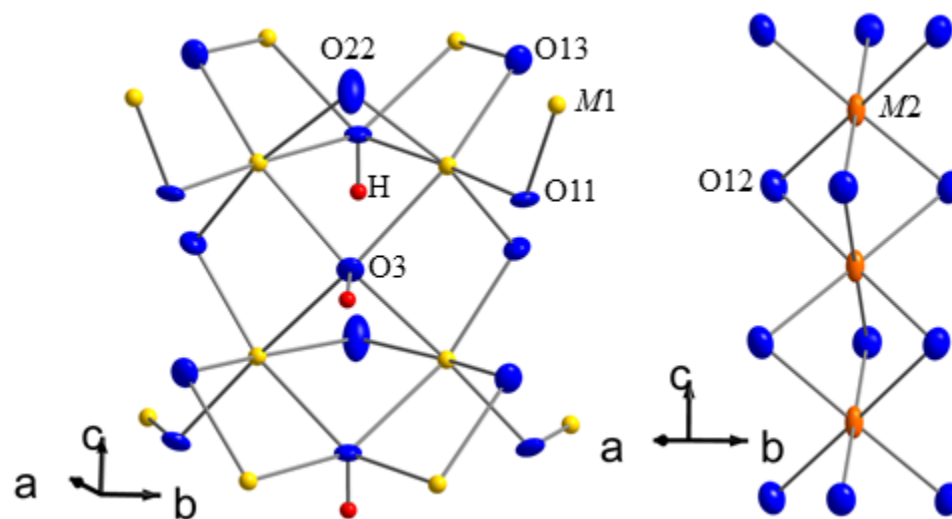


Figure 6.6. Connectivity of  $M1\text{--O--}M1$  (left) and  $M2\text{--O--}M2$  (right). Note the partial occupancy for the  $M2$  site (denoted  $x$ ). Ellipsoids are of 75% probability (here  $M = \text{Co}$ ).

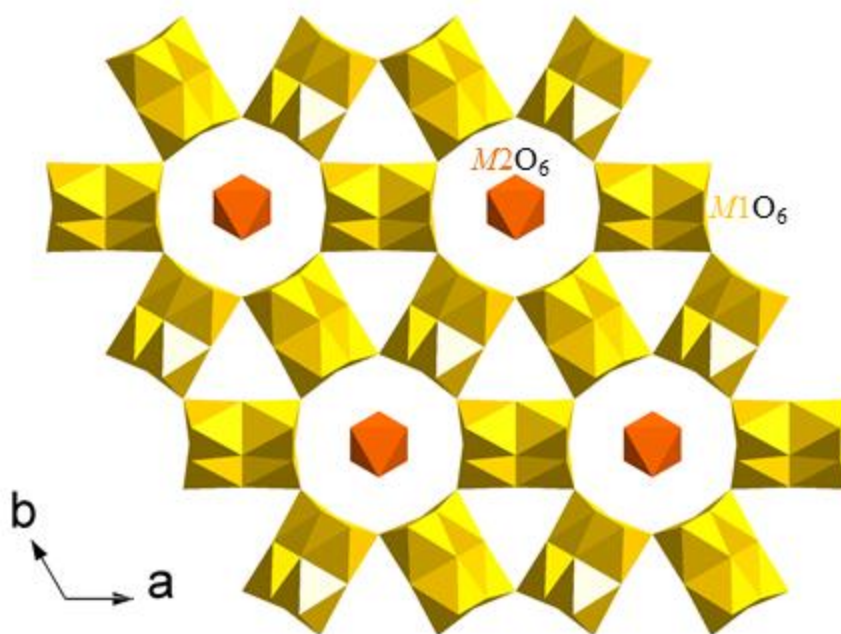


Figure 6.7. Kagome-like arrangement of  $M1$  dimers in a polyhedral representation. Color theme:  $M1$  (gold),  $M2$  (orange).

As shown in Figure 6.6, the  $[M1O_6]$  units are connected pair-wise via a common face ( $M1-M1 \approx 2.9 \text{ \AA}$ ) and via edges ( $M1-M1 \approx 3.1 \text{ \AA}$ ) to zigzag ladders along  $[001]$ . These ladders are further connected via corners to form a framework with six- and three-membered channels, see Figure 6.7.  $[M2O_6]$  units are connected via faces with short  $M2-M2$  distances ( $M2-M2 \approx 2.6 \text{ \AA}$ ) and form chains along  $[001]$ . Those are isolated from the  $M1$  framework and located in the center of the six-membered channels. From the structure refinement, the  $M2$  site is partially occupied. The occupancy is represented by  $x$  ( $x = 0.82-0.93$  for  $M = \text{transition metal}$  and  $0.71$  for  $M = \text{Mg}$ ). This implies large displacements on the  $M2$  sites compare with the ellipsoids shown in Figure

6.6. Through displacements towards vacancies within the chain an increase in  $M2-M2$  distances may be achieved. The larger repulsion between Mg–Mg ions leads to lower occupancy on the  $M2$  site for the MgII compound.

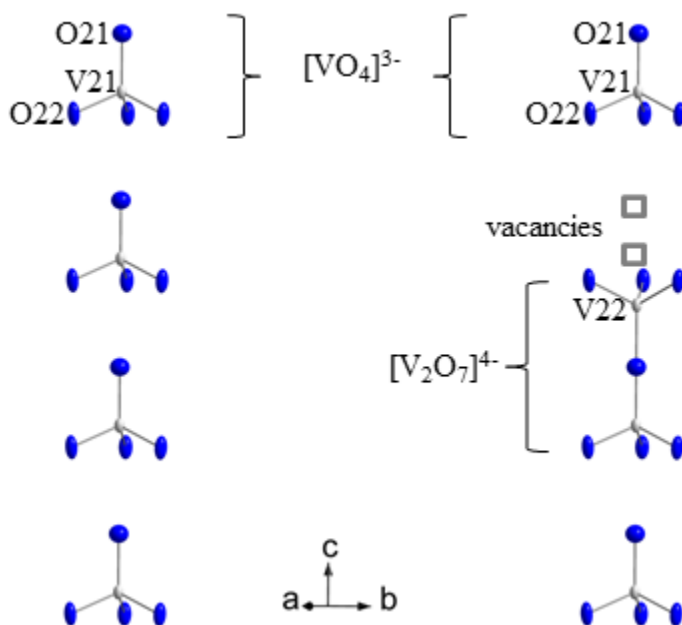


Figure 6.8. Statistical occupancy (denoted  $z$ ) for V21/V22 along  $[001]$ . *Left*: Occupancy only with  $[(V21)O_4]^{3-}$ ,  $z = 0$ . *Right*: Replacement of two  $[(V21)O_4]^{3-}$  units with one  $[V_2O_7]^{4-}$  entity. Ellipsoids are of 75% probability ( $M = Co$ ).

There are two  $[VO_4]$ -units located in the six- and three-membered channels, respectively. In the larger six-membered channels, six  $[(V1)O_4]$  units surround one  $[M2O_6]$  unit and isolate the latter from the framework. The  $[(V2)O_4]$ -units fill the smaller three-membered channels in the idealized structure model. However, from the structure refinement, we found significant residual electron density close to V21 and refined this as a partially

occupied V22 position, see Figure 6.8. The occupancies of V21 and V22 are correlated and represented by  $z$  for V22 and  $1-z$  for V21. Thus, the three-membered channels are actually filled by  $[(V21)O_4]$  and  $[(V21,22)O_7]$  entities. The occupancy with these two entities are given in the general formula as  $\{[VO_4]_{1-2z}[V_2O_7]_z\}$ . The parameter  $z$  varies for different  $M$  cations, 0.13-0.19 for the Mn series, 0.32-0.41 for the Co series, and 0.28 for the MgII compound) and is found unrelated to the occupancy of the  $M2$  site,  $x$ . The thermal ellipsoid of O21 is extended in the  $ab$  plane. This can be attributed to the expected non-linear V–O–V bridging angle for a  $[V_2O_7]^{4-}$  entity.

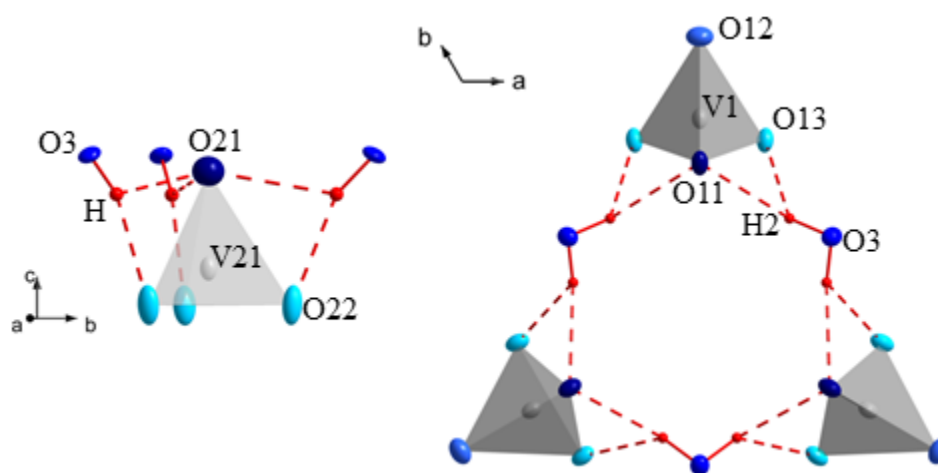


Figure 6.9. *Left*: Hydrogen bonding for hydroxide ( $O3-H$ ). *Right*: Hydrogen bonding for water ( $O3-(H2)_2$ ) in the case of MgII. Ellipsoids are of 75% probability.

We found only hydroxide groups for the Co-series and Mn-series, but alternative additional H positions (H2) for the MgII compound which indicate the presence of water molecules. The hydroxide exhibits only weak donor qualities and is expected to have an

electrostatic type of bonding, whereas the H<sub>2</sub>O molecule can act as a proton donor, and stronger interaction between H and the vanadate is expected. In Figure 6.9, we show the net connectivity involving O3–H...O<sup>acceptor</sup> interactions for these two cases. The hydroxide is involved in three H...O<sup>acceptor</sup> contacts, which are oriented towards O21 and O22 of the [(V21)O<sub>4</sub>] unit. The H...O<sup>acceptor</sup> contacts of the water molecules in the MgII compound involving a [(V1)O<sub>4</sub>] unit and are also bifurcated. It is noteworthy that the change of the average V–O distances is not significant enough to indicate the presence of [HVO<sub>4</sub>] units for the entire series. The change in the orientation of H-bonding and accommodation for water molecules in MgII might be attributed to the increase in the average Mg1–O distances and the relatively larger *a* lattice constant compared with the CoII compound. We also found evidence for the hydrogen bonding of hydroxide and water molecules from infrared data.

The *M* site of the MgII compound can only be divalent. The partial occupancy of Mg2 position (*x* = 0.71) gives a total of 13.42 positive charges. The positive charges need to be balanced by  $3 \times [(V1)O_4]^{3-}$ ,  $0.28 \times [(V21,22)O_7]^{4-}$ ,  $0.44 \times [(V21)O_4]^{3-}$ ,  $3-y \times (OH)^-$ , and  $y \times (H_2O)$ . However, the features of a water molecule in the infrared data are not observed for the compounds with *M* = Co, Mn, or Fe, see below. These ions may occur as divalent or trivalent cations, while Fe is stable in aqueous solutions as a trivalent ion based on standard reduction potentials. Thus, the question of the charge balance is achieved by mixed valency, where only protonation is possible for the MgII case.

For the Co-series we consider Mn<sup>2+</sup>, Mn<sup>3+</sup>, or Fe<sup>3+</sup> as dopants as well as Mn<sup>3+</sup> for the Mn-series. The ratio framework to dopants of 6 : 1 is used for the synthesis to investigate the

above question on charge balanced mixed-valent compounds. The different dopants influence the overall net charge, the parameters of the respective unit cells, and the site preferences of  $M$  positions, as well as the physical property measurements.

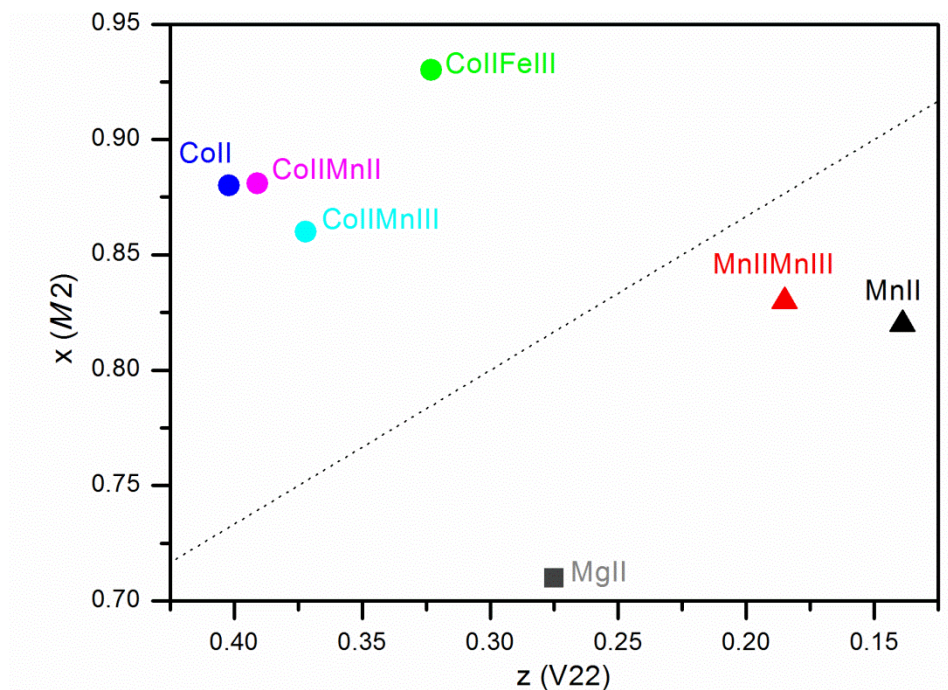


Figure 6.10. Site occupancies  $x(M2)$  and  $z(V22)$ . The dashed line represents the theoretical charge balanced relation: If the  $M2$  site is only occupied by  $M^{3+}$ , then  $x = 1 - 2/3z$  would be required.

The  $x$  and  $z$  parameters are not coupled, see Figure 6.10. It is interesting that for all the compounds with  $M$  = transition metal, the  $x$ -values are similar and much larger than those for MgII. Considering the  $x = 1 - 2/3z$  relation, the members of the Co-series are found above the dashed line indicating an “over-doped” situation on the  $M2$  site (chain), whereas the members of the Mn-series are below the dashed line and considered

“under-doped”. If we assume that no water molecules are present in the transition metal series of compounds, and consider the rather different values of  $x$  and  $z$ , mixed valence has to be taken into account for charge neutrality. The net negative charge is calculated for each compound based on  $z$  and the formula of  $M_{6+x}(\text{OH})_3[\text{VO}_4]_{4-2z}[\text{V}_2\text{O}_7]_z$ , ranging between -14.20 to -14.35 for the Co-series and -14.66 to -14.72 for the Mn-series. Then further divided by the total occupancy of  $M$  ( $6+x$ ), the results suggest effectively the presence of  $M^{n+}$  with  $n \sim 2.07$  (Co-series) and  $\sim 2.15$  (Mn-series). It is interesting to note, that the higher occupancy (“over-doped” case) of the  $M2$  site ( $x$ ) occurs for the Co-series to avoid nominal  $\text{Co}^{3+}$ , whereas for the Mn-series the total charge is “under-doped” for the  $M2$  site (Figure 6.10) which means  $\text{Mn}^{3+}$  cations are relatively favored. Overall, all compounds are deep red and those of the Co-series show metallic-like luster, see Figure 6.2.



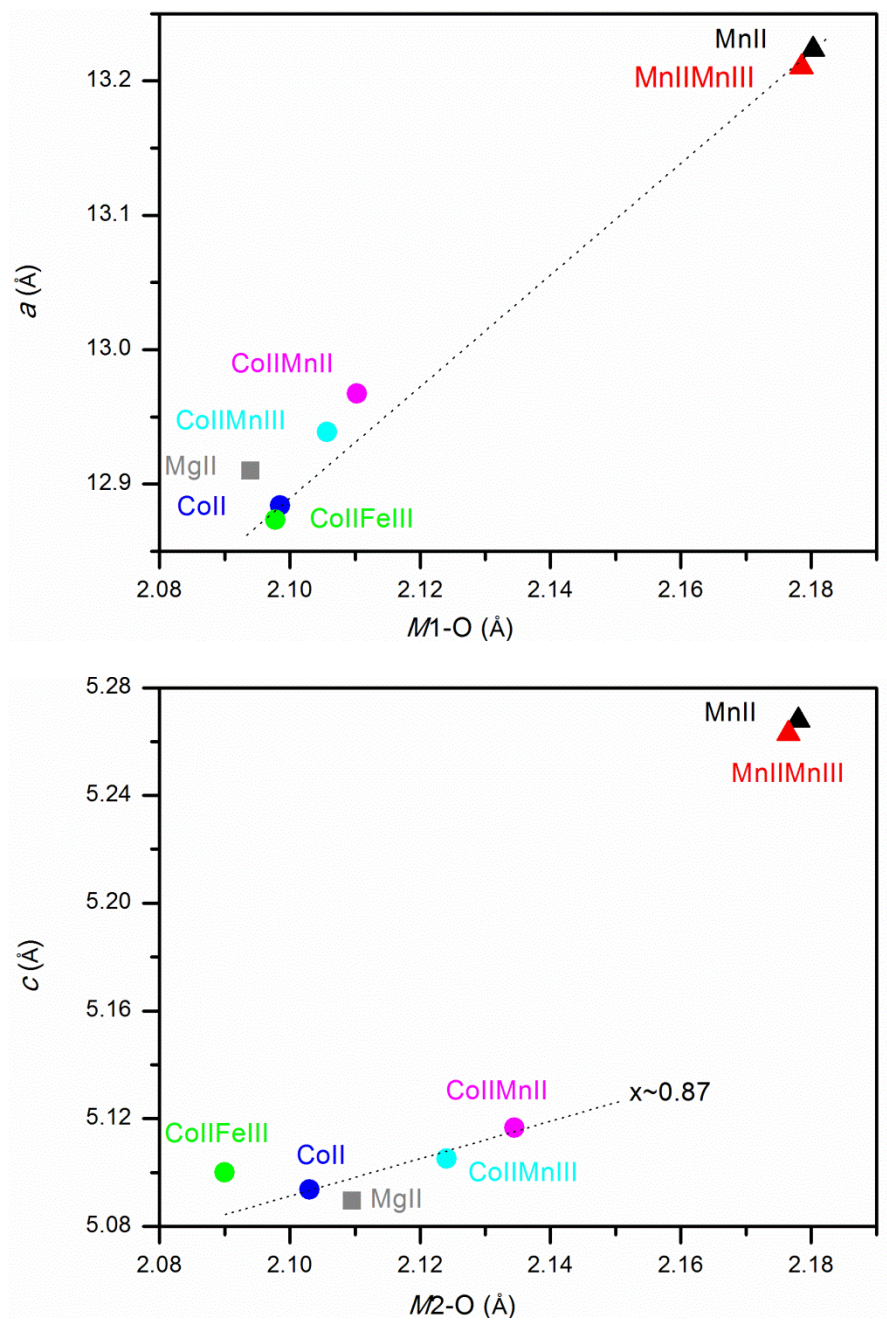


Figure 6.11.  $M$ - $O$  distances in relation to the lattice constants. Dashed lines serve as a guide to the eye. *Top*:  $M1$ - $O$ . *Bottom*:  $M2$ - $O$ .



In Figure 6.11, we give an evaluation of interatomic distances for  $M1-O$  and  $M2-O$  with respect to the cell parameters  $a$  and  $c$ , respectively. Due to the differences in ionic radii, the members of the Mn-series have larger  $M-O$  distances as well as larger cell parameters compared with the Co-series. Within the Co-series, the data suggest that the larger Mn cations acting as dopants might also occupy the  $M1$  site and only a limited portion of the  $M2$  sites since the expansion of the unit cell is found to significantly enlarge  $a$  and leave  $c$  almost unchanged. The smaller  $Fe^{3+}$  cations favor the  $M2$  sites, since there are almost identical  $a$  parameters observed for the CoII and CoIIFeIII compounds. The latter case poses some restrictions for  $M^{3+}$  ions due to the face-sharing arrangement leading to short  $M2-M2$  distances. As a result occupancy with  $M^{3+}$  seems limited for the  $M2$  site, as seen by lower contents of Fe ( $\sim 0.6$ ) from chemical analysis. It also indicates a mixed occupancy of Co and Fe for the  $M2$  sites. On the other hand, the higher value of  $x$  (0.93) compared with the other compounds in the Co-series results in an enlargement of the  $c$  axis despite shorter  $M2-O$  distances. The Mg-compound is included in Figure 6.11 for reference to reveal the difference in terms of the framework ( $a$  parameter) and statistical occupation of the  $M2$  site ( $c$  parameter).

## 6.7 Spectroscopy for $M_{6+x}(\text{OH})_3[\text{VO}_4]_{4-2z}[\text{V}_2\text{O}_7]_z$ .

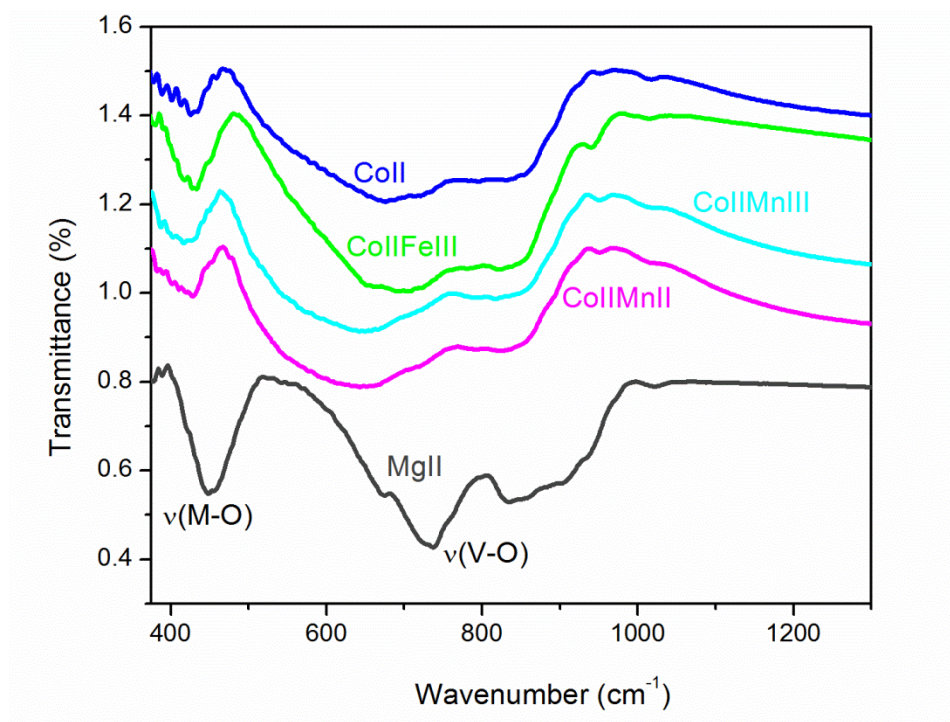


Figure 6.12. IR spectra for the Co-series compared with the MgII compound.

In Figure 6.12, the infrared spectra of the Co-series along with the MgII compound are shown. In general, a blue-shift occurs for all modes for the MgII compound which is expected due to the difference in atomic mass and the more ionic quality of the Mg–O bonds. In the region between  $375 - 450 \text{ cm}^{-1}$  mainly  $M\text{--O}$  stretching,  $\nu(M\text{--O})$ , and asymmetric V–O bending,  $\delta(\text{V--O})$ , are observed. Between  $600$  and  $1000 \text{ cm}^{-1}$ , dominantly V–O stretching occurs. However, from our DFT calculations, these modes are complicated and not entirely fundamental stretching vibrations of a 'free'  $[\text{VO}_4]$  entity ( $T_d$

symmetry), exhibiting three IR active  $\nu_3 \approx 780 \text{ cm}^{-1}$  and one Raman active  $\nu_1 \approx 830 \text{ cm}^{-1}$  modes. [22]

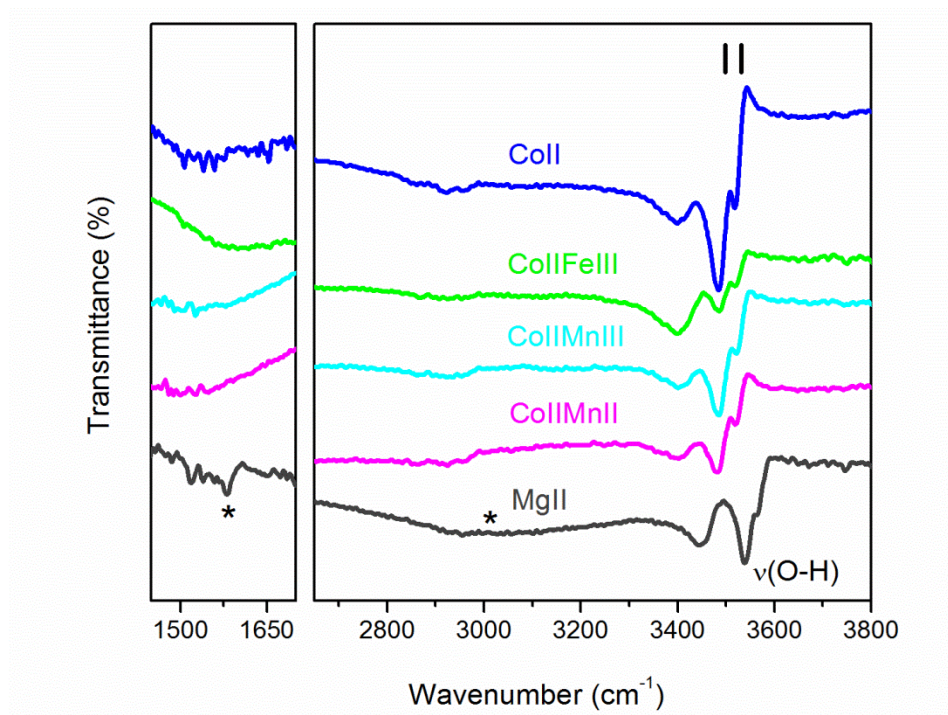


Figure 6.13. IR spectra for the Co-series in comparison with the MgII compound (\*) denotes H<sub>2</sub>O stretching vibrations.

We found evidence for the hydroxide and water molecules from the infrared data. In Figure 6.13, two sharp bands at around  $3500 \text{ cm}^{-1}$  were found which can be assigned as typical O-H stretching vibrations. [23] There is no further sign above the detection limit for the presence of H<sub>2</sub>O in the spectra of the transition metal compounds. However, for the MgII case, vibrations assigned to water molecules are the broad feature (\*) at around  $3000 \text{ cm}^{-1}$  and in addition the H<sub>2</sub>O bending mode is observed at  $1575 \text{ cm}^{-1}$ .

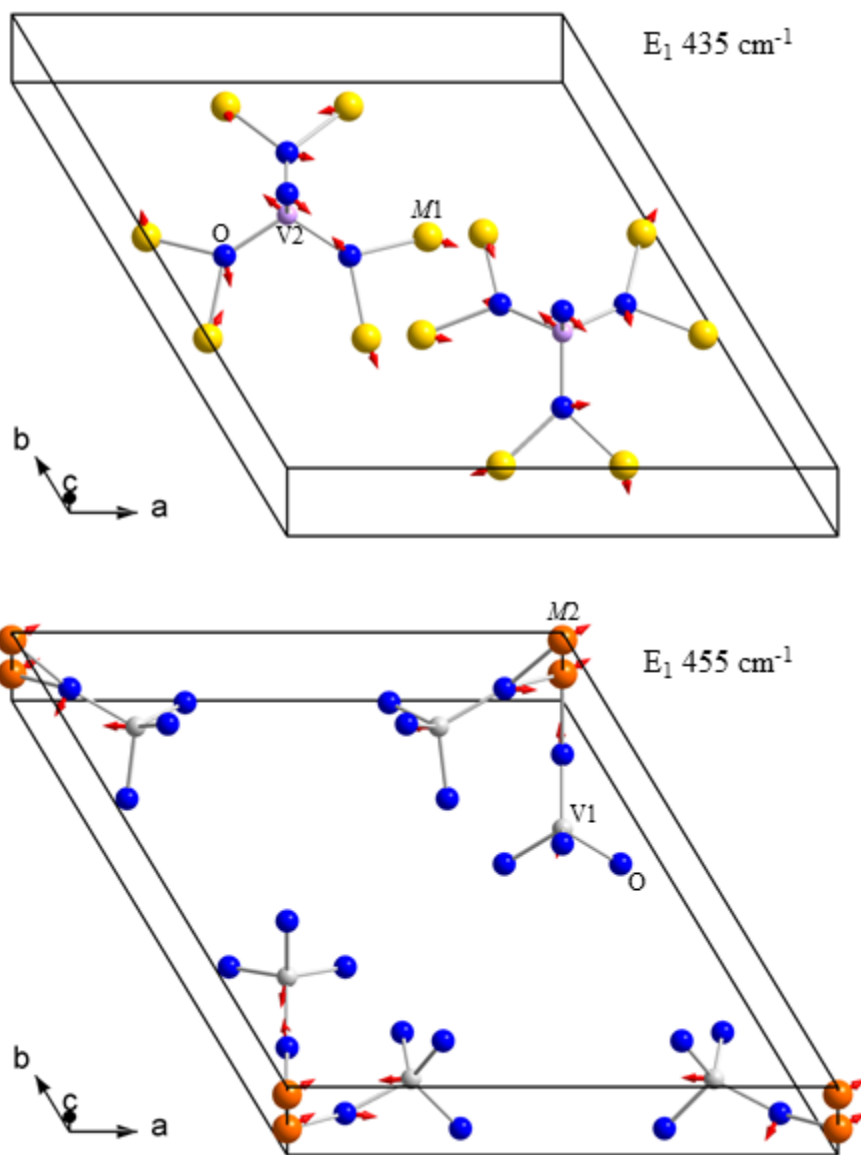


Figure 6.14. Selected displacements of  $\nu(M-O)$  and  $\delta(V-O)$  (375 - 450  $\text{cm}^{-1}$ ) based on DFT calculations for  $\text{Mn}_7(\text{OH})_3[\text{VO}_4]_4$ . Wavenumbers of assigned modes from experimental data for MnII. For better visualization all atoms not involved are omitted.

We have conducted DFT calculations for the idealized  $M_7(\text{OH})_3[\text{VO}_4]_4$  parent structure in order to study the lattice dynamics. Details are given in the supplementary material. (S-5) Out of 198 modes per unit cell, those of  $A_1$  and  $E_1$  are Raman and IR active, while  $E_2$  modes are only Raman active. The remaining modes are silent. In the region around  $375 - 450 \text{ cm}^{-1}$ , three  $E_1$  and one  $A_1$  modes can be assigned to either  $\nu(M1\text{--O})$  or  $\nu(M2\text{--O})$  vibrations coupled to asymmetric  $\delta(\text{V--O})$  displacements. (Figure 6.14)

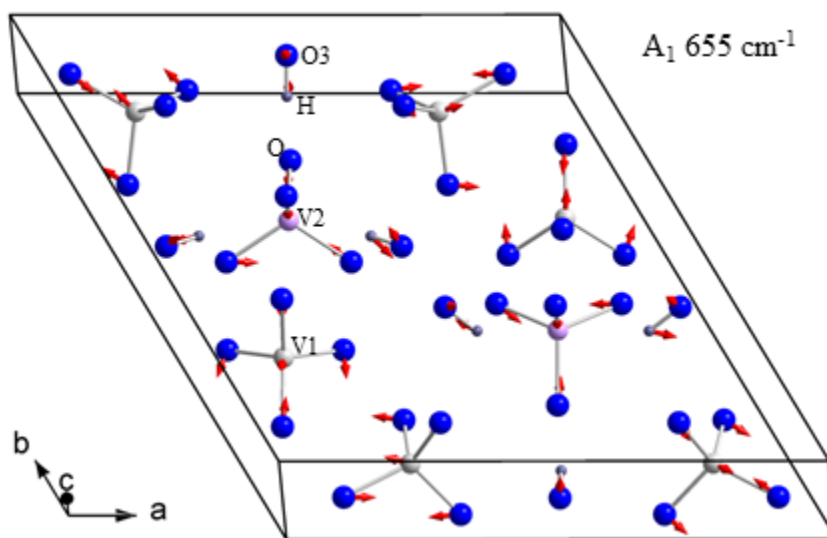


Figure 6.15. Displacements of the coupled V1/V2-type with noticeable H-displacement contributions ( $655 \text{ cm}^{-1}$ ) based on DFT calculations for  $\text{Mn}_7(\text{OH})_3[\text{VO}_4]_4$ . Wavenumbers of assigned modes from experimental data for MnII. For better visualization all atoms not involved are omitted.

Above  $600 \text{ cm}^{-1}$ , we find the modes related to  $\nu(\text{V--O})$  stretching vibrations. Overall, those modes associated with the  $[(\text{V1})\text{O}_4]^{3-}$  units appear at lower wavenumbers compared

with the ones for the  $[(V2)O_4]^{3-}$  units. Some modes involve both  $[(V1)O_4]^{3-}$  and  $[(V2)O_4]^{3-}$  units. Note that one  $A_1$  mode at  $655\text{ cm}^{-1}$  of the coupled V1/V2-type also features in noticeable H displacement contributions. (Figure 6.15)

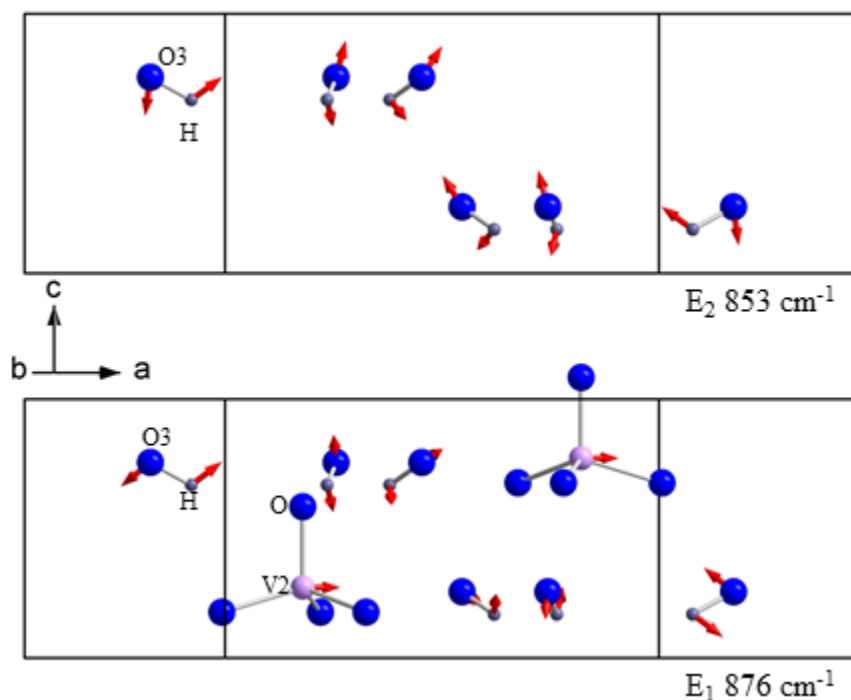


Figure 6.16. Displacements of coupled O–H liberation modes ( $830 - 950\text{ cm}^{-1}$ ) based on DFT calculations for  $Mn_7(OH)_3[VO_4]_4$ . Wavenumbers of assigned modes from experimental data for MnII. For better visualization all atoms not involved are omitted.

An interesting region between the two highest  $A_1$  modes,  $\nu(V2-O) \approx 820\text{ cm}^{-1}$  and  $950\text{ cm}^{-1}$ , contains O–H (liberation) and V–O displacements for the two  $E_1$  modes and only O–H (liberation) for the two  $E_2$  modes. (Figure 6.16)

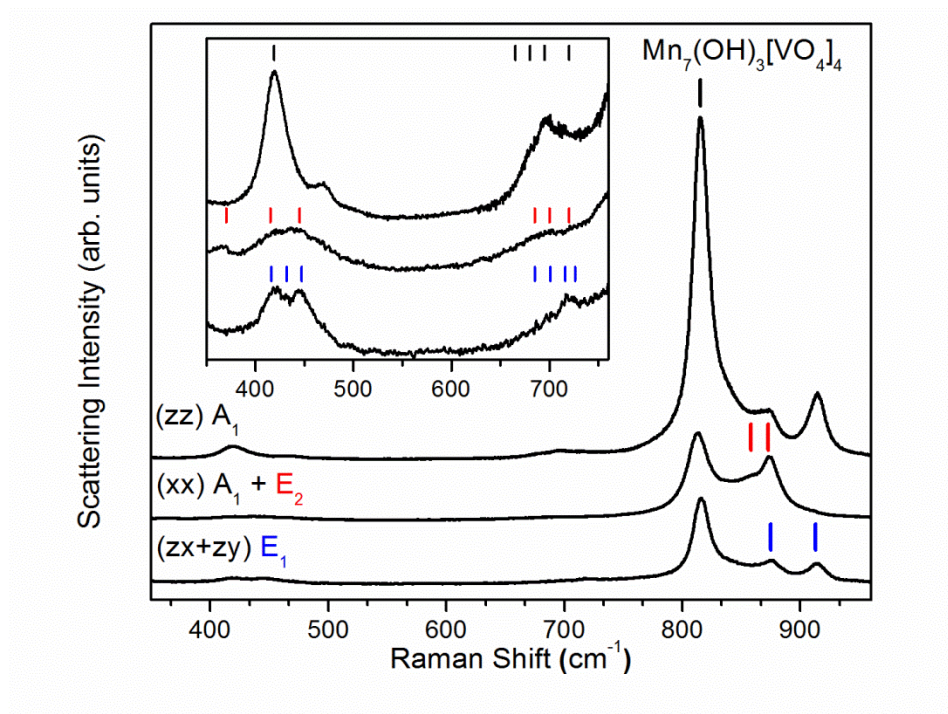


Figure 6.17. Single crystal Raman spectra of the MnII compound. The inset presents a 19 times magnification. Markers: Assigned modes based on phonon calculations for the idealized  $\text{Mn}_7(\text{OH})_3[\text{VO}_4]_4$  structure.

The polarized Raman spectra were measured for a single crystal of MnII. (Figure 6.17) The needle shape of the crystal allowed for orientation with the  $c$  axis parallel to the incident beam for (zz) and (zx+zy) in backscattering mode. Polarized spectra (xx) were taken perpendicular to the  $c$  axis. Based on the DFT calculations and factor group analysis we were able to identify and assign the observed bands to the respective symmetries.

Prominent Raman modes are observed between 800 and 950  $\text{cm}^{-1}$ . We found two  $E_2$  modes in the polarization of (xx) and two  $E_1$  modes in the polarization of (zx+zy). The



most intense band at  $816\text{ cm}^{-1}$  is the  $A_1$  mode. This is in excellent agreement with the fundamental symmetric  $\nu_1(\text{V-O})$  vibration ( $C_{3v}$  symmetry) and is assigned to the  $[(\text{V2})\text{O}_4]^{3-}$  entity located in the triangular channels of the structure. Protonation of these entities within these channels has been suggested by previous reports on the dumortierite-type of compounds. [8-14, 16, 18] However, solution spectra of  $[\text{HVO}_4]^{2-}$  or  $[\text{HV}_2\text{O}_7]^{4-}$  suggest that, in such a case,  $\nu_1(\text{V-O})$  should shift by approximately 50 or  $100\text{ cm}^{-1}$ , respectively [24], which is not observed here.

From DFT calculations the region between 600 and  $800\text{ cm}^{-1}$  is associated with the displacements of asymmetric  $\nu((\text{V1},2)\text{-O})$  and symmetric  $\nu((\text{V1})\text{-O})$  vibrations or a combination of both of them. Remarkably, displacements of the  $[(\text{V1})\text{O}_4]^{3-}$  entity, which links the *M1* framework with the *M2* chains in the hexagonal channels, are exhibiting rather weak Raman intensities.

Our calculations are in an excellent agreement overall with the observations in the Raman spectra except for the region between 600 and  $800\text{ cm}^{-1}$ . Blue shifts of approximately  $130\text{ cm}^{-1}$  ( $\Delta\nu_{\text{av.}} \approx 20\%$ ) were observed in this region. It can be explained by the idealized  $M_7(\text{OH})_3[\text{VO}_4]_4$  structure model used for the calculations with a net charge of -15. The real series show values of -14.3 or -14.7 for the Co- or Mn-series, respectively. This suggests that charge redistribution occurs for the real structures and it appears that the electronic structure derived from DFT calculations effectively favors the V1 site. Note that the calculations suggest V1-O average distances of  $1.79\text{ \AA}$ , which are longer than observed for the  $[(\text{V1})\text{O}_4]^{3-}$  site. Hence, the calculated charge distribution would be best described as 'one hole per 24 oxygen' on average per unit cell, instead of localized mixed



valency on the transition metal cation sites. For the 'real' compounds with lesser net charges an elongation is within the standard deviations of the V1–O distance, e.g.  $1.71 \text{ \AA} + 0.26 \times 0.08 \text{ \AA} = 1.73 \text{ (Co)}$ . Furthermore, the relative reduction of  $\nu(\text{V1–O})$  with respect to  $\nu(\text{V2–O})$  for the  $A_1$  modes on average by up to  $\approx -175 \text{ cm}^{-1}$  supports this electronic structure. However, size effects do play a role for the Mn cases ( $M2$  site), but also the higher stability of a formal  $\text{Mn}^{3+}$  (smaller ionic radius) needs to be taken into account for the higher net charge in comparison with the Co case. We conclude that the site occupancies ( $x$ ,  $z$ ) and dopings support a scenario of individually charge balanced electronic structures ( $M = \text{Co}$  or  $\text{Mn}$ ) and are driven also by size effects of the respective transition metal cations.

As discussed, it is necessary to strictly control the vanadate concentration in the starting solution in order to obtain the dumortierite-like phases. Our synthesis of the MnII compounds under different starting concentrations indicates that the dumortierite-like phases are preferred when the concentration of  $[\text{VO}_4]^{3-}$  was below  $0.05 \text{ mol/l}$ , which marks the borderline between  $[\text{HVO}_4]^{3-}$  and  $[\text{V}_2\text{O}_7]^{4-}$  in the basic aqueous solutions. [25] At higher concentrations the portion of  $\text{Mn}_2\text{V}_2\text{O}_7$  in the product increases and precipitates as the major phase above  $0.1 \text{ mol/l}$ . In Figure 6.18, we compare the IR spectra of MnII and MnIIMnIII with  $\text{Mn}_2\text{V}_2\text{O}_7$ . It is worth mentioning that the shoulder at around  $530 \text{ cm}^{-1}$  in the  $\text{Mn}_2\text{V}_2\text{O}_7$  spectrum is a feature of the  $[\text{V}_2\text{O}_7]^{4-}$  entity. [24] It is expected to be very weak for observation in the spectra of the  $(M1)_6(\text{OH})_3[\text{VO}_4]_3(M2)_x\{[\text{VO}_4]_{1-2z}[\text{V}_2\text{O}_7]_z\}$  series, since  $z = 0.13 - 0.4$  indicates a low concentration of  $[\text{V}_2\text{O}_7]^{4-}$  species. An alternative for  $[\text{V}_2\text{O}_7]^{4-}$  that has been frequently

adopted in the literature of dumortierite-like minerals synthesized in acidic media is the protonated vanadate,  $[\text{HVO}_4]^{2-}$ . [18] According to our synthesis procedure at controlled high pH values, structural and spectroscopic studies we find no strong support for such a scenario for the transition metal series.

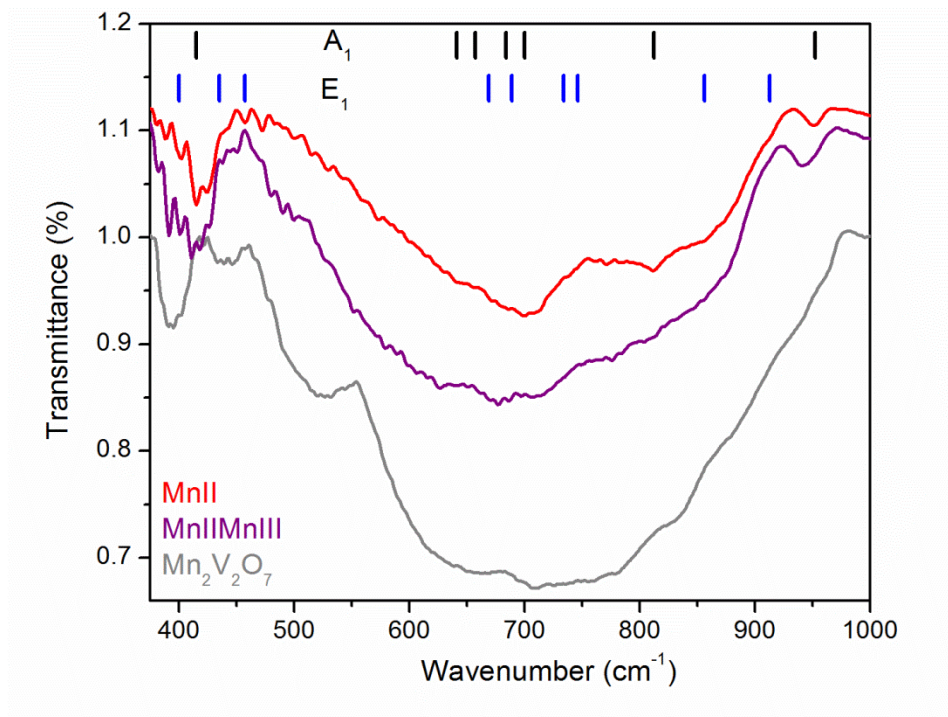


Figure 6.18. IR spectra for the Mn series in comparison with  $\text{Mn}_2\text{V}_2\text{O}_7$ . Markers: Assigned modes based on phonon calculations for the idealized  $\text{Mn}_7(\text{OH})_3[\text{VO}_4]_4$  structure.

## 6.8 Physical Properties of $M_{6+x}(\text{OH})_3[\text{VO}_4]_{4-2z}[\text{V}_2\text{O}_7]_z$ .

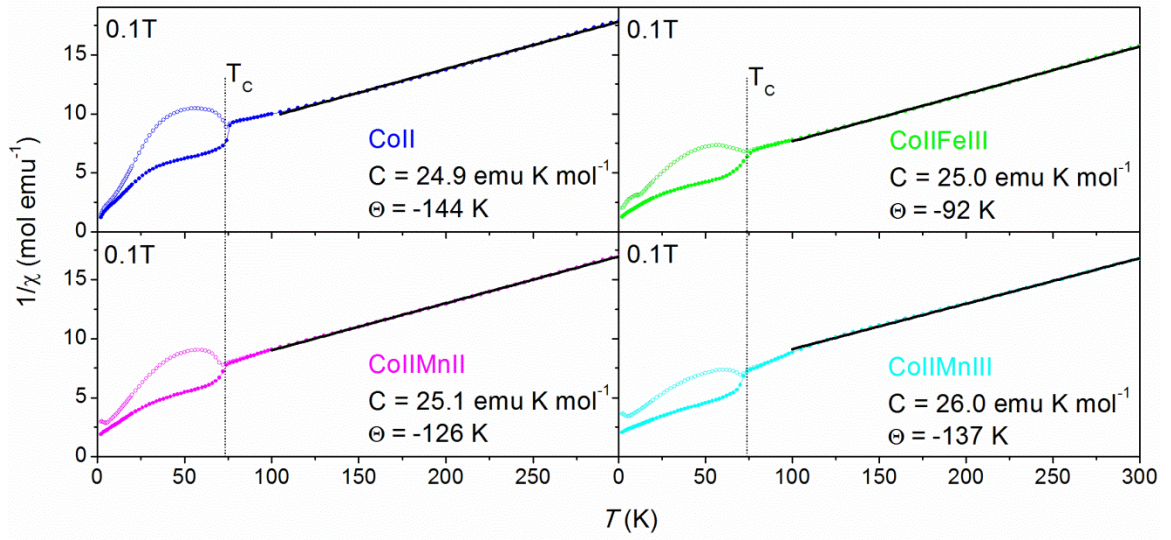


Figure 6.19. Reciprocal susceptibility per formula unit for the compounds of Co-series at 0.1 T (symbols: open (ZFC) and full (FC)). Curie-Weiss fit to the temperature range 100 - 300 K (line). The grey line serves as a guide to the eye and indicates  $T_C$ .

Physical properties were investigated regarding susceptibility and specific heat measurements. Here, we focus on the compounds of Co-series. The susceptibility data at 0.1 T are plotted as the reciprocal susceptibility,  $1/\chi(T)$ , in Figure 6.19 along with a linear fit for the range of 100 K to 300 K for the Curie-Weiss law. Overall, similar Curie constants (expected per formula unit: 24.5 - 26.0 emu K mol<sup>-1</sup>) are observed for CoII, CoIIFeIII, and CoIIMnII. For CoIIMnIII the Curie constant is slightly higher and  $1/\chi(T)$  curves below 100 K approaching the long range order temperature,  $T_C$ . All of the compounds order at around 74 K. The Weiss constants,  $\Theta$ , are rather different and

specific with respect to the different dopant. The  $\Theta$  values indicate dominant antiferromagnetic correlations.

Below  $T_C$  splitting between field cooled (FC) and zero-field cooled (ZFC) measurements are evident and indicate a canted antiferromagnet exhibiting ferrimagnetic behavior. The relative difference between FC and ZFC is again a function of the respective dopant. Likewise, dissimilar features develop below 20 K with respect to the FC data: For CoIIFeIII a plateau is reached around 10 K, which is almost absent for CoII. For both CoIIMnII and CoMnIII an upturn is seen around 5 K.

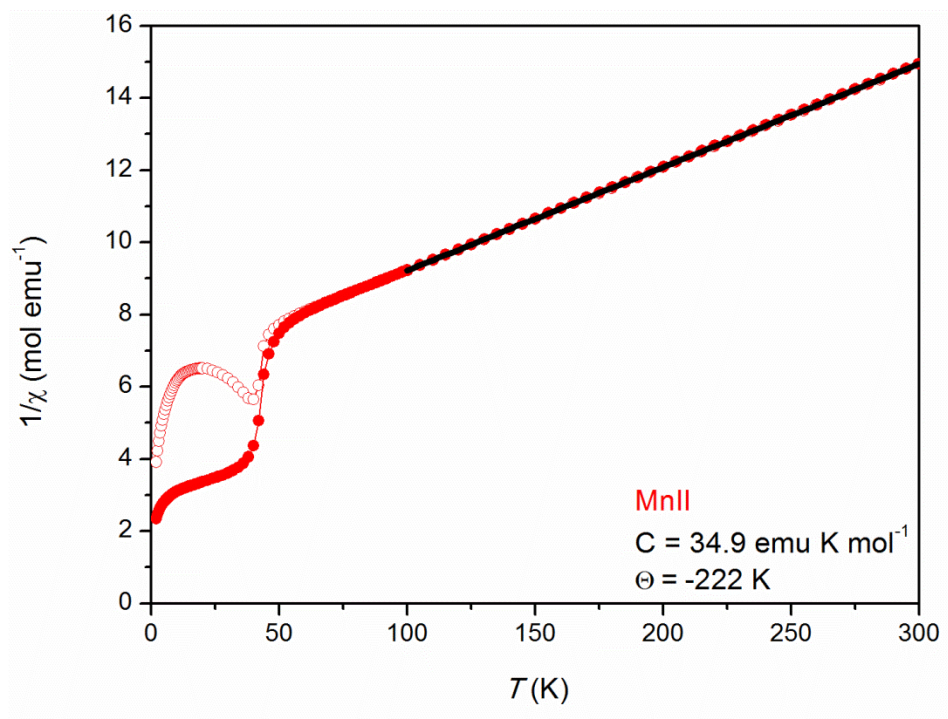


Figure 6.20. Reciprocal susceptibility per formula unit for MnII at 0.1 T (symbols: open (ZFC) and full (FC)). Curie-Weiss fit to the temperature range 100 - 300 K (line).

The reciprocal susceptibility,  $1/\chi(T)$ , for MnII is also plotted, see Figure 6.20. The Curie constant derived from the linear fit for the range of 100 K to 300 K is  $34.9 \text{ emu K mol}^{-1}$  which is higher than the expected value of  $29.9 \text{ emu K mol}^{-1}$  per formula unit. As discussed, the larger Curie constant can be attributed to the small impurities of  $\text{Mn}_2\text{V}_2\text{O}_7$ . The order temperature,  $T_C = 50 \text{ K}$ , for MnII is different from that of the Co-series, which depends on the different metal ions in the framework. The  $\Theta$  value of  $-222 \text{ K}$  indicates dominant antiferromagnetic correlations. Below  $T_C$  splitting between ZFC and FC is also observed for MnII indicating a canted antiferromagnet exhibiting ferrimagnetic behavior.

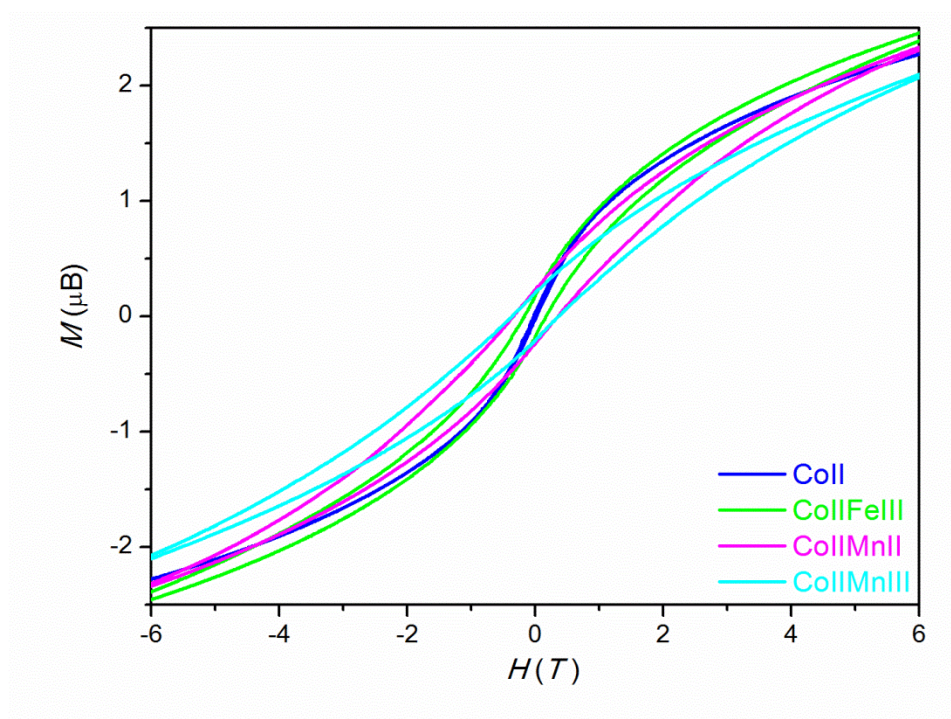


Figure 6.21. Magnetization,  $M(H)$ , per formula unit the compounds of Co series at 2 K.

The magnetization data,  $M(H)$ , at 2 K are presented for the Co-series (Figure 6.21) indicating an approximately effective spin of  $3/2$  at low temperature. CoII and CoIIMnII reach the same  $\mu_B$  value of 2.3 at 6 T, but differ in their respective hysteresis loops. CoIIFeIII and CoIIMnIII exhibit also individual and dissimilar hysteresis loops with  $\mu_B = 2.4$  and 2.1, respectively. The differences can be attributed to the dopants.  $\text{Fe}^{3+}$  and  $\text{Mn}^{2+}$  are  $S = 5/2$  and  $\text{Mn}^{3+}$  represents a  $S = 2$  system, differing from the major component of  $\text{Co}^{2+}$  ( $S = 3/2$ ). Thus, we conclude that our synthetic compounds indeed incorporate the respective dopants and the magnetic structure is susceptible to the specific spin systems of dopants. It is of interest to find significantly different  $M(H)$  data for the two  $S = 5/2$  cases regarding  $\text{Fe}^{3+}$  and  $\text{Mn}^{2+}$ , which suggests that, beyond the nominal doping concentration, preferences in  $M1/M2$  site occupancies differ with respect to specific dopants.



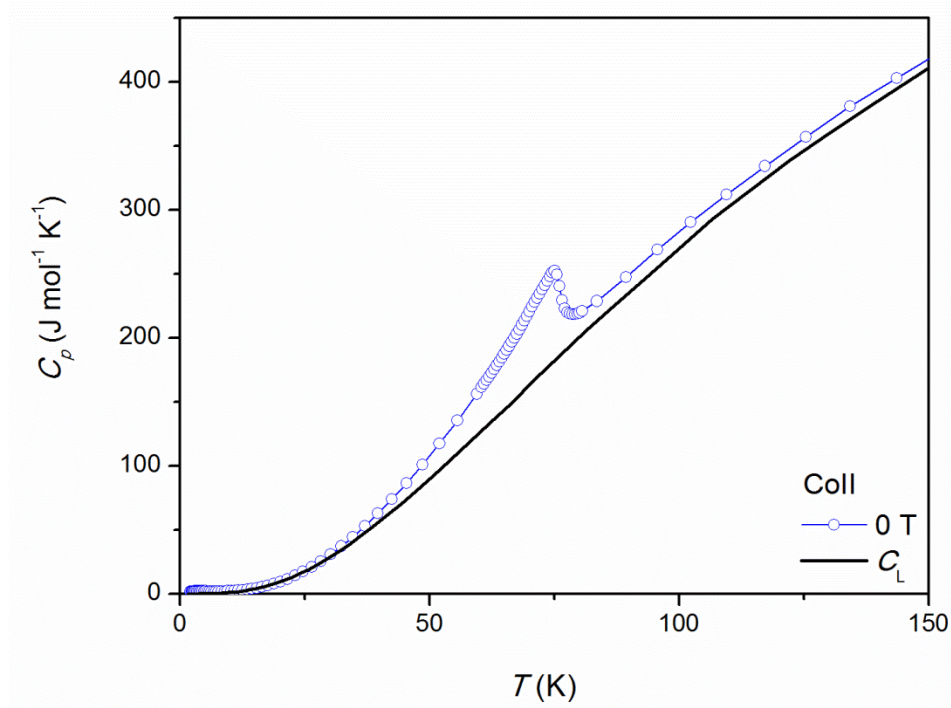


Figure 6.22. Extraction of the magnetic part of specific heat for CoII,  $C_m(T)$ , from the  $C_p(T)$  data by subtracting the lattice contribution,  $C_L(T)$ , represented by a baseline derived from the non-magnetic MgII data.

The specific heat measurements were conducted at 0 T in the temperature range from 2 K to 300 K. From the  $C_p(T)$  data, the lattice contribution,  $C_L(T)$ , represented by a baseline derived from the non-magnetic MgII data has been subtracted. (Figure 6.22) This allows lattice extraction of the magnetic part of specific heat,  $C_m(T)$ .

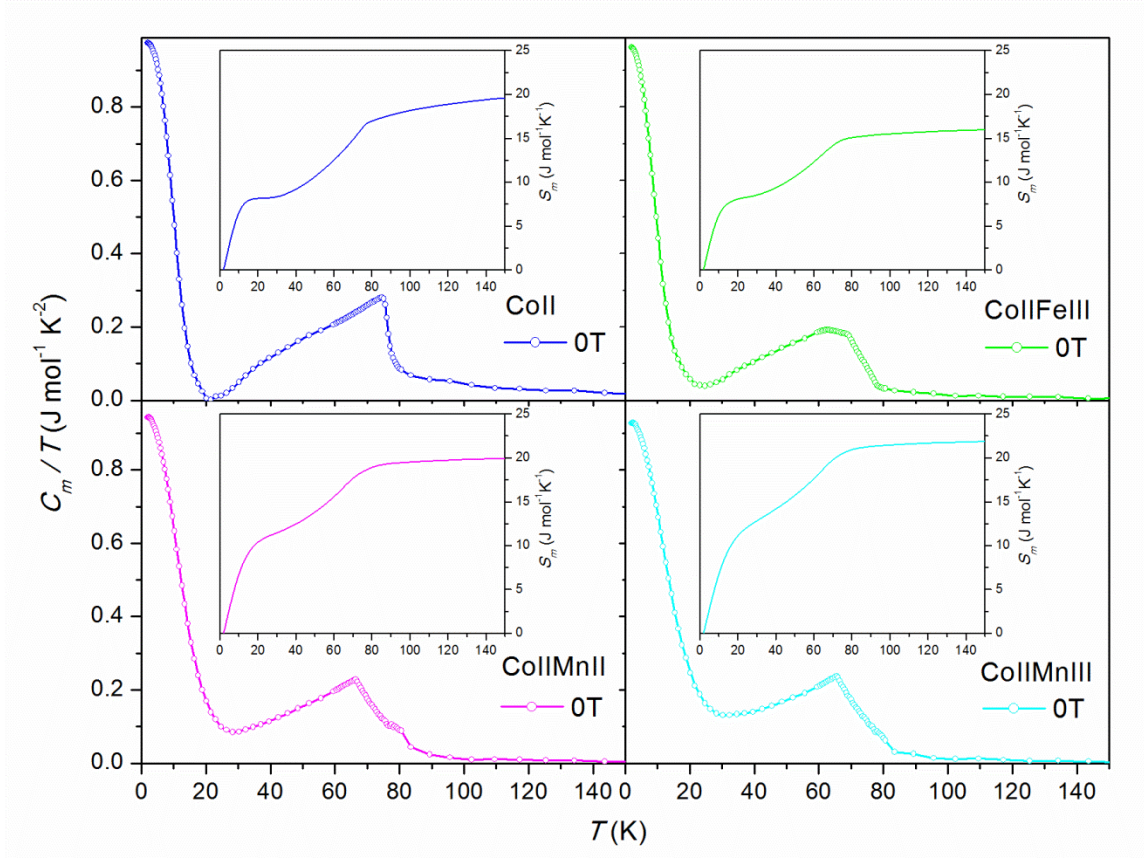


Figure 6.23. Specific heat data for the compounds of Co series at 0 T. *Main panels:* Magnetic part of the specific heat,  $C_m/T$ . *Insets:* Magnetic entropy,  $S_m$ .

In Figure 6.23, we show the magnetic part of the specific heat,  $C_m(T)/T$ , and the associated magnetic entropy,  $S_m(T)$ . In the  $S_m(T)$  plot, Both CoII and CoIIFeIII reach the 20 K plateau at around  $8 \text{ J mol}^{-1} \text{ K}^{-1}$  indicating the same Co framework. At 150 K, they reach different values of  $S_m$ . The difference between the two plateaux is associated with the  $\lambda$ -anomaly of  $C_m(T)/T$  at  $T_c = 74 \text{ K}$ . The low value of CoIIFeIII is probably due to the reduced doping of  $\text{Fe}^{3+}$  on the  $M2$  site forming  $\text{Fe}^{3+}\text{--Fe}^{3+}$  dimers along the chain. The plateau for CoIIMnII and CoIIMnIII reaches  $10 - 11 \text{ J mol}^{-1} \text{ K}^{-1}$  at 20 K suggesting the



preference of framework for the  $\text{Mn}^{2+}$  ions. The differences between the two plateaux of  $\text{CoIIMnII}$  and  $\text{CoIIMnIII}$  are similar to  $\text{CoII}$  indicating the dominance of  $\text{Co}^{2+}$  occupancy of the  $M2$  site.

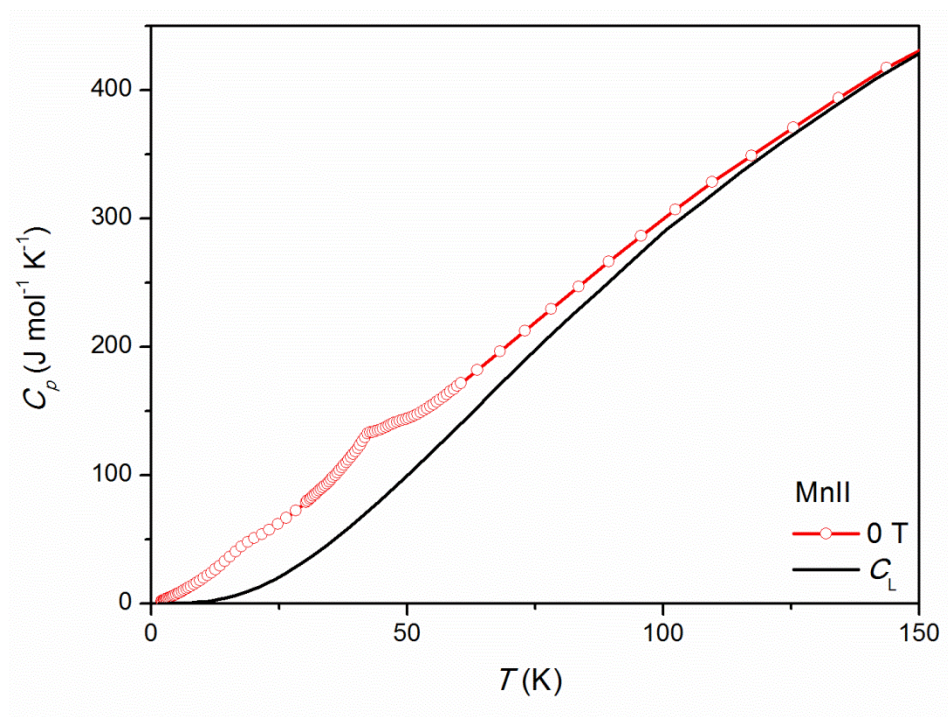


Figure 6.24. Extraction of the magnetic part of specific heat for MnII,  $C_m(T)$ , from the  $C_p(T)$  data by subtracting the lattice contribution,  $C_L(T)$ , represented by a baseline derived from the non-magnetic MgII data.

In Figure 6.24, a weak anomaly is observed at  $T_C = 40$  K for the  $C_p(T)$  data of MnII. The magnetic contribution to the total specific heat,  $C_m(T)$ , was also obtained by subtracting the phonon contribution from the  $C_p(T)$  data. The entropy of MnII reaches a larger value than the Co-series at 150 K due to the  $S = 5/2$  system of  $\text{Mn}^{2+}$ . (Figure 6.25) The probable

impurity in the MnII sample may cause deviation from the expected  $S_m$  of  $\sim 30 \text{ J mol}^{-1} \text{ K}^{-1}$  based on the equation of  $R\ln(2S+1)$ .

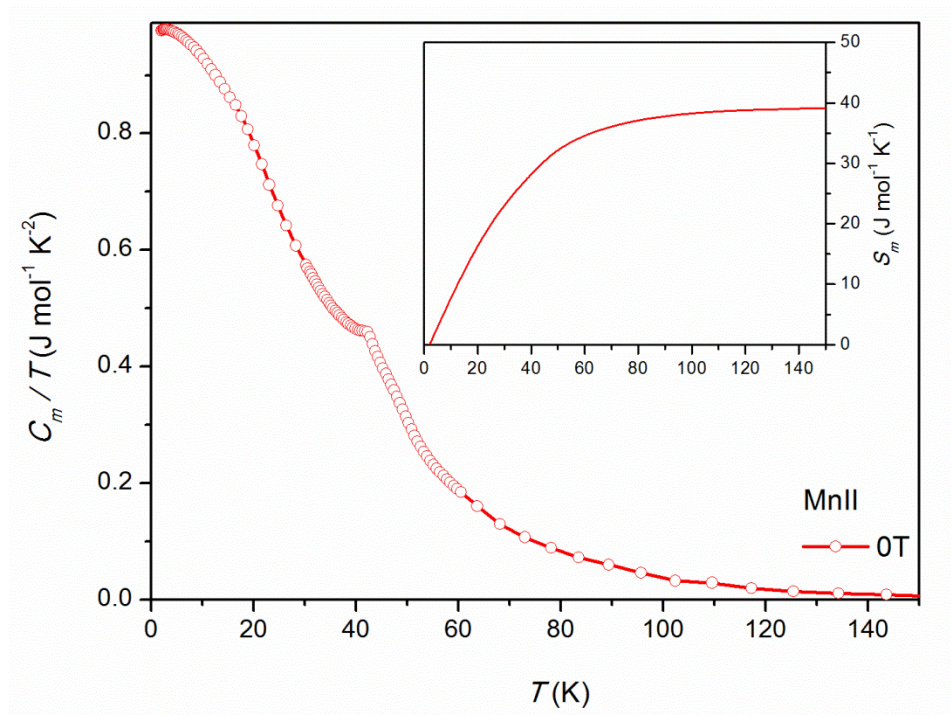


Figure 6.25. Specific heat data for MnII at 0 T. *Main panels*: Magnetic part of the specific heat,  $C_m/T$ . *Insets*: Magnetic entropy,  $S_m$ .

## 6.9 Discussion of the Structure-Property Relationship.

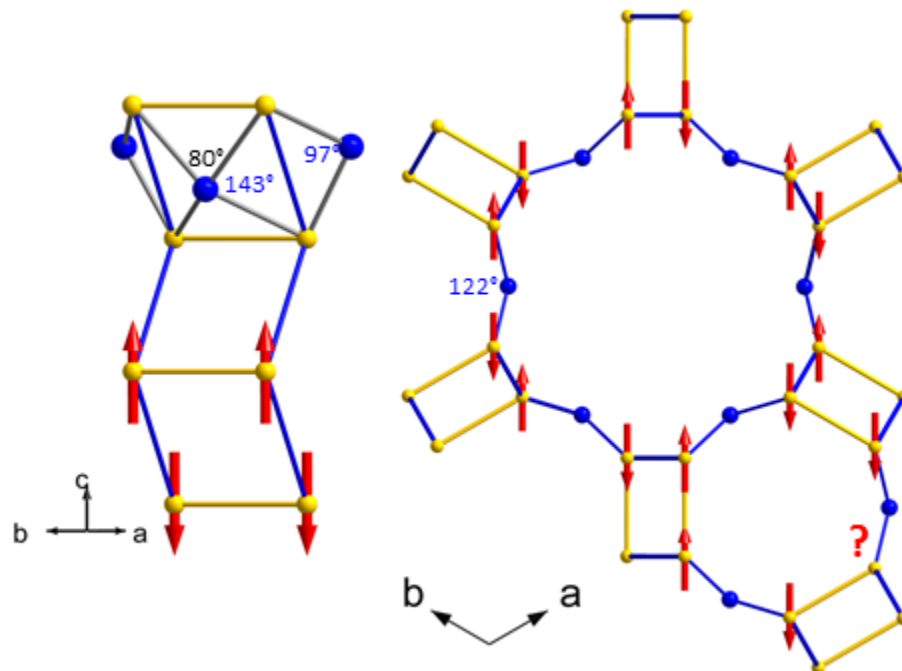


Figure 6.26. Sketch of the proposed spin arrangement of  $M1$  framework. *Left*:  $M1-O-M1$  connectivity for the  $M1$  ladder along  $[001]$ . *Right*: Kagome-like arrangement in the  $ab$  plane. (Blue bond: AFM correlation. Yellow bond: FM correlation. Red arrow: spin)

The  $M1$  framework forms in a kagome-like arrangement in the  $ab$  plane and extended to 3D via zigzag ladders along  $[001]$  as discussed in Figures 6.6 and 6.7. Based on the investigation of  $M1-O-M1$  connectivity on the ladder, we proposed that along the legs antiferromagnetic correlations and within the rungs ferromagnetic coupling can be expected based on the Kanamori-Goodenough rules. [26] The super-exchange via  $M1-O-M1$  should result in the spin orientations as shown in Figure 6.26. The ladders are

further connected via corners with an  $M1-O-M1$  angle of  $\sim 122^\circ$  indicating antiferromagnetic correlation. The six-membered ring of dimers is formed by connecting via the legs of the ladders. Thus, all the correlations within the six-membered channel are antiferromagnetic and the spin orientations are arranged in an alternating up-down fashion. The three-membered rings of dimers connect via the rungs of the ladders, which are presumably ferromagnetic in origin. The consequent alternative antiferromagnetic and ferromagnetic correlations lead to the geometrical frustration. (Figure 6.26)

## 6.10 Conclusions.

In this chapter, we report a series of dumortierite-like compounds. Needle-shaped crystals were synthesized by applying hydrothermal synthesis for  $M_{6+x}(\text{OH})_3[\text{VO}_4]_{4-2z}[\text{V}_2\text{O}_7]_z$  with  $M = \text{Mn}, \text{Co}, \text{Fe}, \text{or Mg}$ . Controlled reactions under different pH values and concentrations were studied, respectively. Thus, we were able to optimize the synthesis conditions to obtain phase pure products. For the Co series,  $\text{Mn}^{2+}$ ,  $\text{Mn}^{3+}$ , and  $\text{Fe}^{3+}$  were integrated into the structure as dopants. Size and charge effects were evaluated for these doped compounds based on the structure analysis. Lattice dynamics were studied by comparing our spectroscopic data with DFT calculations based on the idealized  $M_7(\text{OH})_3[\text{VO}_4]_4$  structure model. The chemical analysis and physical properties confirmed the successful doping. The magnetic properties indicate ferrimagnetic behavior. The polar space group suggests possible multiferroic properties and further investigations are needed.

## 6.11 References.

- [1] Evans, R. J.; Groat, L. A. *Can. Mineral.*, **2012**, *50*, 1197.
- [2] Moore, P.B.; Araki, T. *Neues Jb. Miner. Abh.*, **1978**, *132*, 91.
- [3] Pryce, M. W. *Mineral. Mag.*, **1971**, *38*, 21.
- [4] Ferraris, G.; Ivaldi, G.; Chopin, C. *Eur. J. Mineral.*, **1995**, *7*, 167.
- [5] Chopin, C.; Klaska, R.; Medenbach, O.; Dron, D. *Contrib. Mineral. Petr.*, **1986**, *92*, 316.
- [6] Raade, G.; Rømming, C.; Medenbach, O. *Miner. Petrol*, **1998**, *62*, 89.
- [7] Keller, P. *Eur. J. Mineral.*, **2001**, *13*, 769.
- [8] Marcos, M. D.; Amorós, P.; Beltrán-Porter, A.; Martínez-Máñez, R. *Chem. Mater.*, **1993**, *5*, 121.
- [9] Marcos, M. D.; Amorós, P.; Le Baul, A. *J. Solid. State Chem.*, **1993**, *107*, 250.
- [10] Attfield, M. P.; Morris, R. E.; Cheetham, A. K. *Acta Cryst. C*, **1994**, *50*, 981.
- [11] Che, R. C.; Peng, L.-M.; Zhou, W. Z. *Appl. Phys. Lett.*, **2005**, *87*, 173122.
- [12] Gu, Z.; Zhai, T.; Gao, B.; Zhang, G.; Ke, D.; Ma, Y.; Yao, J. *Cryst. Growth Des.*, **2007**, *7*, 825.
- [13] Ni, Y.; Liao, K.; Hong, J.; Wei, X. *CrystEngComm.*, **2009**, *11*, 570.
- [14] Pizarro, J. L.; Arriortua, M. I.; Lezama, L.; Rojo, T. *Solid State Ionics*, **1993**, *63-65*, 71.
- [15] Marcos, M. D.; Amorós, P.; Beltrán, D.; Beltrán, A.; Attfield, J. P. *J. Mater. Chem.*, **1995**, *5*, 917.
- [16] Hughes, R. W.; Gerrard, L. A.; Price, D. J.; Weller, M. T. *Inorg. Chem.*, **2003**, *42*, 4160.

- [17] F. Zhang, P. Y. Zavalij, M. S. Whittingham, *J. Mater. Chem.*, **1999**, 9, 3137.
- [18] T. Đorđević, Lj. Karanović, E. Tillmanns, *Cryst. Res. Technol.*, **2008**, 43, 1202.
- [19] Hu, T.; Lin, J.-B.; Kong, F.; Mao J.-G.; *Inorg. Chem. Comm.*, **2008**, 11, 1012.
- [20] Kato, K.; Kanke, Y.; Oka, Y.; Yao, T. Z. *Krist. - New Cryst. St.*, **1998**, 213, 26.
- [21] Pizarro, J. L.; Arriortua, M. I.; Lezama, L.; Rojo, T. *Solid State Ionics*, **1993**, 63-65, 71.
- [22] Nakamoto, K. *Infrared and Raman Spectra of Inorganic and Coordination Compounds*, Wiley, New York, **2009**.
- [23] Lutz, H.D. *Structure and Bonding*, **1995**, 82, 81.
- [24] Griffith, W. P.; Wiggins, T. D. *J. Chem. Soc. A*, **1966**, 1087.
- [25] Baes Jr., C. F.; Mesmer, R. E. *The Hydrolysis of Cations*, Wiley, N.Y., **1970**.
- [26] Goodenough, J. B. *Magnetism and the Chemical Bond*, Interscience, New York, **1963**.

## 6.12 Supplemental Material.

S-1: Table 6.7. Atomic composition for  $M_{6+x}(\text{OH})_3[\text{VO}_4]_{4-2z}[\text{V}_2\text{O}_7]_z$ .

CoII		Co	-	V
Position 1	Atomic %	42.24	-	24.48
	Stoichiometry	6.90	-	4.00
Position 2	Atomic %	30.56	-	17.32
	Stoichiometry	7.06	-	4.00
Position 3	Atomic %	45.29	-	26.15
	Stoichiometry	6.93	-	4.00
Position 4	Atomic %	63.4	-	36.6
	Stoichiometry	6.93	-	4.00
Position 5	Atomic %	41.98	-	23.76
	Stoichiometry	7.07	-	4.00
Position 6	Atomic %	32.06	-	18.1
	Stoichiometry	7.09	-	4.00
Average Stoichiometry		7.0(1)	-	4.0(1)
<p>Spectral lines for Position 1 as an example, atomic composition: 42.24 % Co; 24.48 % V.</p>				



Table 6.7. Continued.

CoIIFeIII		Co	Fe	V
Position 1	Atomic %	21.68	2.2	14.66
	Stoichiometry	5.92	0.600	4.00
Position 2	Atomic %	22.6	2.21	15.23
	Stoichiometry	5.94	0.580	4.00
Position 3	Atomic %	21.95	2.2	15.15
	Stoichiometry	5.80	0.581	4.00
Position 4	Atomic %	23.8	2.52	15.34
	Stoichiometry	6.21	0.657	4.00
Position 5	Atomic %	24.03	2.24	15.78
	Stoichiometry	6.09	0.568	4.00
Average Stoichiometry		6.0(2)	0.6(1)	4.0(1)
<p>Lsec: 180.0 0 Cnts 0.000 keV Det: Octane Pro Det</p>				
Spectral lines for Position 1 as an example, atomic composition: 21.68 % Co; 2.2 % Fe; 14.66 % V.				

Table 6.7. Continued.

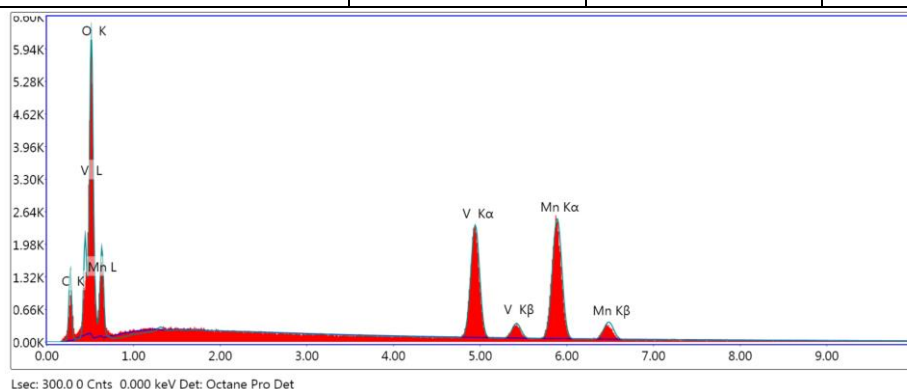
CoHMnII		Co	Mn	V
Position 1	Atomic %	21.09	2.79	14.07
	Stoichiometry	6.00	0.793	4.00
Position 2	Atomic %	23.76	3.51	16.57
	Stoichiometry	5.74	0.847	4.00
Position 3	Atomic %	23.52	3.59	15.54
	Stoichiometry	6.05	0.924	4.00
Position 4	Atomic %	24.67	3.58	16.88
	Stoichiometry	5.85	0.848	4.00
Position 5	Atomic %	23.47	3.82	16.58
	Stoichiometry	5.66	0.922	4.00
Position 6	Atomic %	26.37	4.75	18.5
	Stoichiometry	5.70	1.027	4.00
Average Stoichiometry		5.8(2)	0.9(1)	4.0(1)
<p>Spectral lines for Position 1 as an example, atomic composition: 21.09 % Co; 2.79 % Mn; 14.07 % V.</p>				

Table 6.7. Continued.

CoII MnIII		Co	Mn	V
Position 1	Atomic %	21.32	4.11	15.4
	Stoichiometry	5.54	1.068	4.00
Position 2	Atomic %	26.54	5.37	18.73
	Stoichiometry	5.67	1.147	4.00
Position 3	Atomic %	24.24	4.65	17.36
	Stoichiometry	5.59	1.071	4.00
Position 4	Atomic %	24.32	3.79	16.16
	Stoichiometry	6.02	0.938	4.00
Position 5	Atomic %	21.99	3.8	15.51
	Stoichiometry	5.67	0.980	4.00
Position 6	Atomic %	24.81	4.05	17.11
	Stoichiometry	5.80	0.947	4.00
Average Stoichiometry		5.7(2)	1.0(1)	4.0(1)
<p>Spectral lines for Position 1 as an example, atomic composition: 21.32 % Co; 4.11 % Mn; 15.4 % V.</p>				

Table 6.7. Continued.

MnII		Mn	-	V
Position 1	Atomic %	26.09	-	14.01
	Stoichiometry	7.45	-	4.00
Position 2	Atomic %	33.37	-	18.25
	Stoichiometry	7.31	-	4.00
Position 3	Atomic %	33.68	-	18.82
	Stoichiometry	7.16	-	4.00
Position 4	Atomic %	29.95	-	16.6
	Stoichiometry	7.22	-	4.00
Position 5	Atomic %	30.72	-	15.99
	Stoichiometry	7.68	-	4.00
Position 6	Atomic %	31.25	-	16.92
	Stoichiometry	7.39	-	4.00
Average Stoichiometry		7.4(2)	-	4.0(1)



Spectral lines for Position 1 as an example, atomic composition: 26.09 % Mn; 14.01 % V.

Table 6.7. Continued.

MnIIMnIII		Mn	-	V
Position 1	Atomic %	35.93	-	19.29
	Stoichiometry	7.45	-	4.00
Position 2	Atomic %	44.09	-	23.27
	Stoichiometry	7.58	-	4.00
Position 3	Atomic %	33.31	-	17.8
	Stoichiometry	7.49	-	4.00
Position 4	Atomic %	42.65	-	22.6
	Stoichiometry	7.55	-	4.00
Position 5	Atomic %	30.8	-	16.48
	Stoichiometry	7.48	-	4.00
Average Stoichiometry		7.5(1)	-	4.0(1)
<p>Spectral lines for Position 1 as an example, atomic composition: 35.93 % Mn; 19.29 % V.</p>				

Standard deviation was calculated based on the equation  $\sigma = \sqrt{\frac{\sum(x-\bar{x})^2}{n}}$ , where  $\sigma$  = standard deviation,  $\Sigma$  = sum of,  $x$  = each value in the data set,  $\bar{x}$  = mean value of the data set.  $n$  = number of values in the data set.

S-2: Table 6.8. Fractional atomic coordinates and isotropic or equivalent isotropic displacement parameters ( $\text{\AA}^2$ ) for  $M_{6+x}(\text{OH})_3[\text{VO}_4]_{4-2z}[\text{V}_2\text{O}_7]_z$ .

CoII	Wyckoff	<i>x</i>	<i>y</i>	<i>z</i>	$U_{\text{iso}}^*/U_{\text{eq}}$	Occ.( $<1$ )
Co1	<i>12d</i>	0.07553(8)	0.64922(8)	0.1662(1)	0.0087(2)	
Co2	<i>2a</i>	0	0	-0.0009(7)	0.0171(9)	0.88(1)
V1	<i>6c</i>	0.15047(7)	0.84953(7)	0.6964(3)	0.0079(3)	
O11	<i>6c</i>	0.1943(3)	0.8057(3)	0.980(1)	0.009(1)	
O12	<i>6c</i>	0.0750(3)	0.9250(3)	0.753(2)	0.015(2)	
O13	<i>12d</i>	0.9350(5)	0.6583(5)	0.011(1)	0.011(1)	
V21	<i>2b</i>	1/3	2/3	0.443(1)	0.008(7)	0.598(6)
V22	<i>2b</i>	1/3	2/3	0.165(2)	0.008(7)	0.402(6)
O21	<i>2b</i>	1/3	2/3	0.793(5)	0.023(6)	0.598(6)
O22	<i>6c</i>	0.1912(7)	0.5956(4)	0.319(2)	0.017(2)	
O3	<i>6c</i>	0.0523(7)	0.5261(3)	0.851(1)	0.010(1)	
H	<i>6c</i>	0.1162	0.5581	0.7100	0.014*	

Table 6.8. Continued.

CoIIFeIII	Wyckoff	<i>x</i>	<i>y</i>	<i>z</i>	$U_{\text{iso}}^*/U_{\text{eq}}$	Occ.( $<1$ )
Co1	<i>12d</i>	0.07577(9)	0.64901(9)	0.1663(2)	0.0104(3)	
Fe2	<i>2a</i>	0	0	-0.0015(8)	0.017(1)	0.93(2)
V1	<i>6c</i>	0.15034(8)	0.84966(8)	0.6962(4)	0.0087(4)	
O11	<i>6c</i>	0.1936(4)	0.8064(4)	0.982(2)	0.012(2)	
O12	<i>6c</i>	0.0744(4)	0.9256(4)	0.752(2)	0.016(2)	
O13	<i>12d</i>	0.9352(6)	0.6582(6)	0.011(1)	0.012(1)	
V21	<i>2b</i>	1/3	2/3	0.435(1)	0.0100(8)	0.677(8)
V22	<i>2b</i>	1/3	2/3	0.166(3)	0.0100(8)	0.323(8)
O21	<i>2b</i>	1/3	2/3	0.783(6)	0.030(7)	0.677(8)
O22	<i>6c</i>	0.1900(9)	0.5950(4)	0.314(2)	0.019(2)	
O3	<i>6c</i>	0.0537(9)	0.5268(4)	0.851(2)	0.013(2)	
H	<i>6c</i>	0.1277	0.5638	0.7293	0.019*	

Table 6.8. Continued.

CoIIIMnII	Wyckoff	$x$	$y$	$z$	$U_{\text{iso}}^*/U_{\text{eq}}$	Occ.(<1)
Co1	$12d$	0.07609(8)	0.64929(8)	0.1660(1)	0.0112(2)	
Mn2	$2a$	0	0	-0.003(1)	0.025(1)	0.86(2)
V1	$6c$	0.15163(7)	0.84837(7)	0.6942(4)	0.0099(3)	
O11	$6c$	0.1939(4)	0.8061(4)	-0.020(2)	0.013(1)	
O12	$6c$	0.0762(4)	0.9238(4)	0.751(2)	0.021(2)	
O13	$12d$	0.9345(5)	0.6575(5)	0.013(1)	0.013(1)	
V21	$2b$	1/3	2/3	0.440(1)	0.0115(8)	0.628(7)
V22	$2b$	1/3	2/3	0.161(2)	0.0115(8)	0.372(7)
O21	$2b$	1/3	2/3	-0.210(7)	0.031(7)	0.628(7)
O22	$6c$	0.1915(8)	0.5958(4)	0.309(2)	0.022(2)	
O3	$6c$	0.0520(7)	0.5260(4)	-0.148(2)	0.012(2)	
H	$6c$	0.1187	0.5593	-0.2746	0.018*	



Table 6.8. Continued.

CoII MnIII	Wyckoff	<i>x</i>	<i>y</i>	<i>z</i>	$U_{\text{iso}}^*/U_{\text{eq}}$	Occ.(<1)
Co1	<i>12d</i>	0.07587(3)	0.64915(3)	0.16629(5)	0.00959(9)	
Mn2	<i>2a</i>	0	0	-0.0009(4)	0.0208(4)	0.881(6)
V1	<i>6c</i>	0.15147(3)	0.84853(3)	0.6959(1)	0.0085(1)	
O11	<i>6c</i>	0.1942(1)	0.8058(1)	-0.0189(6)	0.0121(5)	
O12	<i>6c</i>	0.0758(1)	0.9243(1)	0.7526(7)	0.0176(6)	
O13	<i>12d</i>	0.9343(2)	0.6573(2)	0.0123(4)	0.0115(4)	
V21	<i>2b</i>	1/3	2/3	0.4412(4)	0.0085(3)	0.609(3)
V22	<i>2b</i>	1/3	2/3	0.1622(8)	0.0085(3)	0.391(3)
O21	<i>2b</i>	1/3	2/3	0.792(2)	0.027(2)	0.609(3)
O22	<i>6c</i>	0.1921(3)	0.5960(1)	0.3110(7)	0.0181(7)	
O3	<i>6c</i>	0.0517(3)	0.5259(1)	0.8526(5)	0.0110(5)	
H	<i>6c</i>	0.1103	0.5551	0.7173	0.016*	

Table 6.8. Continued.

MnII	Wyckoff	$x$	$y$	$z$	$U_{\text{iso}}^*/U_{\text{eq}}$	Occ.( $<1$ )
Mn1	$12d$	0.07915(8)	0.65350(8)	0.18469(18)	0.0142(2)	
Mn2	$2a$	0	0	0.0001(9)	0.0297(14)	0.834(13)
V1	$6c$	0.15025(7)	0.84975(7)	0.7089(3)	0.0120(3)	
O11	$6c$	0.1897(4)	0.8103(4)	0.9900(15)	0.0177(14)	
O12	$6c$	0.0757(3)	0.9243(3)	0.7536(17)	0.0223(17)	
O13	$12d$	0.9318(5)	0.6573(5)	0.0346(10)	0.0157(10)	
V21	$2b$	1/3	2/3	0.4472(8)	0.0158(8)	0.815(8)
V22	$2b$	1/3	2/3	0.155(4)	0.0158(8)	0.185(8)
O21	$2b$	1/3	2/3	0.777(5)	0.055(7)	0.815(8)
O22	$6c$	0.1956(8)	0.5978(4)	0.326(2)	0.030(2)	
O3	$6c$	0.0507(7)	0.5253(3)	0.8749(14)	0.0163(14)	
H	$6c$	0.0897	0.5449	0.7309	0.024*	

Table 6.8. Continued.

MnIIMnIII	Wyckoff	$x$	$y$	$z$	$U_{\text{iso}}^*/U_{\text{eq}}$	Occ.( $<1$ )
Mn1	$12d$	0.07921(6)	0.65313(6)	0.1852(2)	0.0132(2)	
Mn2	$2a$	0	0	0.0015(8)	0.030(1)	0.822(1)
V1	$6c$	0.15032(5)	0.84968(5)	0.7096(2)	0.0108(2)	
O11	$6c$	0.1900(3)	0.8100(3)	0.992(1)	0.016(1)	
O12	$6c$	0.0758(3)	0.9242(3)	0.755(1)	0.022(1)	
O13	$12d$	0.9323(4)	0.6576(4)	0.0358(8)	0.0163(8)	
V21	$2b$	1/3	2/3	0.4455(6)	0.0134(5)	0.861(6)
V22	$2b$	1/3	2/3	0.165(4)	0.0134(5)	0.139(6)
O21	$2b$	1/3	2/3	0.773(4)	0.056(5)	0.861(6)
O22	$6c$	0.1937(6)	0.5969(3)	0.331(2)	0.031(2)	
O3	$6c$	0.0525(5)	0.5263(3)	0.873(1)	0.016(1)	
H	$6c$	-0.0333	0.4834	0.8299	0.024*	

Table 6.8. Continued.

MgII	Wyckoff	$x$	$y$	$z$	$U_{\text{iso}}^*/U_{\text{eq}}$	Occ.( $<1$ )
Mg1	$12d$	0.3508(1)	0.4273(1)	0.1776(3)	0.0104(2)	
Mg2	$2a$	0	0	0.001(1)	0.020(2)	0.70(1)
V1	$6c$	0.30371(7)	0.15185(3)	0.2052(2)	0.0085(2)	
O11	$6c$	0.3867(3)	0.1934(2)	0.4938(7)	0.0113(7)	
O12	$6c$	0.1505(3)	0.0752(2)	0.2580(7)	0.0164(8)	
O13	$12d$	0.3441(2)	0.2778(2)	0.0256(5)	0.0114(5)	
V21	$2b$	1/3	2/3	0.4407(5)	0.0109(4)	0.726(4)
V22	$2b$	1/3	2/3	0.168(1)	0.0109(4)	0.274(4)
O21	$2b$	1/3	2/3	0.782(3)	0.040(3)	0.726(4)
O22	$6c$	0.4040(2)	0.5960(2)	0.3174(9)	0.0183(8)	
O3	$6c$	0.4756(2)	0.5244(2)	0.8704(7)	0.0111(7)	
H1	$6c$	0.4422	0.5578	0.7864	0.017*	
H2	$12d$	0.4166	0.4812	0.9664	0.017*	0.1667

S-3: Table 6.9. Selected Interatomic Distances (Å) for  $M_{6+x}(\text{OH})_3[\text{VO}_4]_{4-2z}[\text{V}_2\text{O}_7]_z$ .

	CoII	CoIIFeIII	CoIIMnII	CoIIMnIII	MnII	MnIIMnIII	MgII
M1–O13	2.033(5)	2.034(6)	2.048(5)	2.044(2)	2.112(5)	2.117(4)	2.040(3)
M1–O13'	2.034(5)	2.036(6)	2.052(6)	2.044(2)	2.127(5)	2.123(4)	2.041(3)
M1–O11	2.055(3)	2.054(4)	2.065(4)	2.060(1)	2.111(4)	2.107(3)	2.054(2)
M1–O22	2.068(6)	2.058(7)	2.073(6)	2.076(2)	2.145(6)	2.134(5)	2.056(3)
M1–O3	2.168(5)	2.165(7)	2.174(6)	2.170(2)	2.245(6)	2.245(4)	2.143(3)
M1–O3'	2.233(6)	2.240(7)	2.250(6)	2.240(2)	2.342(6)	2.345(5)	2.230(3)
M2–O12 (×3)	2.091(8)	2.08(1)	2.12(1)	2.113(3)	2.167(8)	2.165(6)	2.088(5)
M2–O12' (×3)	2.115(8)	2.10(1)	2.149(9)	2.135(4)	2.189(9)	2.188(7)	2.131(5)
V1–O12	1.709(8)	1.718(9)	1.719(9)	1.722(3)	1.723(7)	1.713(4)	1.734(4)
V1–O13 (×2)	1.721(5)	1.724(6)	1.714(6)	1.716(2)	1.714(5)	1.713(4)	1.704(2)
V1–O11	1.744(7)	1.748(8)	1.746(8)	1.743(3)	1.735(7)	1.741(6)	1.738(4)
V21–O22 (×3)	1.722(8)	1.71(1)	1.728(9)	1.717(3)	1.701(9)	1.706(7)	1.700(4)
V21–O21	1.78(3)	1.78(3)	1.79(4)	1.756(4)	1.74(3)	1.72(2)	1.74(1)
V22–O22 (×3)	1.75(1)	1.71(1)	1.76(1)	1.79(1)	1.82(1)	1.82(1)	1.752(5)
V22–O21	1.90(3)	1.77(1)	1.89(4)	1.89(1)	1.99(3)	2.07(3)	1.96(2)
O3–H1	1.014	1.034	0.992	0.953	0.881	1.008	0.861
H1...O21	2.459	2.309	2.433	2.529	–	–	2.434
H1...O22	2.194	2.230	2.282	2.268	2.454	1.835	2.535
O3...O21	3.151	3.138	3.175	3.171	–	–	3.213
O3...O22	3.155	3.135	3.192	3.181	3.334	2.826	3.238

Table 6.9. Continued.

O3–H2	–	–	–	–	–	–	0.840
H2...O11							2.510
H2...O13							2.324
H2...O22							2.378
O3...O11							3.218
O3...O13							2.870
O3...O22							2.782
M1–M1	2.872(2)	2.861(2)	2.885(2)	2.8781(7)	3.013(2)	2.999(1)	2.864(2)
M1–M1' (×2)	3.054(1)	3.059(1)	3.077(1)	3.067(1)	3.198(1)	3.195(1)	3.066(1)
M2–M2 (×2)	2.5469(3)	2.5500(1)	2.5583(1)	2.5526(1)	2.6340(1)	2.6315(1)	2.5447(1)

S-4: Table 6.10. Selected angles (°) for  $M_{6+x}(\text{OH})_3[\text{VO}_4]_{4-2z}[\text{V}_2\text{O}_7]_z$ .

	CoII	CoIIFeIII	CoIIMnII	CoIIMnIII	MnII	MnIIMnIII	MgII
O3–M1–O3	79.1(1)	79.5(2)	78.9(2)	78.92(5)	77.7(1)	78.1(1)	78.53(7)
O22–M1–O3	78.5(3)	78.5(3)	78.7(3)	78.7(1)	78.1(3)	78.1(2)	78.2(1)
	83.1(3)	83.2(3)	82.9(3)	83.2(1)	82.6(3)	83.0(2)	83.0(1)
O13–M1–O3	85.5(2)	85.4(3)	85.2(2)	85.33(8)	84.3(2)	84.5(2)	84.3(1)
	87.3(2)	87.4(3)	87.3(2)	87.18(9)	86.4(2)	86.9(2)	86.6(1)
	89.8(2)	89.4(3)	89.3(2)	89.38(9)	88.0(2)	87.6(2)	89.6(1)
	164.6(2)	164.8(3)	164.1(2)	164.24(9)	162.0(2)	162.6(2)	162.8(1)
O13–M1–O13	92.2(2)	92.2(2)	92.1(2)	92.26(8)	92.5(2)	92.2(2)	92.4(1)
O13–M1–O11	90.6(2)	90.2(3)	90.8(3)	91.0(1)	89.4(2)	89.3(2)	91.0(1)
	97.4(2)	97.1(3)	97.3(3)	97.3(1)	98.7(3)	98.6(2)	97.1(1)
O13–M1–O22	94.3(3)	94.1(3)	94.5(3)	94.2(1)	94.3(3)	93.8(2)	94.5(2)
	166.0(2)	165.9(3)	165.7(2)	165.88(9)	163.9(2)	163.8(2)	165.3(1)
O11–M1–O3	98.0(2)	98.1(3)	98.5(3)	98.5(1)	99.2(3)	98.8(2)	100.1(2)
	177.0(2)	177.6(3)	177.5(3)	177.4(1)	176.1(3)	175.7(2)	178.5(2)
O11–M1–O22	100.7(3)	101.6(3)	100.9(3)	100.6(1)	104.0(3)	104.6(2)	101.0(2)
O12–M2–O12 (×3)	86.5(3)	86.2(4)	87.2(4)	87.1(2)	86.7(3)	86.7(3)	86.3(2)
O12–M2–O12 (×3)	87.8(3)	87.3(4)	88.5(4)	88.2(2)	87.8(4)	87.8(3)	88.5(2)
O12–M2–O12 (×6)	92.9(2)	93.3(2)	92.2(2)	92.38(7)	92.8(2)	92.8(1)	92.61(9)
O12–M2–O12 (×3)	179.1(4)	179.2(5)	179.1(5)	179.2(2)	179.2(4)	179.2(3)	178.5(3)
O13–V1–O13	104.8(3)	104.8(4)	106.2(4)	105.6(1)	105.5(4)	105.9(3)	106.5(2)

Table 6.10. Continued.

O13–V1– O11 ( $\times 2$ )	107.9(2)	108.1(3)	108.4(2)	108.28(9)	108.1(2)	108.1(2)	108.2(1)
O12–V1– O13 ( $\times 2$ )	110.7(3)	110.7(3)	110.2(3)	110.3(1)	110.7(3)	110.5(2)	110.2(1)
O12–V1– O11	114.4(4)	114.0(5)	113.2(4)	113.7(2)	113.6(4)	113.5(3)	113.4(2)
O22–V21– O22 ( $\times 3$ )	105.9(4)	107.8(5)	105.9(5)	106.0(2)	106.8(4)	108.3(3)	107.2(2)
O22–V21– O21 ( $\times 3$ )	112.9(4)	111.1(4)	112.8(4)	112.8(1)	112.0(4)	110.6(3)	111.7(2)
O22–V22– O22 ( $\times 3$ )	103.2(5)	103.1(7)	102.8(6)	102.7(2)	97.5(8)	98.8(8)	102.6(3)
O22–V22– O21 ( $\times 3$ )	115.2(4)	115.3(6)	115.5(5)	115.6(2)	119.8(6)	118.7(6)	115.7(2)
O3– H1...O21	124.9	136.1	131.2	124.8	–	–	150.7
O3– H1...O22	157.6	145.2	152.0	160.3	179.1	166.8	139.5
O3– H2...O11							142.6
O3– H2...O13							123.0
O3– H2...O22							110.2



S-5: Figure 6.27. Selected Depiction of displacements in the idealized  $\text{Mn}_7(\text{OH})_3[\text{VO}_4]_4$  structure.

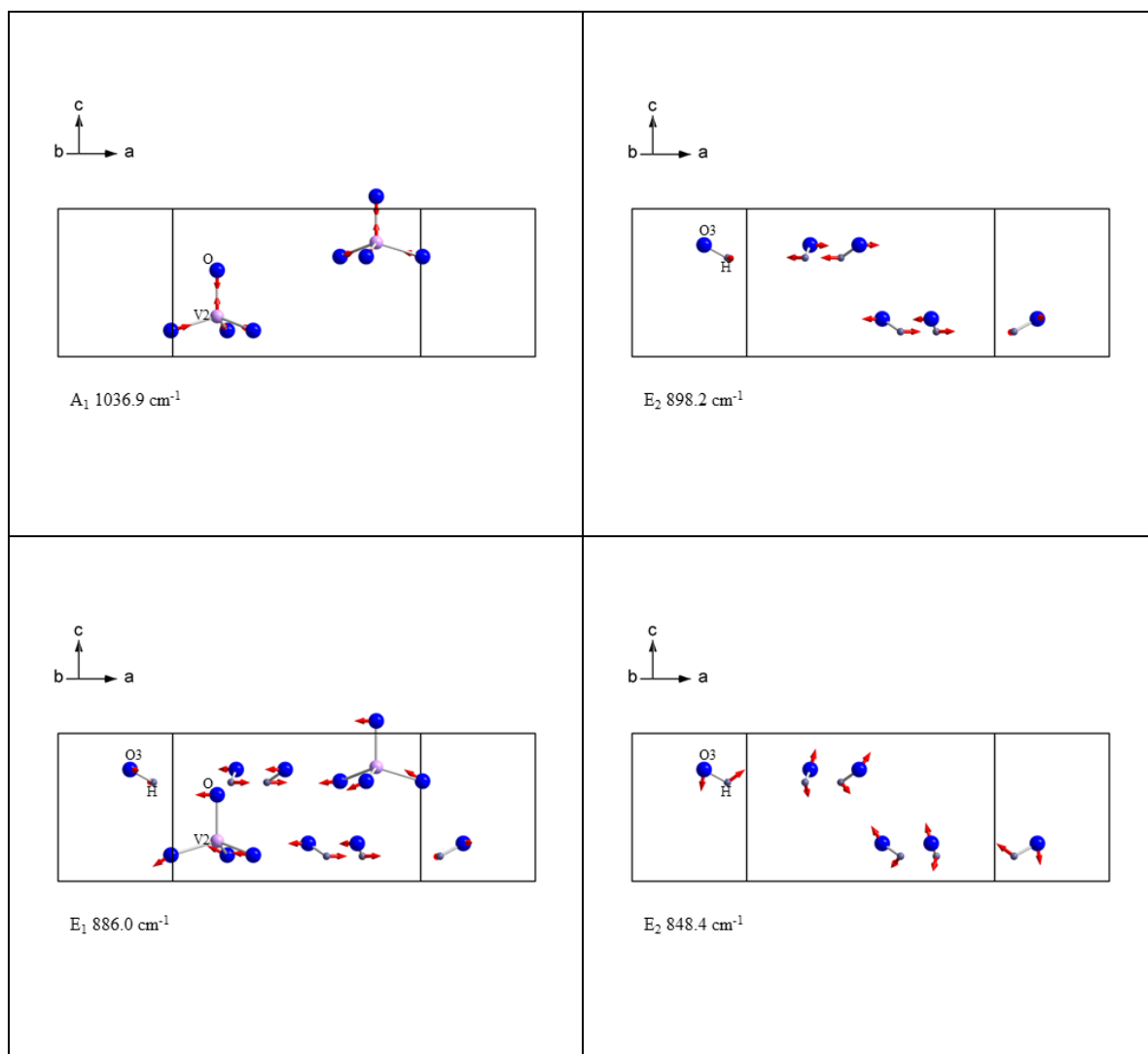


Figure 6.27. Continued.

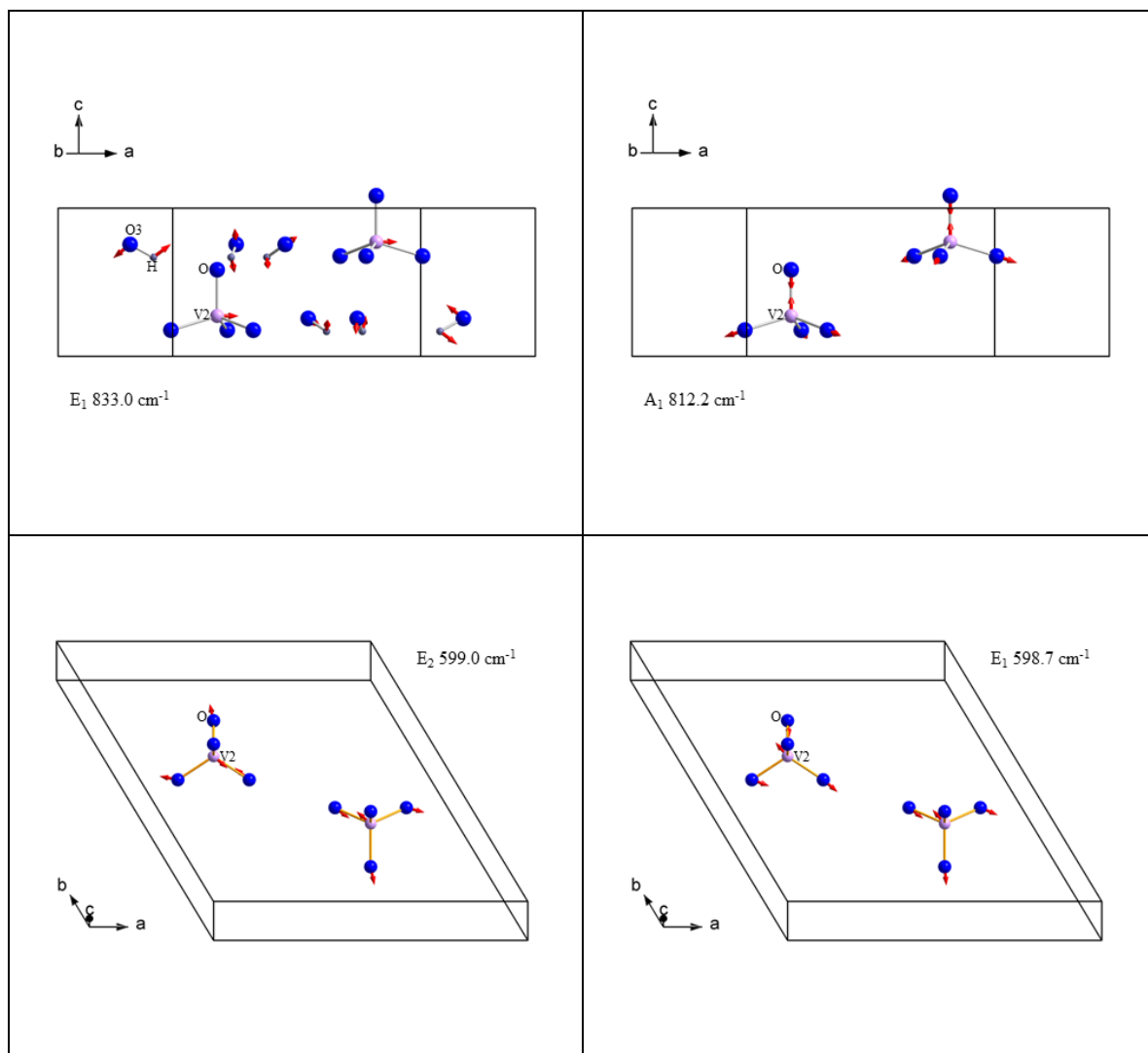


Figure 6.27. Continued.

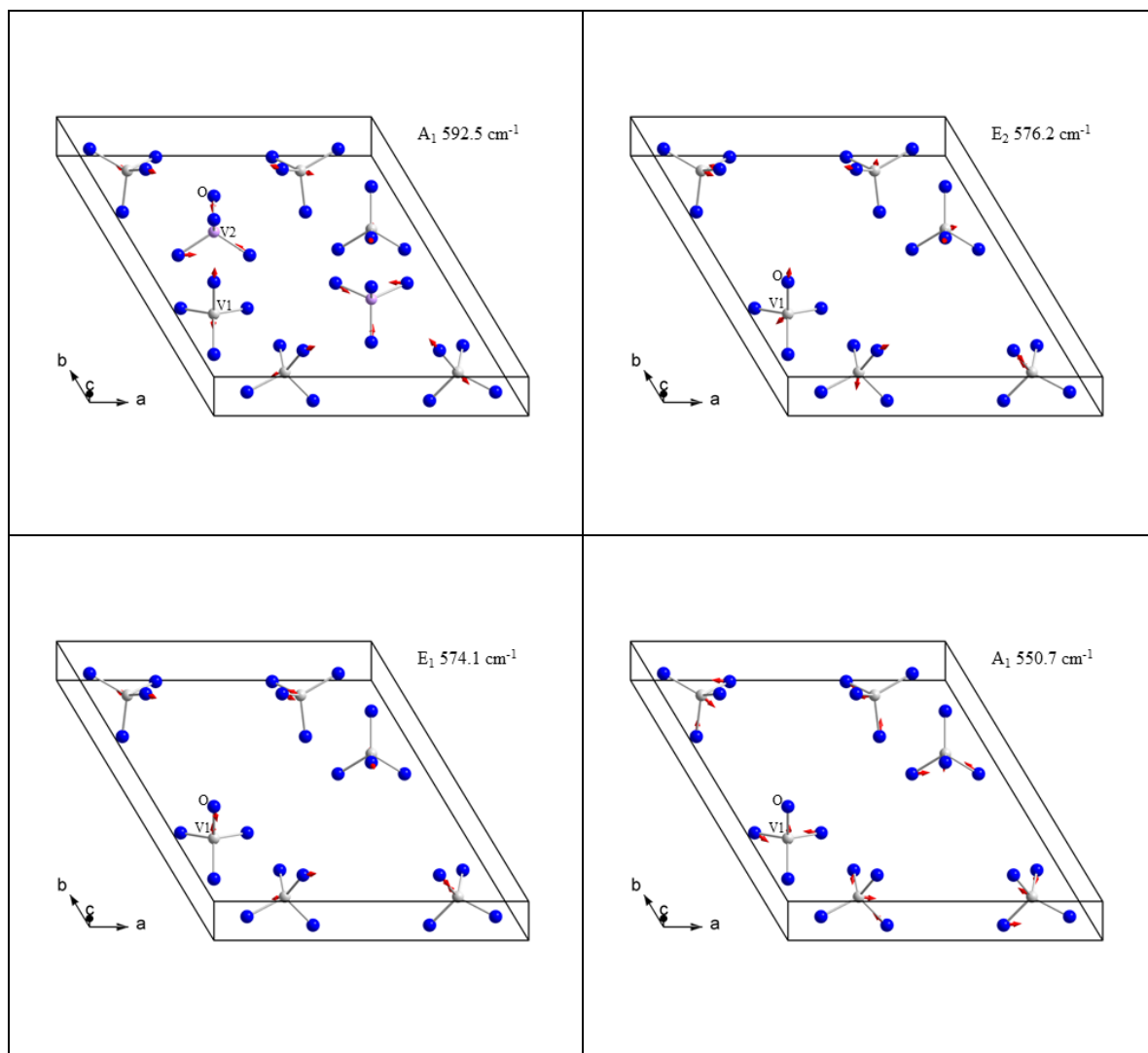


Figure 6.27. Continued.

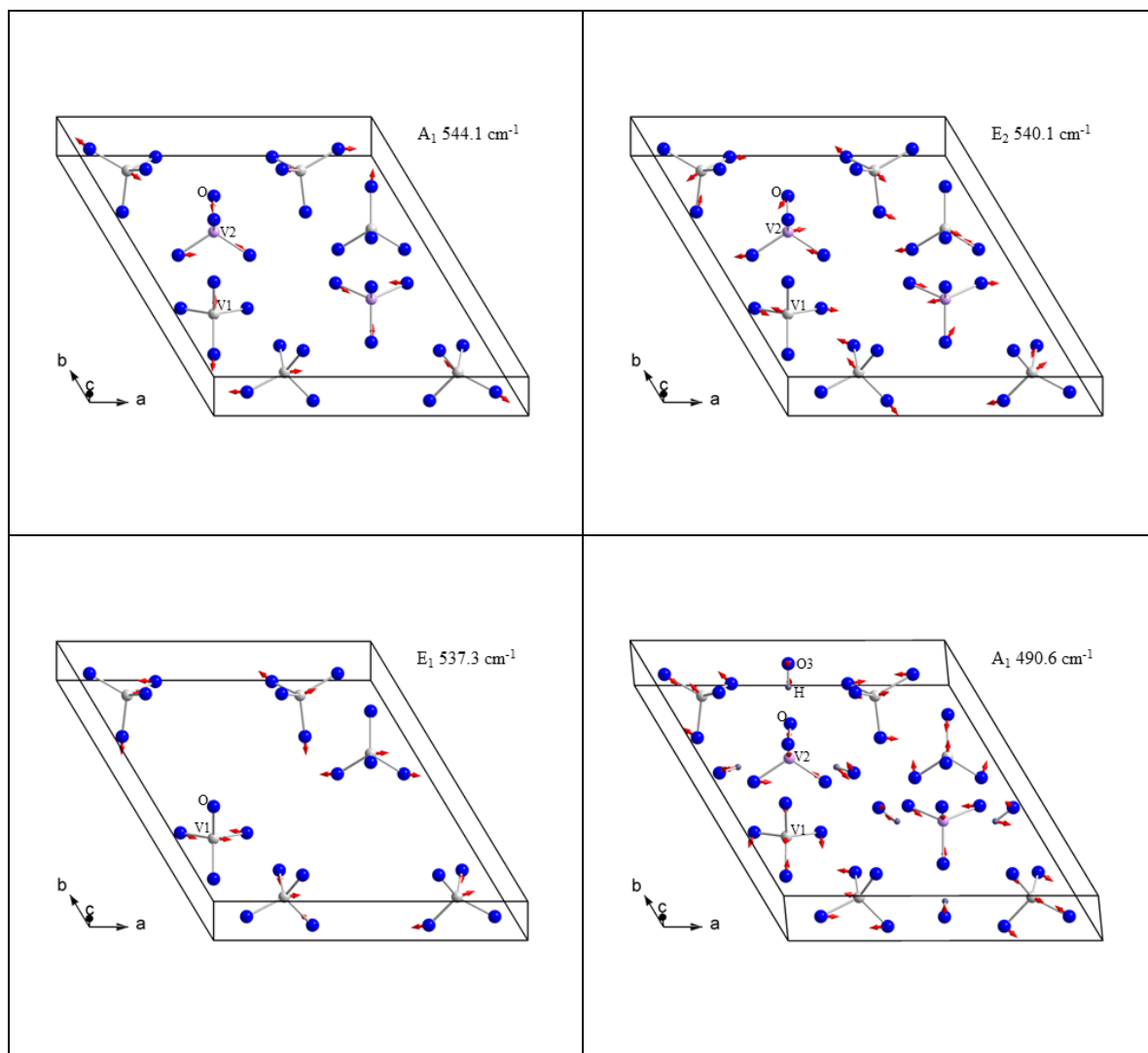
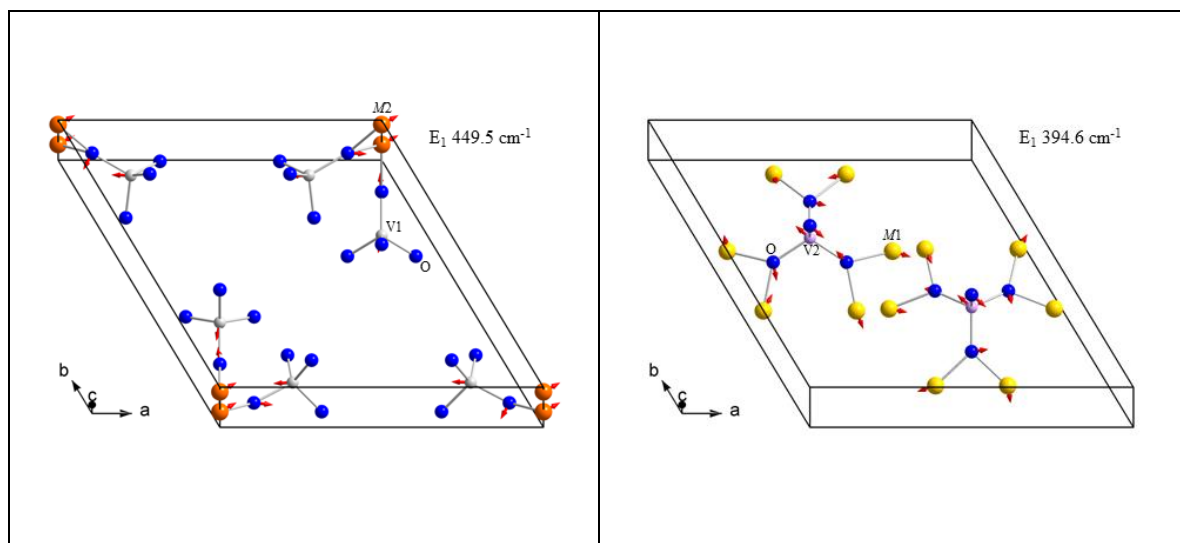


Figure 6.27. Continued.



## Chapter Seven

### Summary

In this work we have explored controlled hydrothermal synthetic routes to synthesize multi-anionic transition metal vanadates. By comparing the products of the reactions under different starting pH-values, vanadate concentrations, and additives such as buffer systems or highly soluble salts, we optimized our synthesis. New compounds crystallizing in an unprecedented structure type were obtained:  $\text{Ba}_2\text{XCu}(\text{OH})[\text{V}_2\text{O}_7]$  with  $X = \text{Cl}, \text{Br}$ . Furthermore,  $\text{BaMn}_9[\text{VO}_4]_6(\text{OH})_2$  and two series of compounds were synthesized:  $M_2(\text{OH})[\text{VO}_4]$  with  $M = \text{Mn}, \text{Cu}$ ;  $M_{6+x}(\text{OH})_3[\text{VO}_4]_{4-2z}[\text{V}_2\text{O}_7]_z$  with  $M = \text{Mn}, \text{Co}, \text{Mg}, \text{Fe}$ . It is interesting to note that  $\text{BaMn}_9[\text{VO}_4]_6(\text{OH})_2$  was only obtained in the very narrow starting pH range of 7.8 to 8.2. The formation of  $\text{Mn}_{6+x}(\text{OH})_3[\text{VO}_4]_{4-2z}[\text{V}_2\text{O}_7]_z$  was found to depend mainly on the vanadate concentration in a buffered basic solution. A solid-solution series ( $M = \text{Co}$  with Mn or Fe) was successfully synthesized for the  $M_{6+x}(\text{OH})_3[\text{VO}_4]_{4-2z}[\text{V}_2\text{O}_7]_z$  type of compounds. Contrary to previous reports on the dumortierite-type of minerals with suggested proton incorporation for charge compensation, we found partial occupancy of vanadate units by divanadate entities under controlled pH-ranges and vanadate concentrations.

The respective crystal structures of twelve compounds in total were determined by single crystal XRD and the phase purity of each sample was confirmed by powder XRD. The presence of hydroxide ions in the structure is indicated from vibrational spectroscopy

(Infrared and Raman). Furthermore, the lattice dynamics with respect to the vanadate ions were studied by theoretical methods (DFT).

As the structures contain low-dimensional connectivities of the magnetic ions, the structure-property relationships were investigated for each compound.  $\text{Ba}_2\text{XCu}(\text{OH})[\text{V}_2\text{O}_7]$  contains  $\text{Cu}^{2+}$  ions with the unpaired electron in the magnetically active  $d_{x^2-y^2}$  orbital. Thus, the relevant connectivity between neighboring Cu-ions is formed via  $\text{OH}^-$  and can be assigned to a quasi 1D  $S = 1/2$  Heisenberg system. The magnetic properties were found to be antiferromagnetic and were described using the theoretical models given by Bonner and Fisher and Klümper *et al.* For  $\text{Cu}_2(\text{OH})[\text{VO}_4]$  with two-dimensional Cu–O–Cu connectivity, canted antiferromagnetic 3D long-range order was confirmed and corroborates the importance of bridging Cu–O–V–O–Cu pathways between adjacent layers.

$\text{BaMn}_9[\text{VO}_4]_6(\text{OH})_2$  exhibits a unique the ‘paddle-wheel’ structural feature of mainly edge-sharing Mn–O<sub>2</sub>–Mn connectivity. The competing ferro- and antiferromagnetic correlations result from the inherent geometrically frustrated equilateral Mn<sub>3</sub>-triangles and are the origin of canted antiferromagnetism here. Furthermore, the anomaly of the dielectric constant at  $T_C$  indicates magneto-dielectric coupling of the magnetic long-range order to the lattice.

The  $M_{6+x}(\text{OH})_3[\text{VO}_4]_{4-2z}[\text{V}_2\text{O}_7]_z$  series of compounds consist of a framework made up by *M*-dimers which connect to a kagome-like arrangement in 2D. This feature relates to the occurrence of two types of channels. The six-membered ones contain isolated face-sharing  ${}^\infty_1[\text{MO}_6]$  chains and the three-membered ones are statistically occupied by

$\text{VO}_4^{3-}$  and  $\text{V}_2\text{O}_7^{4-}$ . The high-temperature fit to a Curie-Weiss law indicates dominant antiferromagnetic interactions. However, the onset of effectively ferromagnetic correlations related to the frustrated nature of the three-membered rings alters the long-range order and ferrimagnetic-like behavior is observed below  $T_C$ . Interestingly, all solid solutions (doped compounds with  $\text{Mn}^{2+}$ ,  $\text{Mn}^{3+}$ , or  $\text{Fe}^{3+}$ ) of the Co-series showed the same  $T_C$  but differed significantly in the respective Weiss-constants, magnetic hysteresis loops, and effective magnetic entropies associated with the  $\lambda$ -anomaly.

Overall, we have achieved the synthesis of several novel magnetic compounds and studied the structure-property relationships by spectroscopic and thermodynamic measurements.